University of Southern Queensland

Faculty of Health, Engineering and Sciences

Analysis of Glaucoma Drainage Devices through Solid Modelling and CFD Flow Behaviour

A dissertation submitted by

James O'Neill

in fulfilment of the requirements of

ENP4111 Professional Engineer Research Project

towards the degree of

Bachelor of Engineering (Honours) (Mechanical)

Submitted November, 2024

Abstract

Glaucoma, the world's leading cause of irreversible blindness, is defined as a group of eye conditions that causes an uncontrolled build-up of aqueous humour within the eye. This fluid build-up, and the resulting increase of intraocular pressure, causes permanent optic nerve damage and vision loss. To combat the most advanced and aggressive cases, Glaucoma Drainage Devices (GDDs) are the most widely used treatment option. Amongst the several types of GDDs, the non-valvular implants (primarily the Baerveldt and Paul) are the most widely used across Australia. With Computational Fluid Dynamics (CFD), a powerful tool used throughout the engineering industry to predict the behaviour of fluid within systems, this project aims to study the differences in flow and pressure drop over several realistic tube geometries and other more experimental variations.

To achieve this, Creo Parametric was used to design the 3D CAD models for the tube geometries. Six tube variations were produced for each of the Baerveldt and Paul glaucoma implants, with the aim to reflect both the realistic surgical procedures and the novel solutions to the most common GDD failure modes. The standard tube was modelled off obtained data and acted as a baseline comparison to the other variations. The sutured tube reflected the realistic surgical procedure where a 10-0 nylon suture is used to limit initial flow rate. Furthermore, the snipped inlet tube reflects the standard surgical practice to make a small cut to the end of the drainage tube to position it within the eye. The single and double finned tubes were experimental solutions to the common issue of biofouling present within GDDs. Finally, the rounded inlet tube was another novel solution to combat the negative effects propagated by the snipped variant seen within surgery.

Using Ansys Fluent, several simulations were run over a variety of flow rates ranging from 1.6μL/min to 25μL/min for each tube variation. This data was tabulated, plotted, and compared within the report to reveal the effectiveness of each solution. The results revealed that at a normal physiological flow rate of 2.5μL/min, the standard Baerveldt tube saw a pressure drop of 3.84 Pa, compared to 143.5 Pa for the Paul. These CFD results suggest the Paul implant's high-pressure drop could enhance surgical outcomes faster, mirroring its rising popularity in Australia. The single fin design appeared to mitigate biofouling while balancing shear stress, and the double fin was found to be problematic through the potential for tube blockage. The flow plots revealed the rounded inlet tube optimised flow, showing potential over the traditional snipped inlet design.

University of Southern Queensland

School of Engineering

ENP4111 Professional Engineer Research Project

Limitations of Use

The Council of the University of Southern Queensland, its School of Engineering, and the staff of the University of Southern Queensland, do not accept any responsibility for the truth, accuracy or completeness of material contained within or associated with this dissertation.

Persons using all or any part of this material do so at their own risk, and not at the risk of the Council of the University of Southern Queensland, its School of Engineering or the staff of the University of Southern Queensland.

This dissertation reports an educational exercise and has no purpose or validity beyond this exercise. The sole purpose of the course pair entitled “Research Project” is to contribute to the overall education within the student’s chosen degree program. This document, the associated hardware, software, drawings, and other material set out in the associated appendices should not be used for any other purpose: if they are so used, it is entirely at the risk of the user.

Certification

I certify that the ideas, designs and experimental work, results, analyses, and conclusions set out in this dissertation are entirely my own effort, except where otherwise indicated and acknowledged.

I further certify that the work is original and has not been previously submitted for assessment in any other course or institution, except where specifically stated.

James O'Neill

Student Number: [redacted]

Acknowledgements

I would like to extend my sincerest gratitude and appreciation to my supervisor for this project, Steven Goh, for his continual and unwavering support over its duration. His guidance through the many meetings, emails, and general discussion regarding the project have assisted me greatly throughout the entire process. The completion of this project has required significant skill development in many unfamiliar areas, which has undoubtedly elevated my engineering ability.

To my family and friends, I greatly appreciate your continued support throughout not only this research project, but my entire study journey thus far. My accomplishments would not be possible without your overwhelming encouragement and continual belief in me, and for that I am eternally grateful.

James O'Neill

Contents

List of Figures

List of Tables

Nomenclature

CFD	Computational Fluid Dynamics
GDD	Glaucoma Drainage Device
IOP	Intraocular Pressure
AH	Aqueous Humour
3D	Three Dimensional
UniSQ	University of Southern Queensland
PDE	Partial Differential Equation
MIGS	Minimally Invasive Glaucoma Surgery
AGV	Ahmed Glaucoma Valve

Chapter 1 – Introduction

1.1 Outline of Study

This study focuses on the analysis of Glaucoma Drainage Devices (GDDs) through solid modelling, and the implementation of Computational Fluid Dynamics (CFD) software to analyse the fluid flow behaviour. Through the 3D modelling software Creo Parametric, multiple variants of the Baerveldt and Paul drainage tubes will be modelled for analysis. The tube variations will be produced in direct reference to realistic surgical procedures, along with theoretical solutions to the major design flaws evident in GDD technology. The CFD software ANSYS Fluent will be used to run analysis on each tube, with aim to investigate the differences in notable variables such as pressure drop, wall shear stress, and the fluid flow profiles.

GDD development began with the initial testing of the Molteno implant in 1969, with an influx of different variations in the early 1990s. The design of the widely used non-valvular implants all consist of a tube to initiate drainage, and an end plate. The Paul implant, developed in 2012, represents the most modern innovation in this branch of technology, yet it continues to follow the foundational principles established by the Molteno. Despite considerable progress in the broader field of medical engineering over recent years, innovation within this specific area has remained relatively stagnant. Subsequently, this study aims to investigate the implications and possibilities with the use of modern CFD software in GDD technology.

1.2 Project Aims and Objectives

The aim of this project, as outlined, is to investigate the fluid flow behaviour of GDDs through solid modelling and CFD analysis. The initial project specification can be found in Appendix A, although through the analysis process some key objectives shifted to be more appropriate for the final project. These aims and objectives can be categorised into the following major sections:

1. Familiarise with the CFD software, become more competent in its utilisation and the fundamental principles required to analyse GDD systems.

2. Conduct background research via the literature review to investigate GDD technology, including common surgical techniques and known methods of failure. Research the most common GDDs used in Australia, employ these implants for the remainder of the study.

3. Research and analyse previous CFD studies in the field of glaucoma and glaucoma drainage devices. Review this research to find the appropriate theoretical calculations, along with exploring other similar methodologies to guide the project.

4. Utilise Creo Parametric to model several variations of the drainage tubes for the most common GDDs, citing the literature review for the models representing the realistic surgical procedures. Theorise and model novel solutions to the most common failure modes for GDDs.

5. Run simulations for the developed models within ANSYS Fluent over a variety of flow rate conditions.

6. Analyse the CFD results, and produce tabular and graphical representations of the data. Make critical observations on the influence the different tube variations have on the fluid flow profile, along with investigating the key variables of pressure drop and wall shear stress. This comparative analysis will provide insight into the effects of the current surgical procedures and the novel solutions proposed via the research gathered within the literature review.

7. Draw final conclusions, recommend future work, outline the success and parameters of the CFD model, and reflect on the overall process of the research project.

1.3 Dissertation Overview

The dissertation is structured into the following chapters:

Chapter 2: Literature Review

This chapter investigates existing research to provide the foundational background knowledge required to understand the research project topic. Key concepts like the existing common GDD failure methods, surgical procedures, and dimensional information are detailed in full. Existing literature related to CFD in glaucoma applications is also reviewed, with crucial findings regarding theoretical calculations and existing methodologies analysed in the context of this study.

Chapter 3: Methodology Project Plan

This chapter provides an initial framework of the project methodology, brief overview, and a project resource plan. The GDD dimensional information extracted from the literature review is also presented, and the initial simulation conditions are outlined for ANSYS Fluent.

Chapter 4: 3D Modelling

This chapter details the creation of the 3D models for the Baerveldt and Paul GDD implants using Creo Parametric. The process of developing the model variations, including the standard, sutured, finned, and modified inlet designs, was displayed. The justifications and assumptions for each model are also discussed, with the accompanying figures to illustrate the designs.

Chapter 5: CFD Simulation

This chapter outlines the CFD simulation process utilised throughout this research project. The initial conditions, theoretical calculations, mesh independency study, and simulation results are displayed for each tube variation modelled in the previous chapter. With tabulated simulation data, along with accompanying pressure and wall shear stress contour plots, this chapter acts as a precursor to the following results discussion section of the dissertation.

Chapter 6: Discussion

This chapter analyses and critiques the raw data presented in Chapter 5. Through graphical representation and Ansys flow plots, the simulation methodology and results are discussed to reveal key patterns within the data and the subsequent major findings of the project. The observed limitations, expansion potential, and potential experimental framework is outlined to conclude this chapter.

Chapter 7: Conclusions

This chapter recapitulates the entire research project by first comparing the results to the initial project objectives and research questions. The project limitations and further work is also summarised and discussed, along with some final statements to conclude the dissertation.

1.4 Summary of Methodology

Detailing a structured and coherent methodology is integral to ensuring replicability, and to outline the logical progression of thoughts and ideas. Following the literature review chapter, all the required data and conditions will be acquired to utilise throughout the solid modelling process. Citing recent works referenced in the literature review will ensure accuracy when developing models to replicate real life surgical procedure. Additionally, explicitly stating the justifications and assumptions used to develop the theoretical models will provide clear insight into the thought process behind these decisions.

The CFD section of this research project aims to simulate the produced models over a variety of flow rates, spanning from realistic physiological flow and beyond, to show the flow patterns over these

elevated flow rates. Each model will be subjected to a mesh independency study, where the industry standard 5% error tolerance will be enforced. This standard requirement for every CFD study ensures simulation accuracy relative to the input conditions.

CFD simulation results for pressure drop and wall shear stress will then be tabulated for each tube variation, with the plots inputted where appropriate. Fluid flow profile plots will also be produced where required, particularly to investigate the fluid behaviour with a variation of inlet geometry.

Simulation data will then be produced graphically, making critical comparisons between tube variations. This section of the methodology will aim to consolidate all the CFD analysis into concise conclusions, critiquing the data before making final recommendations and suggestions for further work.

The methodology devised will adhere to the following:

1. Develop 3D models through Creo Parametric guided by the findings of the literature review for the Baerveldt and Paul GDDs. The tube geometries will separate into two categories, adhering to either:
    a. Realistic surgical techniques (Standard Tube, Sutured Tube, Snipped Tube)
    b. Investigative solutions (Single and Double Finned Tube, Rounded Inlet Tube)
2. Simulate each tube variation through CFD software ANSYS Fluent.
3. Perform the applicable theoretical calculations to verify simulations.
4. Document simulation results for key variables, such as pressure drop, wall shear stress, and fluid flow profiles where appropriate.
5. Produce the simulation data via tabulated and graphical methods.
6. Discuss the results, making critical comparisons between tube variations and theoretical calculations.
7. Draw final conclusions and recommend further work.

1.5 Project Planning

1.5.1 Resource Requirements

Given the computer-based nature of this project, there are minimal physical resource requirements needed to successfully complete this project. Primarily, this project relies on a stable internet connection and the relevant software access. The significant resource requirements are as follows:

- ANSYS Fluent (student access)
- Creo Parametric (student access through Turbo)

- UniSQ approved Student VPN (for Turbo accessibility)
- Internet access with a stable connection
- Vehicle (travelling to and from UniSQ campus when required)
- Computer (for solid modelling, CFD, research, and online meeting purposes)

1.5.2 Risk Assessment

It is a necessity to conduct a risk assessment for any engineering project to ensure each task is being completed with the highest order of safety. As seen in section 1.5.1, this computer-based research project will present minimal direct risks as there is little physical activity involved. However, a comprehensive risk assessment can be found in Appendix B.

An outline of the major risks identified will be presented:

- Hardware and software failure – computer or software failure may corrupt document and simulation files.
- Fatigue effects – continual use of a computer may cause eye strain, dehydration, mental fatigue.
- Physical effects – irregular posture caused by the overuse of a computer can cause physical harm, car accident travelling to the university campus.

A summary of the prevention methods will also be presented:

- Continual backups, saving to multiple places and keeping an external copy on a physical hard drive/USB can mitigate hardware/software failure.
- Scheduling regular breaks, stretching, and positioning the chair/monitors ergonomically can assist in reducing the effects of fatigue and bad posture.
- Following the standard road safety rules and maintaining proper vehicle condition to adhere to safety standards can prevent road accidents.

1.6 Ethical Considerations

This research project is designed to analyse GDDs through CFD, and investigate theoretical solutions to common GDD failure methods. If successful, this research could lead to the improvement of GDD technology, with the potential for alternate designs to be explored in the future. This would directly result in a better quality of life for current and future glaucoma patients. Subsequently, while the initial disclaimer outlines the potential limitations of this dissertation, this research will strive to be conducted with the upmost integrity and accuracy.

Chapter 2 – Literature Review

2.1 Chapter Overview

This chapter details the fundamental background knowledge of glaucoma, as this is imperative to effectively perform and understand the realism of the CFD simulation analysis. The standard surgical procedure for GDD implementation is also detailed in full, which is imperative for the latter sections of this research project, namely the solid modelling chapter where these surgical techniques will be implemented into model development. Furthermore, this chapter provides key details regarding GDD technology, including their development history, function, various types and common complications. The solid modelling section of this chapter details the available dimensional information required to model the selected GDDs in preparation for the ANSYS Fluent simulations. The extensive CFD section outlines background theory, and a detailed review on existing CFD studies in the field of glaucoma and ophthalmology. Each study is summarized with a concise overview, outlining key assumptions and the concluding results. A critical analysis of these reports serves to anchor the methodology within established literature. This chapter is concluded with additional research on the boundary conditions, model selection, mesh refinement and material characteristics specific to this research project. The research gap identified throughout the literature is then presented, with the discrepancy in results being consolidated into a problem definition and governing research questions to refer to throughout the dissertation.

2.2 Glaucoma

2.2.1 Background Research

There are four major types of glaucoma, each with varying degrees of severity and probability of occurring.

1. Open-angle glaucoma

Open-angle glaucoma is the most common type experienced by people who have been diagnosed, with an approximate 90% of all cases being open-angle. In this instance, even though the eye's drainage canals appear to be functioning normally, resistance builds in this area which puts pressure on the optic nerve causing irreversible damage (see figure 2.1). (Cleveland Clinic, 2022)

2. Closed angle glaucoma

This rare type of glaucoma occurs suddenly, often with severe effects. Closed-angle glaucoma is defined as when the angle between the iris and cornea is too narrow. Common causes include rapid dilation of the eye, which blocks drainage canals. Subsequently, this raises eye pressure and damages the optic nerve as the aqueous fluid build-up is prevented from flowing out. (Cleveland Clinic, 2022)

3. Normal-tension glaucoma

More common amongst people with Asian heritage, ophthalmologists are still uncertain on the causes of this type of glaucoma. People diagnosed with this form of glaucoma generally have a normal to low IOP. (Cleveland Clinic, 2022)

4. Congenital glaucoma

Congenital glaucoma is caused by the incorrect formation of drainage canals in the womb. Also known as infantile or paediatric glaucoma, babies can develop this condition with symptoms becoming noticed during infancy or early childhood. (Cleveland Clinic, 2022)

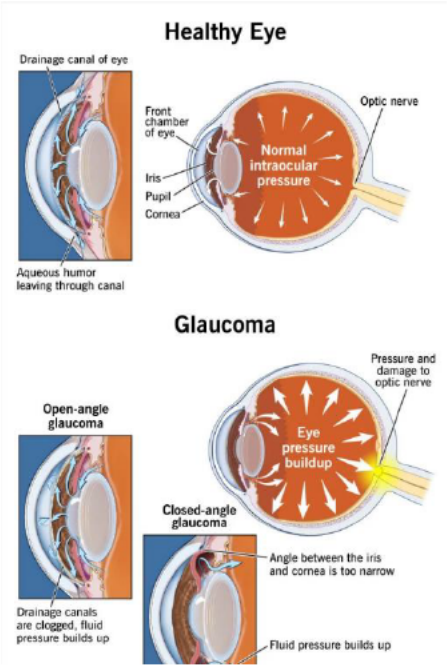

Figure 2.1: Healthy Eye vs Glaucoma Diagram (Cleveland Clinic, 2022)

2.2.2 Alternate Treatment Options

As glaucoma varies significantly in both severity and aggressiveness in each individual case, there have been several treatment options developed to suit the individual needs of the patient. All glaucoma treatment methods prioritise the lowering of IOP, to reduce damage to the optic nerve (Bhattacharya, S.K. et al. 2010).

2.2.2.1 Medication

The most widely used method to treat low to mild glaucoma (and generally the first step for any treatment) is to prescribe glaucoma medication. Delivered in the form of an eye drop, these medications aim to lower IOP by both increasing aqueous humour drainage, and by reducing the amount of aqueous humour that is produced by the eye (Glaucoma Australia, 2017).

The five major medicines prescribed for glaucoma consist of Prostaglandin Analogues, Beta Blockers, Alpha Agonists, Carbonic Anhydrase Inhibitors, and Cholinergic (Miotics) (Glaucoma Australia, 2017).

Prostaglandin Analogues, consisting of bimatoprost, latanoprost, travoprost, and tafluprost, aim to increase the outflow of aqueous humour. This medication, taken once daily, is one of two first

treatment choices (Optometry Australia, 2019). Common side effects include an increase in growth and darkening of eyelashes, eye redness, and an increase in iris pigmentation for certain patients (Glaucoma Australia, 2017).

Beta Blockers, used once to twice daily, reduce the production of aqueous humour within the eye. As another first order treatment option, Timolol is the most used type in this designation. Some common side ocular effects include blurred vision, ocular discomfort, and increased lacrimation (watery eyes) (Optometry Australia, 2019). This medicine must be used with precaution as other notable systemic side effects include general fatigue, slow heart rate, and low blood pressure (Glaucoma Australia, 2017).

Alpha Agonists, a second order treatment choice, may be used multiple times daily to both increase aqueous outflow and decrease aqueous production (Optometry Australia, 2019). Common types, such as Brimonidine, can cause stinging, headaches, fatigue, dry mouth, and general drowsiness (Glaucoma Australia, 2017).

Carbonic Anhydrase Inhibitors, which can come in both eye drop and oral form, are used to decrease aqueous production Glaucoma Australia, 2017). This type of glaucoma medication (used two to three times per day) can cause a mild stinging or burning after instillation, along with other systemic effects similar to the alpha antagonists, such as headaches, dry mouth, fatigue, and nausea (Optometry Australia, 2019).

Cholinergic (Miotics) is a third order treatment choice that increases aqueous humour outflow (Optometry Australia, 2019). This most common cholinergic is Pilocarpine, and the major side effect includes blurred vision through a constriction of the pupil (Glaucoma Australia, 2017).

For convenience, these five major drug types can be also combined in various ways to produce combination therapies. These combinations are applicable in certain applications where patients are required to take multiple differing drugs, which thereby reduces the total cost and amount of drops that are required to be taken daily (Glaucoma Australia, 2017).

2.2.2.2 Selective Laser Trabeculoplasty (SLT)

The most widely used and accepted laser treatment is selective laser trabeculoplasty (SLT), which was originally introduced in 1998 (Conlon, R. et al. 2017). SLT reduces IOP by focusing low-energy pulses of light on the drainage canal within the eye, to widen and improve the natural drainage pathways (Skalicky, D. 2024). Studies suggest that this type of laser therapy, whilst still not fully understood, reduces IOP in the majority of eyes by over 20% after 12 months, with very minimal damage to the trabecular meshwork structure. While effective in the short term, the mean survival time (time that 50% of eyes fail) for SLP is approximately two years, as the IOP lowering effect of SLT reduces with time (Conlon, R. et al. 2017).

2.2.2.3 Trabeculectomy

Trabeculectomy is often required when both medication and laser therapy cannot control the patients IOP (Conlon, R. et al. 2017). This procedure is an invasive surgery in which an incision is made in the sclera to form a flap, and thus, a new drainage pathway is created. This pathway is then protected by both the flap and the conjunctiva of the eye. Upon completion, this surgery results in a small blister of fluid, called a bleb. This fluid blister is situated underneath the eyelid, but still on the eyes top surface. Ideally, there is no additional tearing as the produced fluid inside the blister is absorbed into blood vessels (Johnson, T.V. 2023). While this type of surgery is considered the 'gold standard' throughout the industry, there is an accompanying high rate of complications for both the short and long term (Conlon, R. et al. 2017). The associated risks include surgical failure to control the eye pressure, fluid leaking from the surgery site, hypotony (low pressure that causes blurry vision), eye bleeding, infections, and the increased formation of cataracts (Johnson, T.V. 2023).

2.2.3 MIGS

Throughout recent times, minimally invasive glaucoma surgery (MIGS) has revolutionized management for low to moderate glaucoma cases. This type of surgery, as the name indicates, requires minimal tissue trauma to achieve results. As discussed, the conventional treatments of low to mild glaucoma include glaucoma medication, and laser treatments such as laser iridotomy and trabeculoplasty (Gurnani, B. Tripathy, K. 2023). While these approaches can be very successful, researchers have strived for more long-term methods to reduce IOP, and the recent MIGS developments and implant technologies have produced the most effective results to date.

The four main classifications to reduce IOP via MIGS include (Gurnani, B. Tripathy, K. 2023):

1. Increasing Aqueous Outflow from Trabecular Meshwork and Schlemm Canal
2. Increased Uveoscleral Outflow through Suprachoroidal Space
3. Aqueous Shunt through Subconjunctival Space
4. Ciliary Process Ablation Resulting in Reduced Aqueous Outflow

As the project topic will focus specifically on implant technology to improve aqueous flow, the stent implants will be primary focus for this section of the literature review. The most common devices used to reduce IOP through an increase in aqueous flow is the iStent, iStent Inject, and Hydrus Stent.

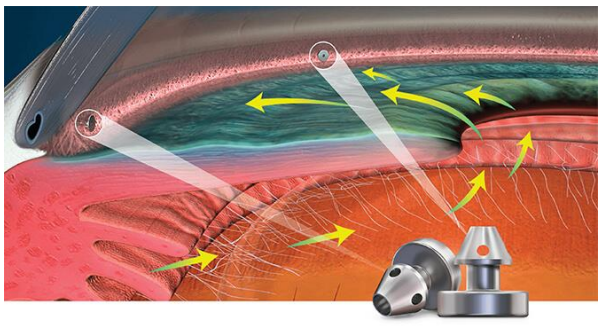

Figure 2.2: iStent Inject Surgery Implementation Diagram (Glaukos, 2023)

The iStent and its second generation, the iStent Inject, is a small (360 x 230µm) heparin-coated and non-ferromagnetic titanium implant that assists with IOP reduction. This tapered head of this stent sits within Schlemm's canal, with the anterior entering

the TM. In surgery, generally two of these stents are placed in the TM, approximately 30-60 degrees from one another (figure 2.2). Using these implants, researchers have seen a 40-44% reduction in IOP in approximately 60% of patients by one year (Gurnani, B. Tripathy, K. 2023).

The crescent-shaped Hydrus stent (figure 2.3) is 8mm in length and 290µm in diameter, and is made of nitinol material. This stent is implanted into the nasal or inferior temporal quadrant, which in application, bypasses the TM and allows better aqueous flow. This stent initially dilates Schlemm's Canal, which allows for easier outflow through the stents collection channels. Researchers have indicated a 20% IOP reduction in 77% of eyes at a 24-month post-surgery, in comparison to antiglaucoma medications (Gurnani, B. Tripathy, K. 2023).

Figure 2.3: Hydrus Stent (Kerr, N. n.d)

As for any implant technology used in medical applications, there are both benefits and potential complications with their installation. Due to the less invasive nature of MIGS implants, the major benefit is seen through the high safety of the procedure, as there is a reduced risk of several complications (such as hypotony, haemorrhage, choroidal detachment, and effusion). Moreover, there is generally very minimal alteration to natural anatomy during the surgery, which reduces the post operative recovery time in comparison to other more invasive surgeries (Gurnani, B. Tripathy, K. 2023).

While still safer than many other eye procedures, there remains to chance of major medical complications that may arise in MIGS can be seen in figure 2.4.

Due to the recent development of many of these technologies, the long-term effects of MIGS, and particularly the stent implants, are still unknown. Moreover, in cases of more aggressive or progressed glaucoma, the IOP lowering effects of MIGS is limited. These issues lead to the requirement for the more invasive glaucoma drainage devices (GDDs). (Kasahara, M. Shoji, N. 2020)

Complications

- Hyphema
- Hypotony
- Stent displacement
- Stent malposition
- Stent obstruction
- Stent migration
- Stent fragmentation
- Conjunctival gaping
- Peripheral anterior synechiae
- Transient IOP elevation
- Post-operative inflammation
- Retinal detachment
- Choroidal detachment
- Cystoid macular edema
- IOL dislocation
- IOL subluxation
- Posterior capsular opacification[45]

Figure 2.4: MIGS Complications List (Kasahara, M. Shoji, N. 2020)

2.2.4 GDDs

2.2.4.1 Background

Glaucoma Drainage Devices (GDDs) are implants that regulate the aqueous fluid drainage for glaucoma patients. These implants are generally reserved for patients with refractory glaucoma, which is defined as uncontrolled IOP causing deterioration of the optic nerve, despite maximal use of glaucoma medications (Kang, Y. Shin, J. Kim, D. 2022). GDDs have various designs that are used for specific applications at the discretion of the ophthalmologist, which is dependent on the condition of the eye. While varied, all GDDs share a similar basic design that consists of a shunting tube, which is inserted into the anterior chamber, and an endplate that receives and disperses the aqueous humour into the surrounding tissues (Agrawal, P. and Bhardwaj, P. 2020). These devices have varied benefits, implications, and risks, depending on the situation. All these factors are evaluated in a case-by-case scenario by Ophthalmologists to determine which implant should be used for the surgery.

Glaucoma drainage devices are separated into two categories, "valvular" and "non-valvular", which is dependent on if the device contains a flow restriction mechanism that limits aqueous humour flow (Agrawal, P. and Bhardwaj, P. 2020). Two of the non-valvular implants, Paul and Baerveldt, are the two most common GDDs seen in Australia (Coote, M. 2017).

The five major types of GDD include:

1. Molteno Implant (non-valvular)
2. Baerveldt Glaucoma Implant (non-valvular)
3. Paul Glaucoma Implant (non-valvular)
4. Ahmed Glaucoma Valve (valvular)
5. Krupin Implant (valvular)

Table 2.1: Major GDDs and Post-Operative Complications (Gupta, S. and Jeria, S. 2022)

Year of development of different Implants and their postoperative complications

Name of glaucoma drainage devices.	Year of development	Types of opening	Postoperative complications.
Molteno	1979	Non-valvular	More chances of hypotony.
Baerveldt	1990	Non-valvular	More chances of hypotony. Greatest amount of chances of diplopia are found with this implant.
Krupin	1990	Valvular	Comparatively fewer chances of hypotony
Ahmed	1993	Valvular	Comparatively fewer chances of hypotony. Choroidal effusion.

2.2.4.2 Surgical Procedure

As outlined by Agrawal and Bhardwaj (2020), all GDDs essentially follow the same surgical procedure, with the average duration spanning up to a maximum approximately 2 hours. The surgery, performed under general anaesthetic, initiates with the cleaning and sterilisation of the eye in a regulatory way in preparation for the initial incision. This cut creates a flap in the supertemporal quadrant, which is then extended by horizontal and vertical incisions to relax the flap area, and to allow for more surgical access (figure 2.5B). With caution, a hook is employed to find the superior and lateral recti muscles to isolate them from the implant site. After sufficient cleaning, the implant plate is tucked into the sub-Tenon's space. Callipers are then utilised to ensure the plate is positioned correctly, and then the implant is secured via 9-0 prolene surgical stitching through the sclera and eyelets on the implant plate (figure 2.5C). The implant tube is then shortened accordingly for entry approximately 1-2mm into the aqueous humour filled anterior chamber. This trimming process will often result in a sharp and angular cut, as visible in figure 2.6. Additional stitching occurs to secure the tube in place, ensuring the tube will not interfere with cornea or iris to prevent further complications (figure 2.5D). For non-valvular implants, an additional 10-0 nylon suture may be implemented to tighten the tube until the flow rate is approximately halved (figure 2.5E). This process reduces the chance of hypotony, while also controlling the initial flow over the end plate. This suturing must not be overly tight, to litigate the chance of tube castration. Finally, after additional sterilisation and cleaning, a connective tissue graft is stitched to fully secure the implant while the flap is returned and sutured to its natural position (figure 2.5F).

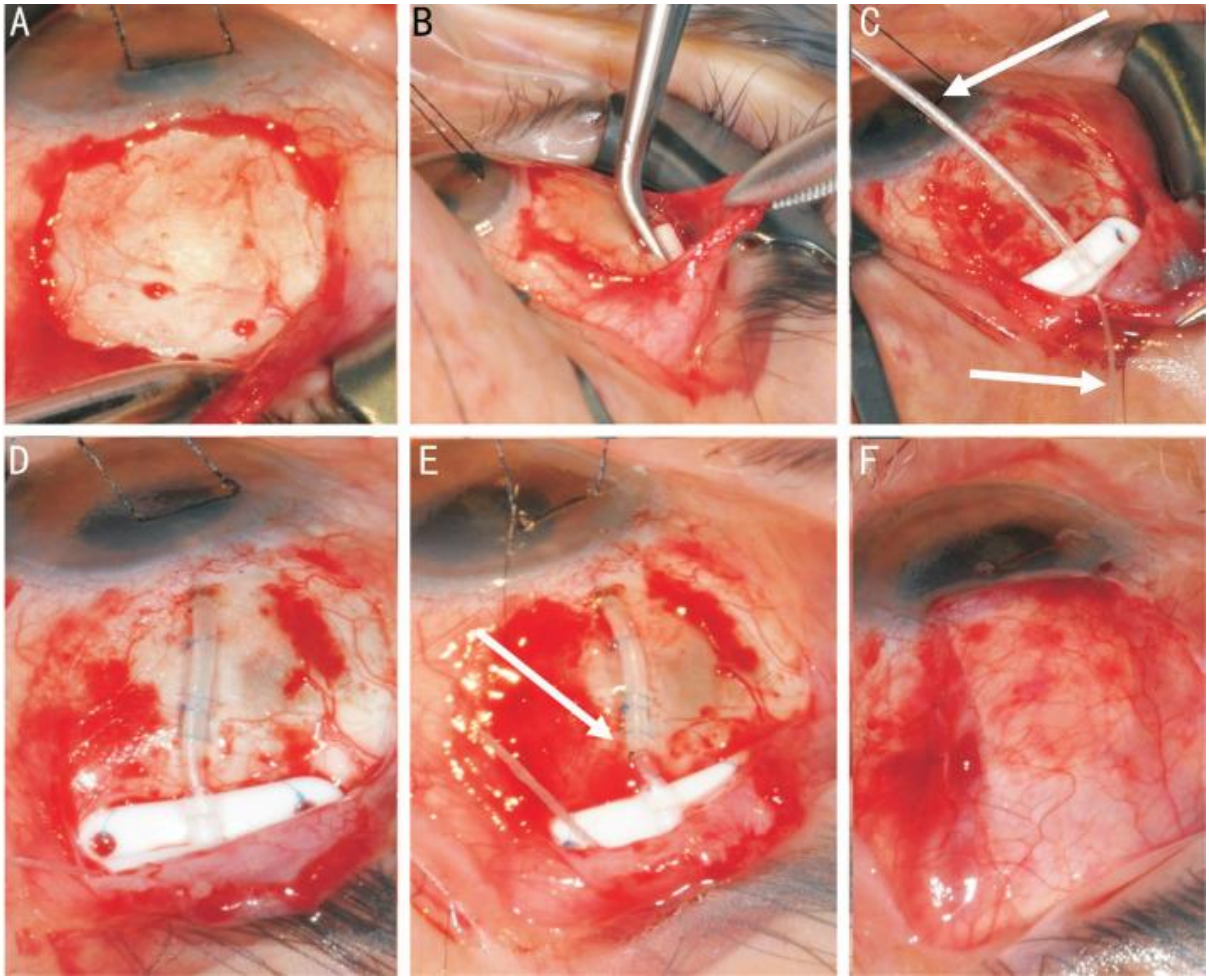

Figure 2.5: Surgical stages of GDD insertion (using a Baerveldt Implant) (Agrawal, P. and Bhardwaj, P. 2020)

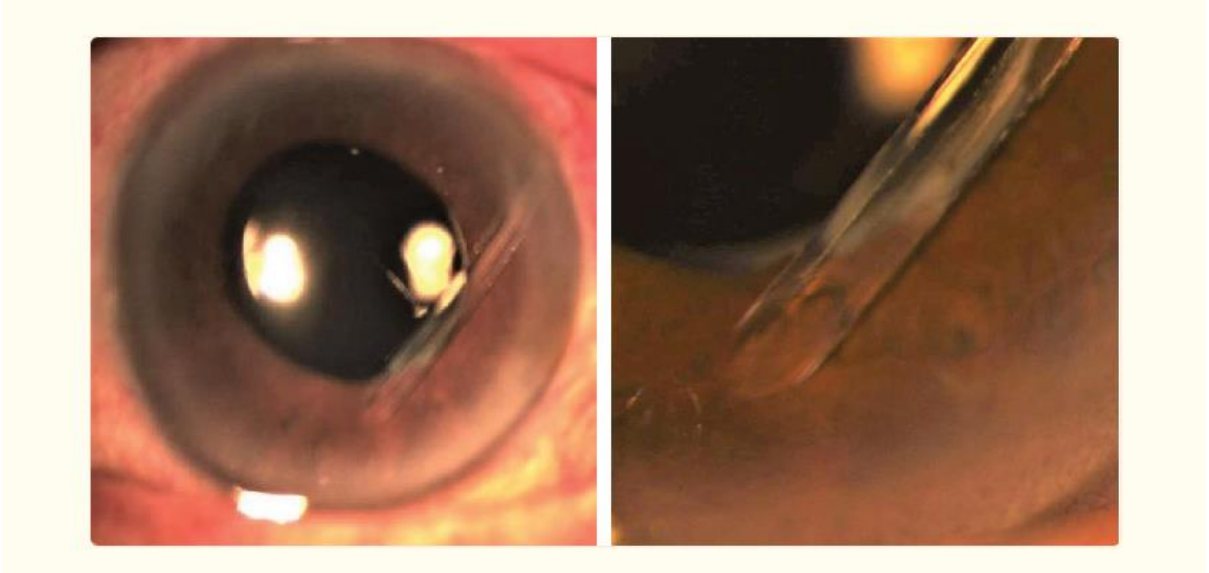

Figure 2.6: Tube Length Adjustment and Tube Trimming Technique in Refractory Glaucoma (Soebijantoro, I. and Noor, N.A. 2020)

2.2.4.3 Designs & Applications

Molteno Implant

All GDDs evolved from the Molteno implant, which was first tested in 1969. This implant is non-valvular, and consists of a 9-10mm silicon tube attached to a round, polypropylene end plate with a varying surface area depending on if the implant is single, or double plate (see figure 2.7). This plate is sutured to the sclera, and covered by tissue and conjunctiva, propagating a bleb to be formed. The implants surface area directly related to final IOP and drainage capability (Gupta, S. and Jeria, S. 2022).

Baerveldt Glaucoma Implant

The Baerveldt glaucoma implant, developed in 1990, contains a non-valved, singular 250-350mm^2 barium-impregnated silicon plate (Agrawal, P. and Bhardwaj, P. 2020). This increased surface area of this device results in a proportionally lower IOP, as the area of the bleb is increased. In comparison to the Molteno implant, this device is considered to maintain a lower and longer control on IOP (Gupta, S. and Jeria, S. 2022).

Ahmed Glaucoma Valve (AGV)

The Ahmed glaucoma valve (AGV), made in both adult and paediatric designs, consists of three parts. The first part is a scarab-shaped end plate made of polypropylene, silicone, or porous polyethene (Gupta, S. and Jeria, S. 2022), which has varied surface area depending on the type (see figure 11). The second part is the silicone drainage tube, and finally the medical-grade venturi valve formed with two silicone membranes. Theoretically, when the IOP is above 8-10mmHg, the membranes are forced apart to allow for aqueous flow. This technology uses the principal of the Bernoulli Equation, where fluid flow rate is inversely proportional to fluid pressure, as the valve inlet is wider than the outlet (Agrawal, P. and Bhardwaj, P. 2020).

Krupin Implant

The Krupin implant, first developed in 1974 but implemented in 1990, is made of an open silastic tube with an oval shaped disc plate. The tube length is varied (20mm initially), as it may be shortened depending on the placement within the anterior chamber. Slits in the tube act as a pressure-sensitive valve, which attempts to regulate the aqueous flow (Gupta, S. and Jeria, S. 2022).

Paul Implant

Development of the newest Glaucoma drainage device, the Paul implant, began in 2012 by a team of clinical scientists from the National University Health System (Sng, C. 2022). The Paul implant is characterized as a non-valvular GDD, with the tube and end plate made of medical grade silicon with a 342.1mm^2 surface area (see figure 2.8). The plate dimensions include a depth of 16.1mm, and breath of 21.9mm, allowing for greater anteroposterior depth compared to the Baerveldt implant (Aref, A. 2023). The total end plate area is slightly smaller than the Baerveldt, but significantly larger than the AGV. The main design features of the Paul implant aim to allow for maximal area for aqueous drainage, along with a reduction of area required to be tucked under the recti muscles due to the slimmer breath (Aref, A. 2023). Subsequently, this theoretically reduces the risk of post operative double vision (diplopia) and eye misalignment (strabismus). The tube has been designed with a significantly smaller internal and external diameter of 0.127mm and 0.467mm, respectively, in comparison to other GDDs. This allows for less contact area between the tube and cornea, resulting in a reduction of corneal damage (Aref, A. 2023). Additionally, a smaller tube diameter will reduce the risk of tube exposure and hypotony. Aqueous flow through the Paul implant is regulated via an internal suture during the implementation procedure, which can be easily controlled and changed by the surgeon where required (Sng, C. 2022). A study, conducted with 72 patients over 6 ophthalmology centres indicated a very low failure rate in comparison to other GDDs of 5.54% after 12 months, with a significant mean IOP reduction for all patients (Aref, A. 2023).

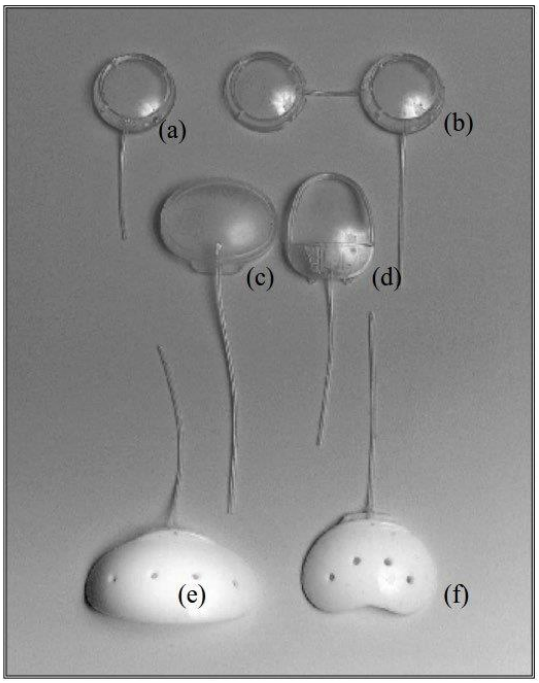

Figure 2.7: Molteno implants (a) single plate + (b) double plate, Krupin slit valve (c), Ahmed Glaucoma Valve (d), Baerveldt Implants (e, f) (Kara, E. 2018)

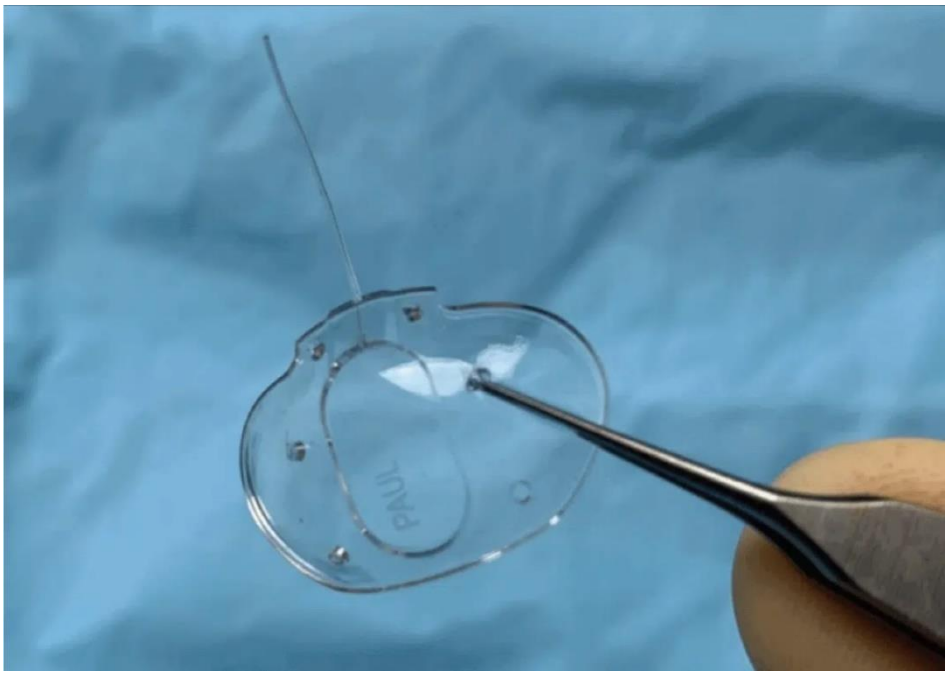

Figure 2.8: Paul Glaucoma Implant (Sng C. 2022)

Advantages and disadvantages of commercially available GDIs for anterior chamber use

Shunt type	Commercially-available GDI	Plate material	Surface area	Advantages	Disadvantages
Non-valved	Baerveldt	Silicone	250 mm^2 350 mm^2	Larger surface area of plate(s) to act as reservoir that may provide increased IOP lowering effect	Delayed functioning until encapsulation of plate occurs More intensive post-operative follow-up required Greater risk of diplopia Greater risk of hypotony
	Molteno	Polypropylene	Single plate 130 mm^2 Double plate 270 mm^2		
	Ahmed Clear Path	Silicone	250mm^2 350mm^2		
Valved	Ahmed	Polypropylene	96 mm^2 (S3) 184 mm^2 (S2) 364 mm^2 (B1)	Immediate post-operative IOP lowering effect Plate placed in between recti muscles hence lower risk of diplopia Valve minimises risk of post-operative hypotony	Higher rate of bleb encapsulation Smaller surface area of plate to act as a reservoir that may provide decreased IOP lowering effect Defective valve mechanism can result in hypotony or obstructed outflow
		Silicone	96 mm^2 (FP8) 184 mm^2 (FP7) 364 mm^2 (FX1)		

GDI: Glaucoma drainage implant. Adapted and updated from Schwartz *et al* 2006[5] and Gedde *et al* 2011[6].

Figure 2.9: Detailed Information of the Baerveldt, Molteno, and Ahmed GDDs (reference seen in figure)

2.2.4.4 Common GDD Complications

Hypotony

Hypotony, defined numerically by the World Glaucoma Association as an IOP of equal to or less than 5mm Hg, is the most common early complication associated with glaucoma drainage device surgery (Agrawal, P. and Bhardwaj, P. 2020). Hypotony occurs due to either inadequate aqueous humour production, or for the case of GDDs, an uncontrolled and excessive outflow of this liquid. Aqueous humour delivers oxygen and nutrients while removing metabolic waste from the ocular system, so it is vital that it is controlled effectively (Wang, Q. et al. 2019). The balance between production and outflow of aqueous humour is imperative to a stable IOP, and thus the success of GDD surgery.

Choroidal Effusion

Choroidal effusion, defined as an abnormal accumulation of fluid in the suprachoroidal space, is another common complication in GDD surgery. Post glaucoma surgery, the primary cause of this complication is hypotony. Choroidal effusion intensifies hypotony by both the reduction of aqueous humour production, and by potentially increasing outflow (Reddy, A. and Salim, S. 2012).

Hyphema & Vitreous Haemorrhage

Hyphema refers to the collection of blood in the eye, due to bleeding from the anterior chamber (Huffman, J. 2023). Similarly, vitreous haemorrhage is defined as any blood in the vitreous cavity (Jena, S. and Tripathy, K. 2022). These early postoperative complications are considered common, and are often caused incidentally throughout surgery (Go, M. et al. 2017).

Tube Blockage & Elevated IOP

GDD tube blockage can be caused by several reasons, and resultantly, the patient may experience an elevated IOP. Common obstructions include blood, iris, fibrovascular membranes, vitreous, silicone oil or fibrin (Agrawal, P. and Bhardwaj, P. 2020). Blockages in a GDD tube can be detrimental to the success of the surgery, as the aqueous humour flow is limited.

Uveitic Glaucoma

Uveitic glaucoma effects an approximate 20% of patients experiencing uveitis, and refers to glaucoma resulting indirectly or directly from uveitis. Leading directly to an increase in IOP, uveitic glaucoma is more commonly associated with anterior and chronic forms of uveitis. The pathogenesis may be acute in onset, with rapid onset inflammation, and an obstruction of intertrabecular spaces (Sheybani, A. 2023). A meta-analysis data study by Ramdas, W. D., et al (2018) suggests the implementation of GDDs into eyes with uveitic glaucoma slightly increased the risk of hypotony and macular edema, though the resources in this field were scarce.

Biofouling

Another complication with GDD technology is biofouling. Microorganisms have been seen to group together within the drainage tube of the GDD, requiring surgical intervention to fix. The microorganism builds up within the tube restricts and effects the aqueous humour flow, leading to tube blockage and a subsequent rise in IOP (Park, H. et al. 2018). Studies have been conducted investigating the potential of self-clearing technology within the drainage tube, to avoid the need of additional surgery in the future (Park, H. et al. 2018).

2.2.4.5 Design Limitations & Complications

Molteno Implant

In comparison to the AGV, patients with the Molteno implant have a higher chance of early postoperative problems, such as choroidal effusions, hypotony, and over filtration. This is attributed to the Molteno implant's lack of a valve, as in most cases a valvular implant can regulate the aqueous humour flow more effectively (Raja, A. et al. 2023). Moreover, studies suggest that in very few cases, there is the possibility of vitreous haemorrhage and retinal detachment (Gupta, S. and Jeria, S. 2022). While the Molteno implant is considered generally as an effective device to drain aqueous humour, the several potential postoperative complications point toward improvements that could be made.

Baerveldt Glaucoma Implant

Multiple studies indicate a vast array of complications with the implementation of the Baerveldt glaucoma implant. A 1998 study of 107 eyes indicated that 21% of patients experienced a varying degree of choroidal effusion, with a very small percentage suffering complete retinal detachment (1%), aqueous humour misdirection (4%), tube blockage (5%), and corneal decompensation (2%). There was also a reported 1 case each of endophthalmitis, tube migration, implant migration, corneal ulcer, and hyphema (Nguyen, Q. et al. 1998). An alternate study indicated that corneal edema (swelling) and tube complications, such as tube occlusion, erosion, and malposition, were the most common Baerveldt glaucoma implant complications (Gupta, S. and Jeria, S. 2022)

Ahmed Glaucoma Valve (AGV)

While studies suggest that the Ahmed Glaucoma Valve is safer than other implant options, the valvular design is not without its complications. People with an AGV implant may experience more long-term complications, such as tube blockage or valve-related fibrosis (Raja, A. et al. 2023). Other studies confirm these theories, suggesting that the most common AGV complication is tube exposure, via conjunctiva and patch erosion (Gupta, S. and Jeria, S. 2022). In addition, while the AGV was designed to limit postoperative hypotony through the valvular design, patients are still at risk (Gupta, S. and Jeria, S. 2022). The cause of this remains unknown, which may be a key design point when studying the GDDs in the CFD software.

Krupin Implant

The Krupin implant, not commonly used in Australia, has several postoperative complications. One study, that tested 28 eyes, found various short-term complications including hypotony (57.1%), choroidal effusion (25%), shallow or flat anterior chamber (53.6%). Additionally, long term complications such as external conjunctival bleb failure (49.9%), tube blockage (17.9%), and tube erosion (7.1%) were seen in the study (Mastropasqua, L. et al. 1996)

Paul Implant

While studies suggest that the Paul implant has the lower failure rate compared to other popular GDDs, there are still postoperative complications and risks that can arise through its implementation. Like other devices, hypotony, tube occlusion, shallow anterior chamber and choroidal effusion are all potential complications (Sng, C. 2022). These complications were evident in a study conducted from 2017 to 2018, where 74 eyes were analysed over a 12-month period. Of these eyes, 5.4% were considered a failure, 68.9% a complete success, and 92.2% a qualified success. Some of the serious postoperative complications included a shallow anterior chamber (14.9%), hypotony (9.5%), tube occlusion (6.8&), tube exposure (4.1%), and one eye losing vision via endophthalmitis (Koh, V. et al. 2020).

2.3 Solid Modelling

Solid modelling is a dynamic tool used throughout many industries across the world, with major applications in design and prototyping for engineering projects. Complex systems of any size can be visualised through solid modelling programs, along with various forms of simulation analysis that can be achieved as a result. As key preparatory work for the computational fluid dynamics software, solid modelling will be utilised throughout this project to create and analyse existing GDDs.

2.3.1 Glaucoma Drainage Device Applications

This project will aim to model the most common GDDs used in Australia, the Paul and Baerveldt implant, to implement them into the CFD software. Thus, major dimensions will be required to model these implants with relatively high accuracy.

2.3.1.1 Paul Implant

The major basic dimensions of the Paul implant are easily accessible across many resources. The geometry of the implant is pictured in figure 2.9, along with some of the major dimensions of the endplate. Further specifications and dimensions are depicted in figure 2.10 for the tube, fenestration holes, and reservoir depth.

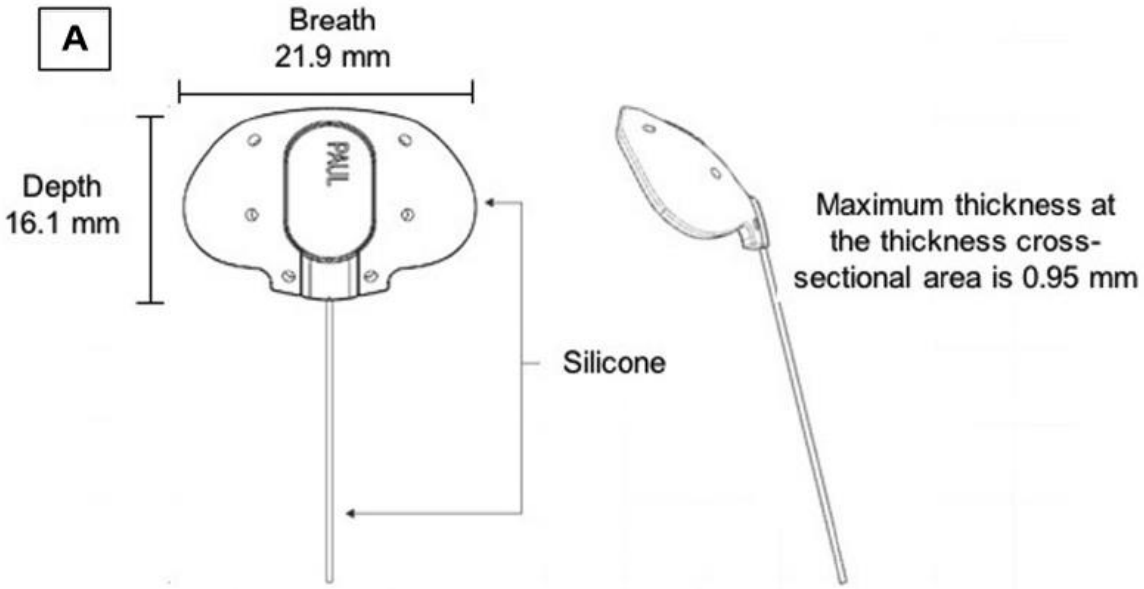

Figure 2.10: Paul Implant major dimensions (Aref, A. 2023)

Table II: Dimensional differences between the Ahmed, Baerveldt and the PAUL Glaucoma Implant

Device/Feature	Ahmed Glaucoma Valve	Baerveldt Glaucoma Implant	Paul Glaucoma Implant	Advantages of the Paul Glaucoma Implant
Plate surface area	184 mm^2	350 mm^2	342 mm^2	Reduces encapsulation
Plate thickness	1.0 mm	0.9 mm	0.95 mm	More IOP control
Plate length (L)	L:13 mm	L:32 mm	L:21.9 mm	Increases effective surface area not covered by recti
Plate width (W)	W:16 mm	W:15 mm	W:16.1 mm	Easier to implant
Fenestration holes	3	4	6	Less micromotion
Reservoir depth	0.5 mm	Nil	0.4 mm	
Tube outer diameter	0.64 mm	0.64 mm	0.467 mm	Less risk of tube erosion and corneal touch
Tube inner diameter	0.3 mm	0.3 mm	0.127 mm	Prevent hypotony

Figure 2.11: Dimensional differences between AGV, Baerveldt, and Paul Implant (Moodley, A. and Williams, S.E.I. 2021)

Qin et al. (2023) have provided an approximation of the tube length of the Paul implant to be around 29.00mm, which will be employed for the study.

2.3.1.2 Baerveldt Implant

Similarly to the Paul implant, there is dimensional data available for all variants of the Baerveldt implant, seen in figure 2.12. Additional information (for the BG101-360) can be seen in figure 2.11.

	BAERVELDT® BG 103-250 Glaucoma Implant	BAERVELDT® BG 101-350 Glaucoma Implant	BAERVELDT® Pars Plana BG 102-350 Glaucoma Implant
Surface Area:	250 mm^2	350 mm^2	350 mm^2
Plate Length:	22 mm	32 mm	32 mm
Tube Length:	32 mm	32 mm	7 mm
Fenestrations:	4	4	4
Placement:	Anterior chamber	Anterior chamber	Posterior chamber (Pars Plana)
Drainage Mechanism:	Open tube	Open tube	Open tube with Hoffman Elbow

Figure 2.12: Baerveldt Implant Dimension Specifications (Johnson & Johnson Vision, 2019)

2.4 Computational Fluid Dynamics

2.4.1 Background Theory

Computational Fluid Dynamics can be defined as the process of mathematically predicting the flow of fluid in a given environment, application, or system, by using computational power to solve complex governing equations (SimScale, 2018). CFD is becoming increasingly more popular in engineering applications, as a physical tool used to assess potential designs by predicting real-world physics.

Variables, such as velocity, pressure, temperature, viscosity, and density, are all commonly used parameters that can be calculated through CFD by employing specific operating conditions. The success of a CFD simulation is entirely dependent on the accuracy of the input parameters, and any other numerical factors that may influence the results. All CFD programs utilise numerical solvers and key governing equations, such as the Navier-Stokes (N-S) equations, to formulate the results of the desired flow behaviour (SimScale, 2018).

2.4.2 Existing CFD in Glaucoma and Ophthalmology Applications

To effectively conduct this research project, the methodology and relevant procedures must be ground in existing literature. Throughout this section, various existing research articles and experimental

reports relating to the use of CFD in glaucoma drainage applications will be discussed. The major research assumptions, results, and applicability to this dissertation will be presented.

- "Computational Fluid Dynamics Analysis of Titanium Outflow Pipe Implant for Glaucoma Treatment in Biomechanical Engineering" (Karaçali, O. 2019)

Karaçali (2019) developed a study on using CFD to analyse a titanium outflow pipe implant (OPIV) with a check valve for glaucoma treatment, via improving the intraocular fluid outflow structure. The implant model was created in SolidWorks and analysed in Ansys, under the following assumptions and conditions.

- Navier-Stokes equation for incompressible aqueous humour.
- OPIV model included with a check valve to stop reverse flow.
- The aqueous humour outflow was governed by modified Goldman flow equations.

The study found that the check valve setting drastically affected intraocular pressure, varying from 25mmHg to 10mmHg. The implant, designed to activate from pressures of 2000-4000Pa, successfully regulated IOP to a flow of 1.9mL/min, primarily due to the implementation of the regulatory check valve. This study concluded that by utilising CFD, ocular implants with check valve implementation has potential for further research into pressure regulation.

- "3D simulation of the aqueous flow in the human eye" (Villamarin, A. et al. 2012)

Villamarin et al. (2012) conducted a study to simulate 3D flow of aqueous humour in the human eye. Using histology images of the human eye, a model was created to use in an Ansys simulation for fluid flow. The study contained several assumptions and conditions:

- Navier-Stokes equation for incompressible aqueous humour.
- Boussinesq approximation for buoyancy effects due to temperature variation throughout the eye structure.
- Boundary conditions and flow parameters to closely model realistic figures, including iris, lens and cornea temperatures, along with ciliary body flow.
- The simulations defined a healthy IOP condition as 13.5 mmHg, with the glaucomatous condition as 27 mmHg.
- Scleral flap (5 mm × 5 mm and 300 μm thick) was created in the model representing typical glaucoma surgery.

The study indicated the importance of Schlemm's canal and the trabecular network in aqueous humour flow and subsequent resistance. The results indicated a comparable pressure differential

throughout the eye under standard conditions to physiological references. The model saw expected increases in IOP when the glaucoma conditions were implemented, contributing the accuracy assessment of the model. The study concluded that additional refinements are required into the boundary conditions, and the trabecular meshwork structure to include its total complexity to ensure maximum accuracy of the results.

- "Computational Modelling of Fluid Flow and Intra-Ocular Pressure following Glaucoma Surgery" (Gardiner, B. et al. 2010)

Gardiner et al. (2010) performed a study comprising of a detailed methodology and results of a computational model used to estimate fluid flow through a bleb.

- Aqueous humour flow is assumed through a drainage tube by the Hagen-Poiseuille equation.
- Fluid production rate is assumed as 2.5μL/min, and fluid loss is assumed by the Goldmann equation.
- Other flow characteristics have been assumed from various literature.
- Bleb dimensions assumed from a functional 'standard' bleb.

The results indicated that the model appeared to align to previous experimental observations, giving validity to the proposal that computational methods can be used to explain successful bleb characteristics and bleb classification post glaucoma surgery.

- "CFD analysis of the Ahmed Glaucoma Valve and design of an alternative device" (Kara, E. and Kutlar, A. 2010)

A study by Kara and Kutlar (2010) was conducted for CFD analysis of the Ahmed Glaucoma Valve and design of an alternative device. These researchers modelled a standard equivalent of an AGV, and a conceptual design that included a Fermat-type, spring-mounted micro check valve. The following assumptions and conditions were employed:

- AH is a Newtonian and incompressible fluid.
- Isothermal, incompressible flow with steady-state conditions.
- Laminar model with mass flow inlet and pressure outlet.
- Gauge pressure of 1200Pa
- 6 flow rates tested, ranging from 1.6 to 25μL/min.

The study produced credible results but ultimately concluded that the alternate device, with the fermat-type spring, yielded similar pressure drop data to the conventional AGV. The study reinforces

the importance of valvular GDDs, and highlights that with continual focus onto valve design alongside the use of CFD, significant enhancements may be possible.

- Panduro, R.M.R., Monterrey, C., Mantari, J.L., Canahuire, R., Alvarez, H., Miranda, M. and Elsheikh, A., 2021. Computational and experimental analysis of a Glaucoma flat drainage device. Journal of Biomechanics, 118, p.110234.

Panduro et al. (2021) performed a study of the computational and experimental analysis of a Glaucoma flat drainage device. The study used a gravitational-driven flow test to validate the simulation process. The flat drainage device, consisting of a folded stainless-steel device inserted into the sclerocorneal limbus, was put under analysis experimentally and via simulation under the following assumptions and conditions:

- GDD implanted into extirpated pig eye for gravitational-driven flow test utilising fluid column, beginning from a pressure of 40mmHg
- Fluid structure interaction analysis
- Navier-Stokes equations for numerical analysis
- Neo-Hookean hyperelastic model for analysis of tissue surrounding the GDD device

While the experimental results showed some uncertainty due to the variation in microstructure of the different pig eye tissue, a linear pressure-flow relationship was observed at higher pressures. The computational model confirmed these findings, concluding that the flat drainage device maintains effective fluid drainage, in comparison to other findings for the AGV.

- Stay, M.S., Pan, T., Brown, J.D., Ziaie, B. and Barocas, V.H., 2005. Thin-film coupled fluid-solid analysis of flow through the Ahmed™ glaucoma drainage device.

A 2005 study performed by Stay, M.S et al was performed for the Thin-film coupled fluid-solid analysis of flow through the Ahmed glaucoma drainage device. This study investigates how thin-film layers interact with fluid dynamics and the structural behaviour of the AGV device. Both simulation and physical experimentation was used within this study under the following conditions:

- Von Karman plate theory and Reynolds lubrication theory to model aqueous humour through the valve.
- 2D coupled steady-state PDE system was solved through the finite element method.
- Syringe driven experimental setup to compare to simulation results.

The results indicated that through careful consideration of the model and its inlet conditions, that the model can accurately predict the behaviour of the AGV. The simulation results compared favourably to previous studies, and the experimental results aligned closely to the theoretical and simulation data.

- Sánchez, G.M., Del Pozo, C.E., Medina, J.R., Naude, J. and Solorzano, A.B., 2020. Numerical simulation of the aqueous humor flow in the eye drainage system; a healthy and pathological condition comparison. Medical engineering & physics, 83, pp.82-92.

A 2020 study by Sanchez et al. was conducted for the numerical simulation of the aqueous humour flow in the eye drainage system: a healthy and pathological condition comparison. Considering several distributions of the collector channels, this study utilises a 3D computational model to simulate aqueous humour flow with relevant buoyancy effects.

- Model was constructed through various other resources and studies.
- 2 arrangements with 29 collector channels.
- 2.5μL/min at inlet, venous pressure of 6mmHg.
- AH assumed as incompressible and Newtonian fluid with constant properties (density and viscosity), described by mass conservation and momentum equations.
- Boussinesq approximation to represent the buoyancy effects.
- Ansys for volume mesh, OpenFOAM for CFD.

The results indicated that the position and number of closed collector channels have a significant influence on velocity and wall shear stress throughout the channels and in Schlemm's canal, but insignificant effect on IOP. The location of the grouped collector channels was noticed to be particularly impactful, standing out as the critical variable. Overall, the study suggests that micro-CT imaging in combination with numerical simulations could be effective in monitoring glaucoma progression.

2.4.3 Boundary Conditions

Boundary conditions are pivotal in any CFD model, as they define the initial conditions that the model will be subjected to. The boundary conditions define all aspects of the connection between the fluid and the domain. In the case of GDDs, these parameters define where the aqueous humour flows into the GDD tube, at what speed this fluid is travelling, boundaries where the fluid cannot exit (through the tube), and where the fluid exits.

There have been several studies into modelling aqueous humour flow, which will be beneficial when determining the boundary conditions for the CFD simulation. A 2010 study on 'Computational Modelling of Fluid Flow and Intra-Ocular Pressure following Glaucoma Surgery' details a

methodology to model fluid flow in and around the eye via many known empirical and theoretical relations and formulae. While this project is primarily focused on the flow through the glaucoma drainage devices, this study provides many useful relations regarding aqueous flow rates and fluid viscosity, to name a few. The rate of production of aqueous humour would likely serve as the inlet boundary condition during the CFD simulations, as this value describes the natural flow produced by the eye in normal circumstances. The major aqueous humour characteristics employed in the study have been tabulated (Gardiner, B.S. et al. 2010):

Parameter	Description	Assumed value	Reference
F_{in}	Rate of production of aqueous humor	4×10^{-11} m^3s^{-1} (2.5 µL min^{-1})	[13]
F_u	Rate or fluid outflow through the uveoscleral pathway	6.25×10^{-12} m^3s^{-1} ($0.15F_{in}$)	[13,15,16]
C_{trab}	Trabecular facility of outflow for healthy eye	3.8×10^{-14} m^3 s^{-1} Pa^{-1} ($0.3\mu Lmin^{-1}mmHg^{-1}$)	[36]
K_r	Mean (ocular) rigidity coefficient	1.7×10^{9} Pa m^{-3} (0.0126 mmHg μL^{-1})	[16]
EVP	Episcleral venous pressure	1.3×10^{3} Pa (10 mmHg)	9 mmHg [37]; 9.5mmHg for control and 11.6–12.1 mmHg for glaucoma [38]
R	Radius of drainage tube	1×10^{-4} m	Molteno3 internal radius 1.7×10^{-4} m [26]
L	Length of drainage tube	1×10^{-3} m	Sclera thickness $0.5–1\times10^{-3}$ m [39]; Molteno tube length $0.75–18\times10^{-3}$ m [26,40]
µ	Viscosity of aqueous humor at 37C	7×10^{-4} Pa s	Viscosity of water at 37C is 7×10^{-4} Pa s [41]
ε	Fraction of normal outflow facility	0.1	See comments in results and Figure 4

doi:10.1371/journal.pone.0013178.t001

Figure 2.13: Eye Model Parameters (Gardiner, B.S. et al. 2010)

This study also details the commonly used Hagen–Poiseuille equation, otherwise known as Poiseuille's Law. This law, out simply, describes the characteristics of laminar flow throughout a tube. This formula describes that as pressure differential along a tube increases, flow does also. Along with this, Poiseuille's law indicates that flow is inversely proportional to length and viscosity (Wittenberg, M. and Gilbert-Kawai, E. 2014).

As aqueous humour flow is very slow, the Reynolds number is considerably small, resulting in a fully developed flow immediately at the GDD tube inlet. Subsequently, this flow is characterized as fully laminar, thus proving the Hagen-Poiseuille to be relevant in this application. In ophthalmology, this equation can be used to estimate intraocular pressure drop through the implementation of a GDD. This relationship will undoubtedly be utilised in the validation stage of the CFD process, and to verify the results against real observed data.

The generalised form of this equation can be utilised to find the pressure drop over a glaucoma drainage device implant (Agujetas, R. et al. 2021):

$$p_{\mathrm{c}} - p_{\mathrm{b}} = \frac{128\,\mathscr{S} L_{\mathrm{v}} \mu Q_i}{\pi D_{\mathrm{h}}^4}$$

Figure 2.14: Generalised Hagen-Poiseuille Equation (Agujetas, R. et al. 2021)

2.4.4 Model Selection

Along with correctly defining the boundary conditions, it is essential in CFD simulations to select the correct CFD model, to obtain realistic results. Different CFD models employ different governing equations, who's accuracy is very dependent on the conditions of the individual problem. As previously defined, the flow through a GDD can be considered laminar. Thus, the laminar flow model will be employed for all simulations.

This model numerically solves the most famous set of governing fluid equations, the Navier-Stokes Equations (N-S). This set of equations consist of multiple time dependent equations, including the conservation of energy, conservation of momentum, and the continuity equation for conservation of mass. For the three-dimensional form of the equations, the dependent variables consist of density, pressure, temperature, and three velocity vector components. These variables are functions of all the independent variables, which include the spatial coordinates of some domain (x, y, and z), and the time, t. This set of equations, along with other N-S simplifications to solve for the boundary layers, are solved simultaneously in the laminar CFD model to produce the desired results (NASA, 2015).

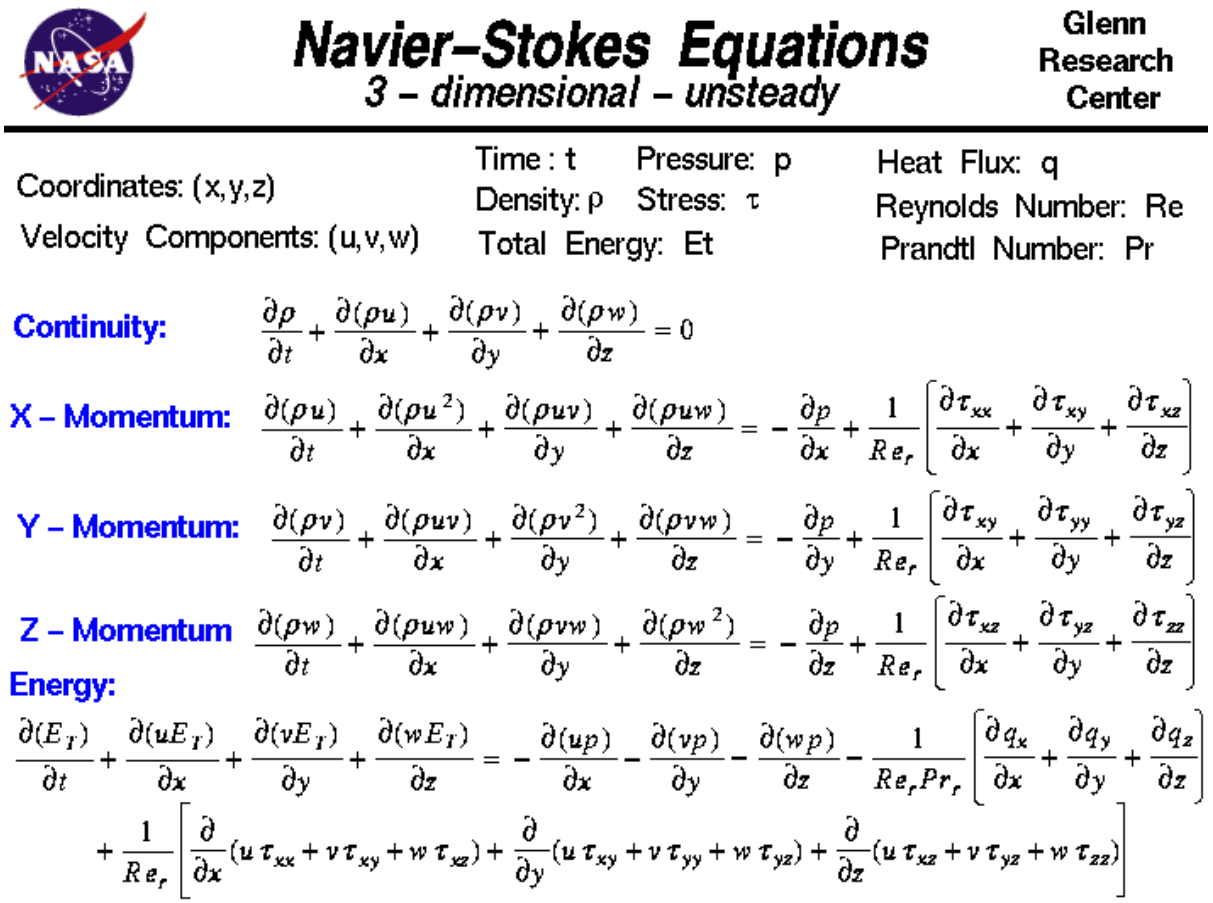

Figure 2.15: 3-D Navier-Stokes Equations (NASA, 2015)

2.4.5 Mesh Refinement

As evident in section 2.3.1, the implant sizes are expectedly very small. Subsequently, the mesh sizing and refinements required throughout the simulations will be at a tiny scale. In CFD, mesh refinement is vital for all types of projects and simulations, to boost results accuracy.

Mesh generation is defined by the sub-division of a larger geometric shape (eg. the GDD implant) into a number of smaller grid elements. These elements belong to the surface mesh and are connected to one another via the element nodes. Meshing is commonly referred to as discretization, where each grid element represents a solution to the relevant partial differential equation (PDE). Subsequently, these equations are solved across the grid to produce the final solution (Dassault Systèmes, 2022).

Mesh refinement, as an overall process, is often optimised by targeting the most critical areas for the simulation. The mesh element size at these locations can be reduced, thus increasing the mesh density. This allows for more PDE equations to be solved at these critical areas, while saving on computational time compared to reducing the mesh element size across the entire geometry (Dassault Systèmes, 2022).

In the context of this research project, the critical areas of the GDD models will likely be the inlet and outlet of the aqueous humour flow. These areas, denoted as the inlet and outlet of the drainage tube, will be of high importance in understanding the flow characteristics.

2.4.6 Material Characteristics

In CFD modelling, the individual characteristics of the selected materials within the simulation will influence the final results. The change in material properties provide unique interactions across various CFD variables. For instance, thermal conductivity properties influence how temperature is distributed throughout the system, thereby influencing parameters such as efficiency, heat transfer, and heat dissipation. Moreover, mechanical properties of materials can affect the integrity of the system's structure when it is interacting with the simulated fluid (Tencom Ltd. 2023)

2.5 Research Gap

2.5.1 Problem Definition

Within this literature review, the most relevant existing CFD centric studies in the field of ophthalmology and GDDs have been analysed. Throughout this analysis, a research gap has been identified, which can be divided into the governing research questions for this dissertation.

GDD technology is inherently outdated, with the most modern designs sharing very similar attributes to the original designs in the early 1990s. With continual innovation in the broader field of medical engineering, there has been a stagnation in innovation for GDDs.

CFD technology is a powerful tool used across many engineering fields, but a review of the literature indicates that its full potential has been underutilised in this instance. Section 2.4.2 reveals that the primary focus of many CFD studies are valvular implants, namely the Ahmed Glaucoma Valve. However, Ophthalmic surgeons in Australia generally opt for the non-valvular implants, primarily the Baerveldt and Paul. Moreover, of the existing CFD studies that focus on design and innovation, the primary research is targeted toward either new valvular constructions or entirely new implant geometries. Very little investigation has been put into tube manipulation through surgery, along with experimental tube and inlet variations.

Subsequently, after a review of the literature, a research gap has been identified which can be used as justification for this project. As to be outlined in the following research questions, this study will focus on analysing popular GDD implants in Australia through the 3D modelling and CFD simulation of both surgical and theoretical tube variations.

2.5.2 Research Questions

By consolidating the findings from the literature review, a research gap can has identified. This gap can be addressed through a set of guiding research questions, which will shape the methodology and be revisited upon project completion.

- How do different GDD tube geometries affect the fluid dynamics within the eye, as analysed through CFD simulations?
- How effective is CFD at investigating the impact the current surgical procedure has on the Baerveldt and Paul implant tubes?
- What alternative methods may be possible within the tubes and at the inlet to combat the common failure modes of GDDs, and how do these results compare through CFD analysis?

2.6 Chapter Summary

This chapter presented the findings of the comprehensive literature review conducted for this research project. The review began by investigating fundamental background knowledge of glaucoma, along with the relevant treatment methods. This transitioned into GDD research, where the common types, uses, limitations, and complications were outlined to inform the research topic. Fundamental knowledge on CFD was then discussed before investigating the current literature regarding CFD in glaucoma and GDD applications. These findings will be used throughout the remainder of the research project to assist in guiding the project and methodology. The chapter concluded with discussion on the clear research gap and problem definition, along with outlining the fundamental research questions for this project.

Chapter 3 – Project Methodology Plan

3.1 Chapter Overview

This chapter details an outline of the methodology for this research project. Initially, an overall summary of the methodology is produced to outline the intended project structure. The solid modelling details are then listed, including the relevant dimensions and data required to produce the GDD models inside of Creo Parametric. The initial simulation details are also provided to outline the required parameters inside of Ansys, to ensure accurate simulations.

3.2 Methodology Outline

The framework for the methodology of this dissertation can be summarised into the following key points:

1) Research existing GDDs to confirm critical dimensions and other relevant parameters, such as surgical procedure.
2) Use solid modelling software to reproduce the designs of the Paul and Baerveldt implant, and make theoretical additions with guidance from the literature review.
3) Run CFD simulations on the implant tube variations, varying the flow rate per the literature review.
4) Analyse and review the simulation results to determine key variables of each implant tube variation.
5) Conduct theoretical simulations to verify the data, using formulae derived from the literature review.
6) Use the solution data to draw conclusions on the most influential parameters for the success of GDD implants.
7) Assess the accuracy and validity of the CFD model for future use in GDD design and development.

3.3 Solid Modelling

The initial stage of this research project is to use solid modelling to reproduce the existing designs for the Paul and Baerveldt implants. These two designs were selected through the literature review, where the research revealed that these implants are the most used in the Australian ophthalmology field.

Using the modelling software accessible via the university, Creo Parametric, the design will be reproduced with aid of the following figures seen in the literature review. As there is limited information on the implant dimensions outside of critical values, several assumptions will need to be

made through the modelling process. Subsequently, there may be slight error through some of the models. However, for the scope of this task, the accuracy of the end plate geometry is not as imperative to the success of the simulations. The dimensional details of the main tubes are all readily available, which is the primary focus of the project.

Figure 3.1: Reference Image for Various Baerveldt Implants (Mivision, 2021)

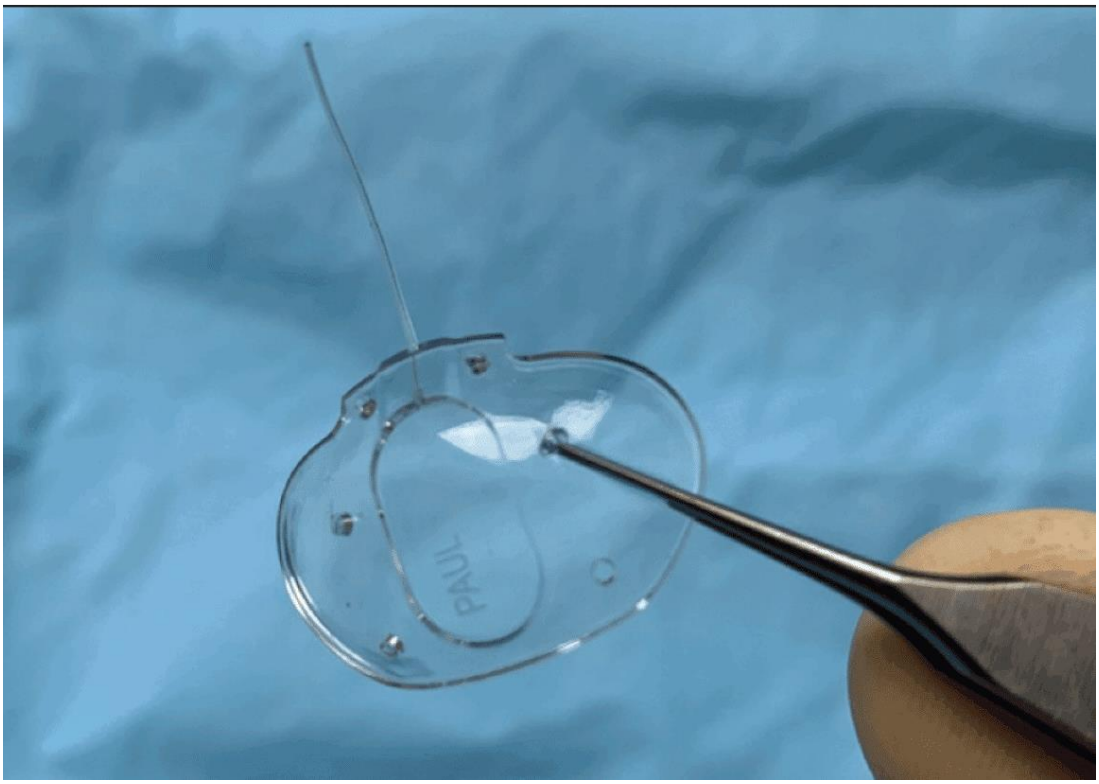

Figure 3.2: Paul Implant Reference (Sng, C. 2022)

3.4 CFD

3.4.1 Simulations

The simulation section of this research project will aim to use CFD to determine the pressure characteristics of aqueous humour flow through the Paul and Baerveldt implants.

The CFD software for this research project will be the university standard, Ansys [Student Edition]. Ansys is a powerful tool that will allow for detailed results analysis of the GDD flow characteristics.

The major simulation parameters have been determined and presented in the literature review. The major characteristics of the simulation can be seen in the following:

- Constant flow rate, consistent with researched values for aqueous humour flow (see literature review).
- Fluid conditions specified by the properties of aqueous humour.
- Inlet condition at the intake of the implant tube, to accurately define where the fluid flows into the GDD.
- Outlet condition at the opposite end of the implant tube.
- Laminar model, aligned to the very slow fluid flow rate.

Several simulations will be run initially to determine mesh independency, a necessity for all CFD simulations. Mesh independency is achieved by changing one major mesh parameter and monitoring results. Once the results are within an acceptable range of error tolerance (generally less than 5%), the mesh is considered independent.

3.4.2 Theoretical Calculations

After completing the CFD simulations, the results require calculations from theoretical formulae to assess the validity of the solutions. These specific formulae have been outlined in the literature review, with the primary calculation stemming from the Hagen-Poiseuille equation. Section 2.4.3 details this equation and its subsequent initial formula to determine the pressure drop over a GDD.

3.5 Project & Resource Plan

This project is based on computer software and programs, so there are limited resources that are required. The resource list will be provided:

Table 3.1: Project Resource List

Project Stage	Item	Source	Cost	Comments
All	Computer/Laptop	Student/UniSQ access	Nil (owned)	Must be powerful enough to handle simulation programs
	Desk Setup	Student	Nil (owned)	Monitors, mouse, keyboard, chair, etc. to ease project reporting
	Microsoft Programs	UniSQ	Nil	Word, Excel, PowerPoint, etc.
	GDDs	Workplace	Nil	Not required, but may be beneficial for informative purposes. Possible access through work, subject to approval
3D Modelling	3D Program (Creo)	UniSQ	Nil	Available through UniSQ Turbo
CFD Simulations	CFD Program (Ansys)	UniSQ	Nil	Available through UniSQ

Due to the nature of the project, there are no additional safety implications that require urgent action or additional resources. The basic risks of this project, primarily the hazards associated with computer work, will be outlined in the risk management plan in appendix B.

Chapter 4 – 3D Modelling

4.1 Chapter Overview

This chapter details the process of creating the 3D models of the GDD implants using Creo Parametric, in preparation of the CFD simulations. The models for the Baerveldt and Paul implant tubes are produced, covering standard designs, sutured versions, finned modifications, and variations of the tube inlets. These models were developed to analyse the effects that key design changes have on fluid flow and pressure drop, simulating both surgical practices and biofouling implications. Each model construction, with the relevant justification and assumptions, are discussed throughout this chapter, with corresponding figures to illustrate the designs.

4.2 3D Model Development

To initialise the project simulation section, 3D models for the GDD implants are to be generated through modelling software. Using known data and via generalised assumptions, the 3D models and subsequent fluid tubes could be modelled inside of Creo Parametric.

4.2.1 Baerveldt Implant Tubes

The initial standard Baerveldt tube is modelled following the dimensional limits advised via Moodley, A & Williams, S.E.I. (2021) and Qin, Q. et al. (2023) with an outer diameter spanning 0.64mm, and inner diameter 0.32mm. While tube length can vary depending on the patient, the standard length of 32mm was applied for this model. While the CFD study will only employ analysis over the length of the tube, an approximate end plate and end plate connection was modelled in accordance with the relevant dimensions outlined in Chapter 2.

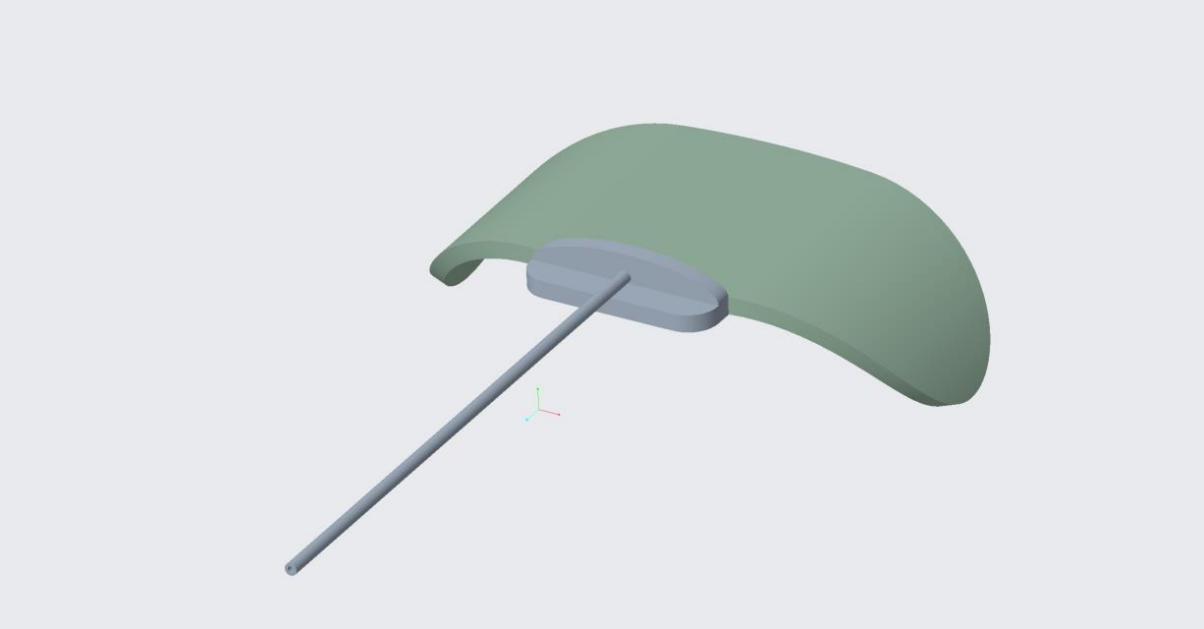

Figure 4.1: Baerveldt Standard Model

The next stage of the modelling process is to apply a suture around the tube to reduce the inner cross section, to simulate the surgical procedure often implemented during practice (Agrawal, P. and Bhardwaj, P. 2020). The elongated shape visible in figures 4.2 and 4.3, was achieved by applying the revolve tool to the original tube, reducing the cross section by 25% with an inner diameter of 0.24mm. This value is an assumption made to investigate the effects this reduction of area has on overall pressure drop. The elongated area was extended out to a gradual curve over a length of 5mm, as in practice, the medical grade silicon tube would warp along the length of the tube rather than bending instantly at the point of the suture. The sutured shape was applied coaxially and positioned toward the centre of the tube, which has been approximated to more accurately predict the behaviour of the tube during surgery.

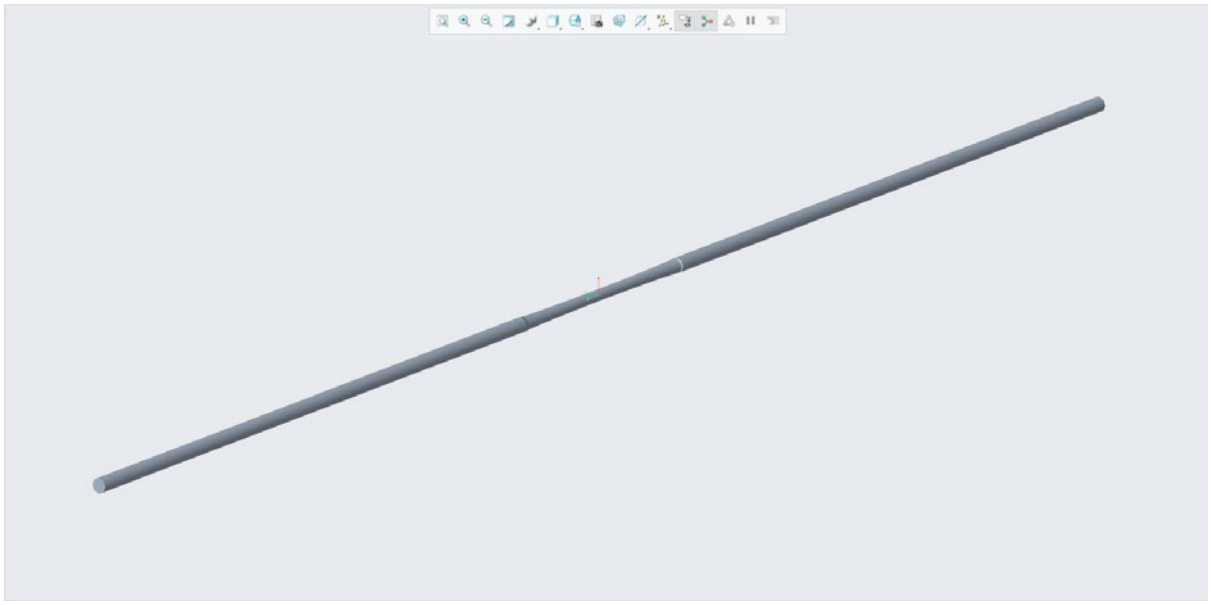

Figure 4.2: Baerveldt Sutured Tube Model

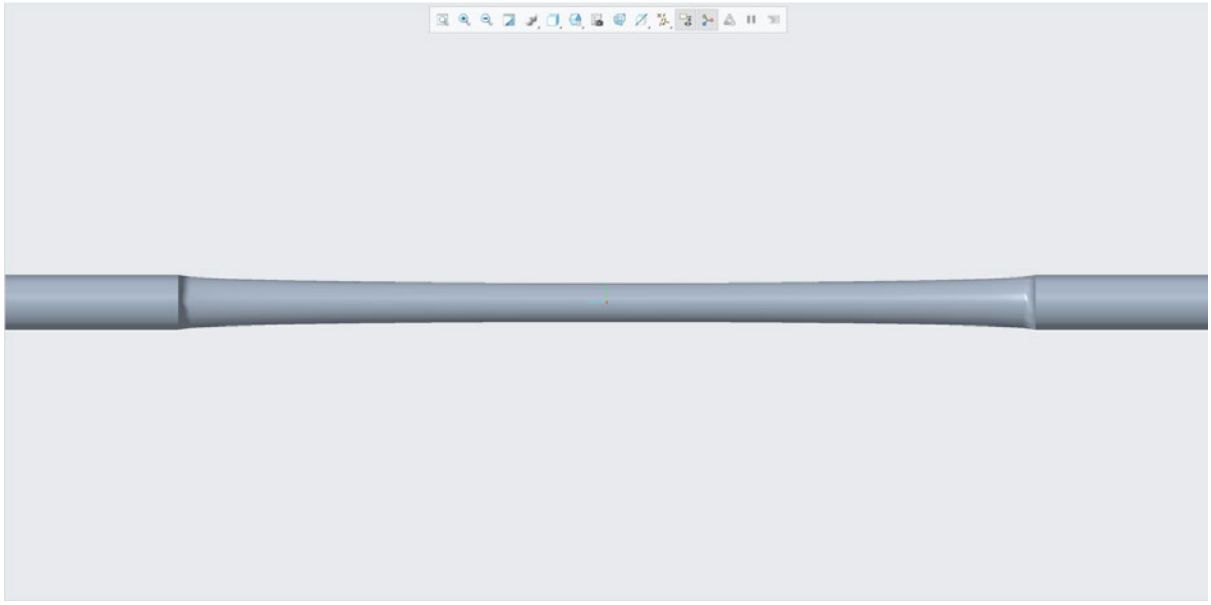

Figure 4.3: Baerveldt Sutured Tube Close-Up

The next model produced for the CFD analysis was a standard tube with a single fin insert into the middle of the tube, to investigate how this new cross section may affect flow and pressure drop over the implant. In some cases of glaucoma, biofouling can cause a build-up of microorganisms within the drainage tube (Park, H. et al. 2018), so this single fin insert has been employed as a high-level initial analysis to investigate how it affects fluid flow and overall pressure drop. To achieve this shape, an extruded cut with dimensions of 0.5mm long and 0.1mm wide was employed through the centre of the tube. By using the maximum width of the fin (0.1mm) the reduction in cross section can be calculated as a decrease of approximately 40%, in comparison to the 25% of the sutured tube.

As only the fluid is simulated within the CFD software, this cut out will simulate aqueous humour flowing around a silicon insert positioned through the middle of the tube. Given the experimental nature of this analysis, and the very limited resources investigating this type of cross-sectional addition currently in literature, the dimensions have been fully assumed and adjusted relative to the tube diameter (between the Baerveldt and Paul implants). The geometry of this tube can be seen over the following figures 4.4 and 4.5.

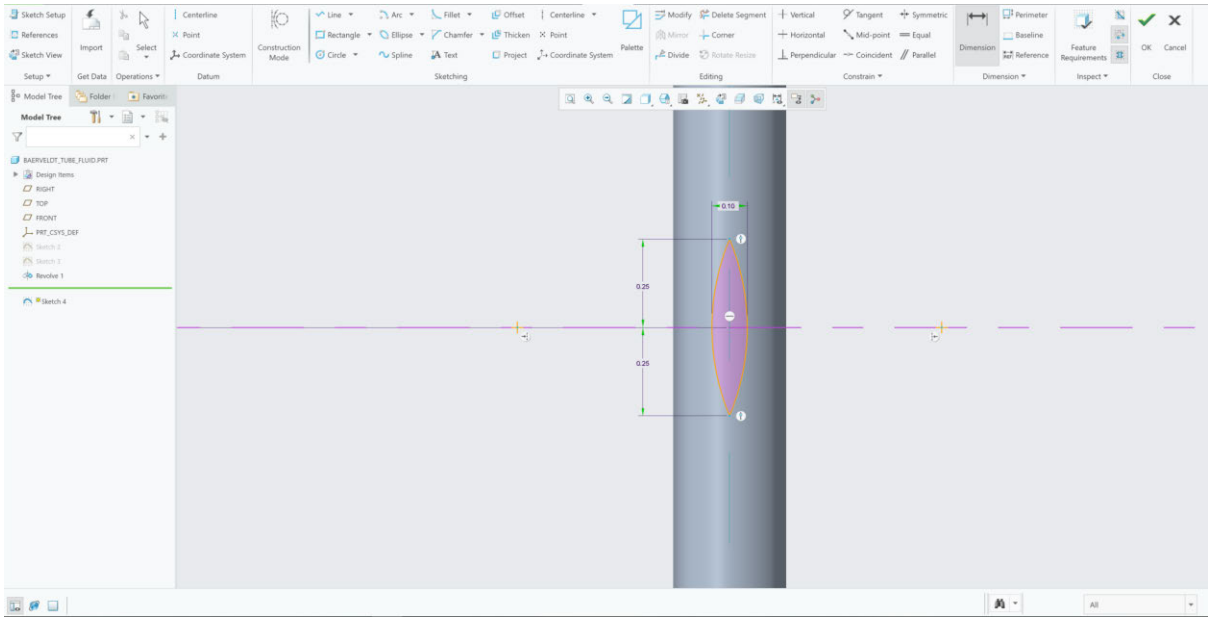

Figure 4.4: Baerveldt Single Fin Tube Extruded Cut

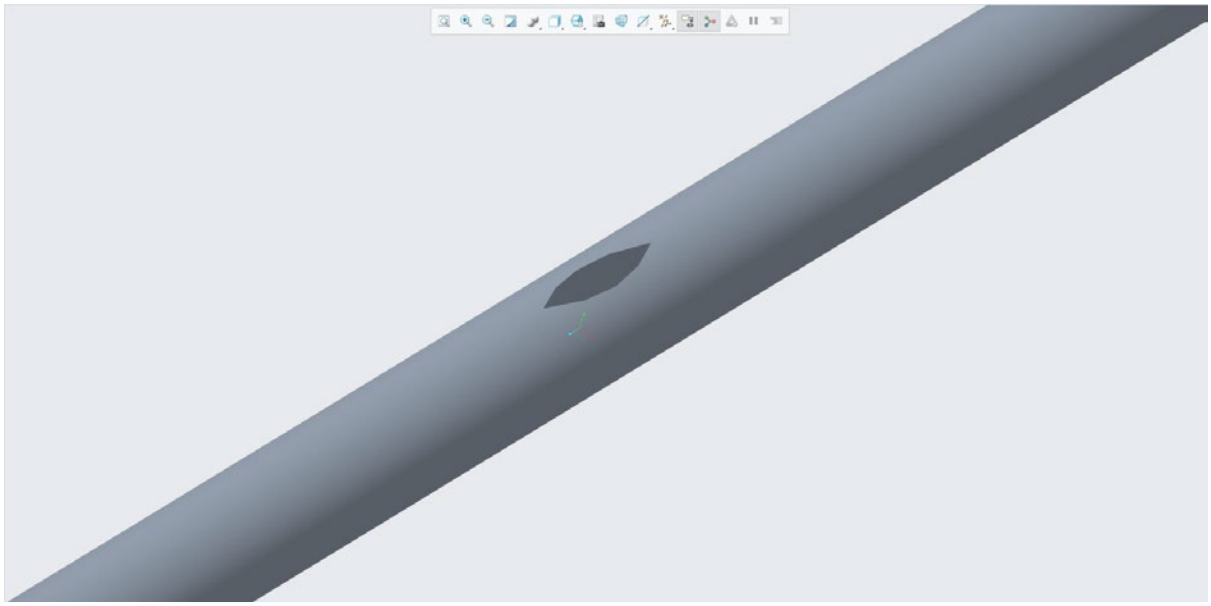

Figure 4.5: Baerveldt Single Fin Tube Model

As an extension of this analysis, a double finned tube equivalent for the Baerveldt tube was produced. By employing the same extruded cut shape horizontally into the side, a modified tube can be produced. The resultant tube will simulate fluid flow through a cross section with two perpendicular

fins, forming an ‘X’ shape in the centre of the tube as depicted in figure 4.6. Using the maximum fin width, resultant calculations produce a cross-section reduction of approximately 80%.

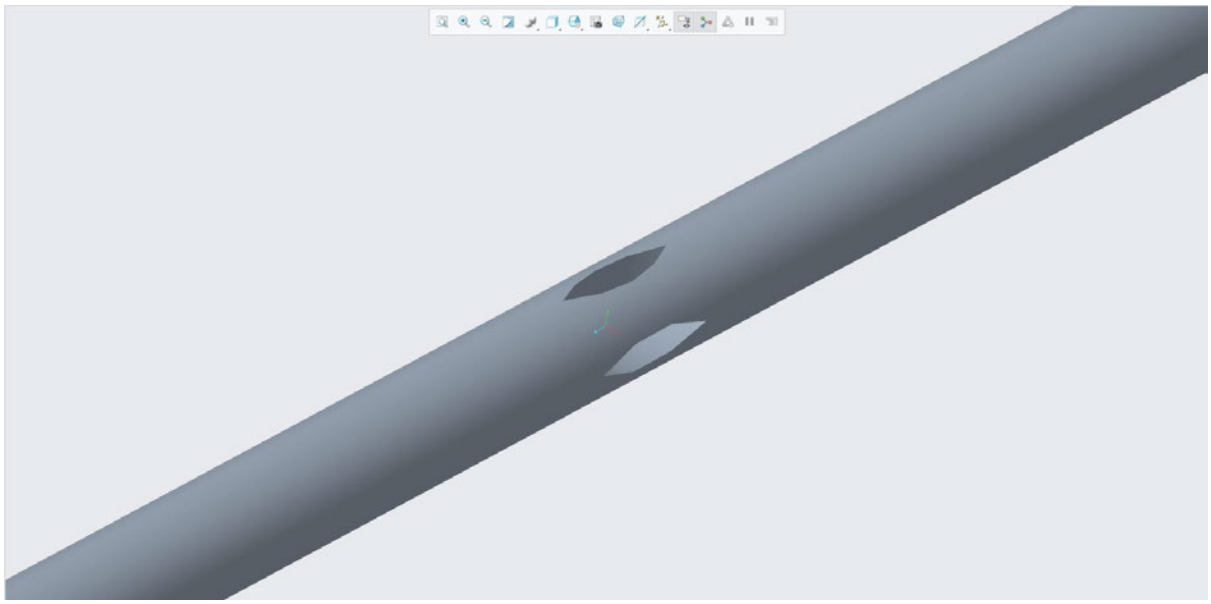

Figure 4.6: Baerveldt Double Fin Tube Model

Alongside the sutured tube construction, another model is developed to simulate realistic surgical practices. As outlined in section 2.2.4.2, the standard surgical technique when fitting the drainage tube is to snip the end, often forming an angular cut. To achieve this shape, a standard extruded cut was made on the standard tube at an angle of 30 degrees to the horizontal. This shape is evident in the following figure 4.7.

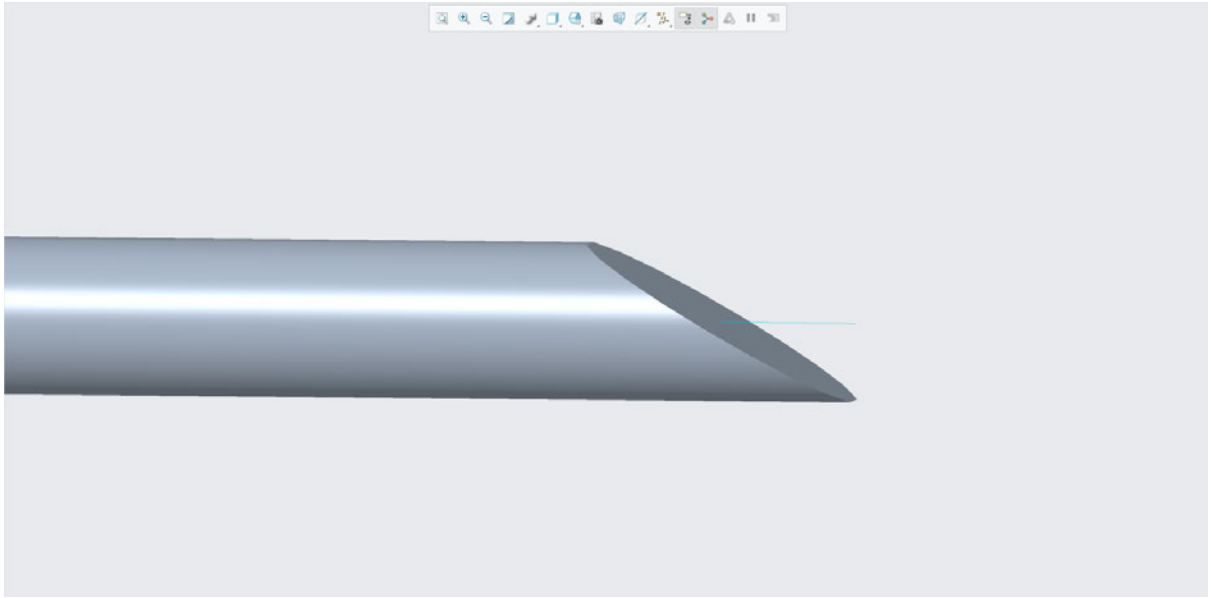

Figure 4.7: Baerveldt Snipped Tube Model

With the realistic snipped end being analysed, another theoretical model can be produced to compare the flow behaviour at different inlets. After discussion with Opthalmic surgeons, a common occurrence and subsequent cause of failure for drainage devices is biofouling and clogging at the implant's inlet. Subsequently, a model with a rounded inlet will be investigated to compare its performance through the flow results. To create a model of this geometry, it was imagined that a fillet would be applied to the edge of the internal tube. Theoretically, the fluid would naturally be encouraged to flow inwards following the curved edge. Similarly to the finned constructions, only the fluid is required to be modelled for the CFD simulations. Using the revolve tool, the resulting model is produced, resembling the path that the fluid would travel.

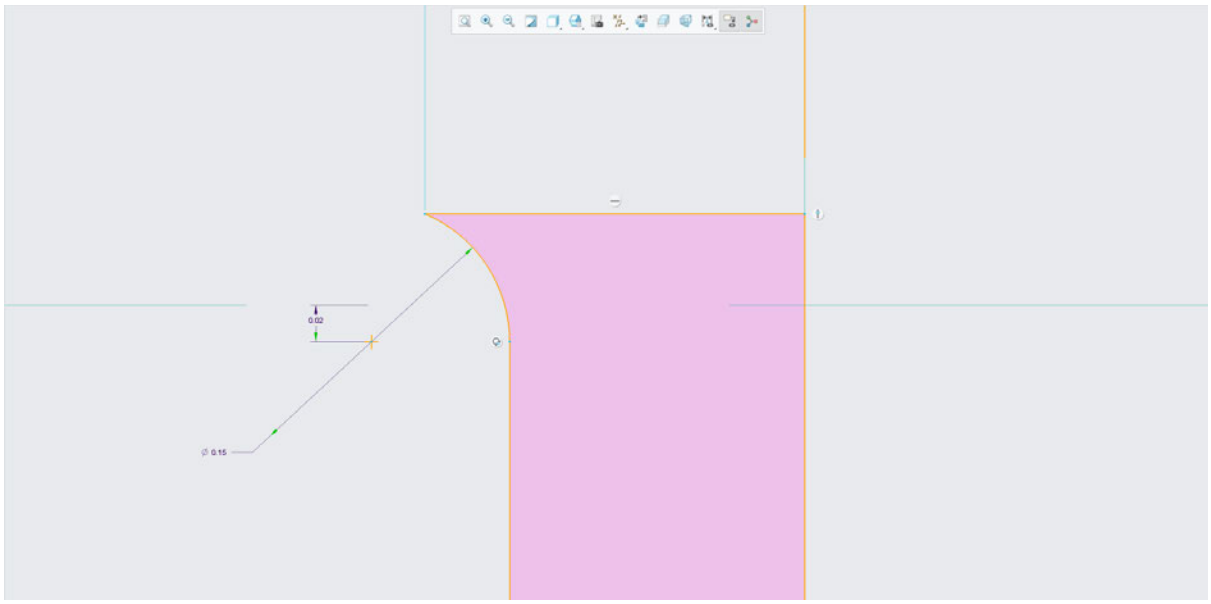

Figure 4.8: Baerveldt Rounded Inlet Tube Revolved Geometry

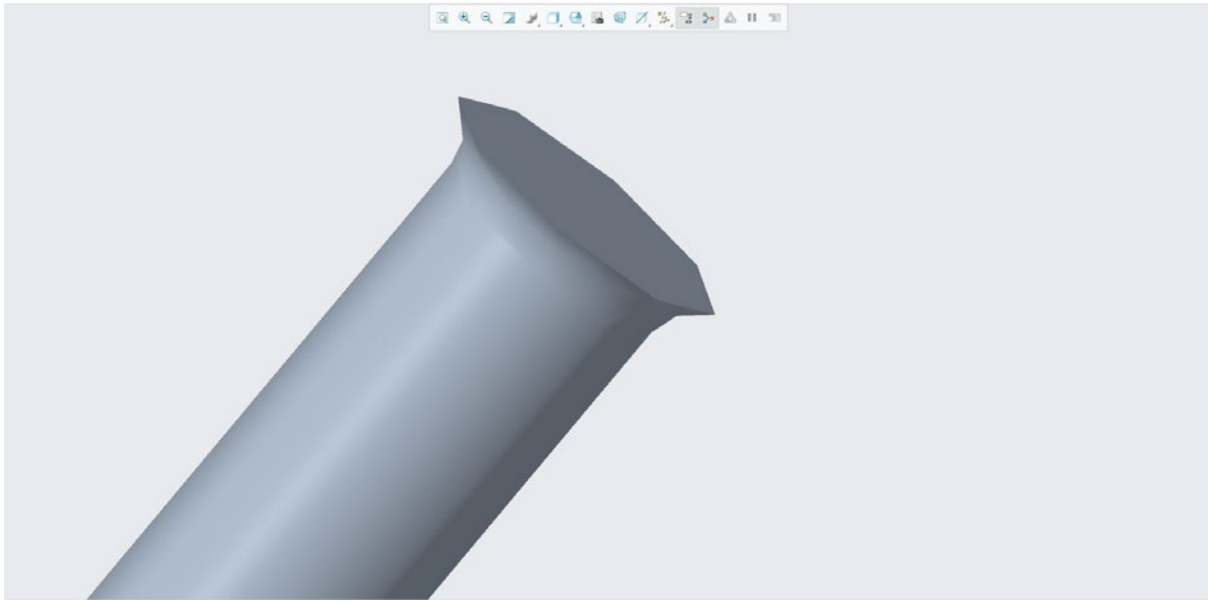

Figure 4.9: Baerveldt Rounded Inlet Tube Model

4.2.2 Paul Implant Tubes

By repeating the sane steps advised in the Baerveldt section, models for the standard, sutured, single, and doubled finned tubes could be produced.

The standard tube for the Paul implant adopts dimensions from Moodley, A. and Williams, S.E.I. (2021) with an outer diameter of 0.467mm, inner diameter of 0.127mm, and standard length of 29mm. Similarly to the Baerveldt, while only the tubular sections are simulated in the CFD software, full models have been produced as seen in figure 4.10.

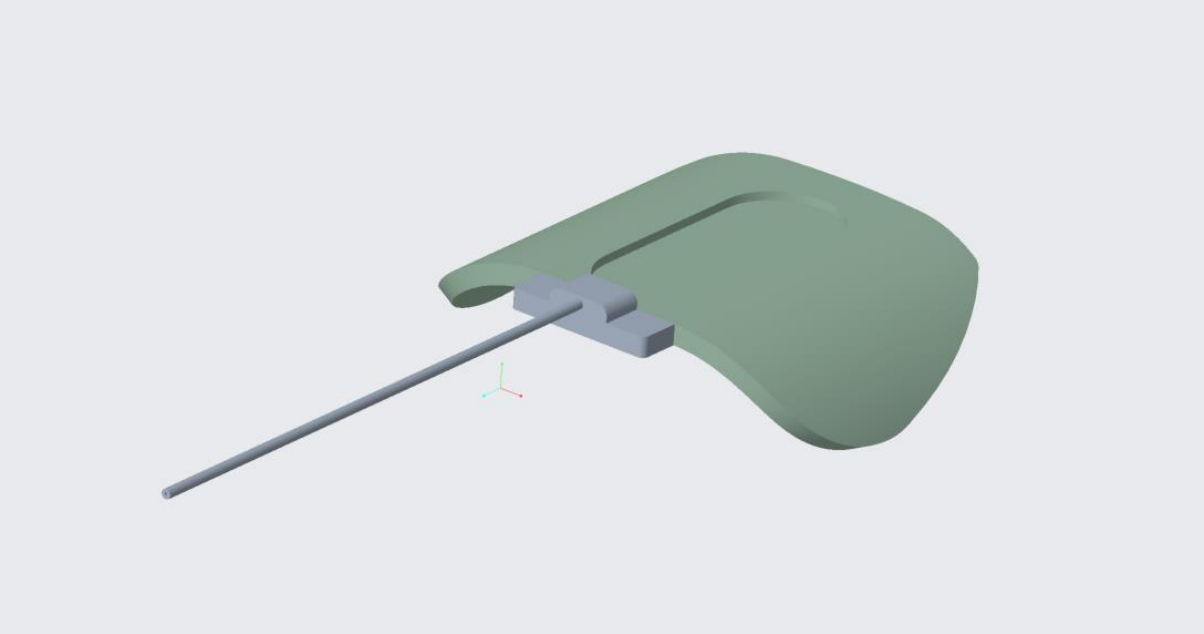

Figure 4.10: Paul Standard Tube Model

The suture was implemented coaxially with the same gradual slope as the Baerveldt, with 5mm in length. The cross section was reduced by 25% with an inner diameter of 0.09525mm. The model is depicted over the following figures 4.11 and 4.12.

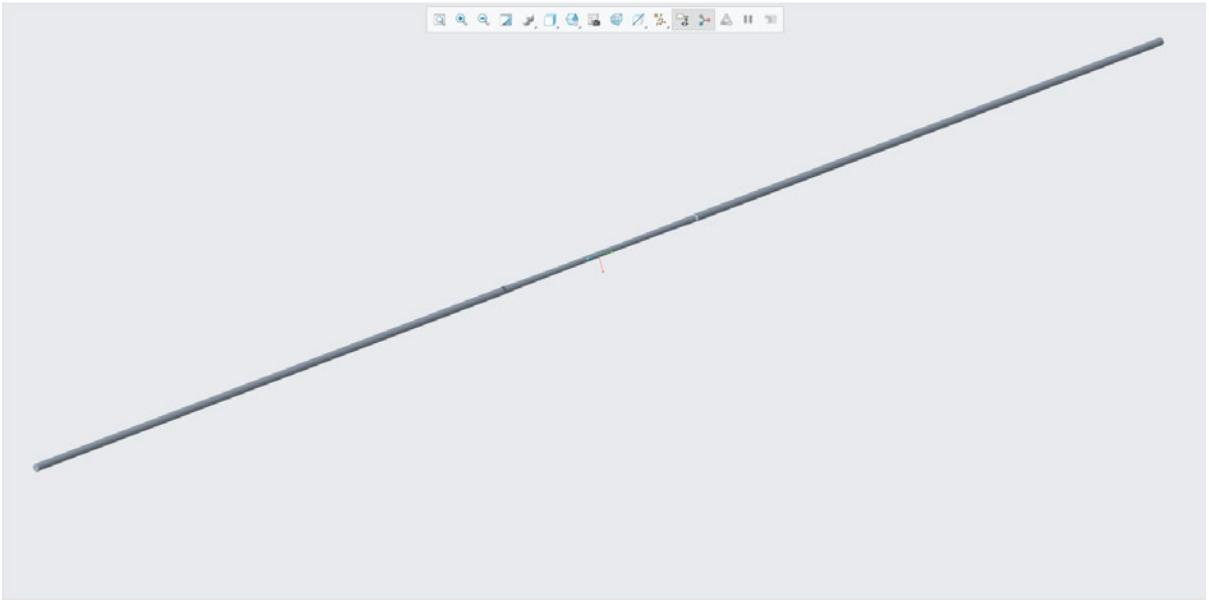

Figure 4.11: Paul Sutured Tube Model

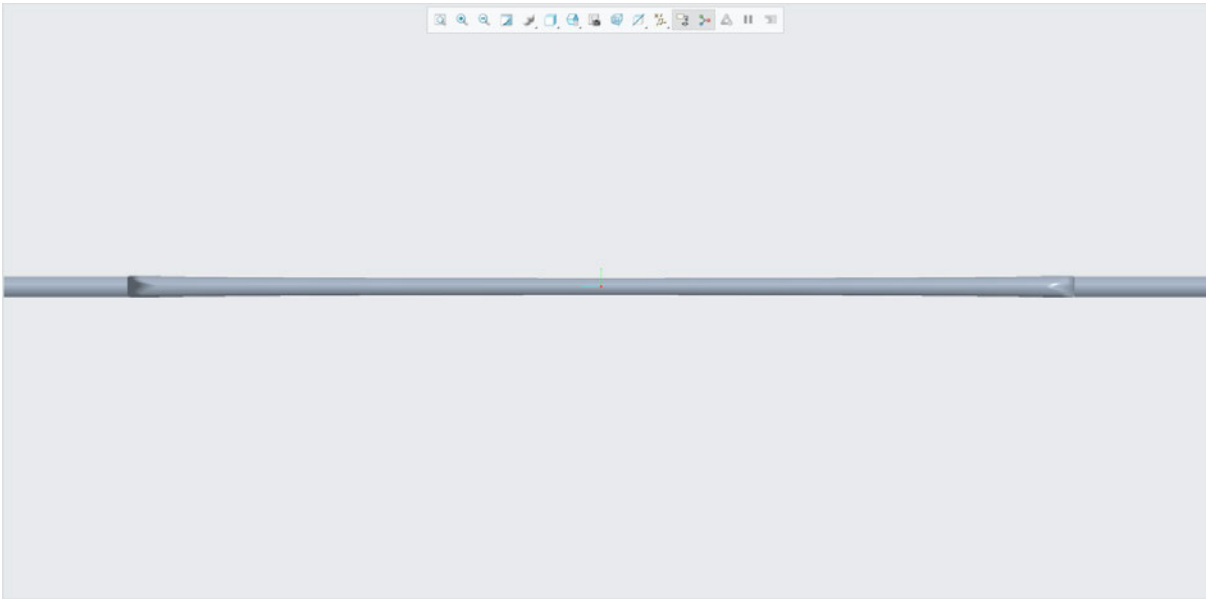

Figure 4.12: Paul Sutured Tube Close-Up

By adjusting the dimensions to be 0.3mm in length and 0.04mm wide, the single fin arrangement was also implemented into the Paul drainage tube. These adjustments held a consistent cross-sectional reduction of approximately 40%, using the maximum fin width at the centre of the tube. Like the Baerveldt, this fin will simulate how fluid interacts while passing through the smaller diameter of the Paul tube. The model geometry and cut out dimensions can be seen over the following figures 4.13 and 4.14.

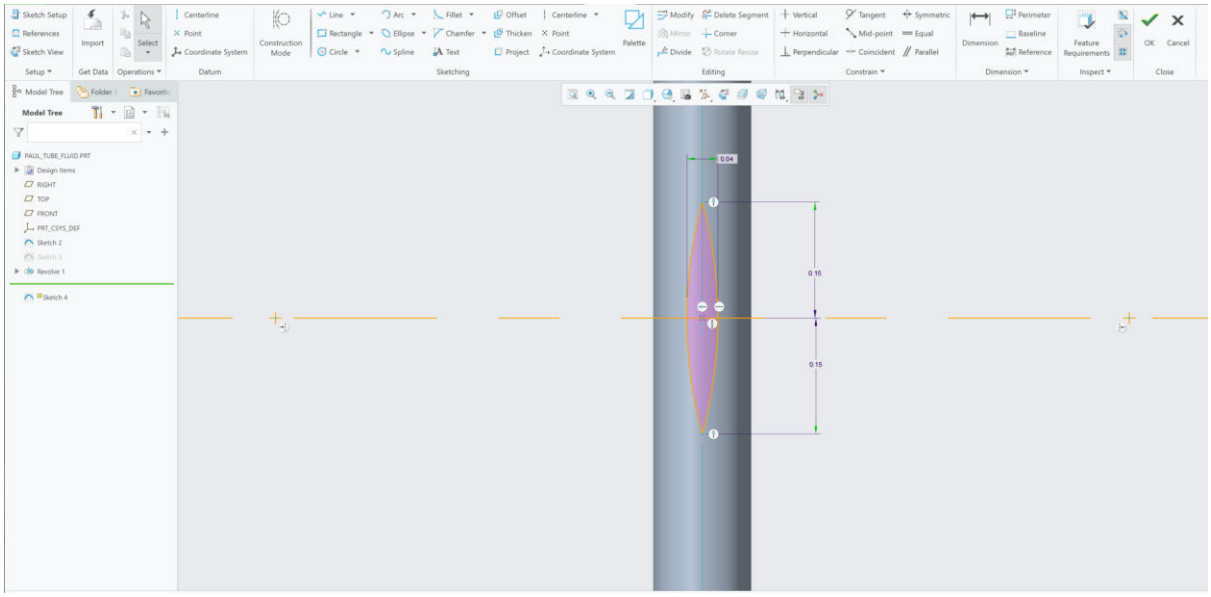

Figure 4.13: Paul Single Fin Tube Extruded Cut

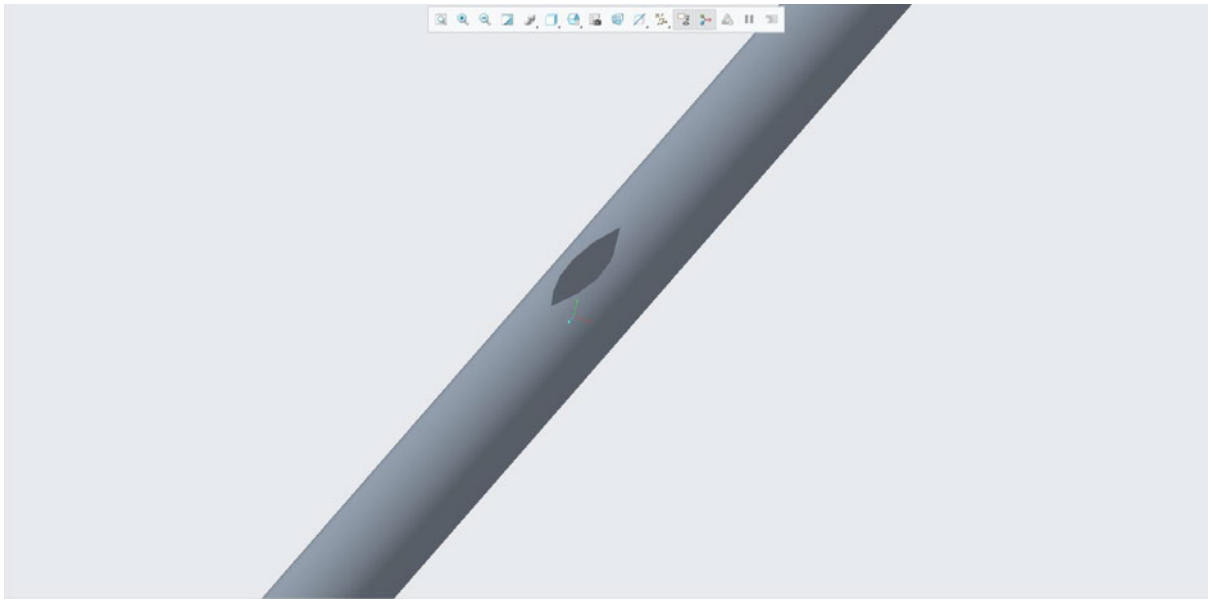

Figure 4.14: Paul Single Fin Tube Model

Furthermore, the double fin model for the Paul drainage tube was produced following the same method outlined in section 4.2.1, with the geometry visible in figure 4.15.

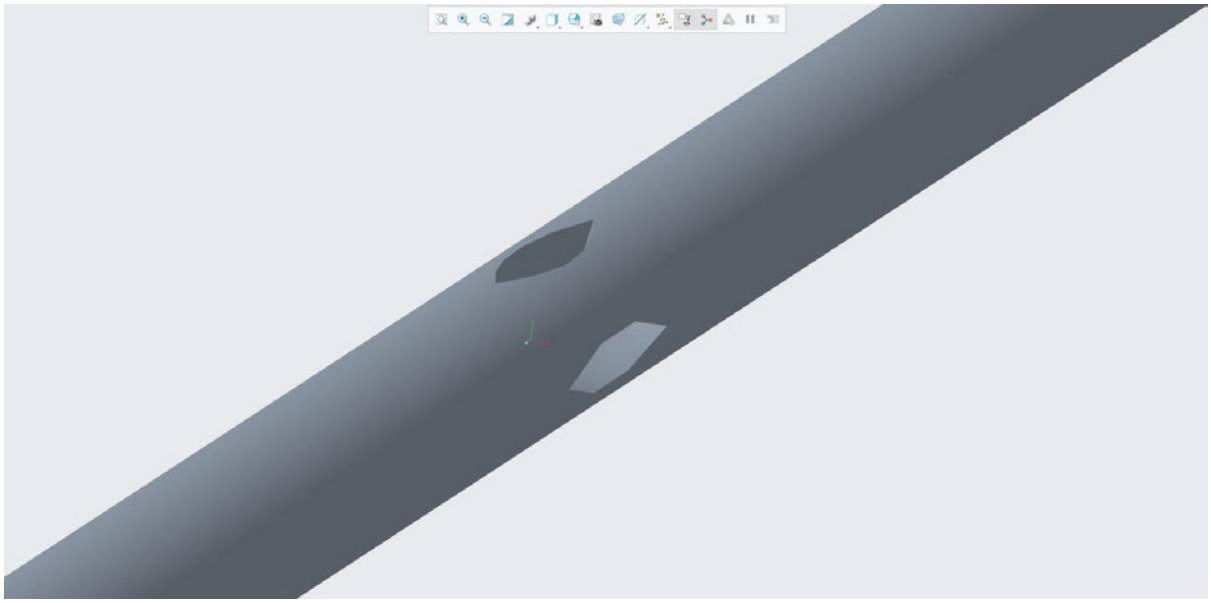

Figure 4.15: Paul Double Fin Tube Model

By repeating the process outlined in section 4.2.1, the snipped cut is applied to the standard Paul drainage tube. Additionally, the rounded inlet is applied on a separate model, producing the two inlet variations to be investigated in this research project. These models and their construction will be detailed over the following figures 4.16, 4.17, and 4.18.

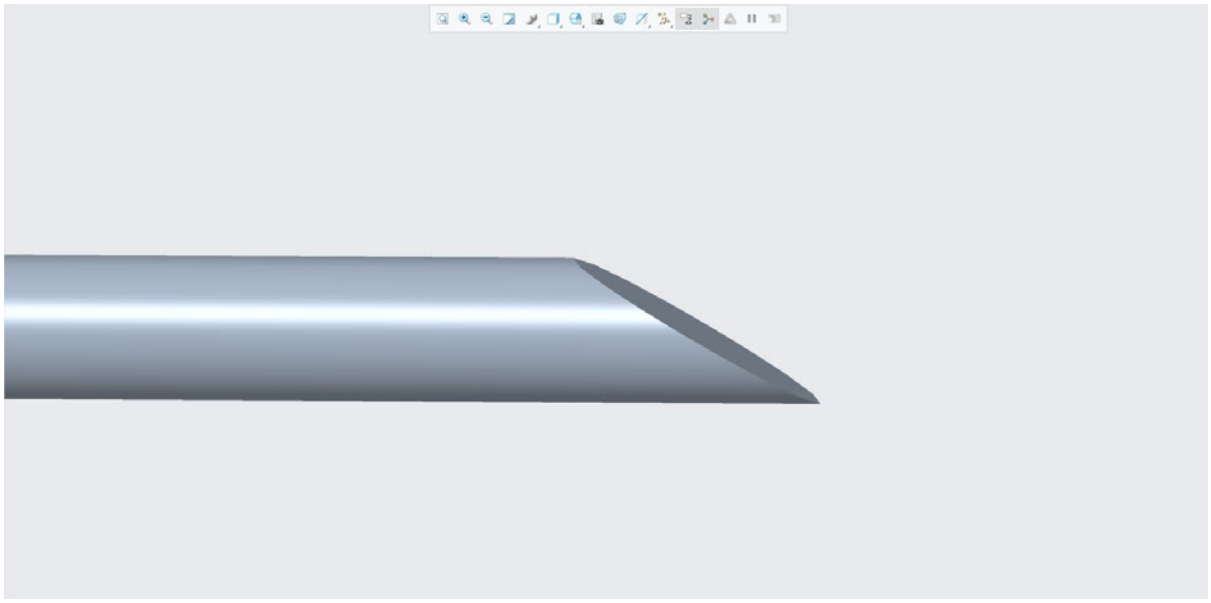

Figure 4.16: Paul Snipped Tube Model

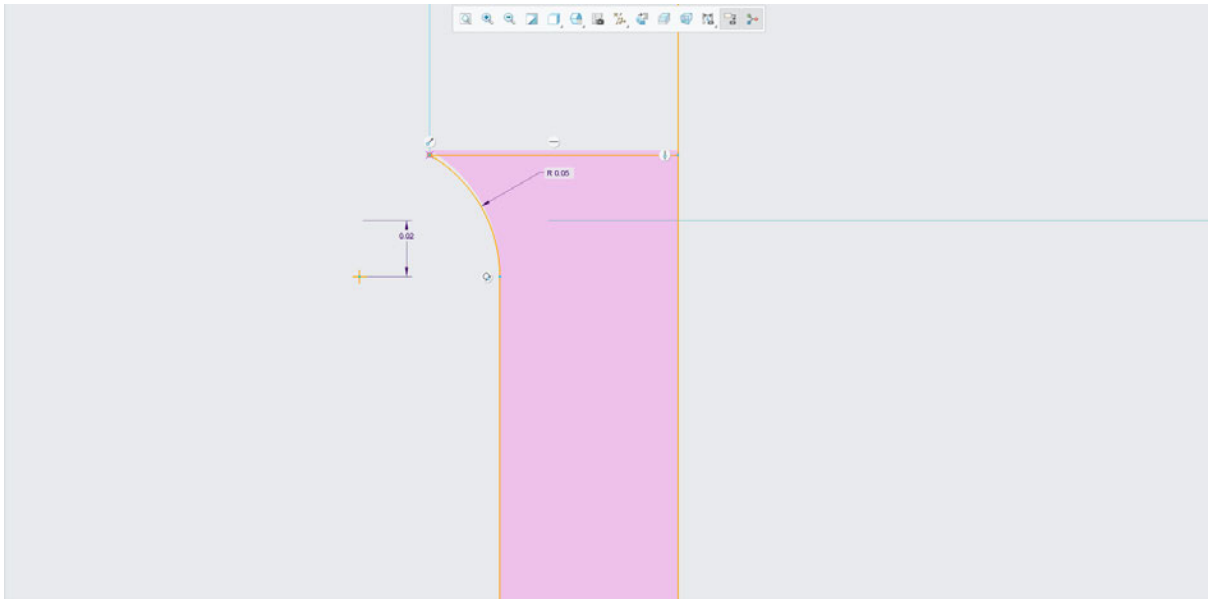

Figure 4.17: Paul Rounded Inlet Tube Revolved Geometry

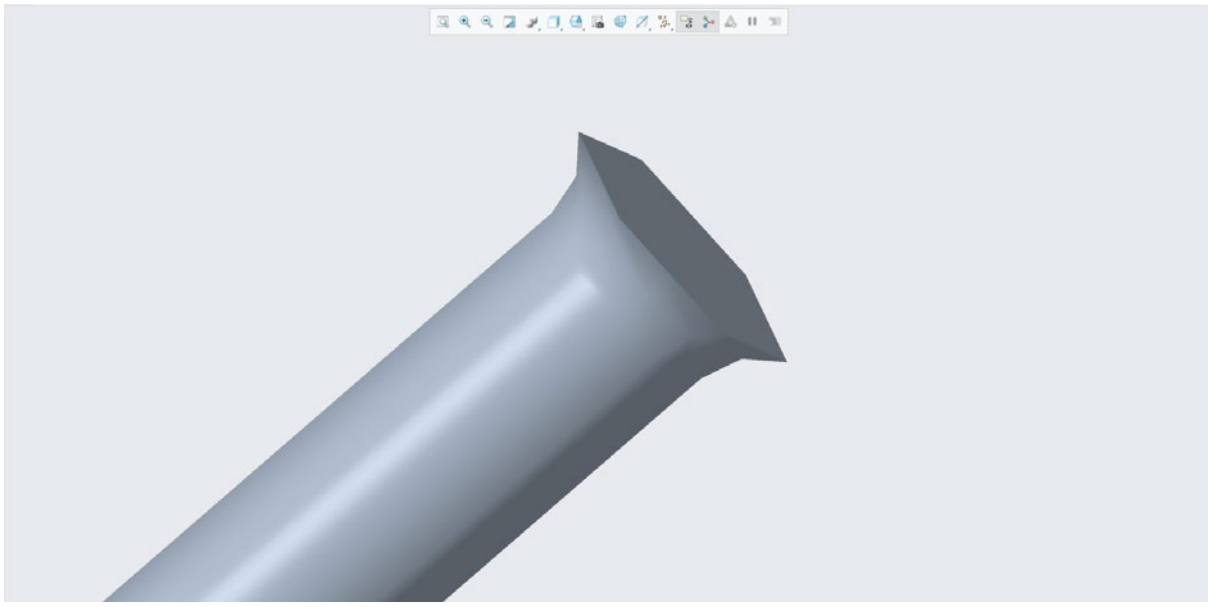

Figure 4.18: Paul Rounded Inlet Tube Model

4.3 Chapter Summary

The twelve models produced, six from each of the Baerveldt and Paul implants, will now be utilised in the CFD software Ansys for simulation. Each model has been produced from available data or justified assumptions, to simulate the fluid region in the drainage tubes of the Glaucoma implants. The standard tube, sutured tube, single finned, double finned, snipped, and rounded inlet tubes will be initialised and simulated for various flow rates to find the unique effects and characteristics of each tube adjustment throughout Chapter 5. These results will be further critiqued, analysed, and compared in the results discussion section of this research project.

Chapter 5 – CFD Simulation

5.1 Chapter Overview

This chapter will display the CFD simulation data, results, and plots for each tube variation considered within this project. The entire simulation process, including the initialisation and boundary conditions, will be outlined to both inform the reader and justify the selections made for the CFD model employed in this study. The theoretical calculations, mesh independency studies, plots, and raw results for each tube variation will be clearly presented before further discussion and analysis in Chapter 6.

5.2 Boundary Conditions and Initialisation

Aqueous humour flows very slowly, subsequently, this flow can be categorised as laminar throughout the eye and into the glaucoma drainage device. Given that aqueous humour consists primarily of water, it is considered as a Newtonian and incompressible fluid. Furthermore, considering the generalised conditions of aqueous humour flow and comparing to similar studies, the solution characteristics of this CFD study will be assumed as isothermal and incompressible flow with steady-state conditions (Kara, E. and Kutlar, A. 2010). Temperature ranges and effects will also be assumed to remain constant, due to the very limited amount of fluid involved in the study. As described, the default Ansys Laminar model will be utilised for all simulations performed throughout.

As mentioned, aqueous humour consists primarily of water, with trace amounts of minerals. Subsequently, to initialise the fluid properties of aqueous humour, the default water-liquid setting within Ansys Fluent was copied and renamed. Additional parameters can be used as Fitt, A.D and Gonzalez, G. (2006) conducted a fluid mechanics study investigating flow in the anterior chamber and assumed aqueous humour density to be 1000kg/m^3. Gardiner, B.S. et al. (2010) completed a study regarding computational modelling of fluid flow and IOP, and suggested an aqueous humour viscosity of 0.0007 Pa.s (or kg.m^{-1}.s^{-1}). Subsequently, these primary fluid property modifications were attributed to the aqueous humour fluid setting and were used throughout the remainder of the study (see figure 5.1).

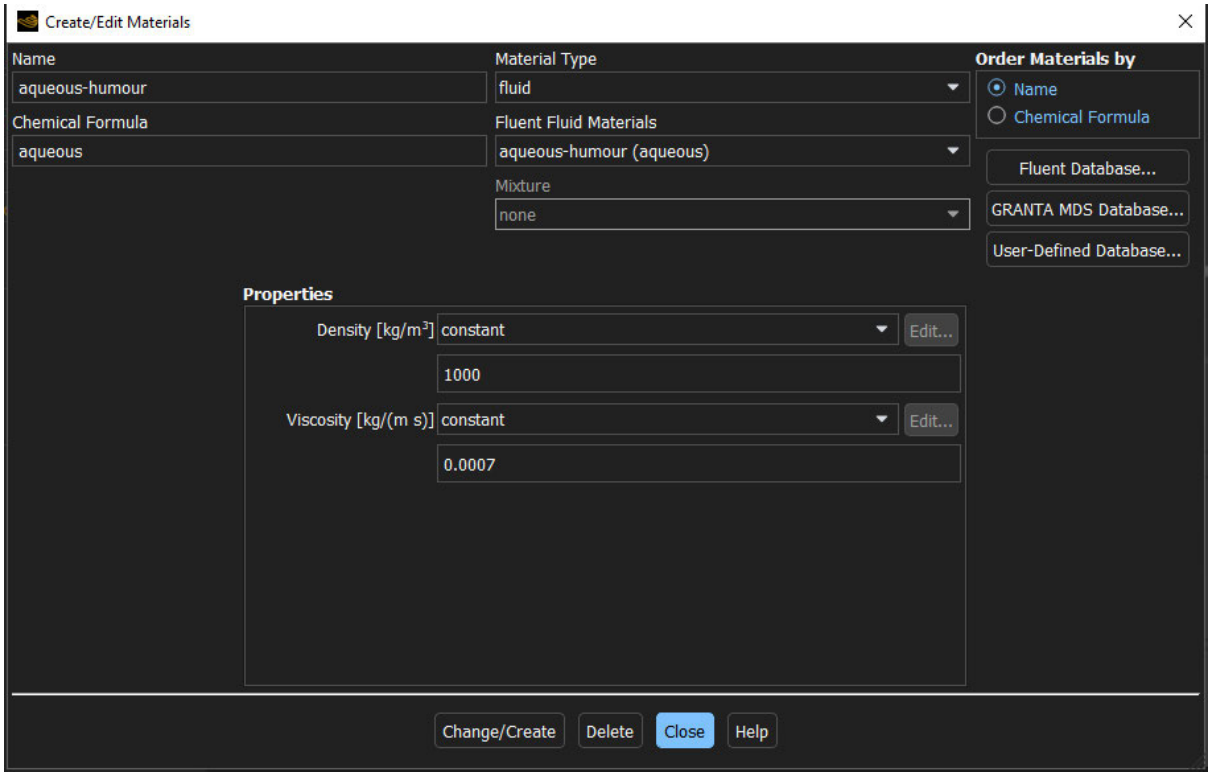

Figure 5.1: Aqueous Humour Ansys Fluent Fluid Properties

Initialising the boundary conditions is imperative to the success of every CFD study. The primary conditions for the drainage tube simulations will consist of a mass-flow inlet and pressure outlet. Each fluid flow rate utilised in the study (µL/min) is converted to a mass-flow rate via the following formula:

$$\dot{m}\left(\frac{kg}{s}\right) = \frac{Q\left(\frac{\mu L}{min}\right)}{60 \times 10^6 \times 1000} \times 1000\left(\frac{kg}{m^3}\right)$$

An initial gauge pressure of 4666Pa, (or ≈ 35mmHg) was employed across the study to simulate a severe case of Glaucoma for all the drainage tube simulations. These conditions, along with an example mass flow rate of 1.6µL/min, is depicted for the mass-flow inlet in figure 5.2.

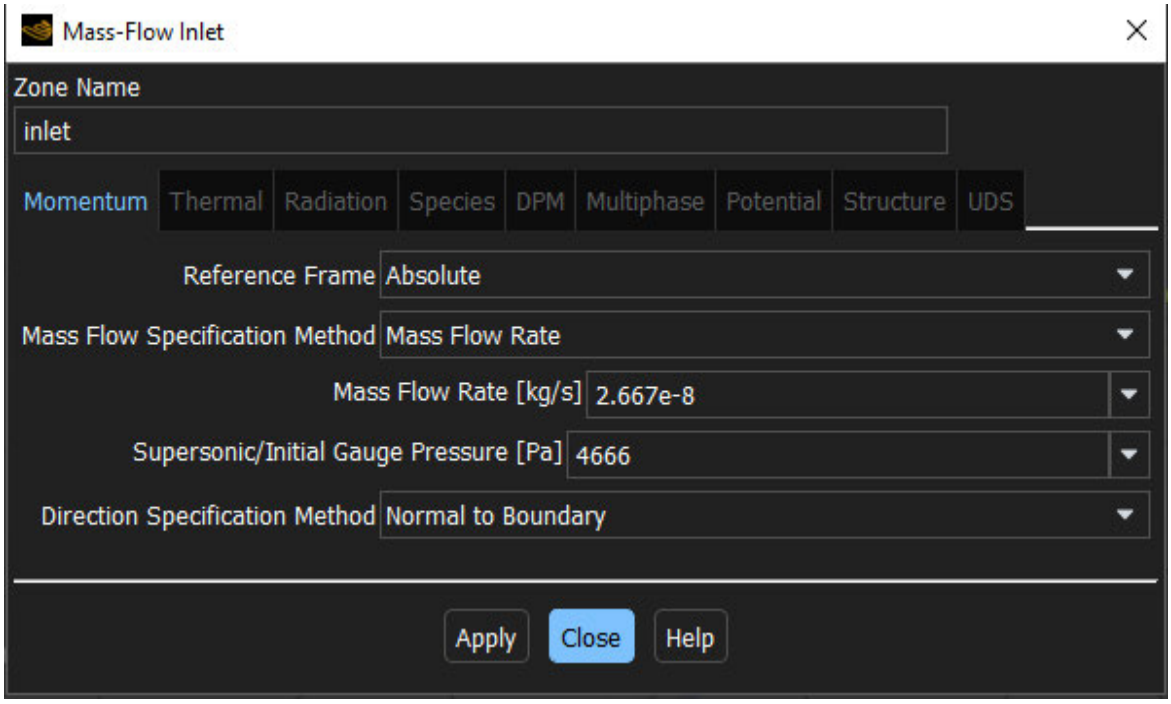

Figure 5.2: Mass Flow Inlet Initialised Conditions

The double precision solver was also utilised throughout all studies to ensure the highest order of accuracy. Given the micro size and speed of the model, the additional computational time required for double precision was not a hinderance on the simulation effectiveness. The hybrid initialisation method was utilised for all simulations, along with a residual error tolerance of 10^{-5}. While each simulation varied, the upper limit for the iterations was approximately 100.

Table 5.1: Summary of the CFD Simulation Parameters

Parameter	**Setting**
Model	Laminar
Precision	Double
Time	Steady State
Inlet	Mass Flow Inlet (kg/s)
Outlet	Pressure Outlet (Pa)
Fluid	Aqueous Humour (modified from default H_2O properties)
Initialisation Method	Hybrid
Residuals	10^{-5}
Iterations (approx.)	Up to 100
Initial Gauge Pressure	4666 Pa (≈ 35mmHg)

5.3 Standard Tube

The standard tube for both implants was simulated with standard conditions to serve as a baseline to compare to the other modifications. The results in this section will be displayed in tabular form, with each mesh independency study presented to verify the accuracy of the results.

5.3.1 Initial Conditions

As described in section 4.2.1, the Baerveldt standard tube fluid will be simulated with a diameter of 0.32mm (inner diameter of the implant tube), and a length of 32mm. The flow will be varied from 1.6µL/min, to 25µL/min. While physiological limits rarely exceed 3µL/min (Kara, E. and Kutlar, A. 2010), higher flow rates will be studied to show pressure drop patterns.

As described in section 4.2.2, the Paul standard tube fluid will be simulated with a diameter of 0.127mm (inner diameter of the implant tube), and a length of 29mm. The flow will also be varied from 1.6µL/min, to 25µL/min.

5.3.2 Theoretical Calculations

As detailed in section 2.4.3, the average pressure drop over a GDD drainage tube is categorised by the generalised Hagen-Poiseuille equation. As detailed by Agujetas, R. et al. 2021, this equation takes the following form:

$$p_{\mathrm{c}} - p_{\mathrm{b}} = \frac{128\,\mathscr{S} L_{\mathrm{v}} \mu Q_i}{\pi D_{\mathrm{h}}^4}$$

Where:

$$Pressure\ Drop, (Pa)\colon \Delta P = p_c - p_b$$

$$Shape\ Factor\colon \varphi$$

$$Tube\ Length\ (m)\colon L_v$$

$$Viscosity\ (Pa.s)\colon \mu$$

$$Flow\ Rate\ \left(\frac{m^3}{s}\right)\colon Q_i$$

$$Hydraulic\ Diameter\ (m)\colon D_h$$

Flow rate can be converted from µL/min to m^3/s via the following formula:

$$Q_i\left(\frac{m^3}{s}\right) = \frac{Q\left(\frac{\mu L}{min}\right)}{60 \times 10^6 \times 1000}$$

This formula can be used to calculate the theoretical pressure drop over a pipe with laminar flow. Hydraulic diameter is equal to the standard diameter for a cylindrical tube, and shape factor is equal to 1 in this instance (Agujetas, R. et al. 2021). This formula was applied to all six flow rates across the Baerveldt and Paul tubes.

Sample Calculation @ 1.6µL/min for Baerveldt Tube

$$\Delta P = \frac{128(1)\left(\frac{32}{1000}\right)(0.0007)\left(\frac{1.6}{60 \times 10^6 \times 1000}\right)}{\pi\left(\frac{0.32}{1000}\right)^4} = 2.321\ Pa$$

This calculation was repeated for each tube and respective flow rate and will be presented tabularly in sections 5.3.4 and 5.3.6.

5.3.3 Baerveldt Mesh Independency Study

Before commencing the various simulations, a mesh independence study is required (as outlined in section 3.4.1) to ensure the model is independent of its mesh, to produce more accurate results. The general limit for this study is to have the result variance within 5%, which will be employed in this case.

The Baerveldt standard tube was subjected to this study under the following conditions:

- Flow 2.5µL/min
- Default surface mesh
- Default boundary layers (3 layers @ 0.272 transition ratio)
- 10^{-5} convergence tolerance, double precision solver

By only varying the global volume element size, the results for pressure drop and wall shear stresses can be seen in the following table:

Table 5.2: Baerveldt Standard Tube Mesh Independency Study

Volume Element Size (m)	Pressure Drop, ΔP (Pa)	Wall Shear Stress Maximum (Pa)	Wall Shear Stress Minimum (Pa)
5.00E-05	3.77	3.93E-02	8.74E-03
4.00E-05	3.8	3.93E-02	8.75E-03
3.00E-05	3.84	3.94E-02	8.82E-03
2.00E-05	3.86	3.95E-02	8.94E-03

As evident, the variance in pressure drop results are within a 5% tolerance:

$$3.77 + (3.77 \times 0.05) = \mathbf{3.96}\ (upper\ limit\ not\ exceeded)$$

Additionally, the shear stress results are also within the 5% tolerance.

Subsequently, the mesh construction and its specified conditions are considered mesh independent and therefore suitable to use throughout the simulations.

5.3.4 Baerveldt Simulations

The volume element size chosen for these simulations is 3.00E-05m, to increase accuracy while maintaining computational time and efficiency (comparatively to 2.00E-0.5m). This mesh had approximately 123,000 elements, with a very high average orthogonal quality and very low skewness, as seen over the following figures 5.3 and 5.4.

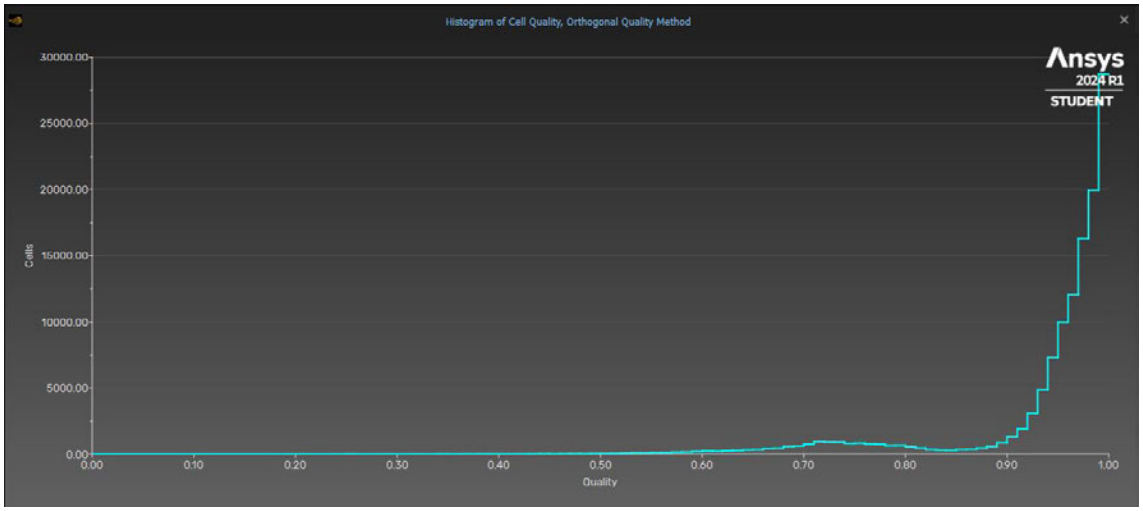

Figure 5.3: Baerveldt Standard Tube Mesh Orthogonal Quality

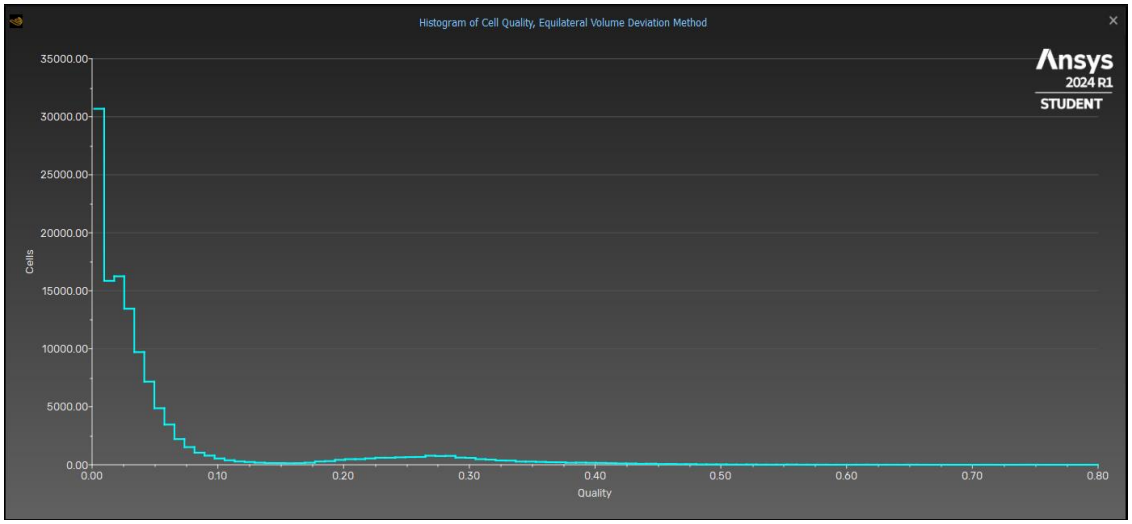

Figure 5.4: Baerveldt Standard Tube Mesh Skewness

By varying the flow rate, the following results were produced and have been tabulated:

Table 5.3: Baerveldt Standard Tube Simulation Results

Flow Rate (µL/min)	Mass Flow Rate (kg/s)	CFD Pressure Drop, ΔP (Pa)	Theoretical Pressure Drop, ΔP (Pa)	Percentage Error (%)
1.6	2.667E-08	2.46	2.321	5.988
2.5	4.167E-08	3.84	3.627	5.885
5	8.333E-08	7.68	7.253	5.885
10	1.667E-07	15.4	14.506	6.161
20	3.333E-07	30.7	29.013	5.816
25	4.167E-07	38.4	36.266	5.885

As evident, the percentage error is within an acceptable range between the simulation and pressure results. The pressure contour gradually decreased along the length of the tube, as displayed in the following 2.5µL/min plot. The remaining plots are found in appendix C.

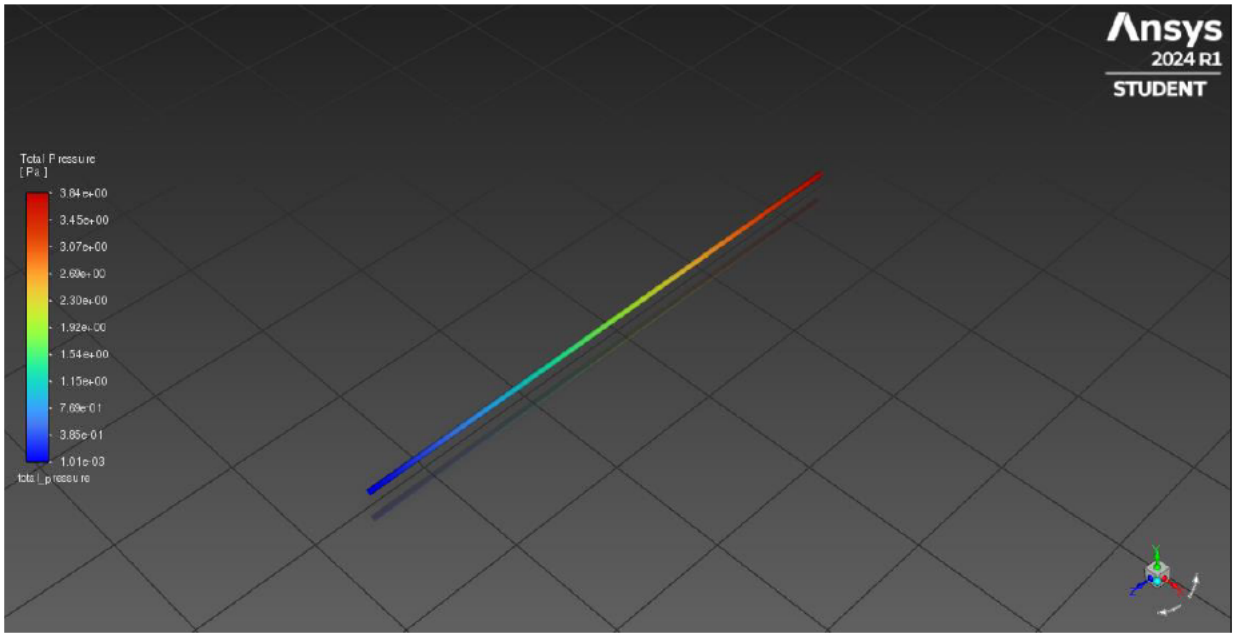

Figure 5.5: Baerveldt Standard Tube 2.5µL/min Pressure Contour Plot

5.3.5 Paul Mesh Independency Study

Similarly to the Baerveldt tube, a mesh independency study is required for the standard Paul tube. The general limit for this study is to have the result variance within 5%, which will be employed in this case.

The Paul standard tube was subjected to this study under the following conditions:

- Flow 1.6μL/min
- Default surface mesh
- Default boundary layers (3 layers @ 0.272 transition ratio)
- 10^{-5} convergence tolerance, double precision solver

By only varying the global volume element size, the results for pressure drop and wall shear stresses can be seen in the following table:

Table 5.4: Paul Standard Tube Mesh Independency Study

Volume Element Size (m)	Pressure Drop, ΔP (Pa)	Wall Shear Stress Maximum (Pa)	Wall Shear Stress Minimum (Pa)
4.50E-05	91.3	2.75E-01	8.98E-02
3.50E-05	91.3	2.75E-01	8.98E-02
2.50E-05	91.8	2.74E-01	9.02E-02
1.50E-05	93.5	2.75E-01	9.28E-02

As evident, the variance in pressure drop results are within a 5% tolerance:

$$91.3 + (91.3 \times 0.05) = \mathbf{95.87}\ (upper\ limit\ not\ exceeded)$$

Additionally, the shear stress results are also within the 5% tolerance.

Subsequently, the mesh construction and its specified conditions are considered mesh independent and therefore suitable to use throughout the simulations.

5.3.6 Paul Simulations

The volume element size chosen for these simulations is 2.50E-05m, to increase accuracy while maintaining computational time and efficiency (comparatively to 1.50E-0.5m). This mesh had approximately 75,000 elements, with a very high average orthogonal quality and very low skewness, as seen over the following figures 5.6 and 5.7.

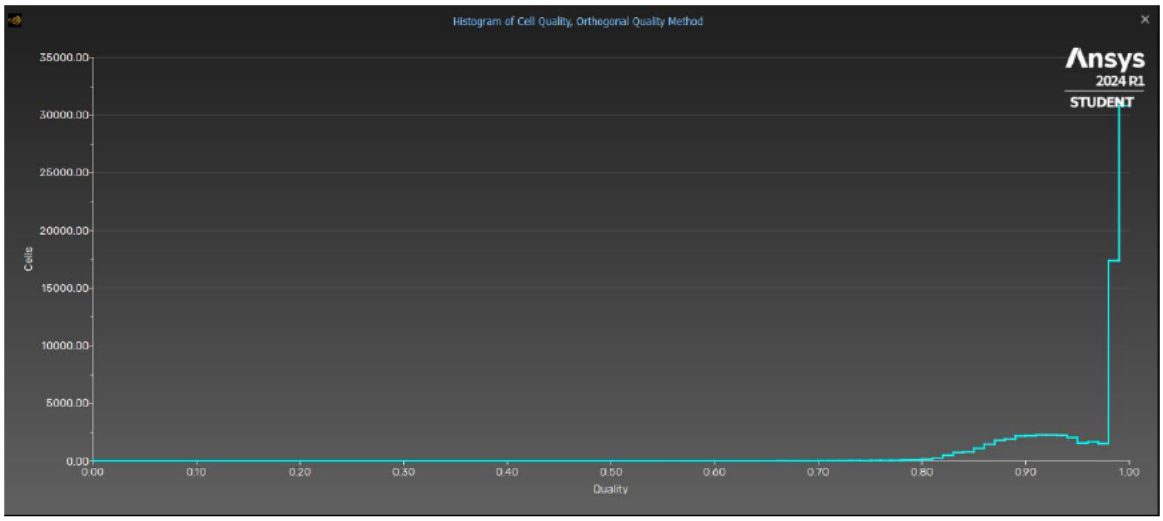

Figure 5.6: Paul Standard Tube Mesh Orthogonal Quality

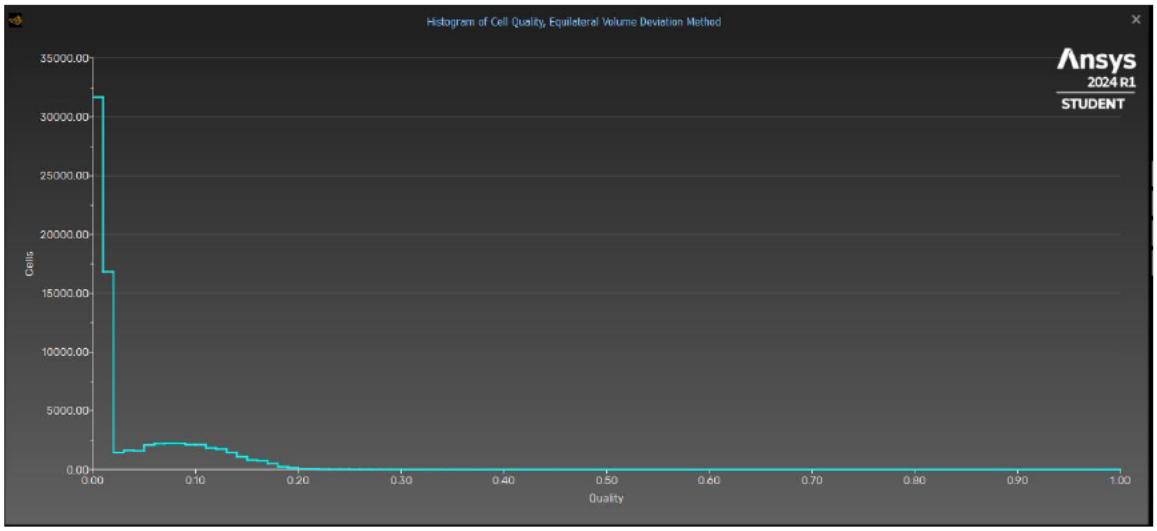

Figure 5.7: Paul Standard Tube Mesh Skewness

Similarly to the Baerveldt, varying the flow rate produces the following tabulated results:

Table 5.5: Paul Standard Tube Simulation Results

Flow Rate (µL/min)	Mass Flow Rate (kg/s)	CFD Pressure Drop, ΔP (Pa)	Theoretical Pressure Drop, ΔP (Pa)	Percentage Error (%)
1.6	2.667E-08	91.8	84.783	8.276
2.5	4.167E-08	143.5	132.474	8.323
5	8.333E-08	287.1	264.948	8.361
10	1.667E-07	575.3	529.895	8.569
20	3.333E-07	1154.3	1059.790	8.918
25	4.167E-07	1445.5	1324.738	9.116

While slightly larger than the Baerveldt, the percentage error is still considered to be within an acceptable range. The pressure contour plot for 2.5µL/min is displayed, with the remaining plots visible in appendix C:

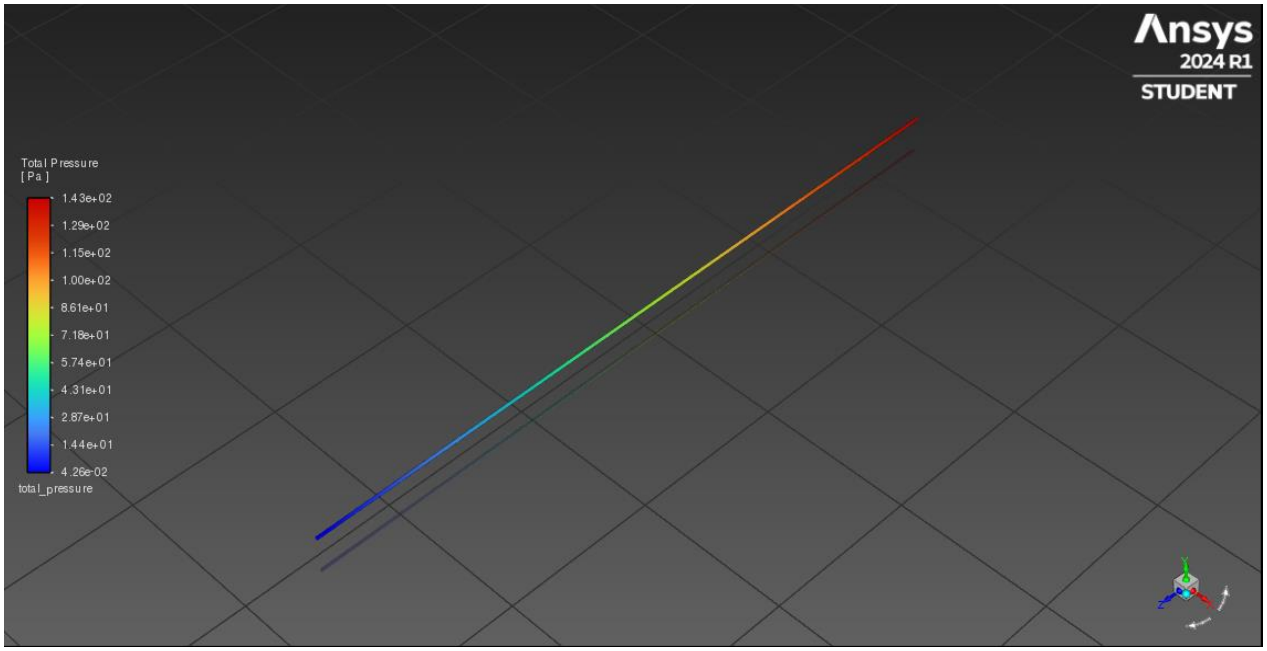

Figure 5.8: Paul Standard Tube 2.5µL/min Pressure Contour Plot

5.4 Sutured Tube

The sutured tube for both implants was simulated to investigate the effect a suture can have on pressure results when implemented in surgery. The results in this section will be displayed in tabular form, with each mesh independency study presented to verify the accuracy of the results.

5.4.1 Initial Conditions

As described in section 4.2.1, the Baerveldt sutured tube fluid will be simulated as a standard tube with a reduced section diameter in the centre of 0.24mm (25% reduction of standard diameter), and a length of 32mm. Like the previous simulations, the flow will be varied from 1.6µL/min, to 25µL/min.

As described in section 4.2.2, the Paul sutured tube fluid will be simulated as a standard tube with a reduced section diameter in the centre of 0.09525mm (25% reduction of standard diameter), and a length of 29mm.

As outlined by Agrawal and Bhardwaj (2020), during the procedure, the surgeon aims to reduce the aqueous humour flow rate by approximately half. Subsequently, to achieve accurate results during simulation, the flow rate will be halved to align with the surgical procedure. The theoretical formulae

will remain with the design flow rate, while the Ansys simulations will adopt the modified flow. This has been introduced to attempt to most accurately represent the surgery suture implementation through CFD simulation.

5.4.2 Theoretical Calculations

In combination with the generalised Hagen-Poiseuille equation, the shape factor for drainage tube suture must be implemented into the calculation. As detailed by Agujetas, R. et al. (2021), the shape factor for a suture of diameter D_s, placed co-axially, is calculated via the following equation:

$$\mathscr{S} = \left(1 - \frac{D_s}{D_i}\right)^4 \left\{1 - \left(\frac{D_s}{D_i}\right)^4 + \frac{[1 - (D_s/D_i)^2]^2}{\ln(D_s/D_i)}\right\}^{-1}.$$

Figure 5.9: Hagen-Poiseuille co-axial Suture Shape Factor Equation

As specified, the suture diameter for the Baerveldt tube and Paul tube is 0.24mm and 0.09525mm, respectively.

$$D_{s,Baerveldt} = 0.24mm$$

$$D_{s,Paul} = 0.09525mm$$

Subsequently, the ratio D_s/D_i can be calculated for both tubes:

$$\frac{D_{s,Baerveldt}}{D_{i,Baerveldt}} = \frac{0.24}{0.32} = 0.75$$

$$\frac{D_{s,Paul}}{D_{i,Paul}} = \frac{0.09525}{0.127} = 0.75$$

As both ratios are equal (given both tubes were reduced by 25%), the shape factor will be consistent for both tubes.

$$\varphi = (1 - 0.75)^4 \left\{1 - 0.75^4 + \frac{[1 - 0.75^2]^2}{\ln 0.75}\right\} = 0.2139914$$

Hydraulic diameter, D_h, for a co-axially sutured tube is characterised by the new internal diameter post suture, per Agujetas, R. et al. (2021).

$$D_{h,Baerveldt} = D_{s,Baerveldt} = 0.24mm$$

$$D_{h,Paul} = D_{s,Paul} = 0.09525mm$$

Repeating the calculation using the Hagen-Poiseuille equation with the updated variables:

Sample Calculation @ 1.6µL/min for Baerveldt Sutured Tube

$$\Delta P = \frac{128\,(0.2139914)\left(\frac{32}{1000}\right)(0.0007)\left(\frac{1.6}{60\times10^{6}\times1000}\right)}{\pi\left(\frac{0.24}{1000}\right)^{4}} = 1.57\,Pa$$

This calculation was repeated for each tube and respective flow rate and will be presented tabularly in sections 5.4.4 and 5.4.6.

5.4.3 Baerveldt Mesh Independency Study

Consistent with the standard tubes, a mesh independence study is required (as outlined in section 3.4.1) to ensure the model is independent of its mesh, to produce more accurate results. The general limit for this study is to have the result variance within 5%, which will be employed in this case.

The Baerveldt sutured tube was subjected to this study under the following conditions:

- Flow 1.6µL/min
- Default surface mesh
- Default boundary layers (3 layers @ 0.272 transition ratio)
- 10^{-5} convergence tolerance, double precision solver

By only varying the global volume element size, the results for pressure drop and wall shear stresses can be seen in the following table:

Table 5.6: Baerveldt Sutured Tube Mesh Independence Study

Volume Element Size (m)	Pressure Drop, ΔP (Pa)	Wall Shear Stress Maximum (Pa)	Wall Shear Stress Minimum (Pa)
5.00E-05	1.29	1.34E-02	2.82E-03
4.00E-05	1.34	1.34E-02	2.80E-03
3.00E-05	1.35	1.34E-02	2.80E-03
2.00E-05	1.35	1.35E-02	2.77E-03

As evident, the variance in pressure drop results are within a 5% tolerance:

$$1.29 + (1.29 \times 0.05) = \mathbf{1.3545}\ (upper\ limit\ not\ exceeded)$$

Additionally, the shear stress results are also within the 5% tolerance.

Subsequently, the mesh construction and its specified conditions are considered mesh independent and therefore suitable to use throughout the simulations.

5.4.4 Baerveldt Simulations

The volume element size chosen for these simulations is 3.00E-05m, to increase accuracy while maintaining computational time and efficiency (comparatively to 2.50E-0.5m). This mesh had approximately 122,000 elements, with a very high average orthogonal quality and very low skewness, as seen over the following figures 5.10 and 5.11.

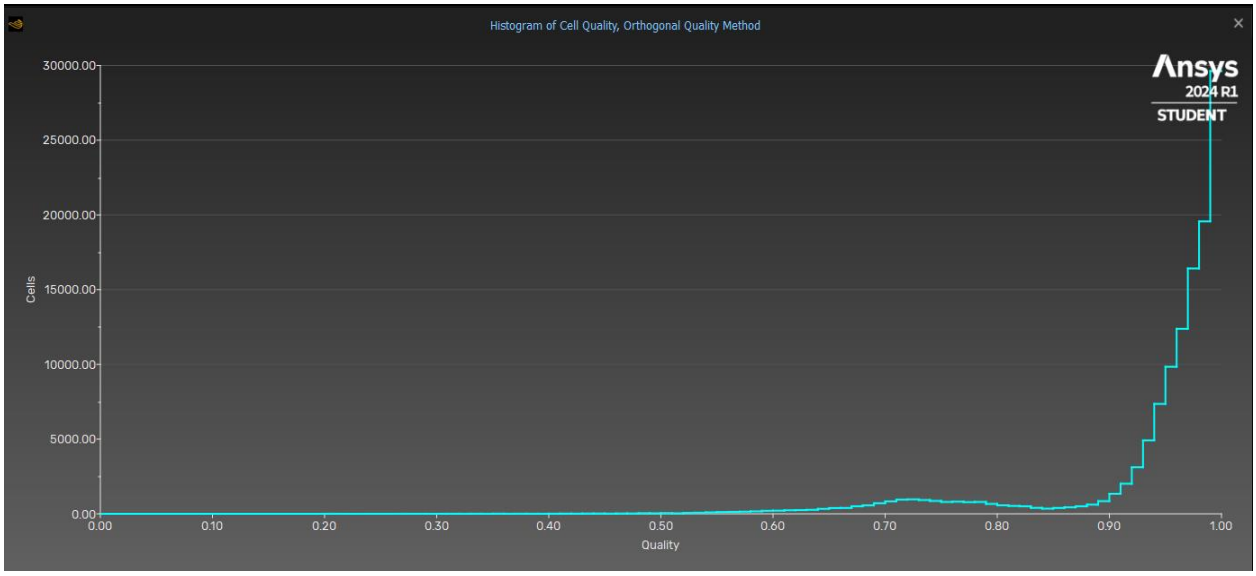

Figure 5.10: Baerveldt Sutured Tube Mesh Orthogonal Quality

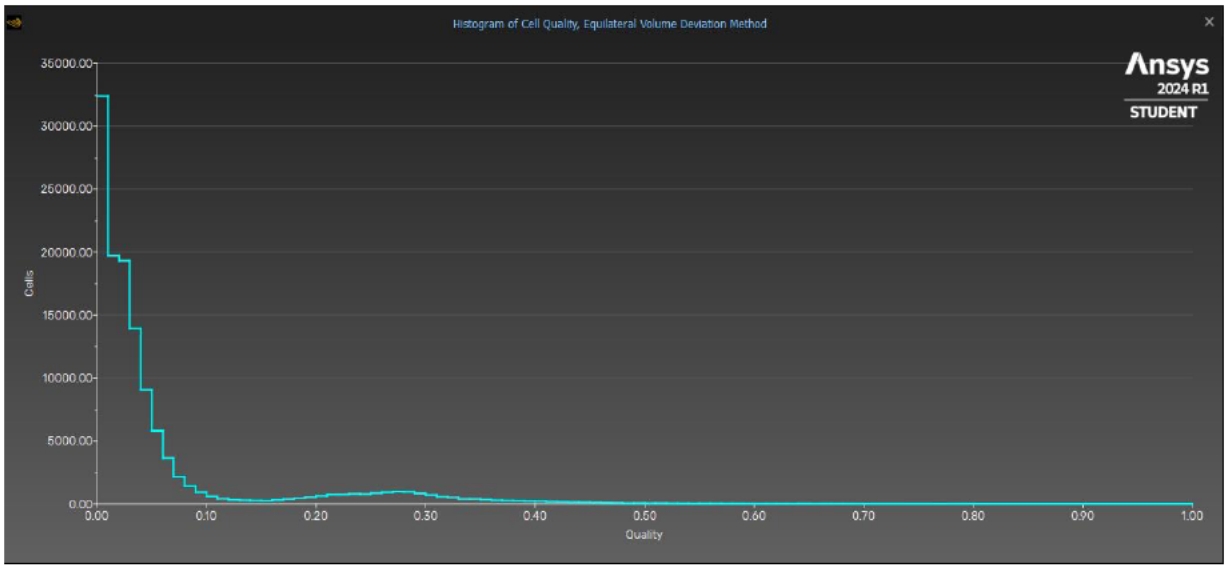

Figure 5.11: Baerveldt Sutured Tube Mesh Skewness

By varying the sutured mass flow rate and repeating the simulations, the results can be tabulated:

Table 5.7: Baerveldt Sutured Tube Simulation Results

Design Flow Rate (µL/min)	Mass Flow Rate (kg/s)	Sutured Mass Flow Rate (kg/s)	CFD Pressure Drop, ΔP (Pa)	Theoretical Pressure Drop, ΔP (Pa)	Percentage Error (%)
1.6	2.667E-08	1.333E-08	1.35	1.570	13.999
2.5	4.167E-08	2.083E-08	2.07	2.453	15.604
5	8.333E-08	4.167E-08	5.07	4.905	3.355
10	1.667E-07	8.333E-08	10.1	9.811	2.947
20	3.333E-07	1.667E-07	20.3	19.622	3.457
25	4.167E-07	2.083E-07	25.4	24.527	3.558

The percentage error is within an acceptable range for design flow rates 5µL/min through 25µL/min. While the error is much higher for 1.6 and 2.5µL/min at 14.0% and 15.6%, respectively, given the very small Pascal difference relatively, these results are considered acceptable. The pressure contour plot for 2.5µL/min is displayed, with the remaining plots in appendix C:

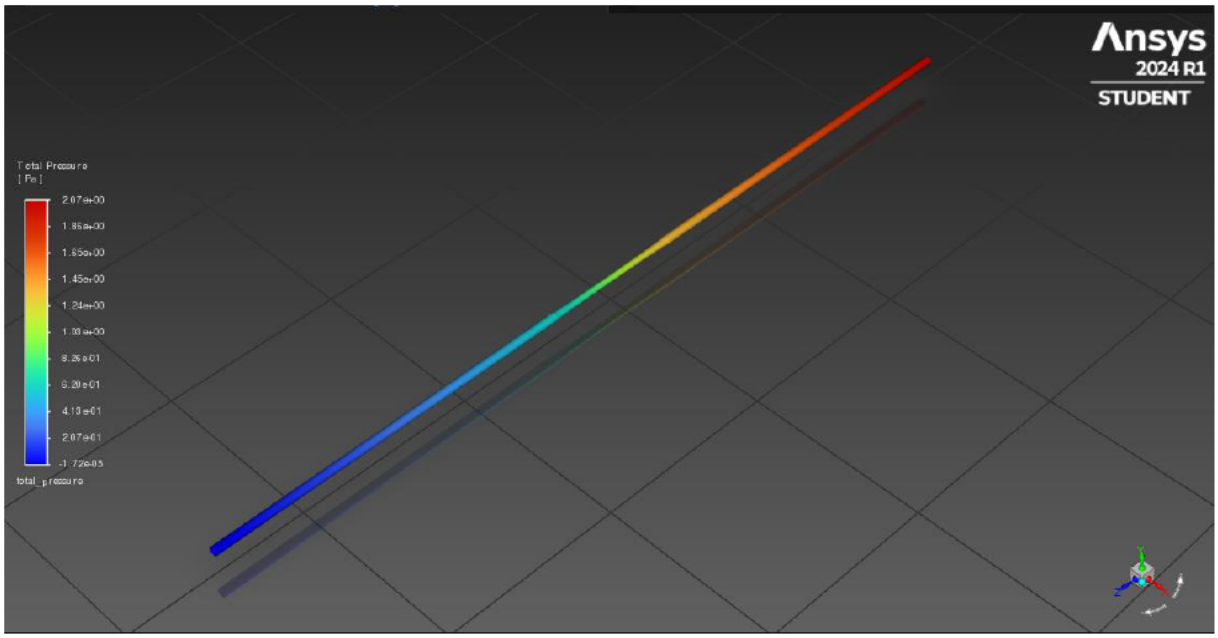

Figure 5.12: Baerveldt Sutured Tube 2.5µL/min Pressure Contour Plot

5.4.5 Paul Mesh Independency Study

Repeating the same process, a mesh independency study is required for the sutured Paul tube. The general limit for this study is to have the result variance within 5%, which will be employed in this case.

The Paul sutured tube was subjected to this study under the following conditions:

- Flow 1.6µL/min
- Default surface mesh
- Default boundary layers (3 layers @ 0.272 transition ratio)
- 10^{-5} convergence tolerance, double precision solver

By only varying the global volume element size, the results for pressure drop and wall shear stresses can be seen in the following table:

Table 5.8: Paul Sutured Tube Mesh Independency Study

Volume Element Size (m)	Pressure Drop, ΔP (Pa)	Wall Shear Stress Maximum (Pa)	Wall Shear Stress Minimum (Pa)
4.50E-05	58.5	1.37E-01	4.57E-02
3.50E-05	58.5	1.37E-01	4.57E-02
2.50E-05	58.8	1.37E-01	4.59E-02
1.50E-05	60	1.37E-01	4.71E-02

As evident, the variance in pressure drop results are within a 5% tolerance:

$$58.5 + (58.5 \times 0.05) = \mathbf{61.43}\ (upper\ limit\ not\ exceeded)$$

Additionally, the shear stress results are also within the 5% tolerance.

Subsequently, the mesh construction and its specified conditions are considered mesh independent and therefore suitable to use throughout the simulations.

5.4.6 Paul Simulations

Remaining consistent with the previous Paul simulations, the volume element size chosen for these simulations is 2.50E-05m, to increase accuracy while maintaining computational time and efficiency (comparatively to 1.50E-0.5m). This mesh had approximately 72,000 elements, with a very high average orthogonal quality and very low skewness, as seen over the following figures 5.13 and 5.14.

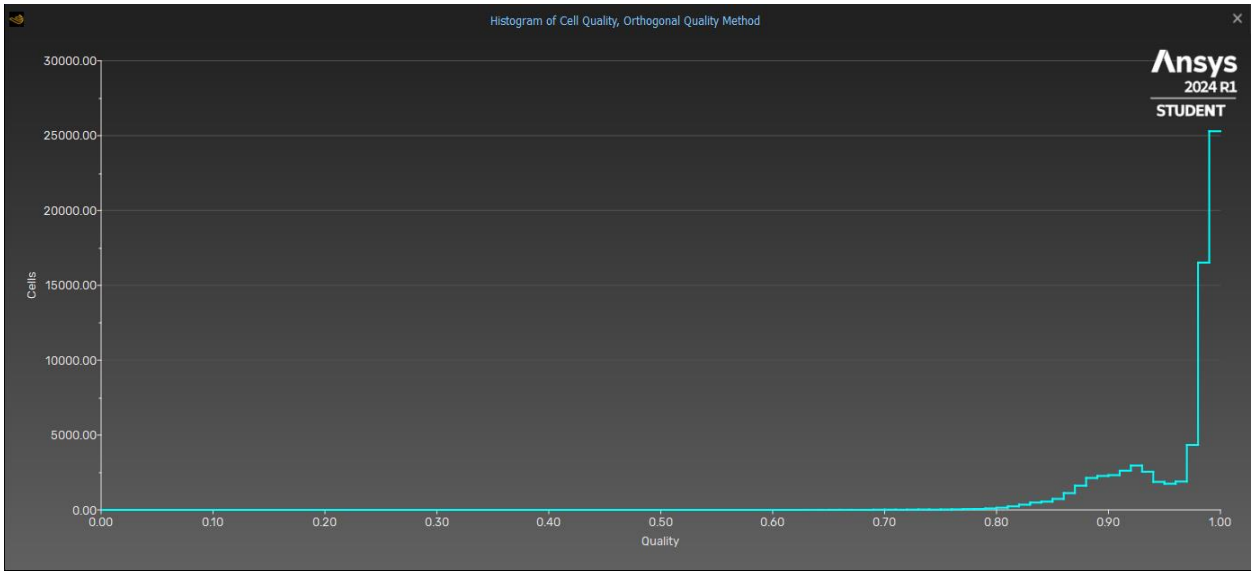

Figure 5.13: Paul Sutured Tube Mesh Orthogonal Quality

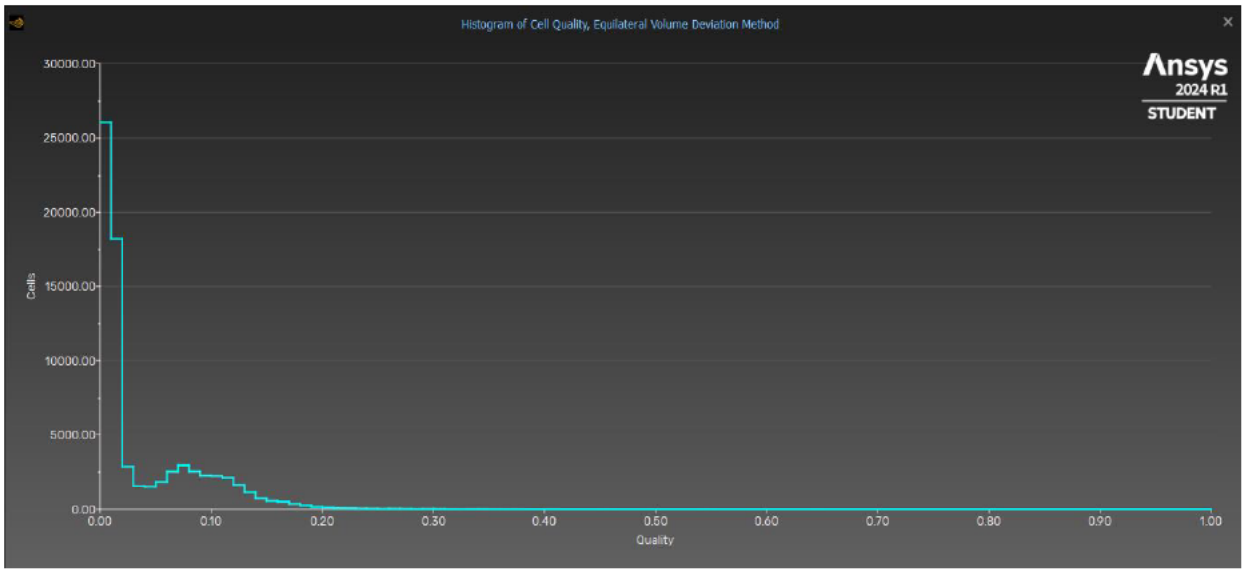

Figure 5.14: Paul Sutured Tube Mesh Skewness

By varying the sutured mass flow rate and repeating the simulations, the results can be tabulated:

Table 5.9: Paul Sutured Tube Simulation Results

Design Flow Rate (µL/min)	Mass Flow Rate (kg/s)	Sutured Mass Flow Rate (kg/s)	CFD Pressure Drop, ΔP (Pa)	Theoretical Pressure Drop, ΔP (Pa)	Percentage Error (%)
1.6	2.667E-08	1.333E-08	58.8	57.340	2.545
2.5	4.167E-08	2.083E-08	91.9	89.594	2.573
5	8.333E-08	4.167E-08	183.9	179.189	2.629
10	1.667E-07	8.333E-08	368.1	358.378	2.713
20	3.333E-07	1.667E-07	737.9	716.756	2.950
25	4.167E-07	2.083E-07	923.0	895.945	3.020

The percentage error in this case is well within the acceptable range. The pressure contour plot for 2.5µL/min is displayed, with the remaining plots in appendix C:

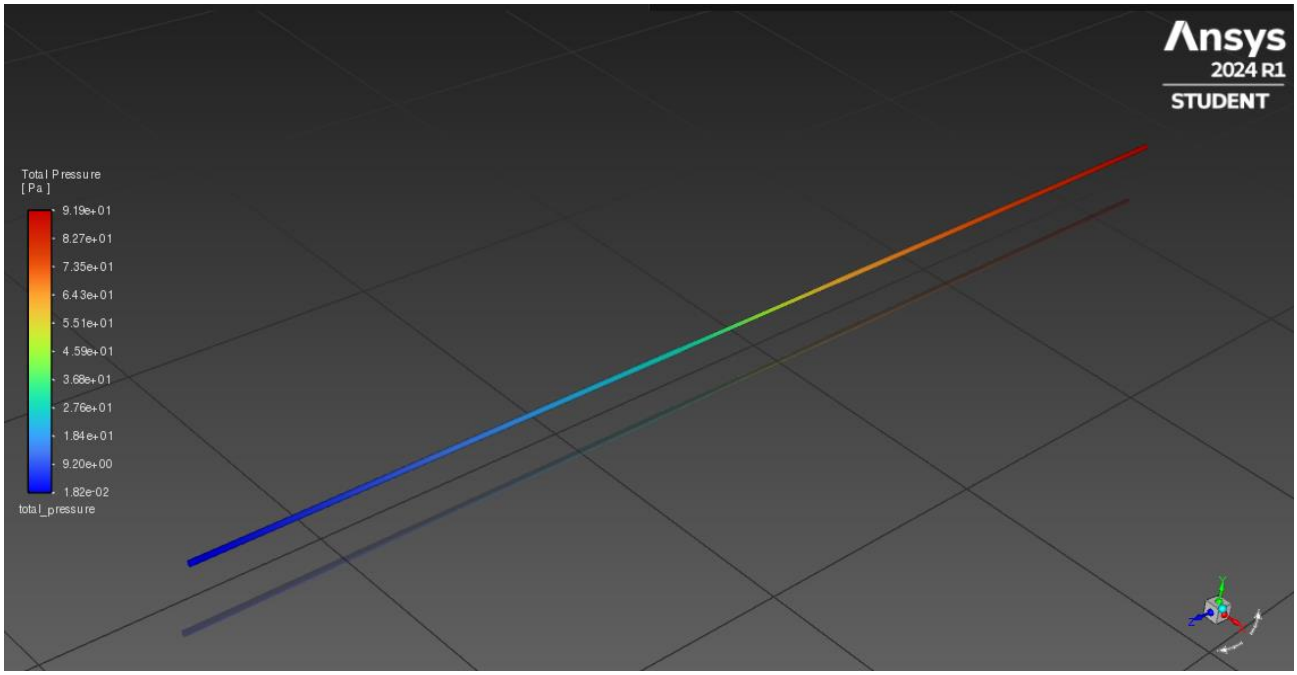

Figure 5.15: Paul Sutured Tube 2.5µL/min Pressure Contour Plot

5.5 Single Fin Tube

The single finned tube for both implants was simulated to investigate the effect a small fin within the bounds of the inner diameter can have on flow and pressure results. The results in this section will be displayed in tabular form, with each mesh independency study presented to verify the accuracy of the results. Given the experimental nature of this analysis, various assumptions will need to be made and justified when initialising the simulations and theoretical calculations.

5.5.1 Initial Conditions

As described in section 4.2.1, the Baerveldt single fin tube fluid will be simulated as a standard tube with a single fin-like shape in the centre of 0.5mm length and 0.1mm width (≈40% reduction of cross-sectional area), and a tube length of 32mm. Like the previous simulations, the flow will be varied from 1.6µL/min to 25µL/min.

As described in section 4.2.2, the Paul single fin tube fluid will be simulated as a standard tube with a single fin-like shape in the centre of 0.3mm length and 0.04mm width (≈40% reduction of cross-sectional area), and a tube length of 29mm.

5.5.2 Theoretical Calculations

As these fin extrusions are unlike anything studied in modern literature, there is limited theoretical background to draw from. Subsequently, several assumptions will need to be made to produce theoretical pressure drop data.

As seen in section 5.4.2, shape factor for a co-axial suture is defined by the given formula. For the sutured tubes, the inner diameter being reduced by 25% resulted in a D_s/D_i ratio of 0.75. In this case, if hydraulic diameter is assumed as the inner diameter minus the width of the fin (at the widest point) then 'suture' diameter, D_s, may be assumed as this hydraulic diameter, as it is the overall reduction in width. Therefore:

$$D_{h,baerveldt} = D_s = D_i - t_f = 0.32 - 0.1 = 0.22mm$$

$$\frac{D_{s,baervedlt}}{D_{i,baerveldt}} = \frac{0.22}{0.32} = 0.6875$$

$$D_{h,paul} = D_s = D_i - t_f = 0.127 - 0.04 = 0.087mm$$

$$\frac{D_{s,paul}}{D_{i,paul}} = \frac{0.087}{0.127} = 0.685$$

Given both diameter ratios are smaller than the suture ratio in section 5.4.2, as more of the inner diameter cross sectional area is covered, this theoretical analysis appears to be suitable. While the initial equations are for cylindrical sutures, these figures will provide some theoretical comparison for this very experimental analysis.

$$\varphi_{baerveldt} = (1 - 0.6875)^4 \left\{1 - 0.6875^4 + \frac{[1 - 0.6875^2]^2}{\ln 0.6875}\right\} = 0.2771325$$

$$\varphi_{paul} = (1 - 0.685)^4 \left\{1 - 0.685^4 + \frac{[1 - 0.6875^2]^2}{\ln 0.6875}\right\} = 0.27971014$$

Repeating the calculations using the Hagen-Poiseuille equation with the updated variables:

Sample Calculation @ 1.6µL/min for Baerveldt Single Fin Tube

$$\Delta P = \frac{128\,(0.2771325)\left(\frac{32}{1000}\right)(0.0007)\left(\frac{1.6}{60 \times 10^6 \times 1000}\right)}{\pi\left(\frac{0.22}{1000}\right)^4} = 2.879\ Pa$$

Sample Calculation @ 1.6µL/min for Paul Single Fin Tube

$$\Delta P = \frac{128\,(0.27971014)\left(\frac{29}{1000}\right)(0.0007)\left(\frac{1.6}{60 \times 10^6 \times 1000}\right)}{\pi\left(\frac{0.087}{1000}\right)^4} = 107.685\ Pa$$

These calculations were repeated for each respective flow rate and will be presented tabularly in sections 5.5.4 and 5.5.6.

5.5.3 Baerveldt Mesh Independency Study

The mesh independency study for the Baerveldt single fin tube was completed with the same conditions as previous tube variations. The general 5% error tolerance is also employed in this case.

The Baerveldt single fin tube was subjected to this study under the following conditions:

- Flow 1.6μL/min
- Default surface mesh
- Default boundary layers (3 layers @ 0.272 transition ratio)
- 10^{-5} convergence tolerance, double precision solver

By only varying the global volume element size, the results for pressure drop and wall shear stresses can be seen in the following table:

Table 5.10: Baerveldt Single Fin Tube Mesh Independency Study

Volume Element Size (m)	Pressure Drop, ΔP (Pa)	Wall Shear Stress Maximum (Pa)	Wall Shear Stress Minimum (Pa)
5.00E-05	2.61	2.90E-02	1.91E-03
4.00E-05	2.62	2.96E-02	1.93E-03
3.00E-05	2.65	2.95E-02	1.96E-03
2.00E-05	2.67	3.01E-02	2.03E-03

As evident, the variance in pressure drop results are within a 5% tolerance:

$$2.61 + (2.61 \times 0.05) = \mathbf{2.74}\ (upper\ limit\ not\ exceeded)$$

Additionally, the shear stress results are also within the 5% tolerance.

Subsequently, the mesh construction and its specified conditions are considered mesh independent and therefore suitable to use throughout the simulations.

5.5.4 Baerveldt Simulations

The volume element size chosen for these simulations is 3.00E-05m, to increase accuracy while maintaining computational time and efficiency (comparatively to 2.00E-0.5m). This mesh had approximately 123,000 elements, with a very high average orthogonal quality and very low skewness, as seen over the following figures 5.16 and 5.17.

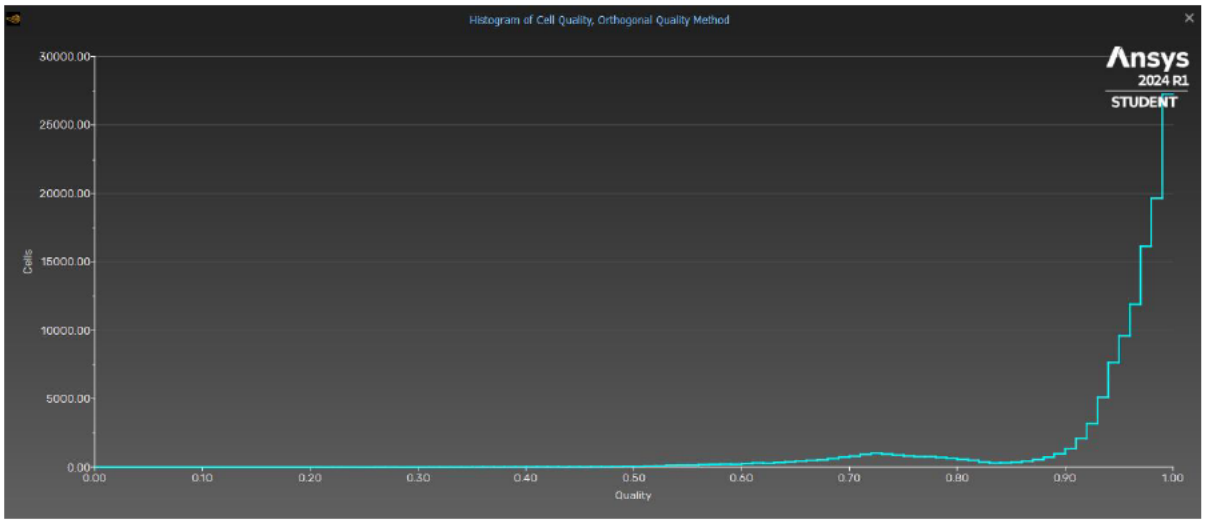

Figure 5.16: Baerveldt Single Fin Tube Mesh Orthogonal Quality

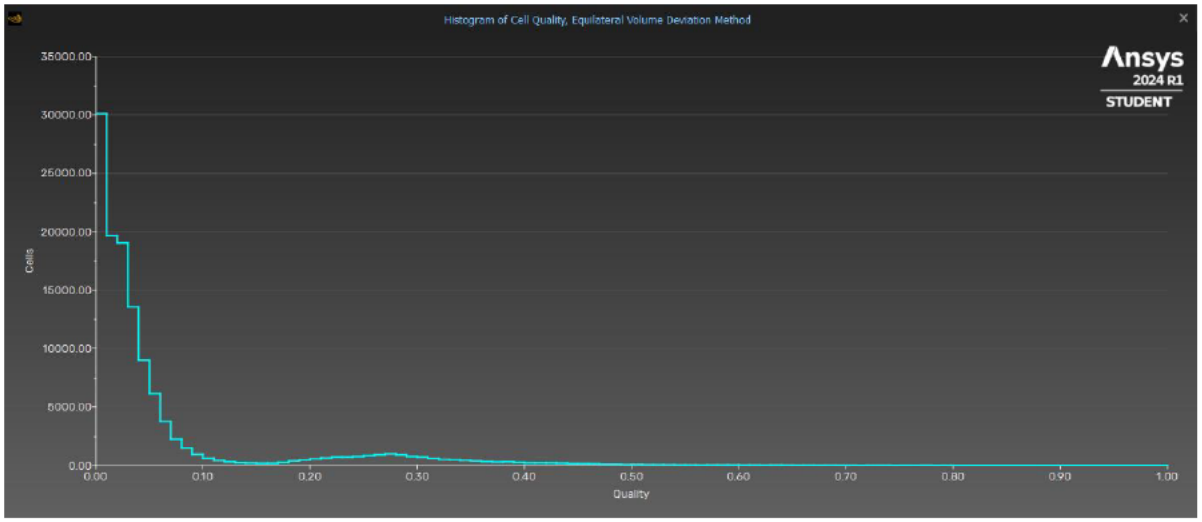

Figure 5.17: Baerveldt Single Fin Tube Mesh Skewness

Employing the various flow rates used throughout the study with the defined mesh yields the following results:

Table 5.11: Baerveldt Single Fin Tube Simulation Results

Flow Rate (µL/min)	Mass Flow Rate (kg/s)	CFD Pressure Drop, ΔP (Pa)	Theoretical Pressure Drop, ΔP (Pa)	Percentage Error (%)
1.6	2.667E-08	2.65	2.879	7.961
2.5	4.167E-08	4.14	4.499	7.975
5	8.333E-08	8.28	8.998	7.975
10	1.667E-07	16.6	17.995	7.753
20	3.333E-07	33.2	35.990	7.753
25	4.167E-07	41.5	44.988	7.753

Given the minimal variance of the data, the percentage error in this case is within the acceptable range. The pressure contour plot and wall shear stress plot for 2.5µL/min is displayed, with the remaining plots in appendix C:

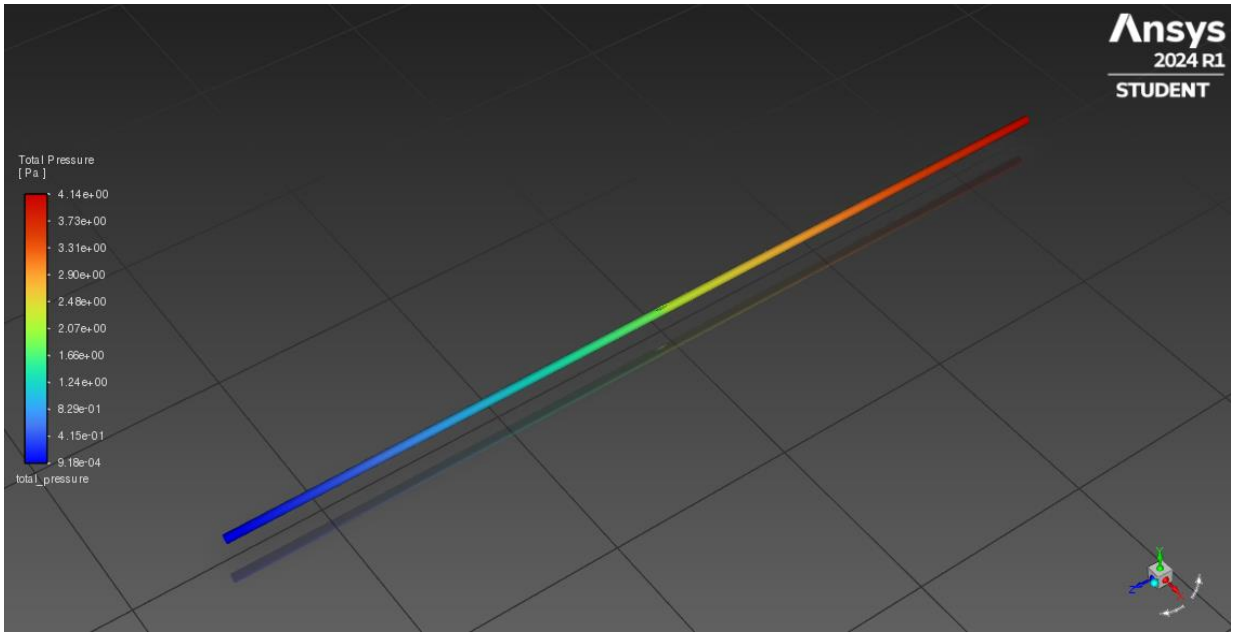

Figure 5.18: Baerveldt Single Fin Tube 2.5µL/min Pressure Contour Plot

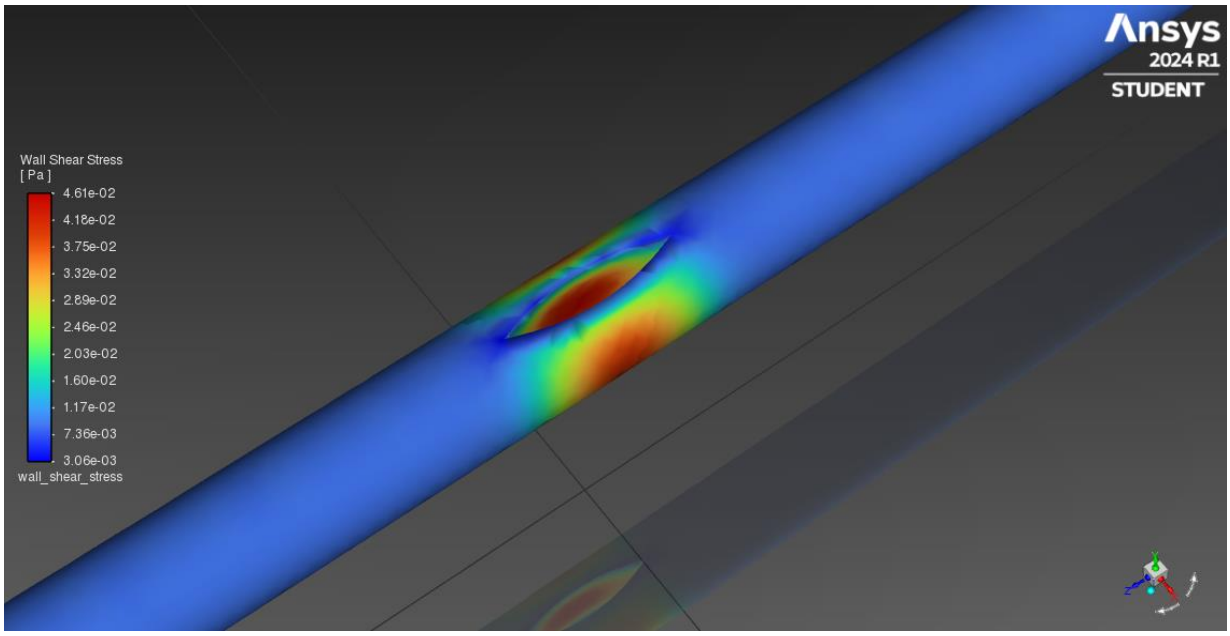

Figure 5.19: Baerveldt Single Fin Tube 2.5µL/min Wall Shear Stress Distribution at Fin

5.5.5 Paul Mesh Independency Study

The Paul single fin tube was subjected to a mesh independency study under the following conditions:

- Flow 1.6μL/min
- Default surface mesh
- Default boundary layers (3 layers @ 0.272 transition ratio)
- 10^{-5} convergence tolerance, double precision solver

By only varying the global volume element size, the results for pressure drop and wall shear stresses can be seen in the following table:

Table 5.12: Paul Single Fin Tube Mesh Independency Study

Volume Element Size (m)	Pressure Drop, ΔP (Pa)	Wall Shear Stress Maximum (Pa)	Wall Shear Stress Minimum (Pa)
4.50E-05	96.3	5.05E-01	5.43E-02
3.50E-05	96.3	5.04E-01	5.60E-02
2.50E-05	96.8	5.05E-01	5.61E-02
1.50E-05	98.5	5.05E-01	5.02E-02

As evident, the variance in pressure drop results are within a 5% tolerance:

$$96.3 + (96.3 \times 0.05) = \mathbf{101.15}\ (upper\ limit\ not\ exceeded)$$

Additionally, the shear stress results are also within the 5% tolerance.

Subsequently, the mesh construction and its specified conditions are considered mesh independent and therefore suitable to use throughout the simulations.

5.5.6 Paul Simulations

Remaining consistent with other Paul simulations, the volume element size chosen for these simulations is 2.50E-05m, to increase accuracy while maintaining computational time and efficiency (comparatively to 1.50E-0.5m). This mesh had approximately 75,000 elements, with a very high average orthogonal quality and very low skewness, as seen over the following figures 5.20 and 5.21.

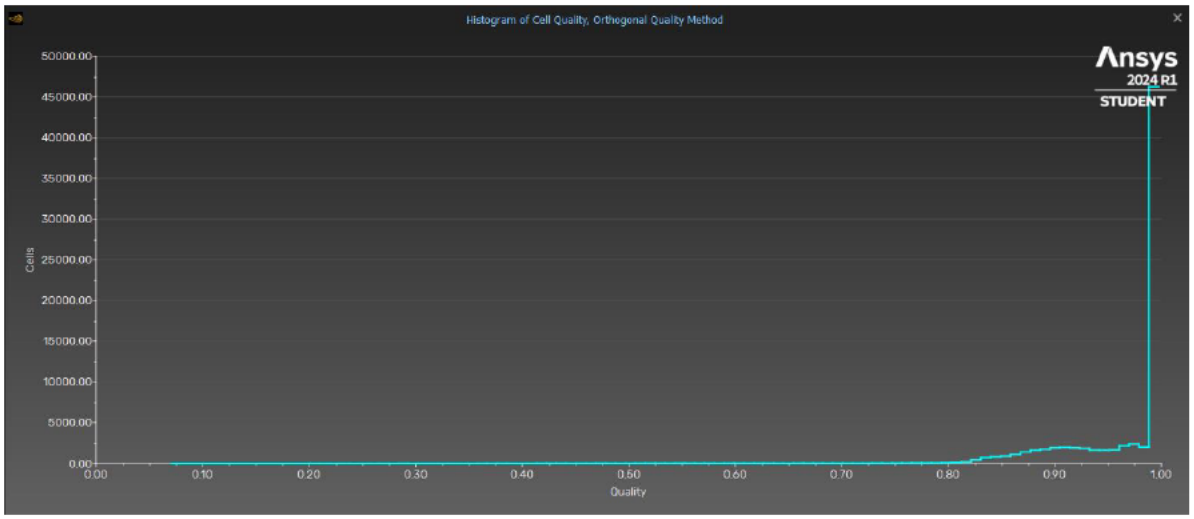

Figure 5.20: Paul Single Fin Tube Mesh Orthogonal Quality

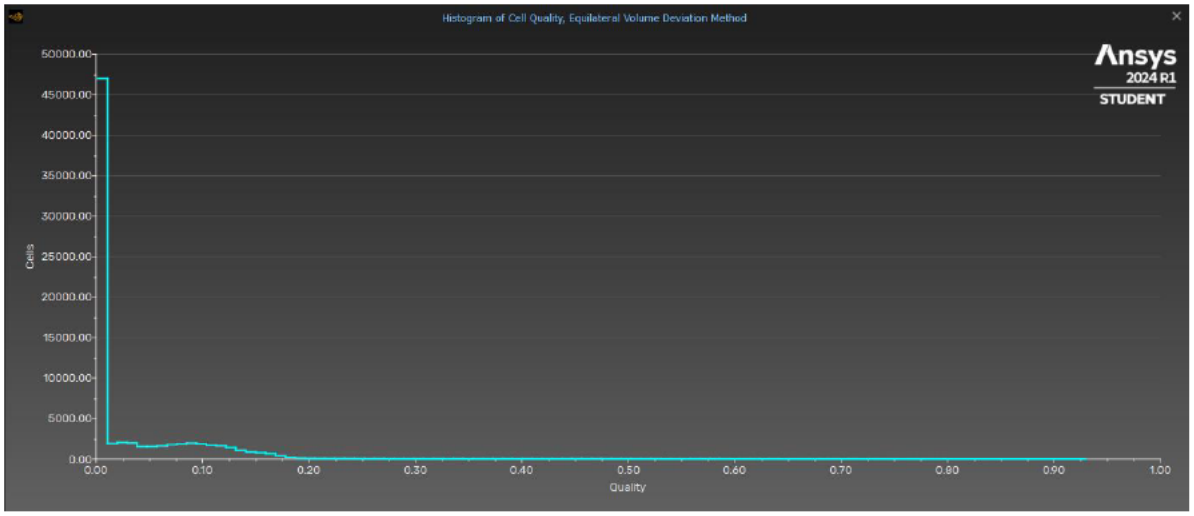

Figure 5.21: Paul Single Fin Tube Mesh Skewness

The simulations for this single fin arrangement yielded the following results:

Table 5.13: Paul Single Fin Tube Simulation Results

Flow Rate (µL/min)	Mass Flow Rate (kg/s)	CFD Pressure Drop, ΔP (Pa)	Theoretical Pressure Drop, ΔP (Pa)	Percentage Error (%)
1.6	2.667E-08	96.8	107.685	10.108
2.5	4.167E-08	151.1	168.258	10.198
5	8.333E-08	302.3	336.516	10.168
10	1.667E-07	607	673.033	9.811
20	3.333E-07	1215.7	1346.065	9.685
25	4.167E-07	1522.5	1682.581	9.514

The pressure contour plot and wall shear stress for 2.5µL/min is displayed, with the remaining plots in appendix C:

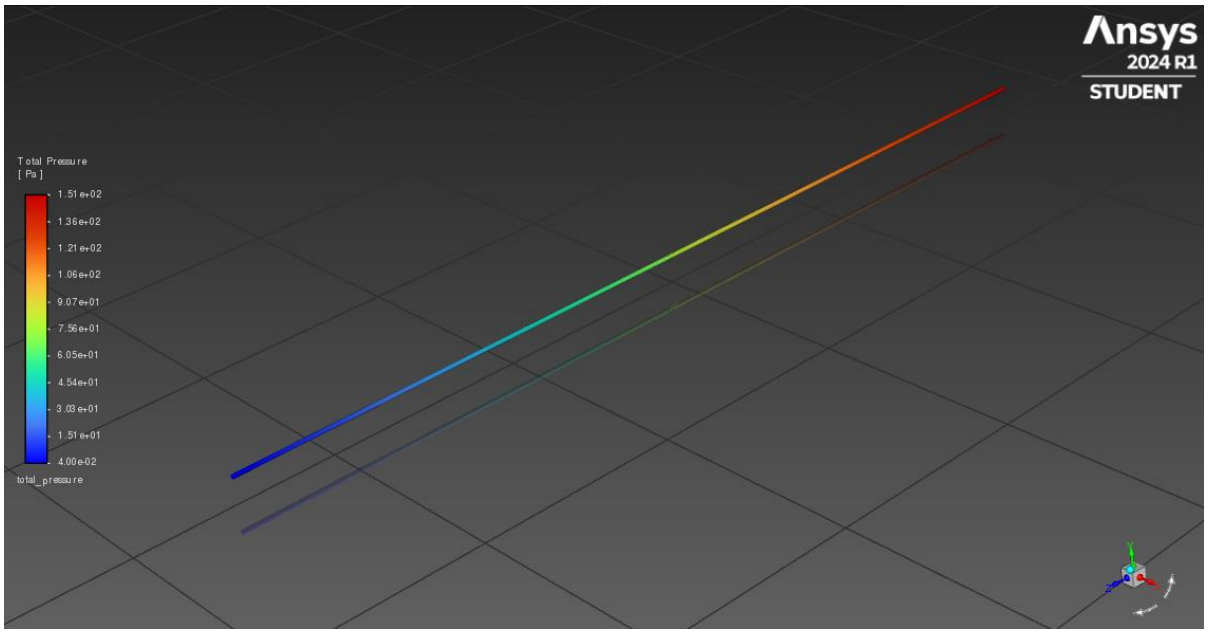

Figure 5.22: Paul Single Fin Tube 2.5µL/min Pressure Contour Plot

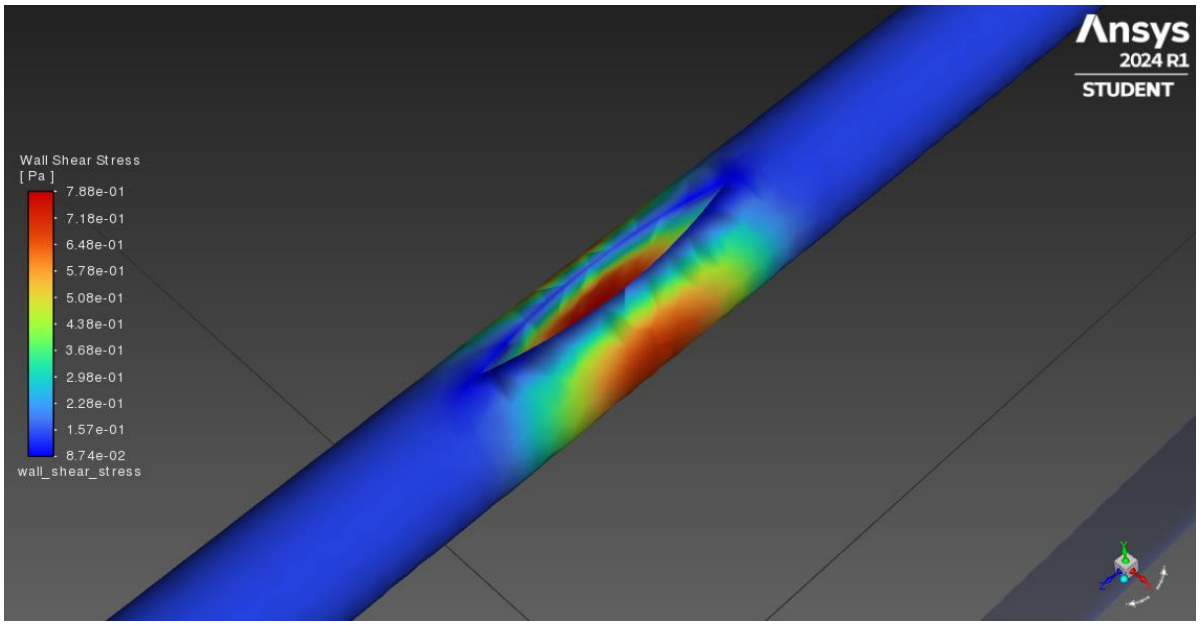

Figure 5.23: Paul Single Fin Tube 2.5µL/min Wall Shear Stress Distribution at Fin

5.6 Double Fin Tube

5.6.1 Initial Conditions

As described in section 4.2.1, the Baerveldt double fin tube fluid will be simulated as a standard tube with a double fin-like shape in the centre, consisting of two fins with 0.5mm length and 0.1mm width (≈80% reduction of cross-sectional area), and a tube length of 32mm. Like the previous simulations, the flow will be varied from 1.6µL/min, to 25µL/min.

As described in section 4.2.2, the Paul double fin tube fluid will be simulated as a standard tube with a double fin-like shape in the centre, consisting of two fins with 0.3mm length and 0.04mm width (≈80% reduction of cross-sectional area), and a tube length of 29mm.

5.6.2 Theoretical Calculations

By following the outline for the theoretical calculations discerned in section 5.5.2, many of the same assumptions can be made for the double finned model. The largest exception is the definition of the hydraulic diameter, which can be promptly updated through the principles of the Pythagorean theorem. At the centre of the tube, the fins will intersect with a maximum intersection measuring 0.1mm x 0.1mm (for the Baerveldt) and 0.04mm x 0.04mm (for the Paul). Subsequently, the hypotenuse adjoining these two fins can be found:

$$a^2 + b^2 = c^2$$

$$c_{baerveldt} = \sqrt{a^2 + b^2} = \sqrt{0.1 + 0.1^2} = 0.1414mm$$

$$c_{paul} = \sqrt{a^2 + b^2} = \sqrt{0.04 + 0.04^2} = 0.05657mm$$

By implementing this value as the fin thickness, the theoretical hydraulic diameter and diameter ratio for both the Baerveldt and Paul double finned tubes can be determined.

$$D_{h,baerveldt} = D_s = D_i - t_f = 0.32 - 0.1414 = 0.1786mm$$

$$\frac{D_{s,baervedlt}}{D_{i,baerveldt}} = \frac{0.1786}{0.32} = 0.5581$$

$$D_{h,paul} = D_s = D_i - t_f = 0.127 - 0.05657 = 0.07043mm$$

$$\frac{D_{s,paul}}{D_{i,paul}} = \frac{0.07043}{0.127} = 0.5546$$

Both diameter ratios are expectedly smaller than the suture ratio in section 5.4.2 and single fin ratio in 5.5.2, as more of the inner diameter cross sectional area is covered. The shape factor can now be

determined using these diameter ratio values. While the initial equations are for cylindrical sutures, these figures will provide some theoretical comparison for this very experimental analysis.

$$\varphi_{baerveldt} = (1 - 0.5581)^4 \left\{1 - 0.5581^4 + \frac{[1 - 0.5581^2]^2}{\ln 0.5581}\right\} = 0.42302213$$

$$\varphi_{paul} = (1 - 0.5546)^4 \left\{1 - 0.5546^4 + \frac{[1 - 0.5546^2]^2}{\ln 0.5546}\right\} = 0.42735256$$

Repeating the calculations using the Hagen-Poiseuille equation with the updated variables:

Sample Calculation @ 1.6µL/min for Baerveldt Double Fin Tube

$$\Delta P = \frac{128\,(0.42302213)\left(\frac{32}{1000}\right)(0.0007)\left(\frac{1.6}{60 \times 10^6 \times 1000}\right)}{\pi\left(\frac{0.1414}{1000}\right)^4} = 10.118\ Pa$$

Sample Calculation @ 1.6µL/min for Paul Double Fin Tube

$$\Delta P = \frac{128\,(0.42735256)\left(\frac{29}{1000}\right)(0.0007)\left(\frac{1.6}{60 \times 10^6 \times 1000}\right)}{\pi\left(\frac{0.05657}{1000}\right)^4} = 422.70\ Pa$$

These calculations were repeated for each respective flow rate and will be presented tabularly in sections 5.6.4 and 5.6.6.

5.6.3 Baerveldt Mesh Independency Study

The Baerveldt double fin tube was subjected to a mesh independency study under the following conditions:

- Flow 1.6µL/min
- Default surface mesh
- Default boundary layers (3 layers @ 0.272 transition ratio)
- 10^{-5} convergence tolerance, double precision solver

By only varying the global volume element size, the results for pressure drop and wall shear stresses can be seen in the following table:

Table 5.14: Baerveldt Double Fin Tube Mesh Independency Study

Volume Element Size (m)	Pressure Drop, ΔP (Pa)	Wall Shear Stress Maximum (Pa)	Wall Shear Stress Minimum (Pa)
5.00E-05	3.27	7.66E-02	4.69E-03
4.00E-05	3.29	7.67E-02	4.73E-03
3.00E-05	3.31	7.65E-02	4.78E-03
2.00E-05	3.33	7.71E-02	4.98E-03

As evident, the variance in pressure drop results are within a 5% tolerance:

$$3.27 + (3.27 \times 0.05) = \mathbf{3.43}\ (upper\ limit\ not\ exceeded)$$

Additionally, the shear stress results are also within the 5% tolerance.

Subsequently, the mesh construction and its specified conditions are considered mesh independent and therefore suitable to use throughout the simulations.

5.6.4 Baerveldt Simulations

Remaining consistent with previous Baerveldt tube iterations, the volume element size chosen for these simulations is 3.00E-05m. This mesh had approximately 122,000 elements, with a very high average orthogonal quality and very low skewness, as seen over the following figures 5.24 and 5.25.

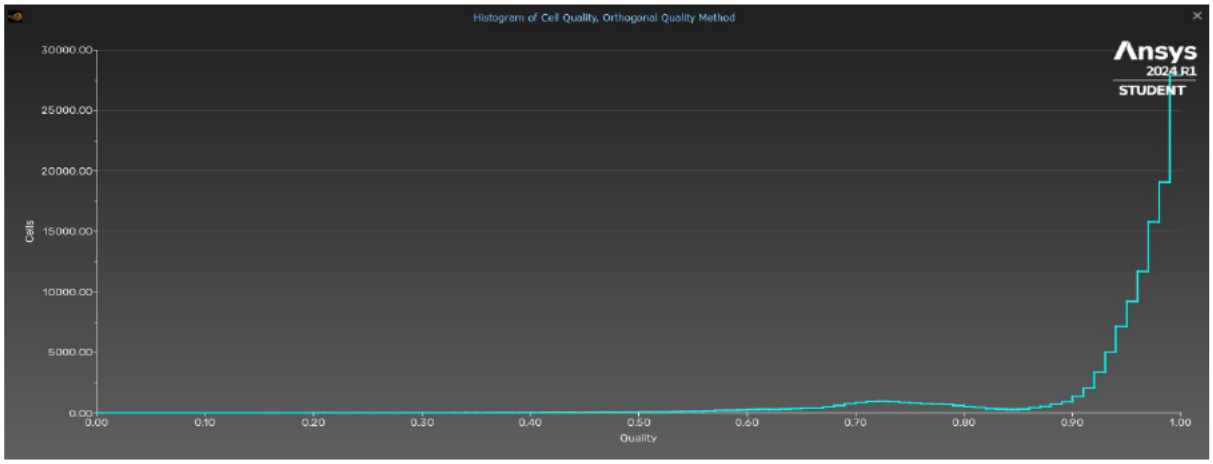

Figure 5.24: Baerveldt Double Fin Tube Mesh Orthogonal Quality

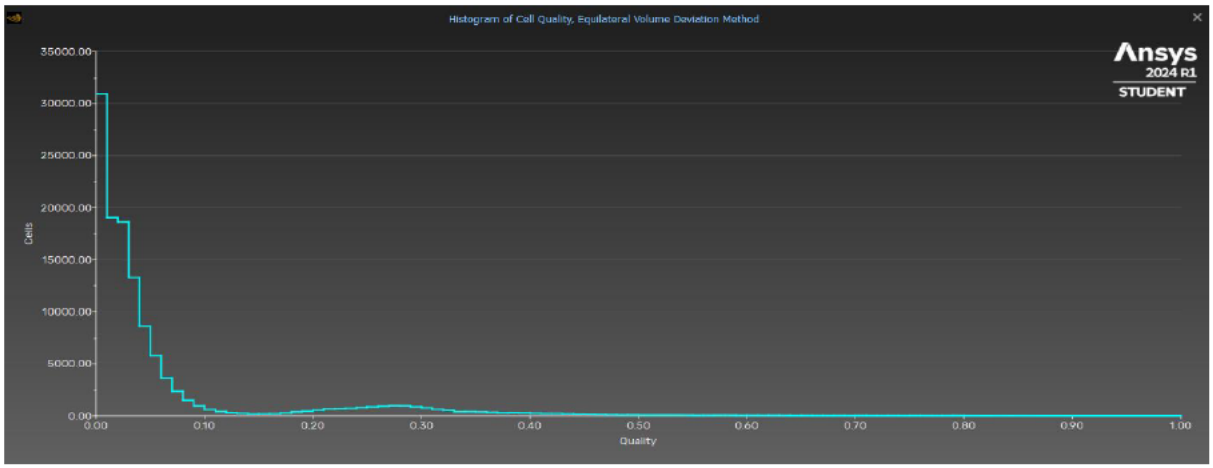

Figure 5.25: Baerveldt Double Fin Tube Mesh Skewness

By employing this mesh and the varied flow rate, the simulations for the double fin tube arrangement yielded the following results:

Table 5.15: Baerveldt Double Fin Tube Simulation Results

Flow Rate (µL/min)	Mass Flow Rate (kg/s)	CFD Pressure Drop, ΔP (Pa)	Theoretical Pressure Drop, ΔP (Pa)	Percentage Error (%)
1.6	2.667E-08	3.31	10.118	67.287
2.5	4.167E-08	5.17	15.810	67.299
5	8.333E-08	10.3	31.620	67.426
10	1.667E-07	20.7	63.240	67.268
20	3.333E-07	41.4	126.481	67.268
25	4.167E-07	51.8	158.101	67.236

In this case, the disparity between the simulation data and theoretical results is significant. These limitations will be discussed further within Chapter 6. As seen in the following figures, 5.26 and 5.27, the pressure contour and wall shear stress plots have been provided for 2.5µL/min. The remaining plots can be found in appendix section C.

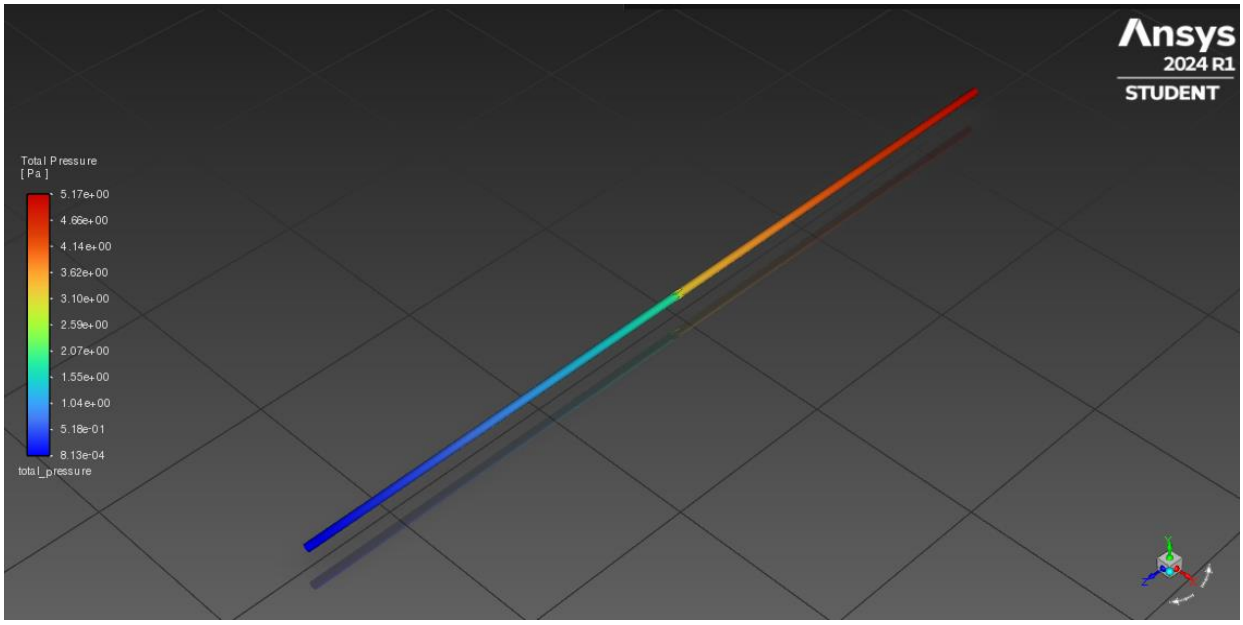

Figure 5.26: Baerveldt Double Fin Tube 2.5µL/min Pressure Contour Plot

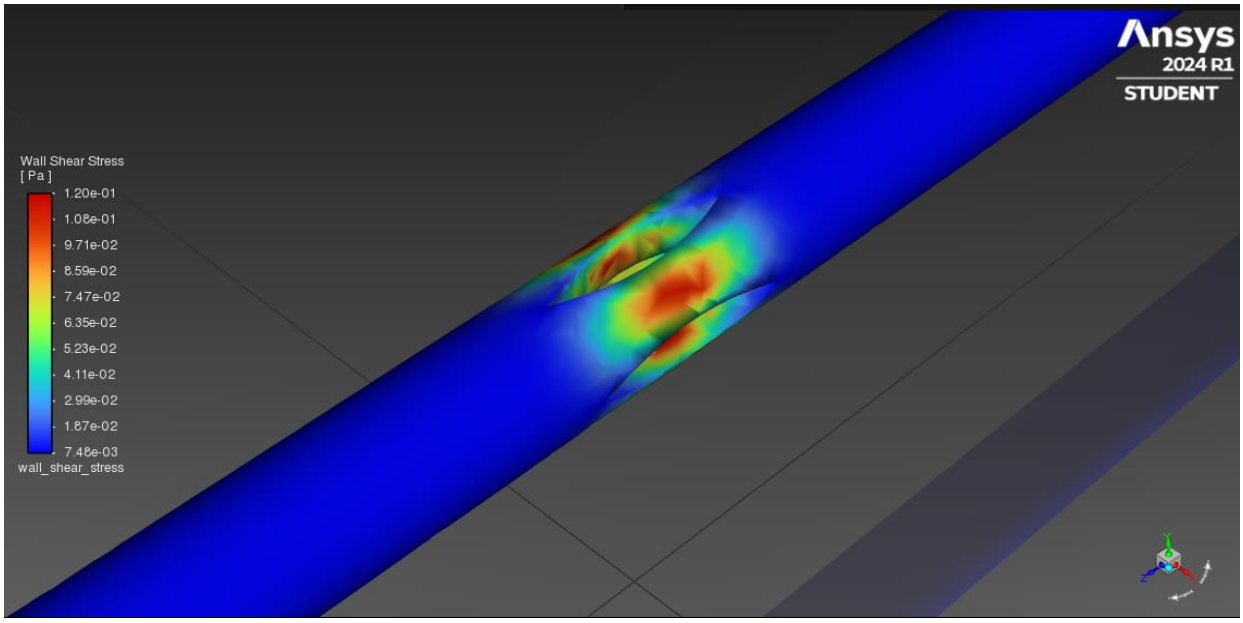

Figure 5.27: Baerveldt Double Fin Tube 2.5µL/min Wall Shear Stress Distribution at Fins

5.6.5 Paul Mesh Independency Study

The Paul double fin tube was also subjected to a mesh independency study under the following conditions:

- Flow 1.6µL/min
- Default surface mesh
- Default boundary layers (3 layers @ 0.272 transition ratio)
- 10^{-5} convergence tolerance, double precision solver

By only varying the global volume element size, the results for pressure drop and wall shear stresses can be seen in the following table:

Table 5.16: Paul Double Fin Tube Mesh Independency Study

Volume Element Size (m)	Pressure Drop, ΔP (Pa)	Wall Shear Stress Maximum (Pa)	Wall Shear Stress Minimum (Pa)
4.50E-05	112.3	1.25E+00	9.11E-02
3.50E-05	112.3	1.25E+00	9.11E-02
2.50E-05	112.8	1.24E+00	9.15E-02
1.50E-05	114.2	1.25E+00	9.33E-02

As evident, the variance in pressure drop results are within a 5% tolerance:

$$112.3 + (112.3 \times 0.05) = \mathbf{117.92}\ (upper\ limit\ not\ exceeded)$$

Additionally, the shear stress results are also within the 5% tolerance.

Subsequently, the mesh construction and its specified conditions are considered mesh independent and therefore suitable to use throughout the simulations.

5.6.6 Paul Simulations

The resulting mesh for the Paul double fin tube, as aligned with previous Paul tube variations, employs a volume element size of 2.50E-05m. This mesh had approximately 75,000 elements, with a very high average orthogonal quality and very low skewness, as seen over the following figures 5.28 and 5.29.

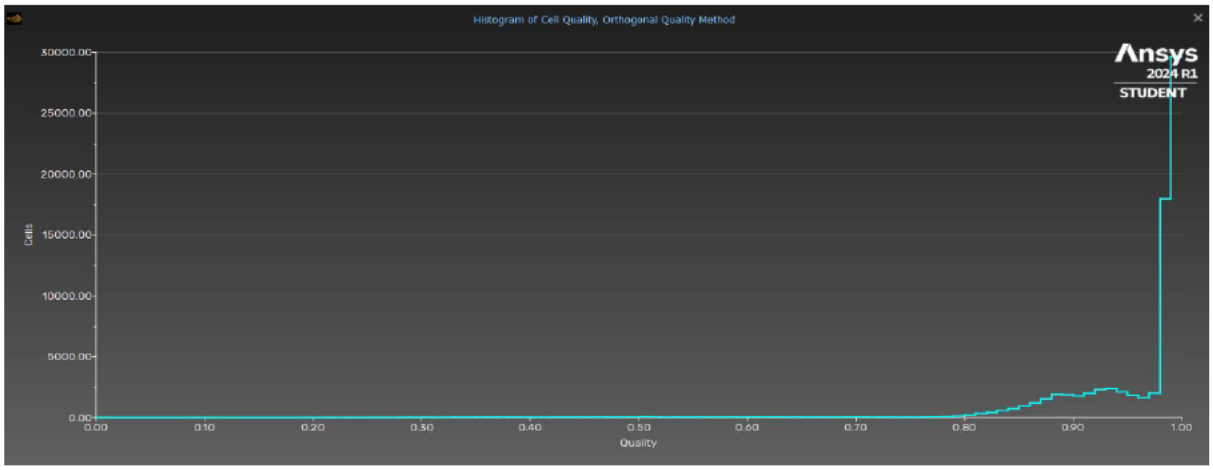

Figure 5.28: Paul Double Fin Tube Mesh Orthogonal Quality

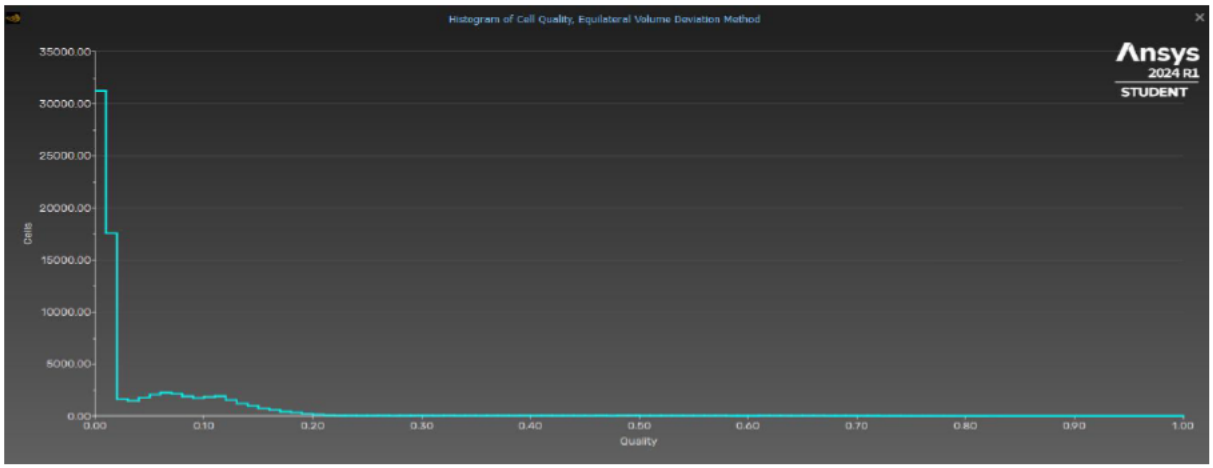

Figure 5.29: Paul Double Fin Tube Mesh Skewness

Utilising this mesh and the initial conditions outlined throughout section 5.7.1, the simulations yielded the following results:

Table 5.17: Paul Double Fin Tube Simulation Results

Flow Rate (µL/min)	Mass Flow Rate (kg/s)	CFD Pressure Drop, ΔP (Pa)	Theoretical Pressure Drop, ΔP (Pa)	Percentage Error (%)
1.6	2.667E-08	112.8	422.700	73.314
2.5	4.167E-08	176.2	660.469	73.322
5	8.333E-08	352.7	1320.938	73.299
10	1.667E-07	706.8	2641.876	73.246
20	3.333E-07	1417.7	5283.752	73.169
25	4.167E-07	1775.3	6604.690	73.121

As seen in the following figures, 5.30 and 5.31, the pressure contour and wall shear stress plots have been provided for 2.5µL/min. The remaining plots can be found in appendix section C.

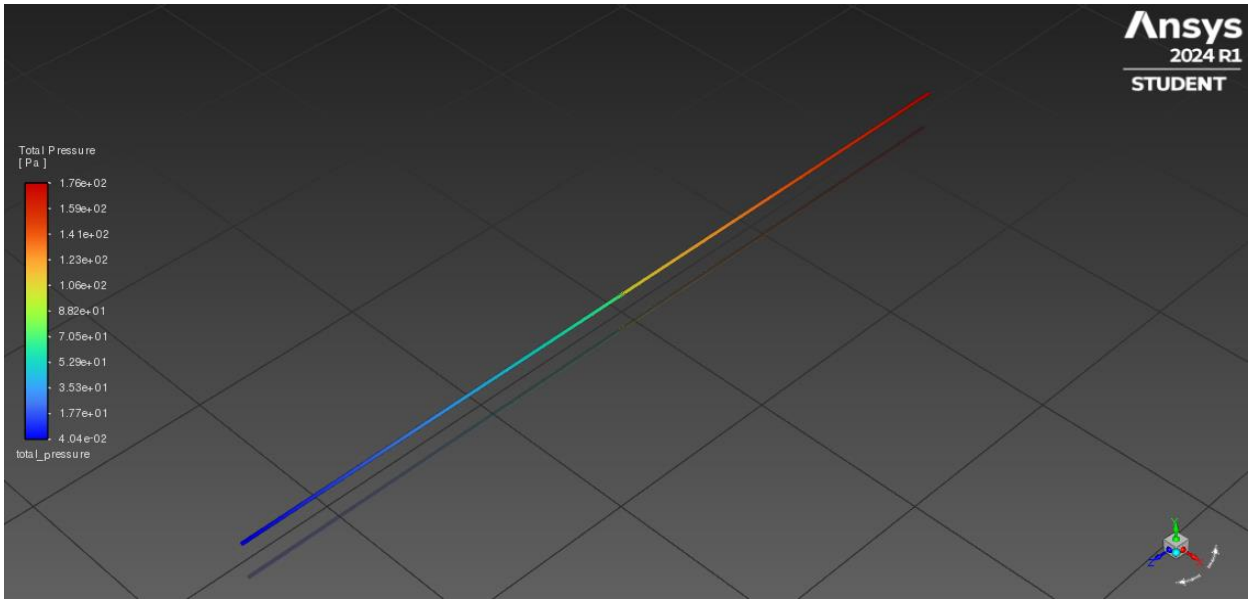

Figure 5.30: Paul Double Fin Tube 2.5µL/min Pressure Contour Plot

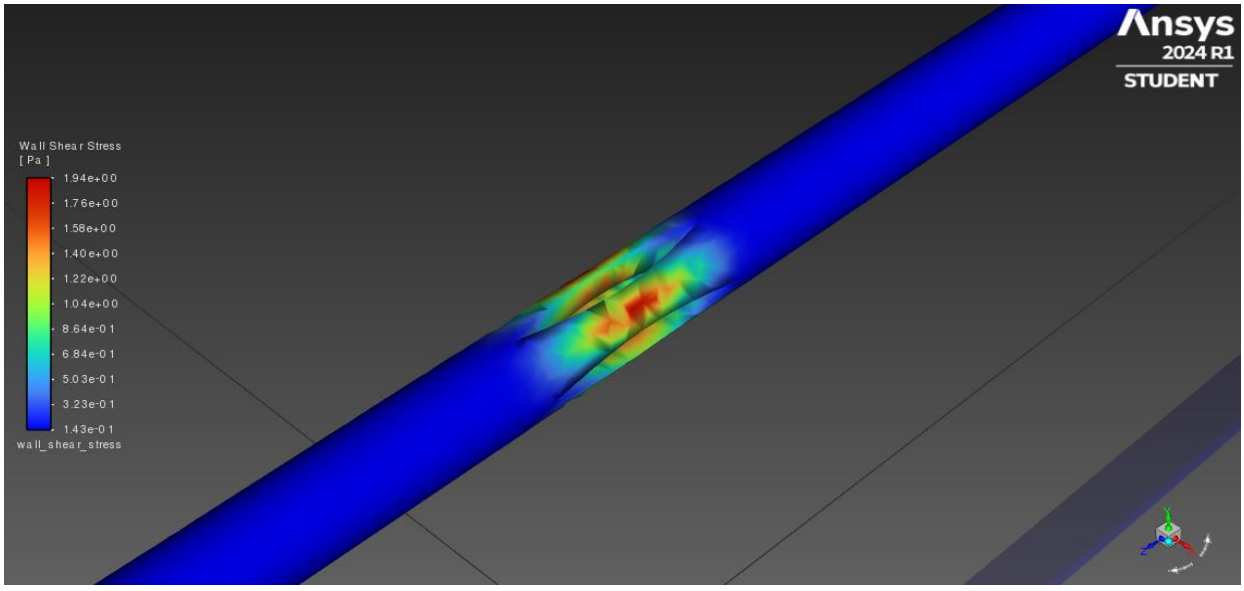

Figure 5.31: Paul Double Fin Tube 2.5µL/min Wall Shear Stress at Fins

5.7 Snipped Tube

5.7.1 Initial Conditions

As described in section 4.2.1, the Baerveldt snipped tube will be simulated as a standard Baerveldt tube (32mm length and 0.32mm diameter), with an angled cut at the inlet. This cut, 30 degrees from horizontal, aims to simulate the realistic surgical procedure outlined in 2.2.4.2. Like the previous simulations, the flow will be varied from 1.6μL/min, to 25μL/min.

The Paul snipped tube adopts the same conditions specified for the Baerveldt, outside of updating the tube length and diameter characteristics.

5.7.2 Theoretical Calculations

Due to the very subtle change in geometry, there is minimal that would influence the pressure drop between the snipped and standard tubes. Subsequently, the snipped tube CFD results will be compared directly to the theoretical calculations of the standard tube. These theoretical values will be visible in section 5.7.4 and 5.7.6, with the original calculations seen in section 5.3.2.

The snipped variation of the inlet is primarily to analyse the behaviour of the fluid flowing into drainage tube, which will be observed through stress concentration and 3D vector plots. This analysis hopes to provide insight into realistic surgical conditions, along with why and where failure may occur during this process.

5.7.3 Baerveldt Mesh Independency Study

The Baerveldt snipped tube was subjected to a mesh independency study under the following conditions:

- Flow 1.6μL/min
- Default surface mesh
- Default boundary layers (3 layers @ 0.272 transition ratio)
- 10^{-5} convergence tolerance, double precision solver

By only varying the global volume element size, the results for pressure drop and wall shear stresses can be seen in the following table:

Table 5.18: Baerveldt Snipped Tube Mesh Independency Study

Volume Element Size (m)	Pressure Drop, ΔP (Pa)	Wall Shear Stress Maximum (Pa)	Wall Shear Stress Minimum (Pa)
5.00E-05* outlier	2.39	5.18E-02	6.17E-03
4.00E-05	2.95	6.12E-02	4.26E-03
2.50E-05	2.99	6.15E-02	4.31E-03
2.00E-05	3.00	6.16E-02	4.32E-03

The volume element size of 5.00E-05m converged in less than 5 iterations. This will be considered as an outlier, as other Baerveldt tube geometries consistently converged from 40 to 60 iterations. While the mesh may have not be fine enough, the full reasoning for this is unknown. The variance in the pressure drop for the next three volume element sizes are within a 5% tolerance, so the analysis will continue with these figures.

$$2.95 + (2.95 \times 0.05) = \mathbf{3.10}\ (upper\ limit\ not\ exceeded)$$

The shear stress results are also within the 5% tolerance.

Subsequently, the mesh construction and its specified conditions are considered mesh independent and therefore suitable to use throughout the simulations.

5.7.4 Baerveldt Simulations

The volume element size chosen for these simulations is 2.50E-05m. This slightly finer mesh will provide an accurate and refined view of the fluid behaviour at the inlet. This mesh had approximately 175,000 elements, with a very high average orthogonal quality and very low skewness, as seen over the following figures 5.32 and 5.33.

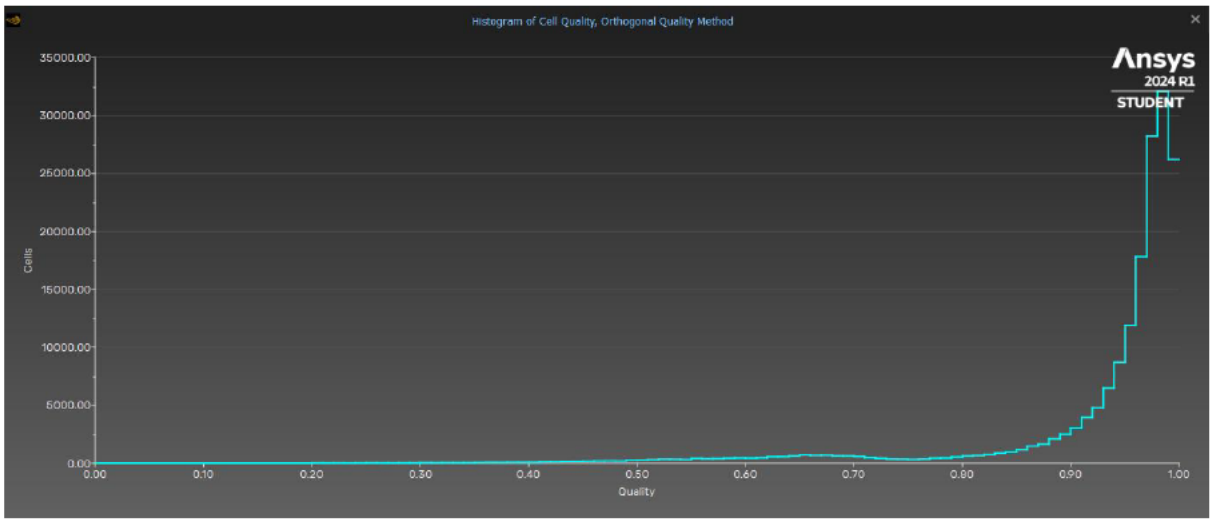

Figure 5.32: Baerveldt Snipped Tube Mesh Orthogonal Quality

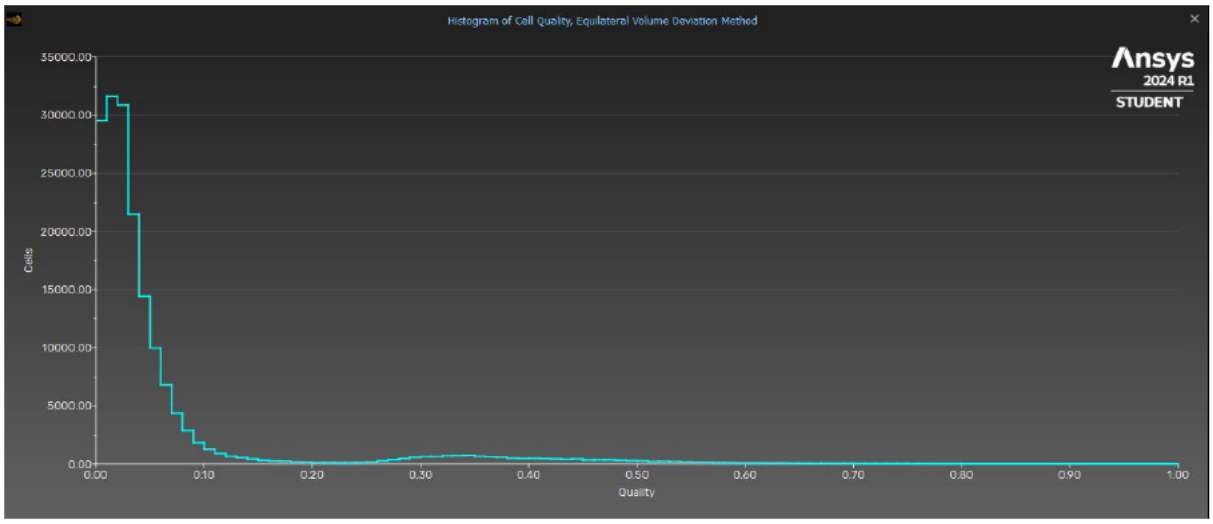

Figure 5.33: Baerveldt Snipped Tube Mesh Skewness

Employing this mesh with the specified flow rates produces the following results seen in table 5.19. As outlined in section 5.7.2, the theoretical pressure results from the standard Baerveldt have been included in the table. Subsequently, percentage error value has been updated to a measure of percentage variance, directly comparing the difference between the CFD snipped tube results and the theoretical standard tube calculations.

Table 5.19: Baerveldt Snipped Tube Simulation Results

Flow Rate (µL/min)	Mass Flow Rate (kg/s)	CFD Pressure Drop, ΔP (Pa)	Theoretical Pressure Drop - Standard Pipe, ΔP (Pa)	Percentage Variance (%)
1.6	2.667E-08	2.99	2.321	28.823
2.5	4.167E-08	4.67	3.627	28.772
5	8.333E-08	9.34	7.253	28.772
10	1.667E-07	18.7	14.506	28.909
20	3.333E-07	37.4	29.013	28.909
25	4.167E-07	46.8	36.266	29.047

As seen in the following figures, 5.34 and 5.35, the pressure contour and wall shear stress plots have been provided for 2.5µL/min. The remaining plots can be found in appendix section C.

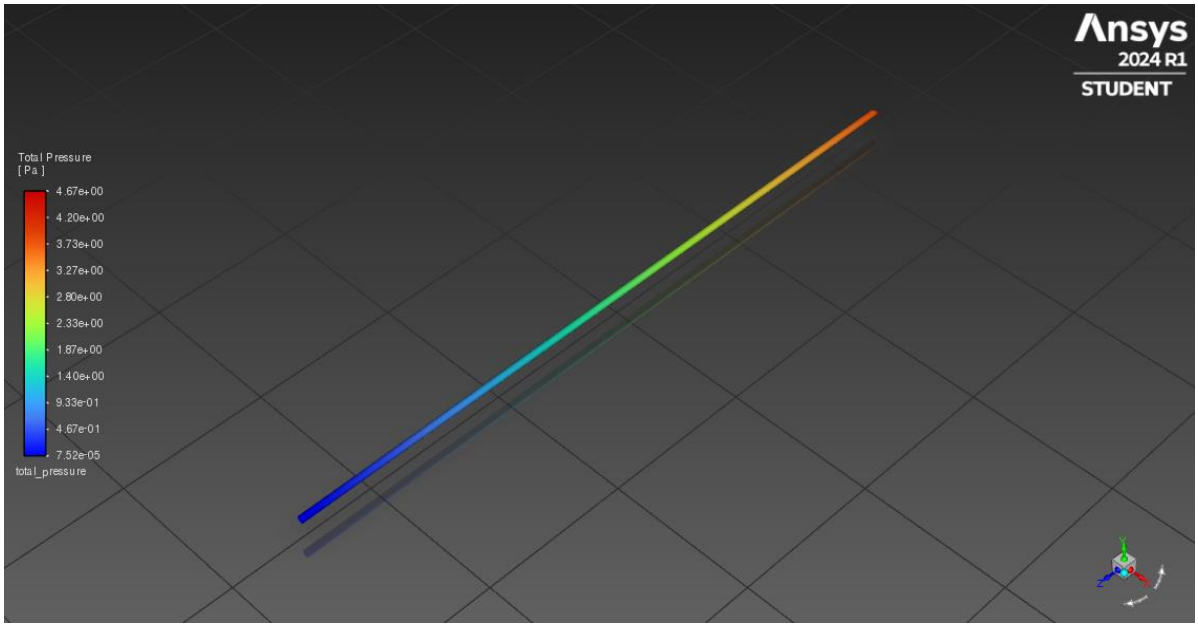

Figure 5.34: Baerveldt Snipped Tube 2.5µL/min Pressure Contour Plot

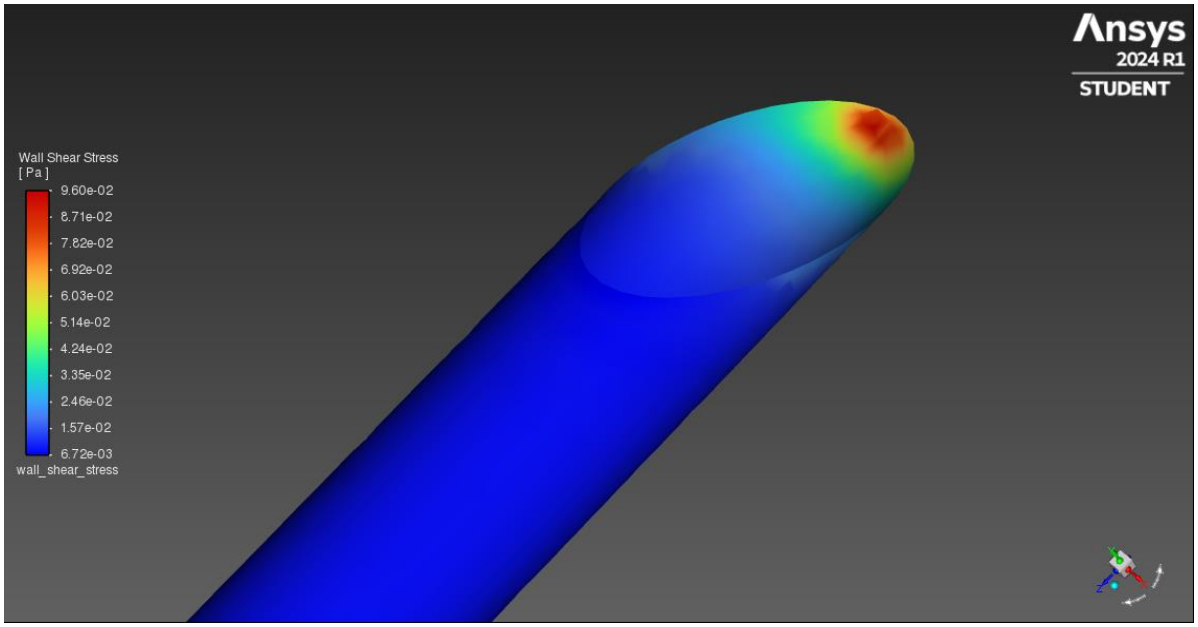

Figure 5.35: Baerveldt Snipped Tube 2.5µL/min Wall Shear Stress at Inlet

5.7.5 Paul Mesh Independency Study

The Baerveldt snipped tube was subjected to a mesh independency study under the following conditions:

- Flow 1.6µL/min
- Default surface mesh
- Default boundary layers (3 layers @ 0.272 transition ratio)
- 10^{-5} convergence tolerance, double precision solver

By only varying the global volume element size, the results for pressure drop and wall shear stresses can be seen in the following table:

Table 5.20: Paul Snipped Tube Mesh Independency Study

Volume Element Size (m)	Pressure Drop, ΔP (Pa)	Wall Shear Stress Maximum (Pa)	Wall Shear Stress Minimum (Pa)
4.50E-05	96.1	5.13E-01	6.98E-02
3.50E-05	96.1	5.13E-01	6.98E-02
2.50E-05	96.4	5.12E-01	7.05E-02
1.50E-05	98.3	5.11E-01	7.16E-02

As evident, the variance in pressure drop results are within a 5% tolerance:

$$96.1 + (96.1 \times 0.05) = \mathbf{100.91}\ (upper\ limit\ not\ exceeded)$$

Additionally, the shear stress results are also within the 5% tolerance.

Subsequently, the mesh construction and its specified conditions are considered mesh independent and therefore suitable to use throughout the simulations.

5.7.6 Paul Simulations

The volume element size chosen for these simulations is 2.50E-05m. This mesh will provide an accurate and refined view of the fluid behaviour at the inlet. With approximately 75,000 elements, this mesh has a very high average orthogonal quality and very low skewness, as seen over the following figures 5.36 and 5.37.

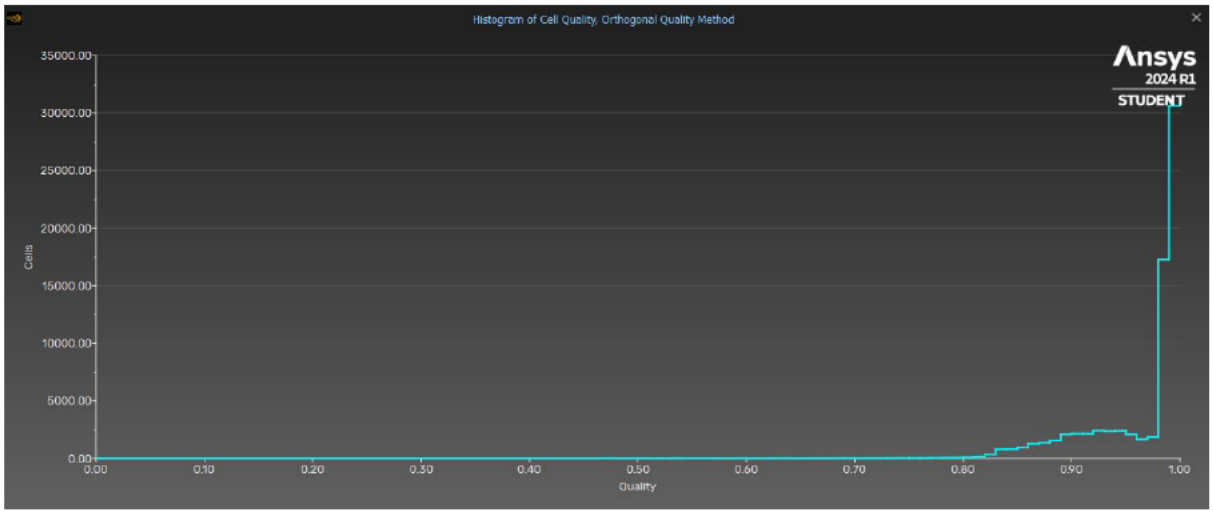

Figure 5.36: Paul Snipped Tube Mesh Orthogonal Quality

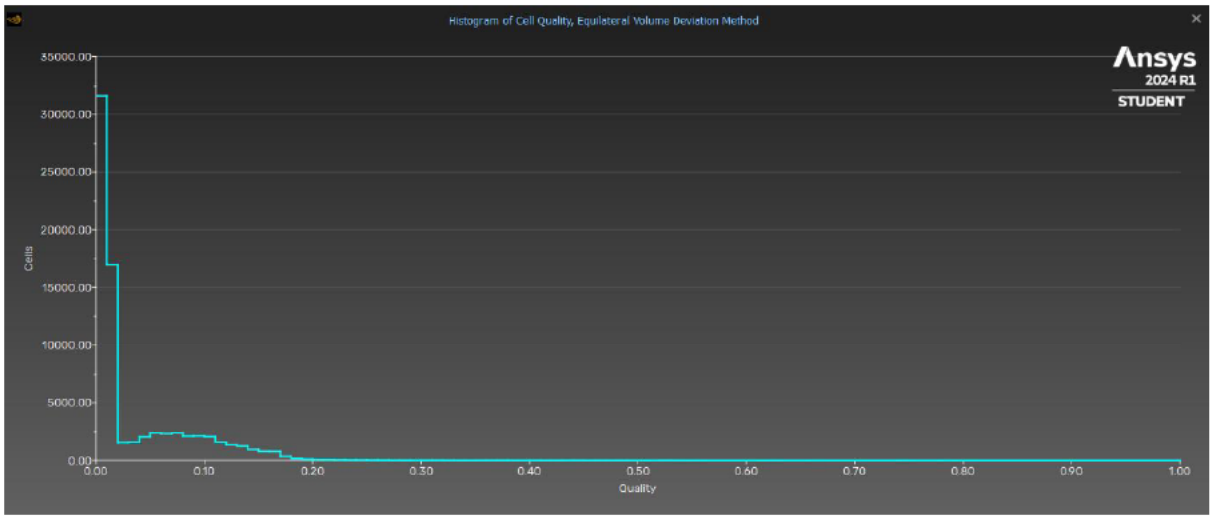

Figure 5.37: Paul Snipped Tube Mesh Skewness

Under the specified conditions and alterations outlined in section 5.7.4, this mesh produced the following results:

Table 5.21: Paul Snipped Tube Simulation Results

Flow Rate (µL/min)	Mass Flow Rate (kg/s)	CFD Pressure Drop, ΔP (Pa)	Theoretical Pressure Drop - Standard Pipe, ΔP (Pa)	Percentage Variance (%)
1.6	2.667E-08	96.4	84.783	13.702
2.5	4.167E-08	150.7	132.474	13.758
5	8.333E-08	301.6	264.948	13.834
10	1.667E-07	604.8	529.895	14.136
20	3.333E-07	1215.1	1059.790	14.655
25	4.167E-07	1522.7	1324.738	14.943

As seen in the following figures, 5.38 and 5.39, the pressure contour and wall shear stress plots have been provided for 2.5µL/min. The remaining plots can be found in appendix section C.

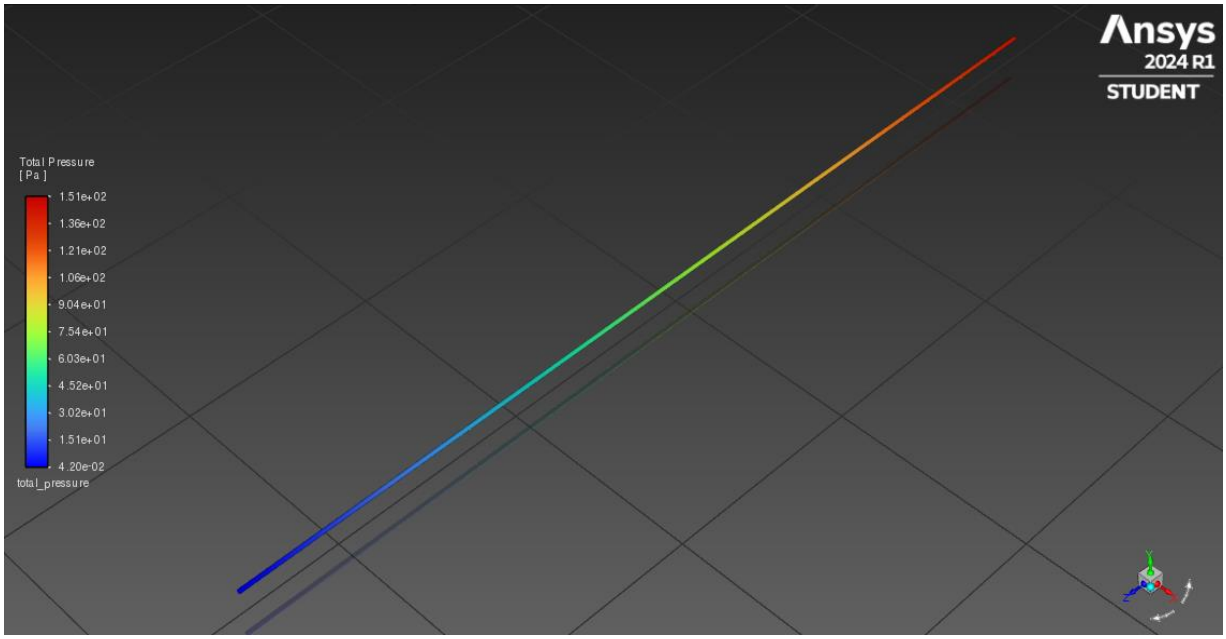

Figure 5.38: Paul Snipped Tube 2.5µL/min Pressure Contour Plot

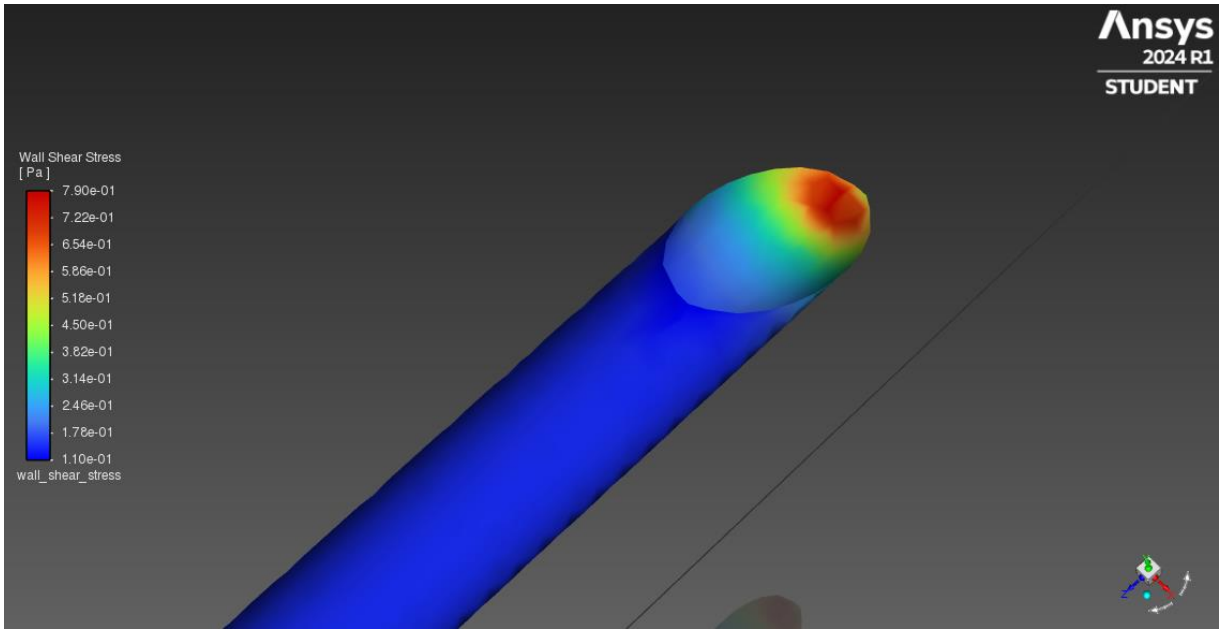

Figure 5.39: Paul Snipped Tube 2.5µL/min Wall Shear Stress at Inlet

5.8 Rounded Inlet Tube

5.8.1 Initial Conditions

As described in section 4.2.1, the Baerveldt rounded inlet tube will be simulated as a standard Baerveldt tube (32mm length and 0.32mm diameter), with a simulated shape representing an interior edge fillet at the inlet. This rounding aims to simulate a theoretical solution to combat biofouling, and to investigate the flow behaviour in comparison to the standard and snipped tubes. Aligned with the previous simulations, the flow will be varied from 1.6µL/min, to 25µL/min.

The Paul rounded inlet tube adopts the exact same conditions specified for the Baerveldt, outside of updating the tube length and diameter characteristics.

5.8.2 Theoretical Calculations

Similarly to the snipped tube, the rounded inlet tube variation will prioritise the investigation of the fluid flow behaviour due to the rounded inlet. Subsequently, the CFD pressure drop results will be directly compared to the theoretical calculations of the standard tube, given there is little variation between the two. These theoretical values will be visible in section 5.8.4 and 5.8.6, with the original calculations seen in section 5.3.2.

5.8.3 Baerveldt Mesh Independency Study

The Baerveldt rounded inlet tube was subjected to a mesh independency study under the following conditions:

- Flow 1.6µL/min
- Default surface mesh
- Default boundary layers (3 layers @ 0.272 transition ratio)
- 10^{-5} convergence tolerance, double precision solver

By only varying the global volume element size, the results for pressure drop and wall shear stresses can be seen in the following table:

Table 5.22: Baerveldt Rounded Inlet Tube Mesh Independency Study

Volume Element Size (m)	Pressure Drop, ΔP (Pa)	Wall Shear Stress Maximum (Pa)	Wall Shear Stress Minimum (Pa)
5.00E-05* outlier	2.30	6.16E-02	5.76E-03
4.00E-05	2.75	6.23E-02	5.62E-03
2.50E-05	2.79	6.25E-02	5.63E-03
2.00E-05	2.79	6.28E-02	5.72E-03

The volume element size of 5.00E-05m converged in less than 5 iterations. This will be considered as an outlier, as other Baerveldt tube geometries consistently converged from 40 to 60 iterations. While the mesh may have not be fine enough, the full reasoning for this is unknown. The variance in the pressure drop for the next three volume element sizes are within a 5% tolerance, so continuing with these figures:

$$2.75 + (2.75 \times 0.05) = \mathbf{2.89}\ (upper\ limit\ not\ exceeded)$$

Additionally, the shear stress results are also within the 5% tolerance.

Subsequently, the mesh construction and its specified conditions are considered mesh independent and therefore suitable to use throughout the simulations.

5.8.4 Baerveldt Simulations

The volume element size chosen for these simulations is 2.50E-05m. This slightly finer mesh will provide an accurate and refined view of the fluid behaviour at the rounded inlet. With approximately 177,000 elements, the mesh had a very high average orthogonal quality and very low skewness, as seen over the following figures 5.40 and 5.41.

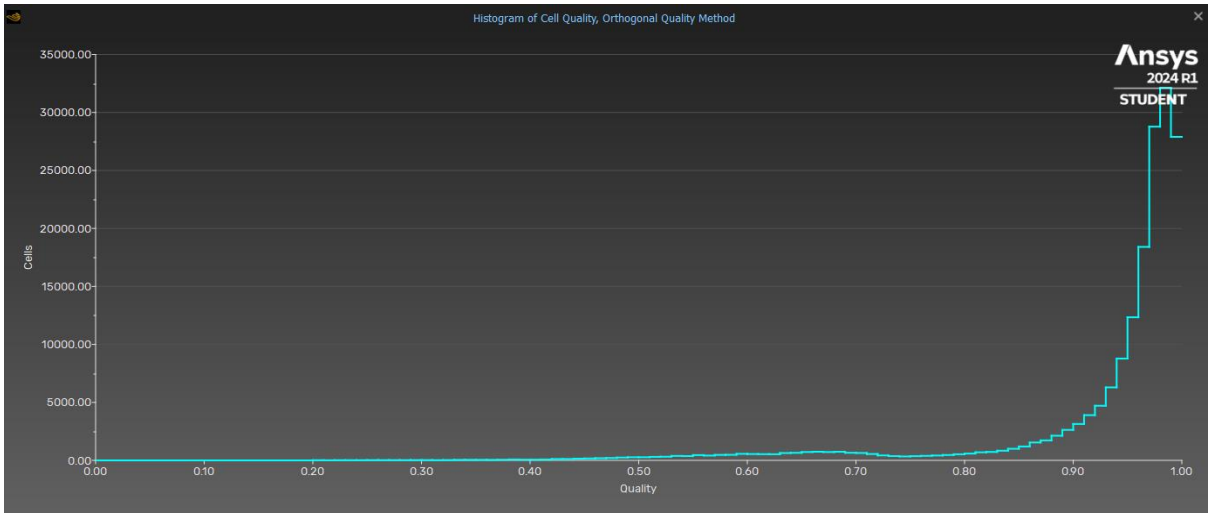

Figure 5.40: Baerveldt Rounded Inlet Tube Mesh Orthogonal Quality

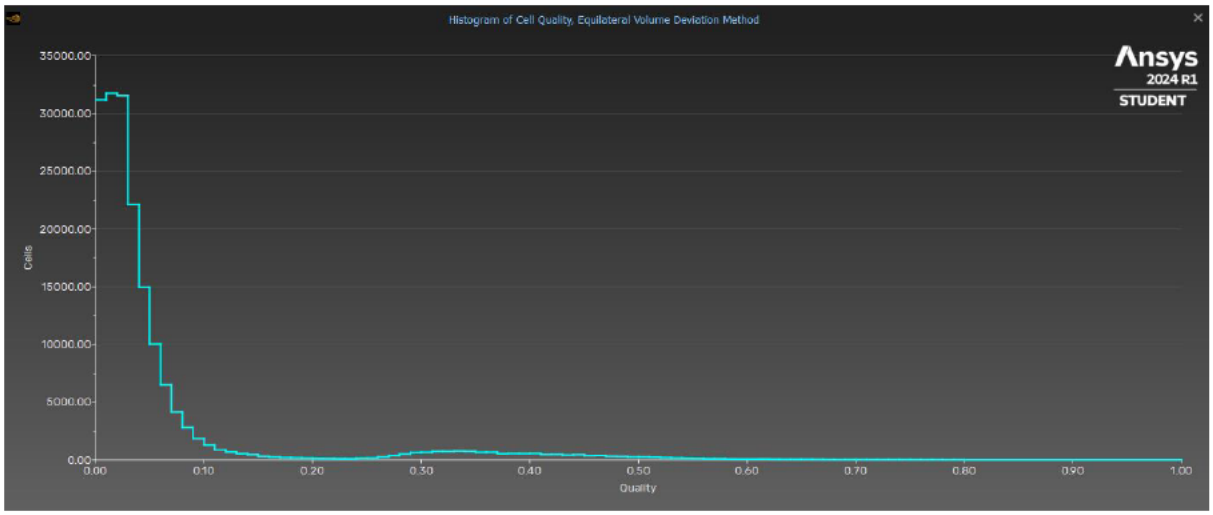

Figure 5.41: Baerveldt Rounded Inlet Tube Mesh Skewness

Employing this mesh with the specified flow rates produces the following results seen in table 5.23, following the guidelines provided in section 5.8.2.

Table 5.23: Baerveldt Rounded Inlet Tube Simulation Results

Flow Rate (µL/min)	Mass Flow Rate (kg/s)	CFD Pressure Drop, ΔP (Pa)	Theoretical Pressure Drop - Standard Pipe, ΔP (Pa)	Percentage Variance (%)
1.6	2.667E-08	2.79	2.321	20.206
2.5	4.167E-08	4.35	3.627	19.948
5	8.333E-08	8.71	7.253	20.086
10	1.667E-07	17.4	14.506	19.948
20	3.333E-07	34.9	29.013	20.292
25	4.167E-07	43.5	36.266	19.948

As seen in the following figures, 5.42 and 5.43, the pressure contour and wall shear stress plots have been provided for 2.5µL/min. The remaining plots can be found in appendix section C.

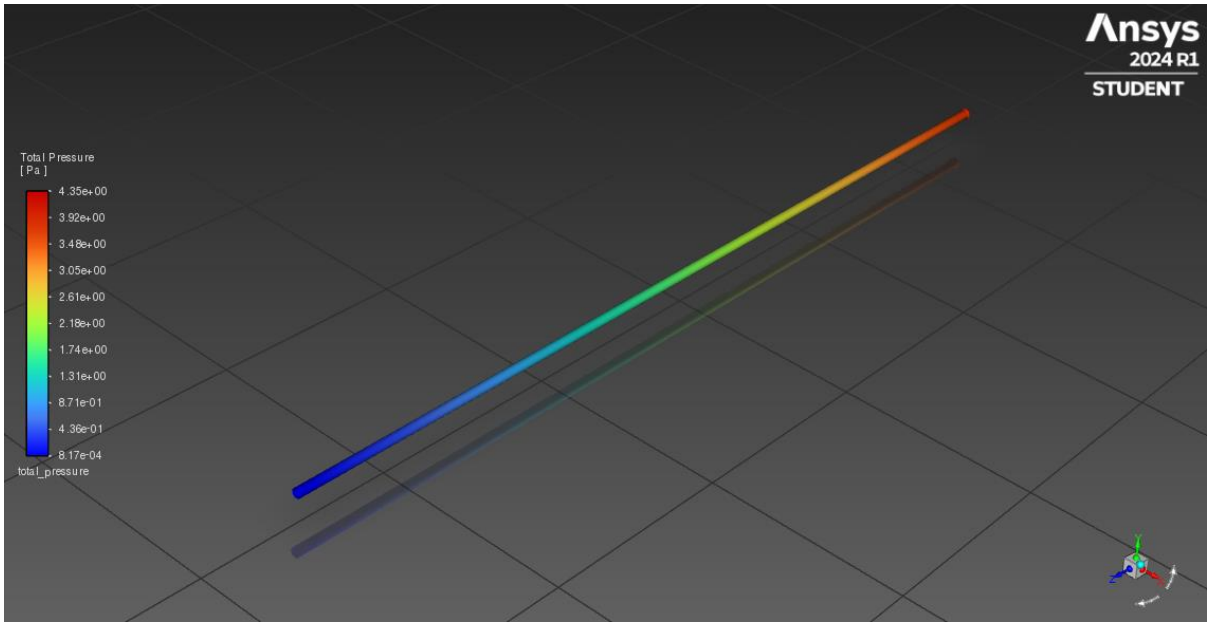

Figure 5.42: Baerveldt Rounded Inlet Tube 2.5µL/min Pressure Contour Plot

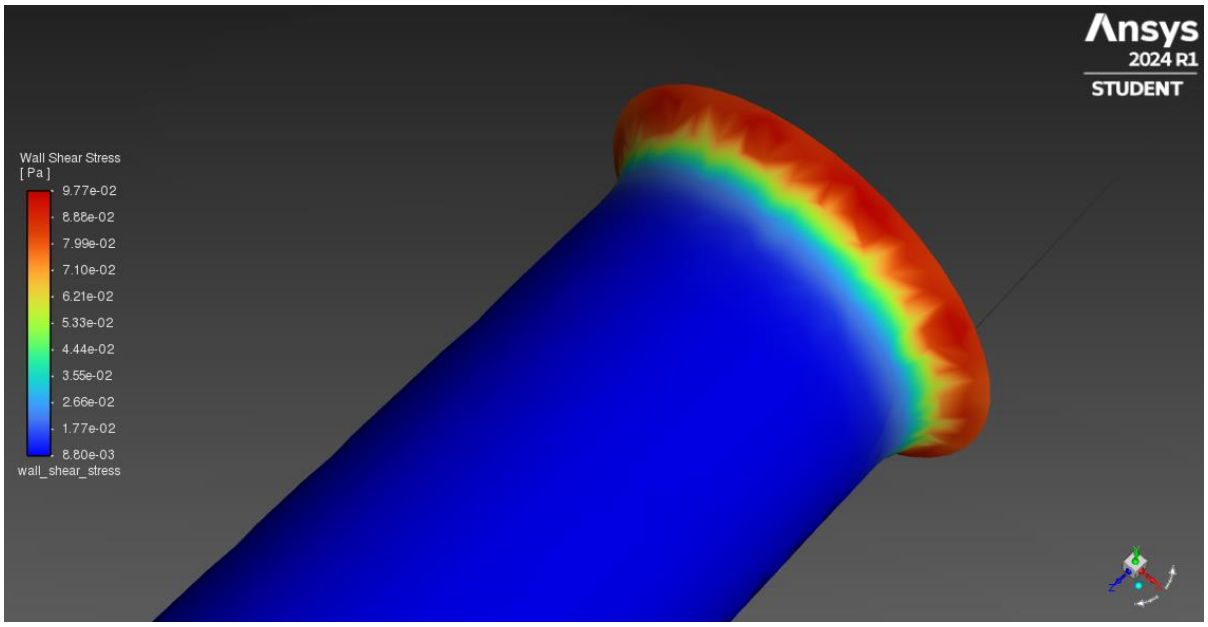

Figure 5.43: Baerveldt Rounded Inlet Tube 2.5µL/min Wall Shear Stress at Inlet

5.8.5 Paul Mesh Independency Study

The Paul rounded inlet tube was subjected to a mesh independency study under the following conditions:

- Flow 1.6μL/min
- Default surface mesh
- Default boundary layers (3 layers @ 0.272 transition ratio)
- 10^{-5} convergence tolerance, double precision solver

By only varying the global volume element size, the results for pressure drop and wall shear stresses can be seen in the following table:

Table 5.24: Paul Rounded Inlet Tube Mesh Independency Study

Volume Element Size (m)	Pressure Drop, ΔP (Pa)	Wall Shear Stress Maximum (Pa)	Wall Shear Stress Minimum (Pa)
4.50E-05	92.1	3.27E-01	9.11E-02
3.50E-05	92.1	3.27E-01	9.11E-02
2.50E-05	92.7	3.29E-01	9.26E-02
1.50E-05	94.4	3.31E-01	9.40E-02

As evident, the variance in pressure drop results are within a 5% tolerance:

$$92.1 + (92.1 \times 0.05) = \mathbf{96.71}\ (upper\ limit\ not\ exceeded)$$

Additionally, the shear stress results are also within the 5% tolerance.

Subsequently, the mesh construction and its specified conditions are considered mesh independent and therefore suitable to use throughout the simulations.

5.8.6 Paul Simulations

The volume element size chosen for these simulations is 2.50E-05m. This mesh will provide an accurate and refined view of the fluid behaviour at the rounded inlet. With approximately 75,000 elements, the mesh had a very high average orthogonal quality and very low skewness, as seen over the following figures 5.44 and 5.45.

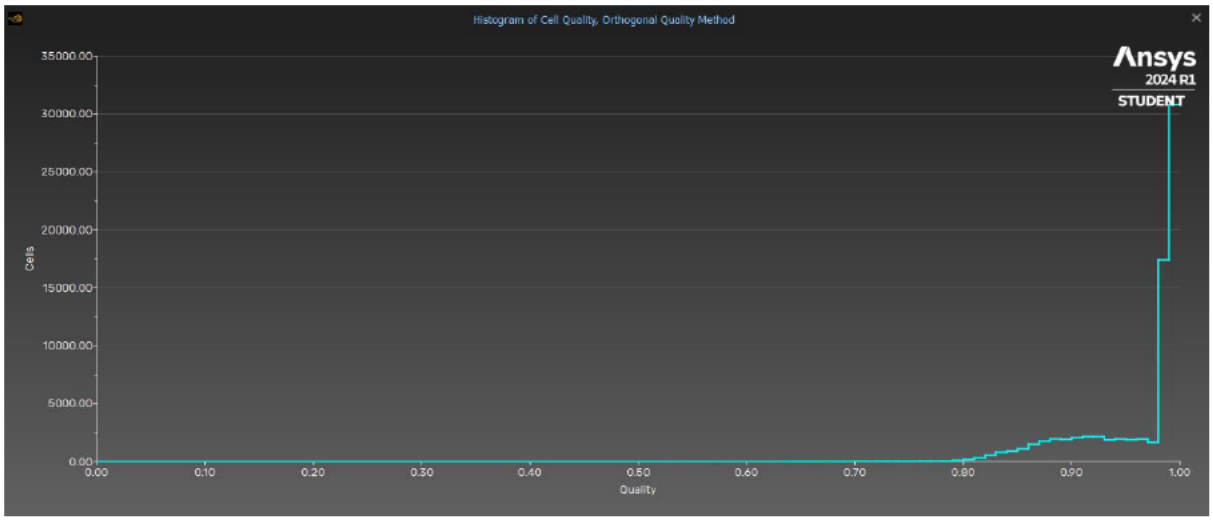

Figure 5.44: Paul Rounded Inlet Tube Mesh Orthogonal Quality

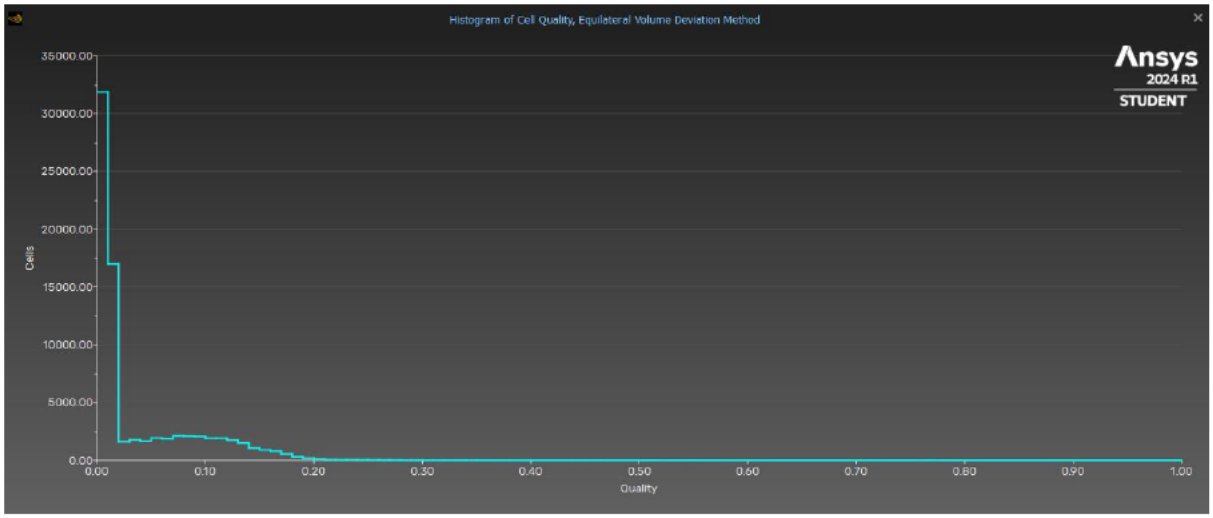

Figure 5.45: Paul Rounded Inlet Tube Mesh Skewness

Employing this mesh with the specified flow rates produces the following results seen in table 5.25, following the guidelines provided in section 5.8.2.

Table 5.25: Paul Rounded Inlet Tube Simulation Results

Flow Rate (µL/min)	Mass Flow Rate (kg/s)	CFD Pressure Drop, ΔP (Pa)	Theoretical Pressure Drop - Standard Pipe, ΔP (Pa)	Percentage Variance (%)
1.6	2.667E-08	92.7	84.783	9.338
2.5	4.167E-08	144.8	132.474	9.305
5	8.333E-08	290.1	264.948	9.493
10	1.667E-07	580.8	529.895	9.607
20	3.333E-07	1164.4	1059.790	9.871
25	4.167E-07	1459.3	1324.738	10.158

As seen in the following figures, 5.46 and 5.47, the pressure contour and wall shear stress plots have been provided for 2.5µL/min. The remaining plots can be found in appendix section C.

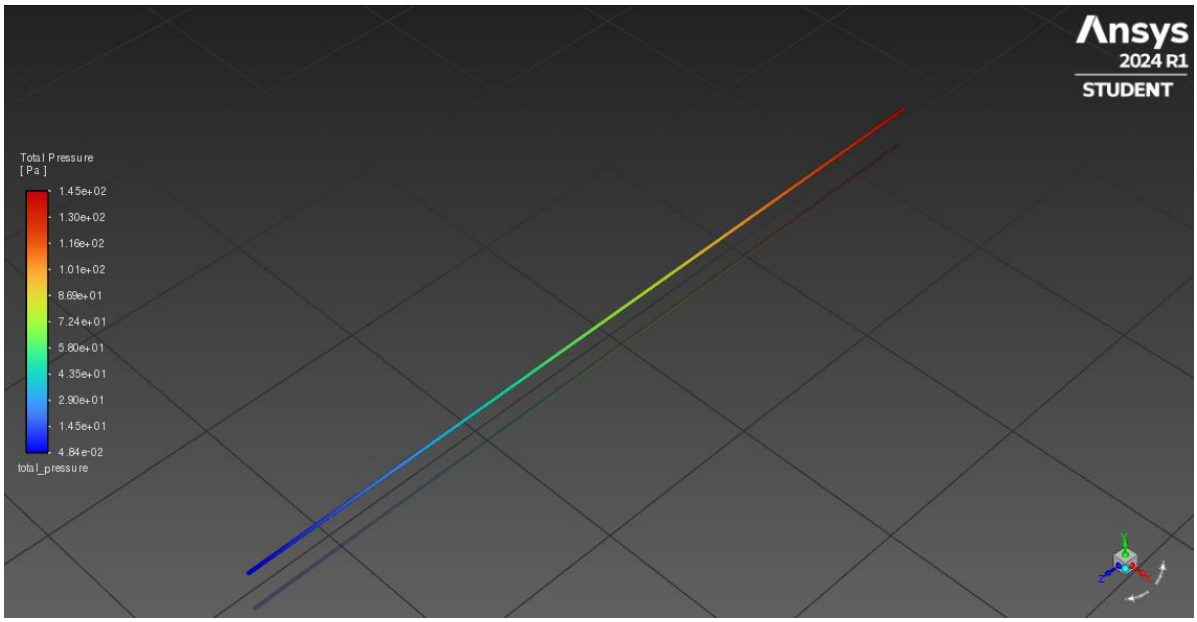

Figure 5.46: Paul Rounded Inlet Tube 2.5µL/min Pressure Contour Plot

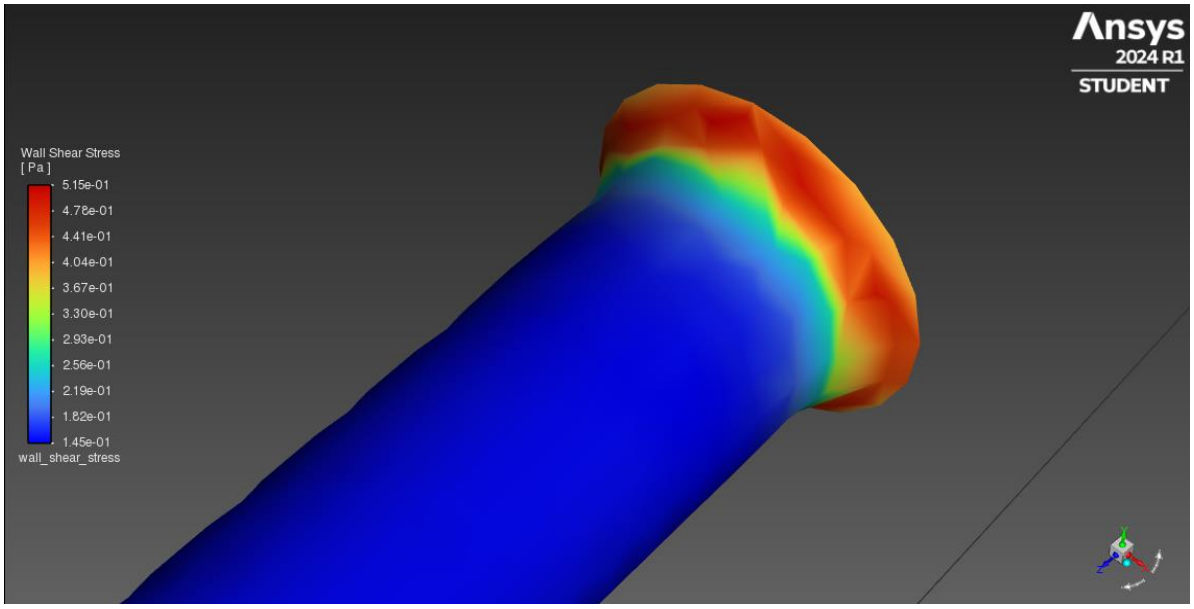

Figure 5.47: Paul Rounded Inlet Tube 2.5µL/min Wall Shear Stress at Inlet

5.9 Chapter Summary

This chapter has presented the simulation results for each tube variation considered in this study. The raw data has been synthesized into tabular formats, and the initial pressure and wall shear stress contour plots have been displayed for a flow rate of 2.5µL/min. Further critical analysis and relevant conclusions regarding the data presented within this chapter will be presented in the following Chapter 6.

Chapter 6 – Discussion

6.1 Chapter Overview

This chapter provides a detailed discussion of the raw CFD data results presented in Chapter 5. The key variables across the tube variations will be analysed for each GDD, using comparative graphical figures and Ansys flow plots. The relationships between pressure drop, wall shear stress, and flow behaviour will be examined to offer a comprehensive analysis of the simulation methodology. Through these tools, the major findings will be presented, critiqued, and analysed, along with a discussion of the principal limitations of the research project. Additionally, potential areas for project expansion will be explored, and a framework for a future experimental procedure will be outlined.

6.2 Baerveldt Tube

6.2.1 Pressure Drop Analysis

As the primary goal of a GDD implant is to reduce eye pressure via the drainage of aqueous humour, the pressure drop data must be studied and compared to theoretical calculations. The pressure results have been tabulated for each Baerveldt tube variation within chapter 5, and can be compared graphically.

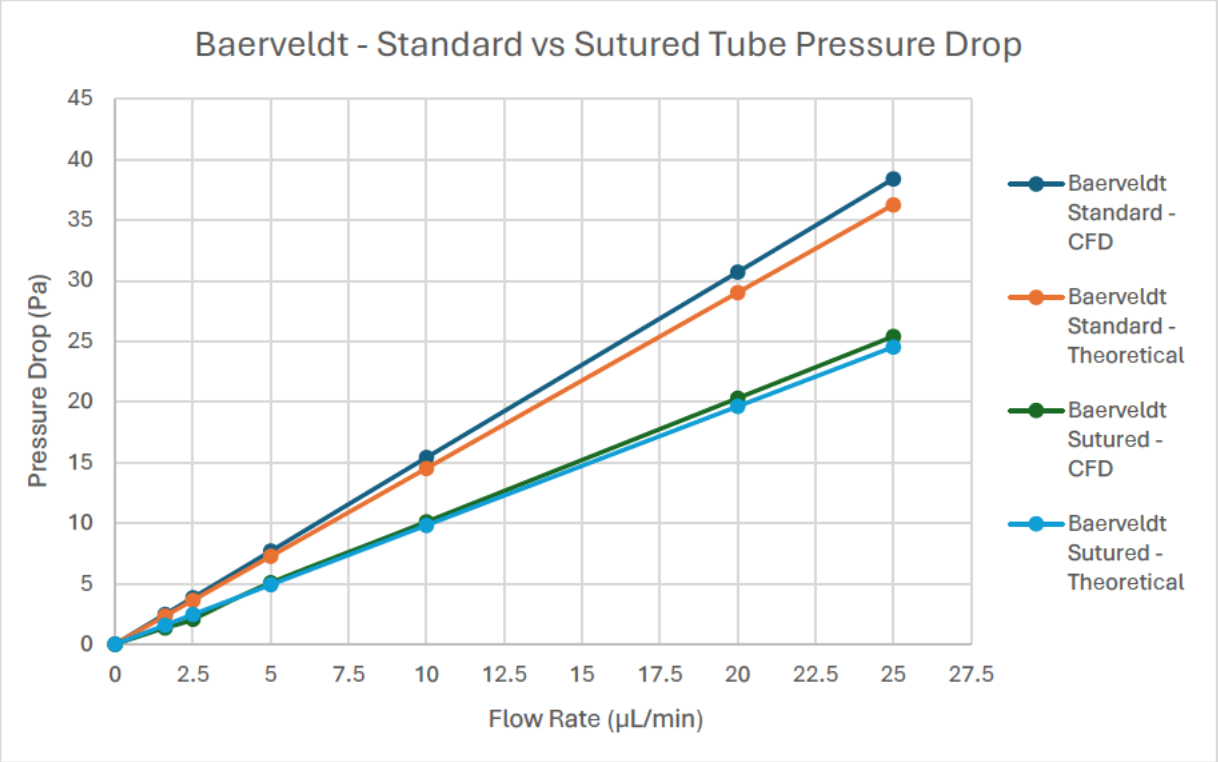

Figure 6.1: Baerveldt - Standard vs Sutured Tube Pressure Drop

As evident in figure 6.1, the suture expectedly reduced the drop in pressure compared to the standard variation. Moreover, the theoretical calculations adapted from Agujetas, R. et al. (2021), appear to be accurate to verify the CFD simulations. The CFD predicted a 3.84 Pa drop at the normal physiological flow rate of 2.5µL/min, compared to that of 2.07 Pa of the sutured tube. These results align with the expected reduction in pressure drop, caused primarily by the halving of flow rate caused through the suture in clinical practice. While these results appear credible, the drop in pressure was driven by largely by the flow rate reduction. While flow rate is undoubtedly the most influential factor seen throughout these simulations, further CFD analysis may be useful to investigate the effects the suture geometry has on pressure drop, outside of just the proposed design given in section 4.2.1. Subsequently, further research and physical inspection may prove necessary to more accurately model the tube under suture.

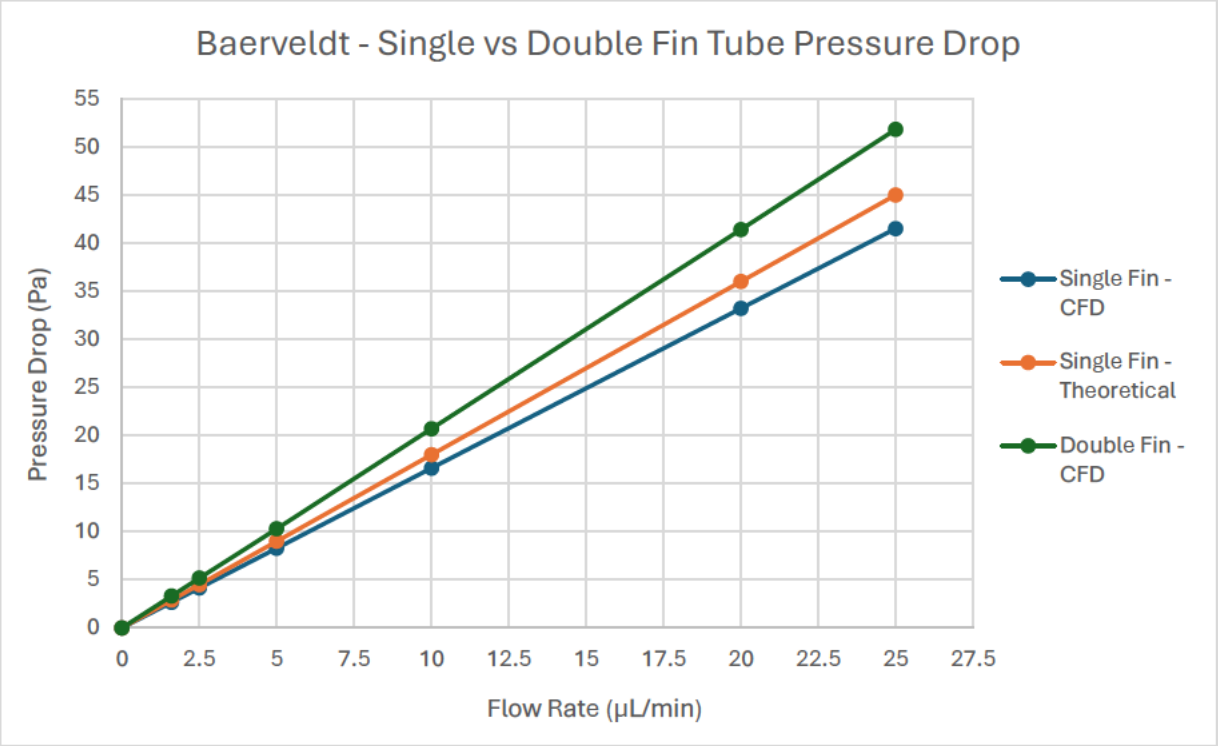

Figure 6.2: Baerveldt - Single vs Double Fin Tube Pressure Drop

Figure 6.2 displays the pressure drop CFD results for the experimental geometries of the single and double finned Baerveldt tubes. While these finned geometries were designed to investigate how they interrupt and interact with the laminar flow (see section 6.2.3), it is important to analyse any potential improvements in pressure drop. The CFD results predicted the double fin to have an elevated pressure drop of 5.17 Pa compared to 4.14 Pa of the single fin for a flow rate of 2.5µL/min. This will be discussed further at the end of this section, but this pressure drop can likely be attributed to the larger reduction of cross section. As outlined in section 5.5.2 and 5.6.2, the theoretical calculations were very experimental due to the unique nature of this analysis. Subsequently, little emphasis should be placed on the accuracy of these calculations. While the single fin theoretical results closely resemble

the CFD results, the double fin theoretical calculations have been excluded from the graph as they severely overshot the expected CFD values. The overestimation of these calculations would not only suggest the inaccuracy of the proposed theoretical analysis in the finned cases, but also highlight the significance of the cross-sectional area and relevant shape factor variable discussed in the sutured tube sections.

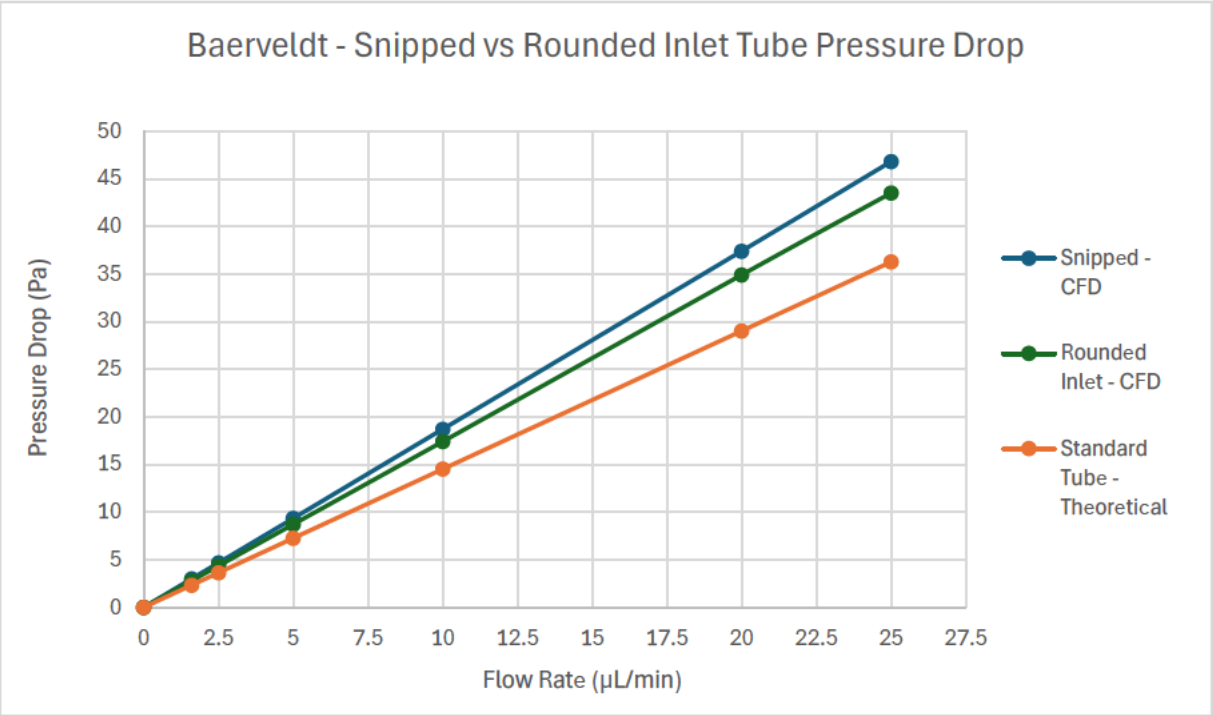

Figure 6.3: Baerveldt - Snipped vs Rounded Inlet Tube Pressure Drop

Figure 6.3 displays the CFD pressure drop results for the inlet variations analysed in this study, being the surgically snipped inlet and theoretical rounded inlet. The CFD results are compared to the standard tube theoretical calculations in the figure, as outside of the inlet variation there is minimal changes to affect the theory. The snipped tube saw a pressure drop at 2.5µL/min of 4.67 Pa, which is compared to the rounded inlet of 4.35 Pa and the standard tube theoretical value of 3.63 Pa. Evidently, inlet variation slightly increased the pressure drop for both geometries. Increasing pressure drop in a GDD is inherently a positive quality, however, doing so evenly is imperative to the long-term success of the implant. As will be discussed further in section 6.2.2, the increase is likely due to the concentrated build-up of fluid caused by the sharper edge of the snipped tube, and the more condensed flow of the rounded inlet.

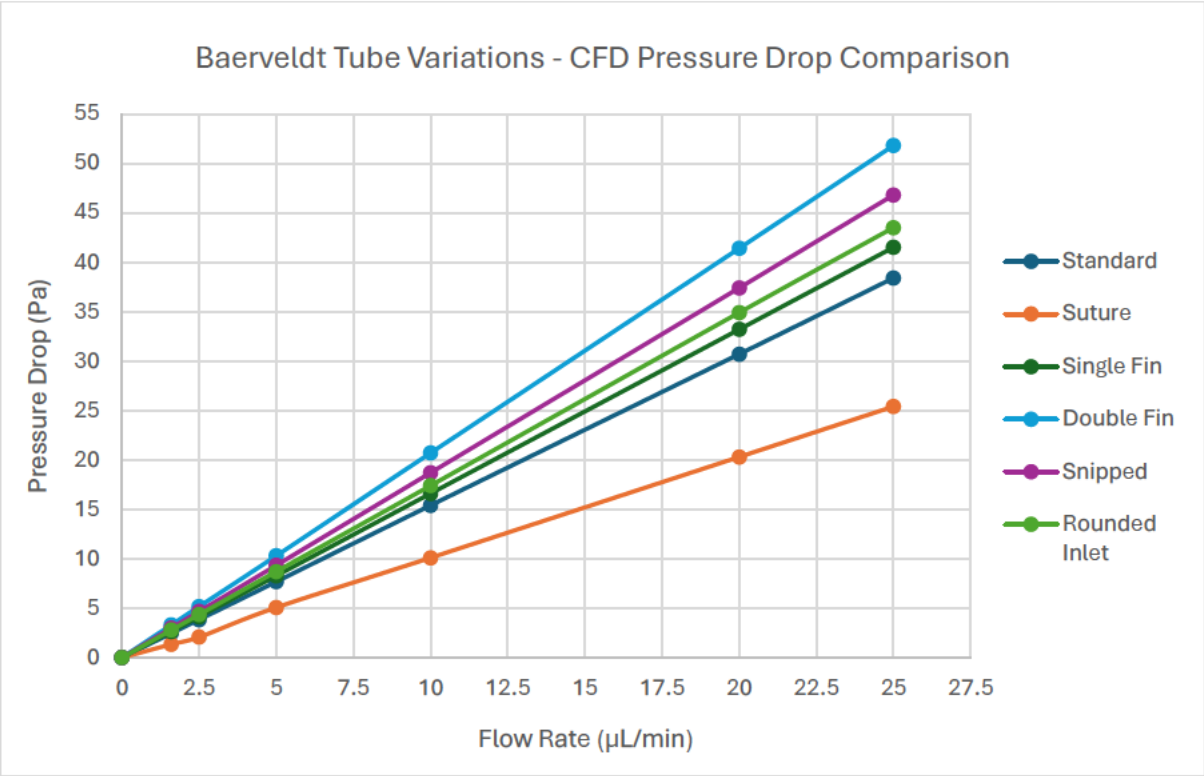

Figure 6.4: Baerveldt Tube Variations - CFD Pressure Drop Comparison

To investigate the trends and overall impact each Baerveldt tube variation had on pressure drop, a graph comparing each of the six tube variations can be produced. Figure 6.4 displays the CFD pressure drop results of each major Baerveldt variation analysed throughout this study. Outside of the sutured tube, all other variations saw an increase in pressure drop compared to the standard Baerveldt tube. The most significant change is seen by the double fin tube, with an increase of approximately 35% for all flow rates. The snipped tube saw in increase of 20%, followed by the rounded inlet with 13.5%, and the single fin of 8%, approximately. The increase in pressure is largely due to a reduction in cross-section, micro-frictional effects, or the condensation of flow. The finned geometries, to be outlined further in section 6.2.2, reduce the cross-sectional area of flow at the middle of the tube. The additional contact area restricts the flow slightly, increasing pressure drop across the length of the tube. To properly review the inlet variants, the flow behaviour plots, and relevant wall shear stress concentrations will be analysed to reveal where the increase in pressure drop has occurred.

6.2.2 Flow Behaviour and Wall Shear Stress

To further investigate the effect that each tube variation has on overall pressure drop, the flow behaviours and wall shear stress results can be analysed to reveal the key characteristics that have influenced these results.

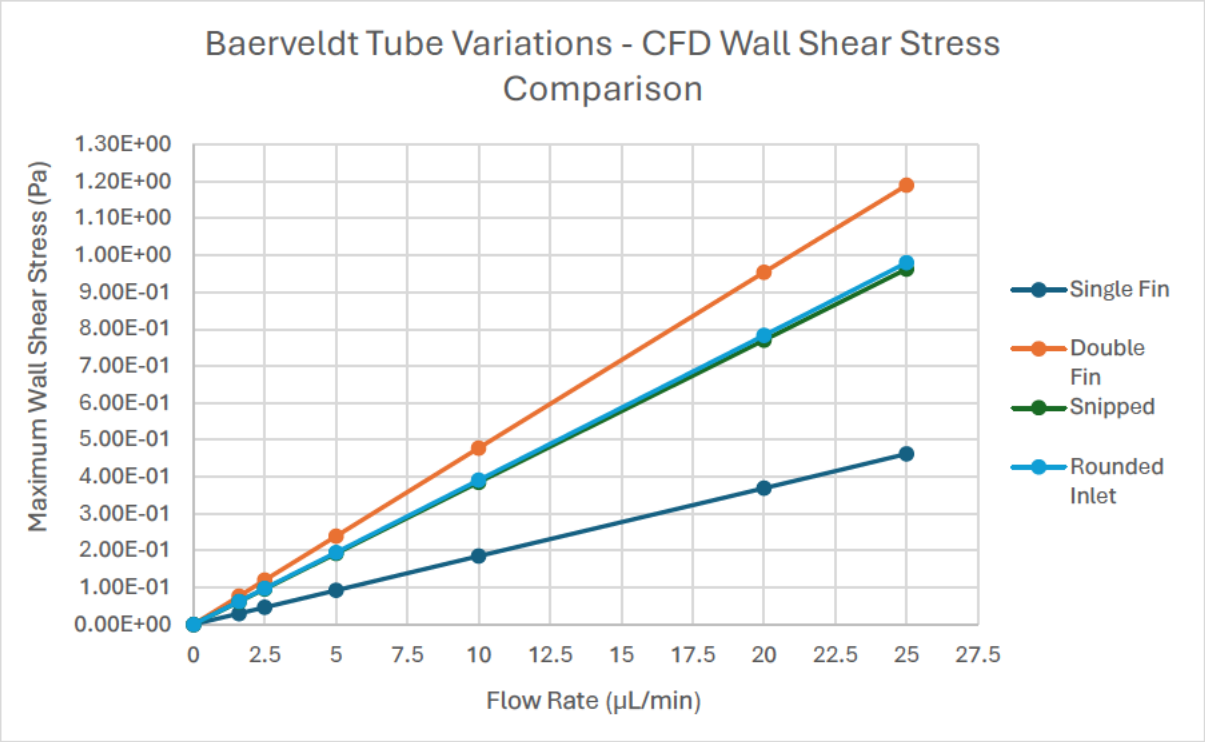

Figure 6.5: Baerveldt Tube Variations - CFD Wall Shear Stress Comparison

Figure 6.5 reveals the double fin has a significantly larger maximum wall shear stress than its single fin counterpart, with the snipped and rounded inlet sharing very similar results. With an exposure to more surface area at the centre of the tube, the double fin had an elevated shear stress concentration on the outer wall.

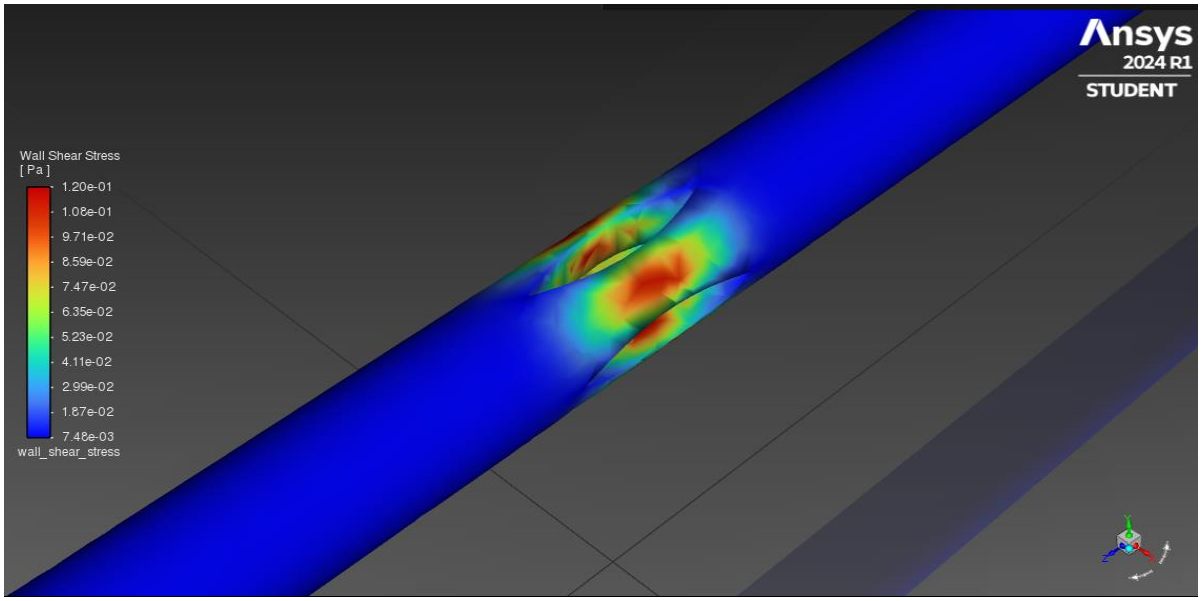

Figure 6.6: Baerveldt Double Fin Tube 2.5µL/min Wall Shear Stress Distribution at Fins

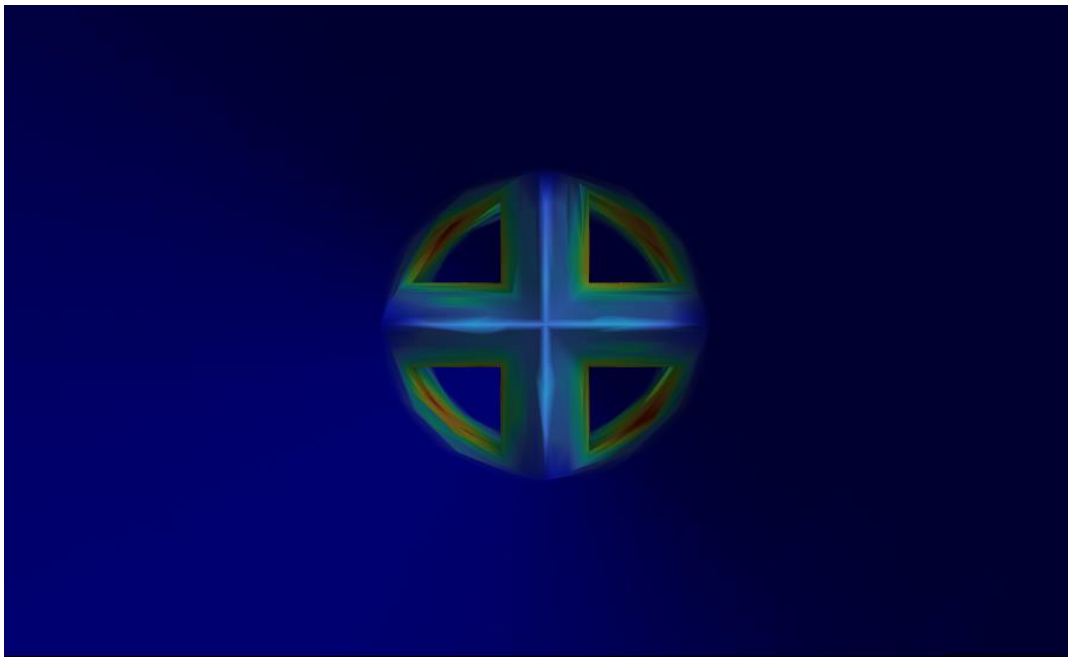

Figure 6.7: Baerveldt Double Fin Tube Interior Wall Shear Stress Distribution

As the double finned geometry provided less area for the AH to travel through, a higher concentration of stress was forced to the walls at these locations (see figure 6.6 and 6.7). Moreover, this caused an elevated fluid velocity that likely contributed to both the increase in stress and frictional effects, leading to a higher pressure drop. The restriction of flow through these reduced sections is confirmed by a streamline plot seen in figure 6.8. With a maximum stress of 0.12 Pa for a flow rate of 2.5µL/min, the possibility of tube failure under stress is very low. However, the risk of other issues such as tube clogging through biofouling may be elevated with the reduction of cross-sectional area.

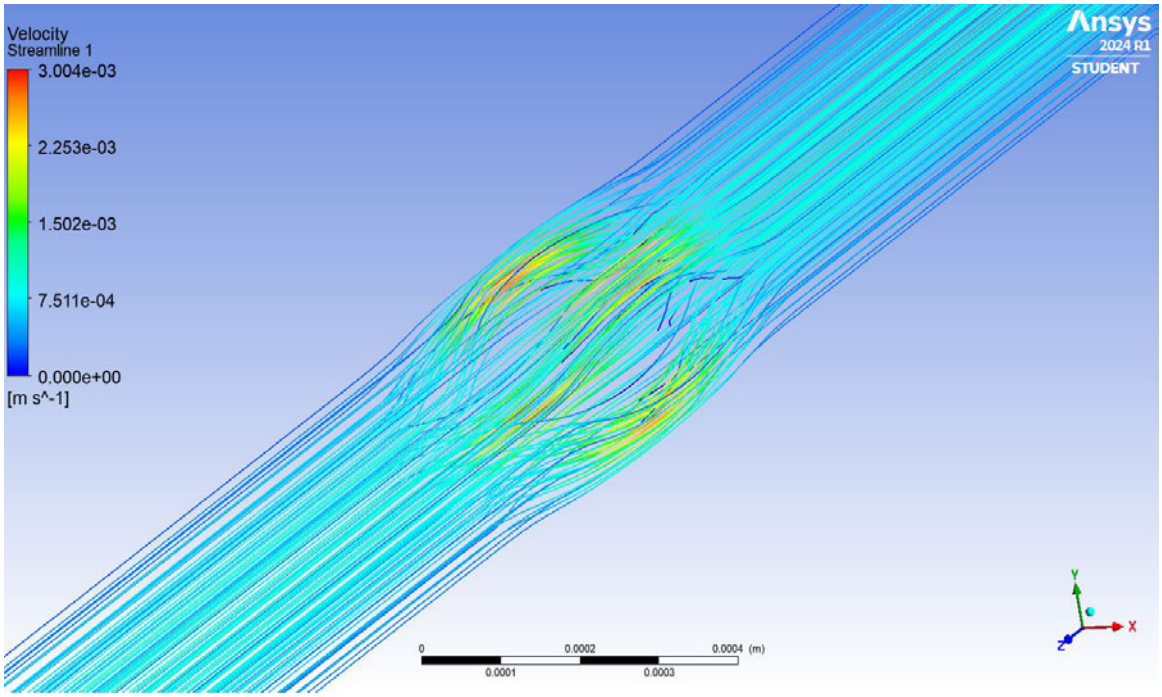

Figure 6.8: Baerveldt Double Fin Tube Velocity Streamline Plot

Dissimilar to the double fin, the single fin tube had a lower maximum average stress compared to the varied inlet tubes as seen in figure 6.5. The elevated stress concentration at the wall explains the increased drop in pressure discussed in section 6.2.1. Moreover, while the velocity was slightly elevated at the smallest sections near the tube wall (see figure 6.10), the flow was generally consistent throughout. Subsequently, this would suggest the flow through the single fin was only minorly disturbed, likely due to the streamlined shape of the fin itself. Much like the double fin, there is very minimal risk of tube failure through stress with a maximum value of 0.0461 Pa.

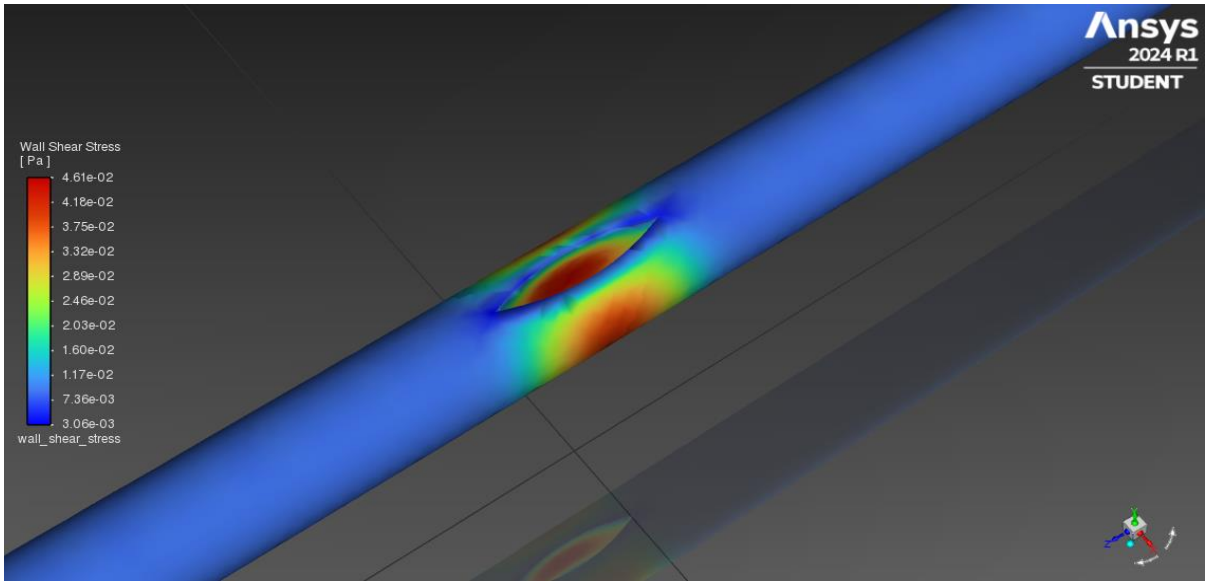

Figure 6.9: Baerveldt Single Fin Tube 2.5µL/min Wall Shear Stress Distribution at Fins

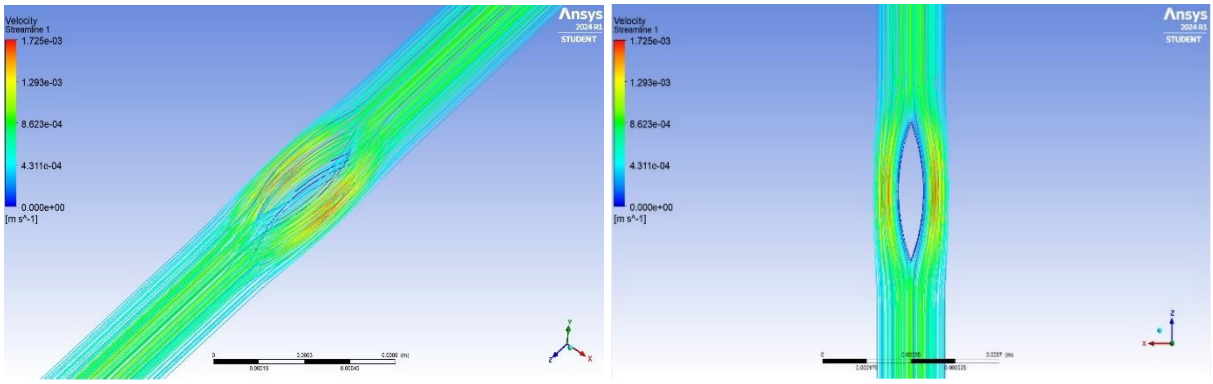

Figure 6.10: Baerveldt Single Fin Tube Velocity Streamline Plots

While figure 6.5 indicated the varied inlet tubes had a similar maximum shear stress, section 6.2.1 displayed the snipped and rounded Baerveldt tubes both had an elevated pressure drop in comparison to the standard tube. Using 3D arrow streamlines, the flow behaviour can be investigated at these two inlet configurations.

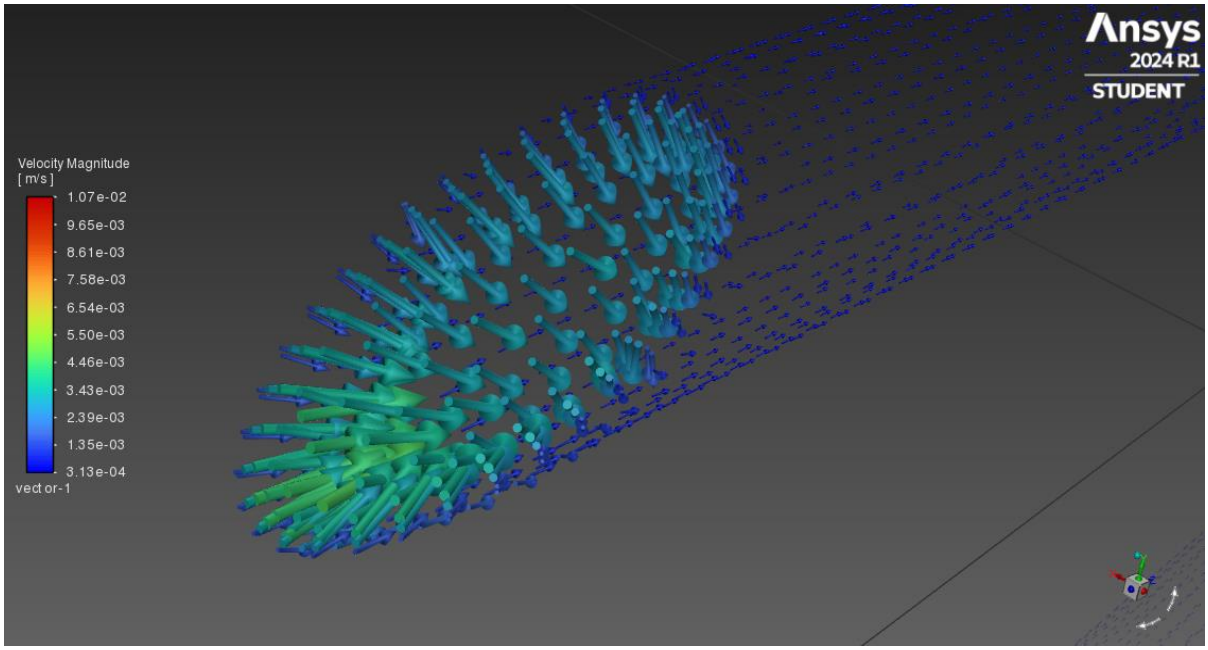

Figure 6.11: Baerveldt Snipped Tube Inlet Flow Streamline Plot

Confirming both the research and the discussion with ophthalmic surgeons as mentioned in section 4.2.1, the snipped inlet appears to create a build-up of fluid at the sharp edge when flowing into the tube (see figure 6.11). Subsequently, this confirms the cause for flow blockages during surgery, which is a common failure mode for GDDs. This grouping of fluid is also confirmed through the evident concentration of wall shear stress in figure 6.12.

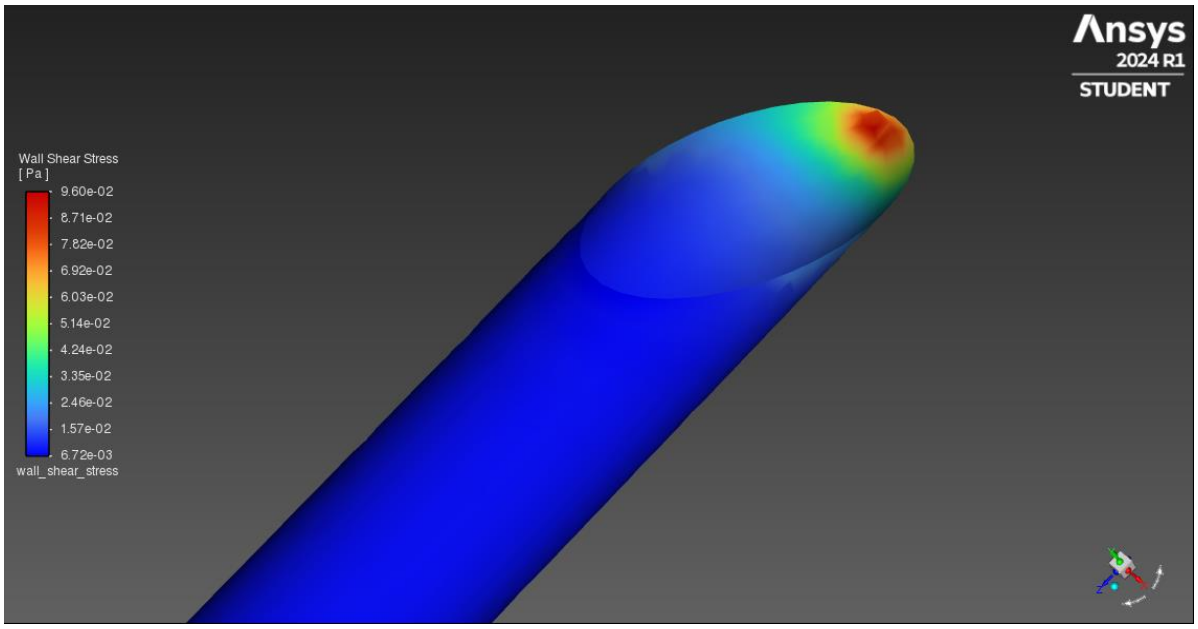

Figure 6.12: Baerveldt Snipped Tube 2.5µL/min Wall Shear Stress at Inlet

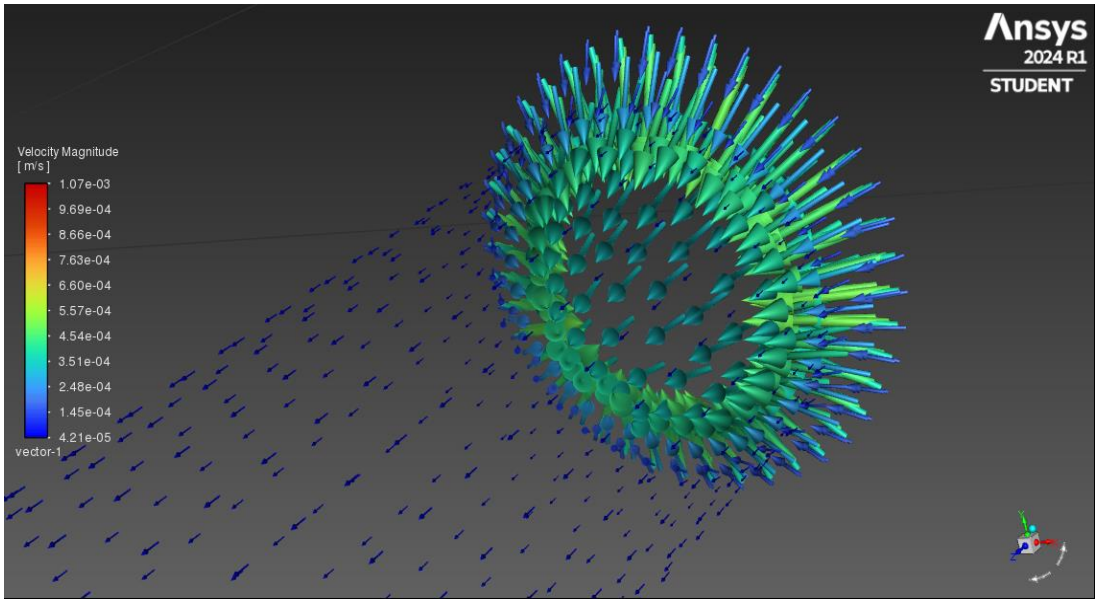

Figure 6.13: Baerveldt Rounded Inlet Tube Flow Streamline Plot

The rounded inlet streamline plot in figure 6.13 reveals a more evenly distributed flow in comparison to the snipped tube. This experimental inlet appears to allow for the flow to more easily follow the curve without a concentrated build-up of aqueous humour. Subsequently, this would indicate this design is less likely to block flow upon insertion, improving the overall reliability of the GDD tube. As explored in section 6.2.1, the rounded inlet has a slight increase in pressure drop compared to that of the standard tube, but a lower drop than the snipped configuration. This wall shear stress concentration is also evenly distributed around the inlet, with a maximum value of 0.00977 Pa as evident in figure 6.14. This slightly increased stress value would have contributed to the elevated drop in pressure, but is not a concern when considering the long-term degradation of the GDD tube.

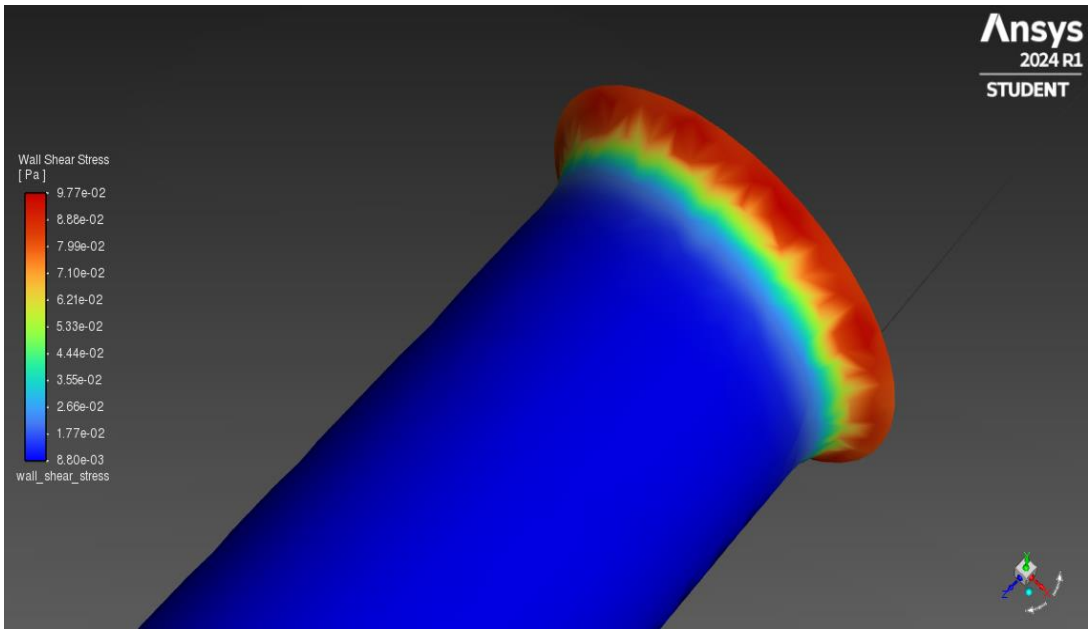

Figure 6.14: Baerveldt Rounded Inlet Tube 2.5µL/min Wall Shear Stress at Inlet

6.3 Paul Tube

6.3.1 Pressure Drop Analysis

Following the analysis of the Baerveldt tubes, the pressure results for the Paul implant will be compared graphically from the tabulated data for each tube variation presented within Chapter 5. The analysis method will have little variance, as aside from the inner and outer dimensions, there are no other major differences between tubes.

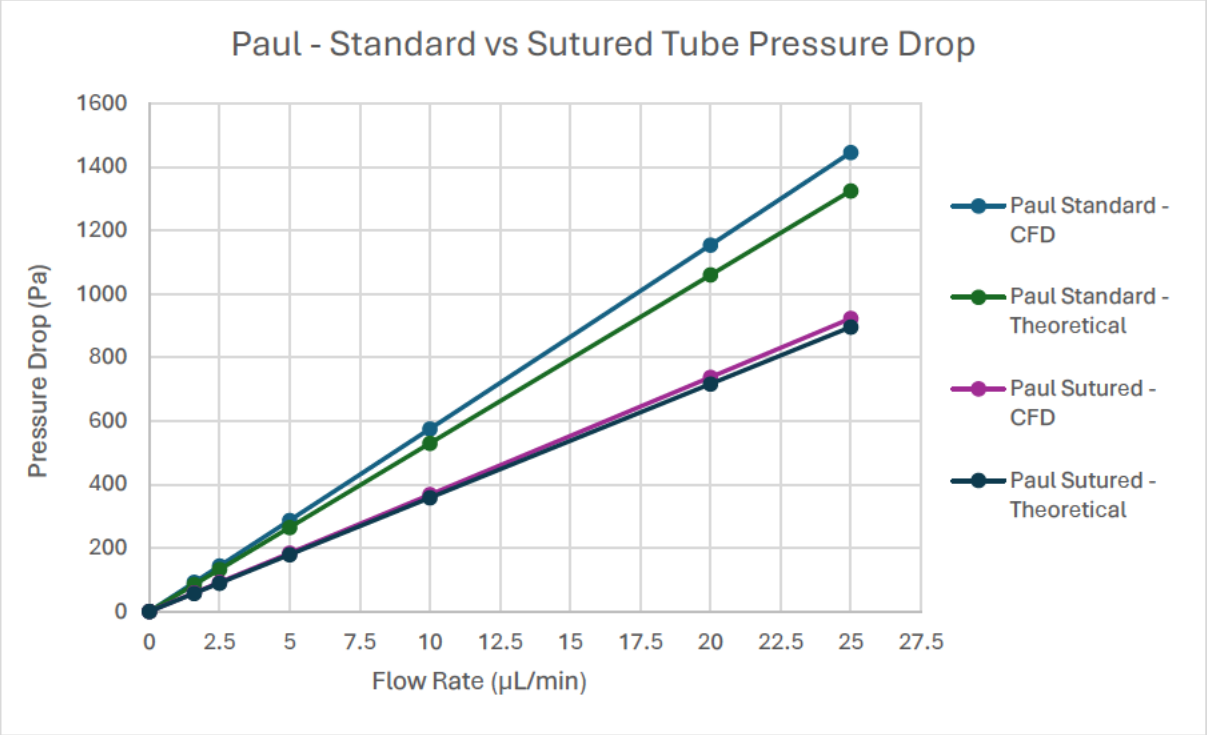

Figure 6.15: Paul - Standard vs Sutured Tube Pressure Drop

As evident in figure 6.15, the suture expectedly reduced the drop in pressure compared to the standard variation. Moreover, the theoretical calculations adapted from Agujetas, R. et al. (2021), appear to be accurate to verify the CFD simulations. The CFD predicted a 143.5 Pa drop at the normal physiological flow rate of 2.5µL/min, compared to that of 91.9 Pa for the sutured tube.

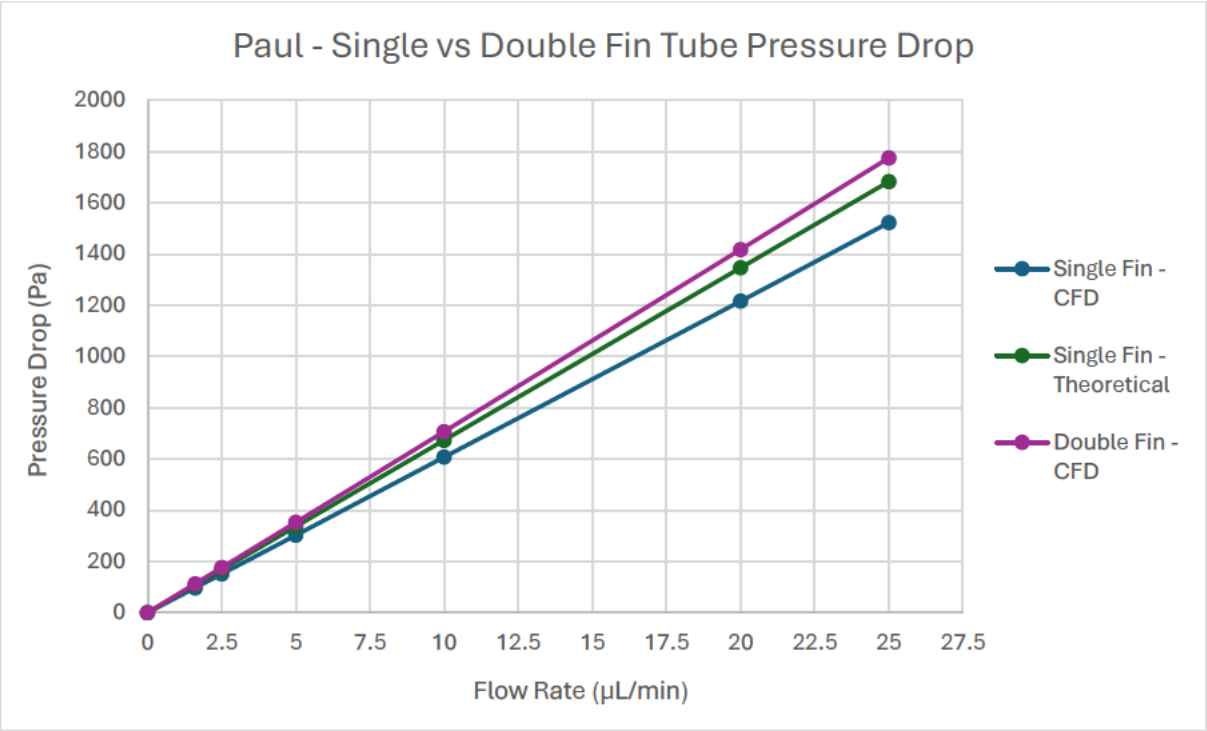

Figure 6.16: Paul - Single vs Double Fin Tube Pressure Drop

Aligned with the Baerveldt analysis, the Paul double finned tube had a higher pressure drop than its single fin counterpart with 176.2 Pa and 151.1 Pa, respectively (at 2.5µL/min). The double fin theoretical results have been excluded from figure 6.16, as these results were deemed inaccurate due to the limitations of the theoretical analysis.

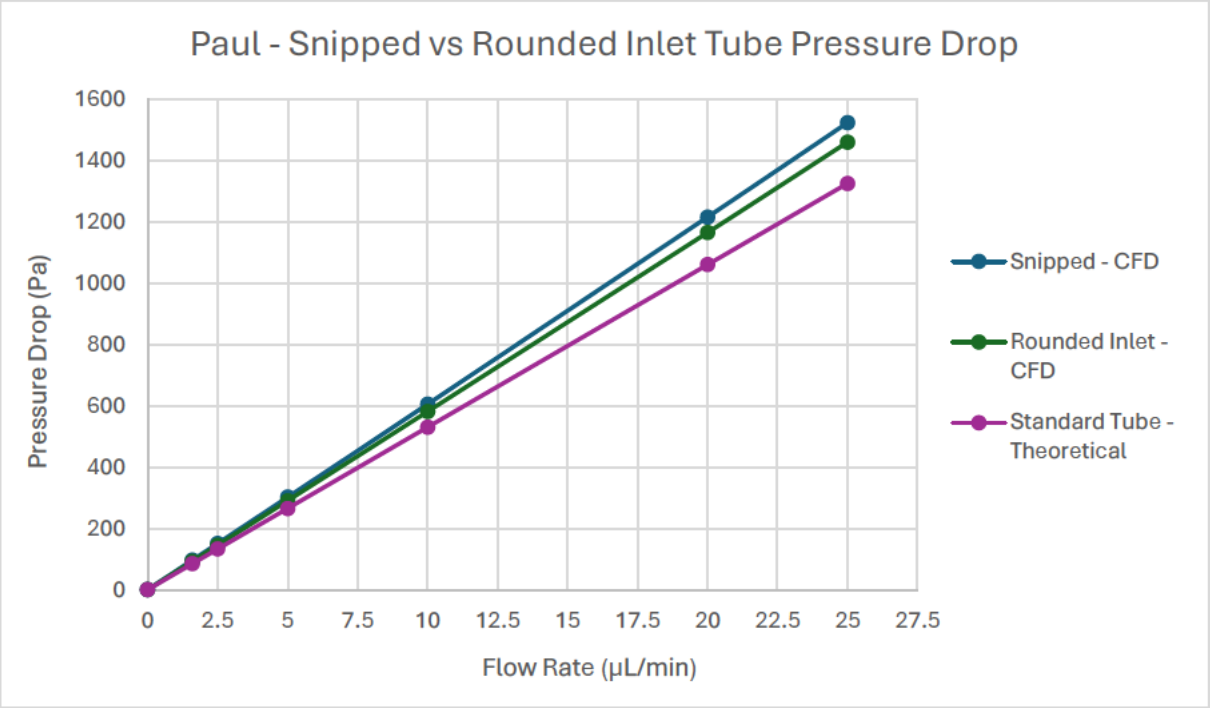

Figure 6.17: Paul - Snipped vs Rounded Inlet Tube Pressure Drop

Similarly to the Baerveldt implant tubes, figure 6.17 displays the patterns of the Paul snipped and rounded inlet variations compared to the theoretical results of the standard tube. Both inlet geometries have an increased pressure drop compared to the standard variation, with the snipped tube displaying a 150.7 Pa drop, the rounded inlet with 144.8 Pa, and the theoretical calculations for the standard tube showing a drop of 132.47 Pa (at 2.5µL/min). The increase in pressure drop is likely caused through the variation in concentration of flow, as depicted in the previous Baerveldt section. A similar analysis will be conducted in section 6.3.2 to analyse the flow behaviour of the Paul implant tube to confirm these assumptions.

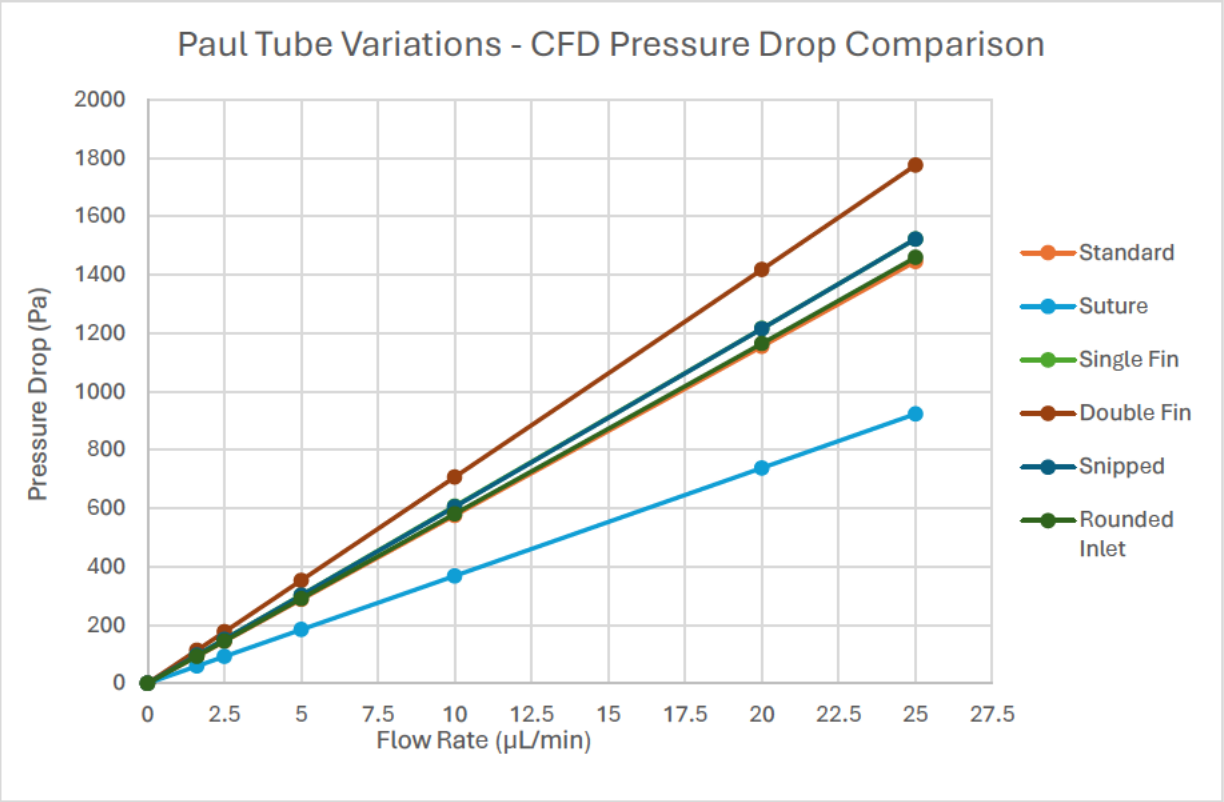

Figure 6.18: Paul Tube Variations - CFD Pressure Drop Comparison

To wholistically analyse each Paul implant variation, a graph can be produced to compare the CFD pressure drop results. Figure 6.18 displays the sutured tube produced the lowest pressure drop, with the double fin tube showing the highest. In contrast to the Baerveldt tube, the grouping for the remaining variations is far tighter. In comparison to the standard tube, the rounded inlet variation saw an approximate increase of just 1%, along with both the snipped and single fin tubes at 5%. As mentioned, the double fin was the highest increase by approximately 23%. These pressure drop increases largely occur through additional micro-frictional effects and flow condensation caused by the tube variations. As explored throughout the Baerveldt section, the flow behaviour and wall shear stress plots will reveal the disparity and cause for the rise in pressure drop.

6.3.2 Flow Behaviour and Wall Shear Stress

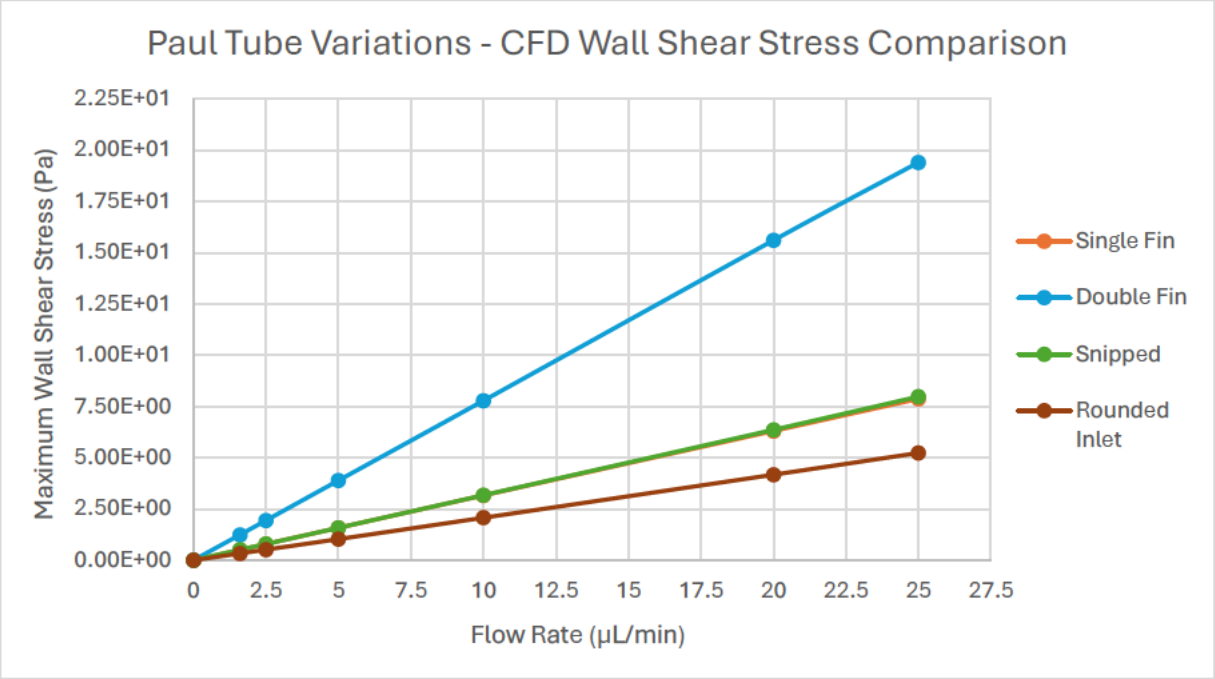

Figure 6.19: Paul Tube Variations - CFD Wall Shear Stress Comparison

Figure 6.19 displays a clear disparity between the maximum wall shear stress values for the single fin, double fin, snipped, and rounded inlet tube variations. The double fin tube had the largest shear stress values for all flow rates. In contrast to the Baerveldt tube where the single fin configuration had the lowest maximum wall shear stress, the Paul implant saw the rounded inlet variation produce the lowest stress values amongst the four variations. The snipped tube and single fin tube shared very similar results.

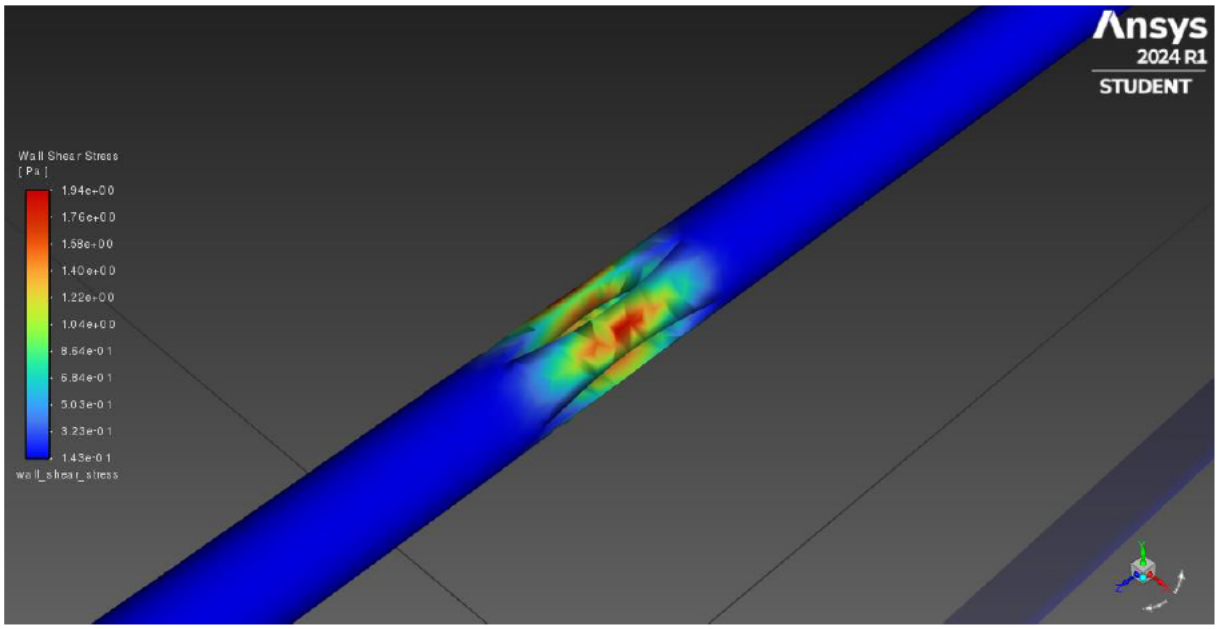

Figure 6.20: Paul Double Fin Tube 2.5µL/min Wall Shear Stress Distribution at Fins

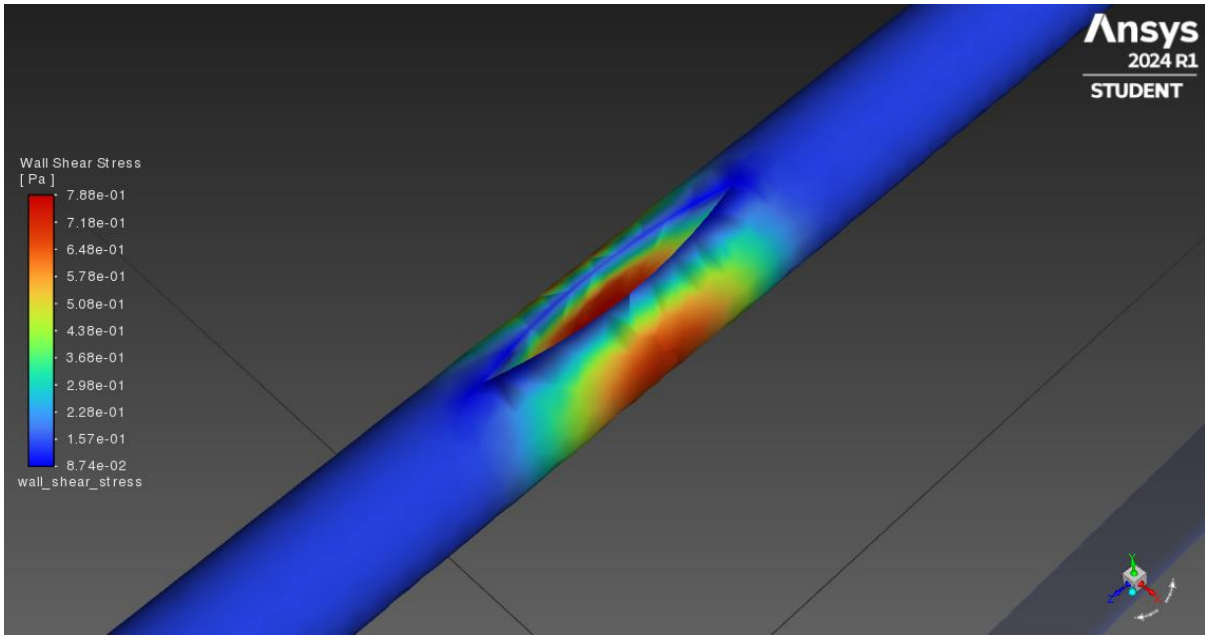

Figure 6.21: Paul Single Fin Tube 2.5µL/min Wall Shear Stress Distribution at Fins

While the fin dimensions were approximately scaled down from the Baerveldt to suit the Paul inner dimensions in section 4.2.2, the model geometry was left with thinner sections and openings (see figure 6.20). Subsequently, this caused an increased velocity and flow concentration at these locations within the tube, leading to the elevated stress values depicted in figure 6.19. This geometry also may have influenced the single fin results (see figure 6.21), causing a rise in wall shear stress compared to its counterpart in the Baerveldt section. While the maximum stress values are still relatively low for the Paul tubes being 1.94 Pa and 0.788 Pa for the double and single fin variations, respectively, this is a considerable increase from the Baerveldt geometries. This is likely due to the significantly smaller cross-sectional diameter employed by the Paul implant, which effectively increases pressure drop, but may be more susceptible to stress related failures. To investigate the influence that this smaller diameter has on the Paul inlet variations, the wall shear stress and flow behaviour plots can be analysed accordingly.

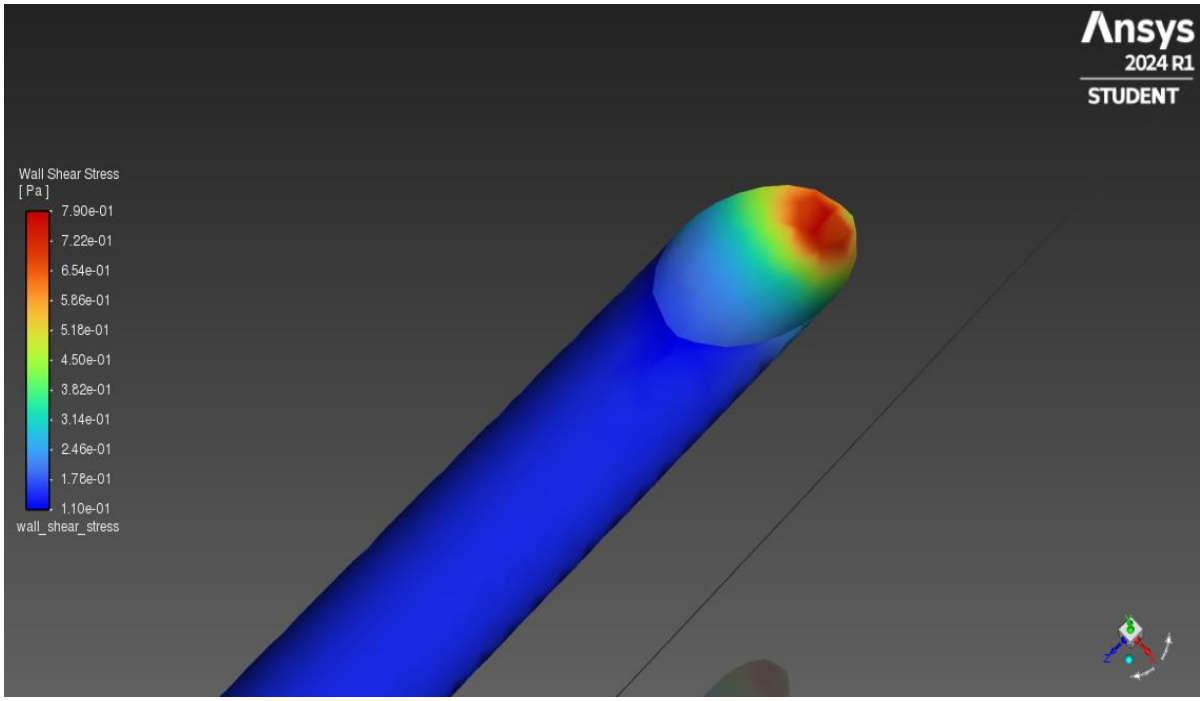

Figure 6.22: Paul Snipped Tube 2.5µL/min Wall Shear Stress at Inlet

The wall shear stress plot for the Paul snipped tube in figure 6.22 reveals a larger stress concentration at the tip that that seen in 6.12 for the Baerveldt implant. Due to the far smaller internal diameter used by the Paul implant, the aqueous humour has less surface area to travel over when entering the snipped tube. Subsequently, this fluid is more likely to concentrate at the tip causing problems during surgery. This is confirmed by the velocity streamline plot in figure 6.23, which displays the obvious concentration of fluid at the snipped sharp end seen flowing into the implant.

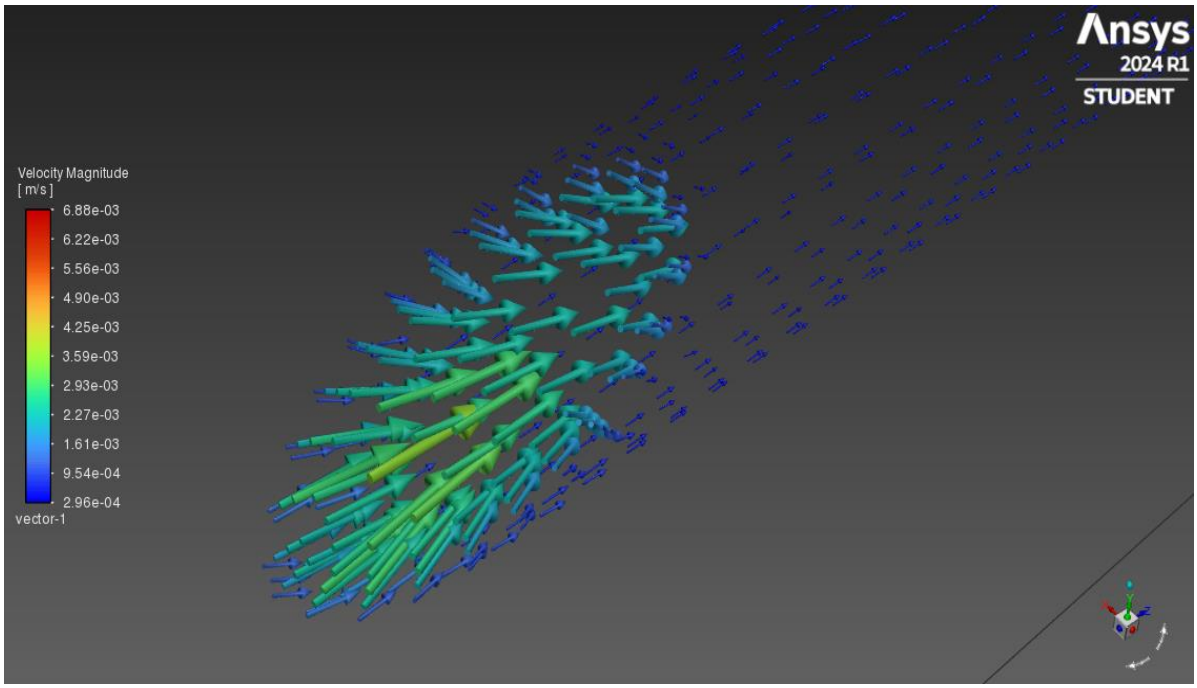

Figure 6.23: Paul Snipped Tube Inlet Flow Streamline Plot

The Paul rounded inlet configuration appears to remain relatively consistent with the Baerveldt, with an evenly distributed flow and stress concentration around the inlet. The smaller diameter of the Paul implant increased the wall shear stress to 0.515 Pa at 2.5µL/min, compared to 0.0977 Pa for the Baerveldt. While this is a significant increase in terms of percentage, 0.515 Pa is an inconsiderable figure when reviewing the likelihood of long-term implant failure. Figure 6.24 displays the flow pattern at the inlet of the Paul rounded inlet tube, which appears to be evenly distributed and organised. The wall shear stress plot aligns with the expectations outlined previously, with an even distribution of stress around the curved inlet edge (see figure 6.25).

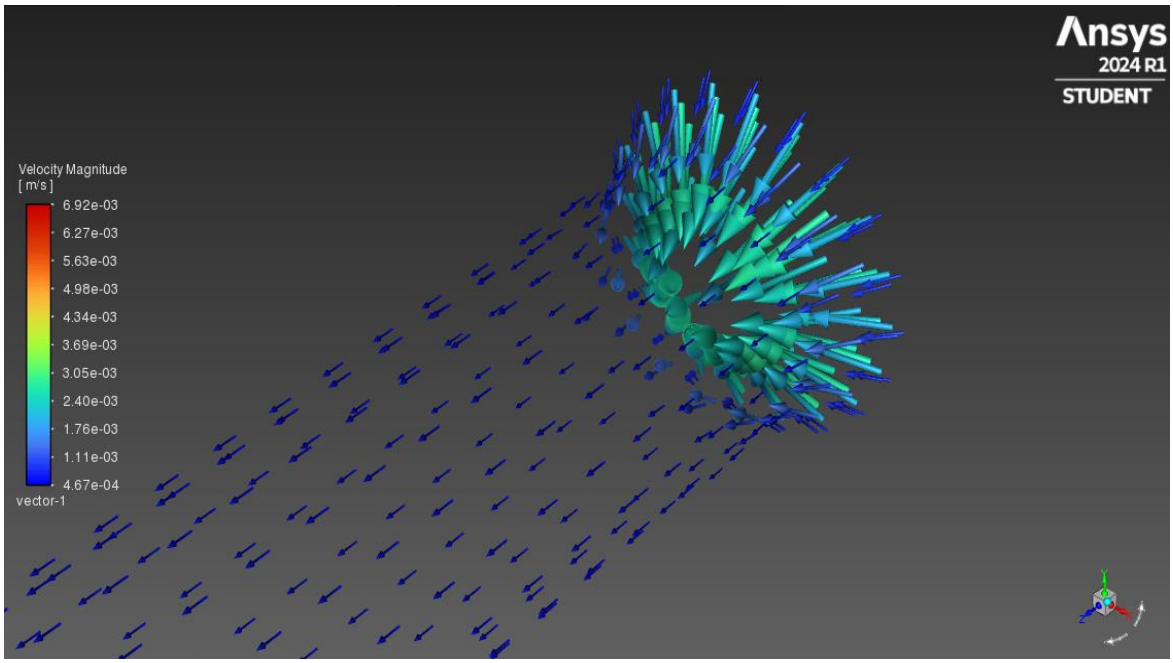

Figure 6.24: Paul Rounded Inlet Tube Flow Streamline Plot

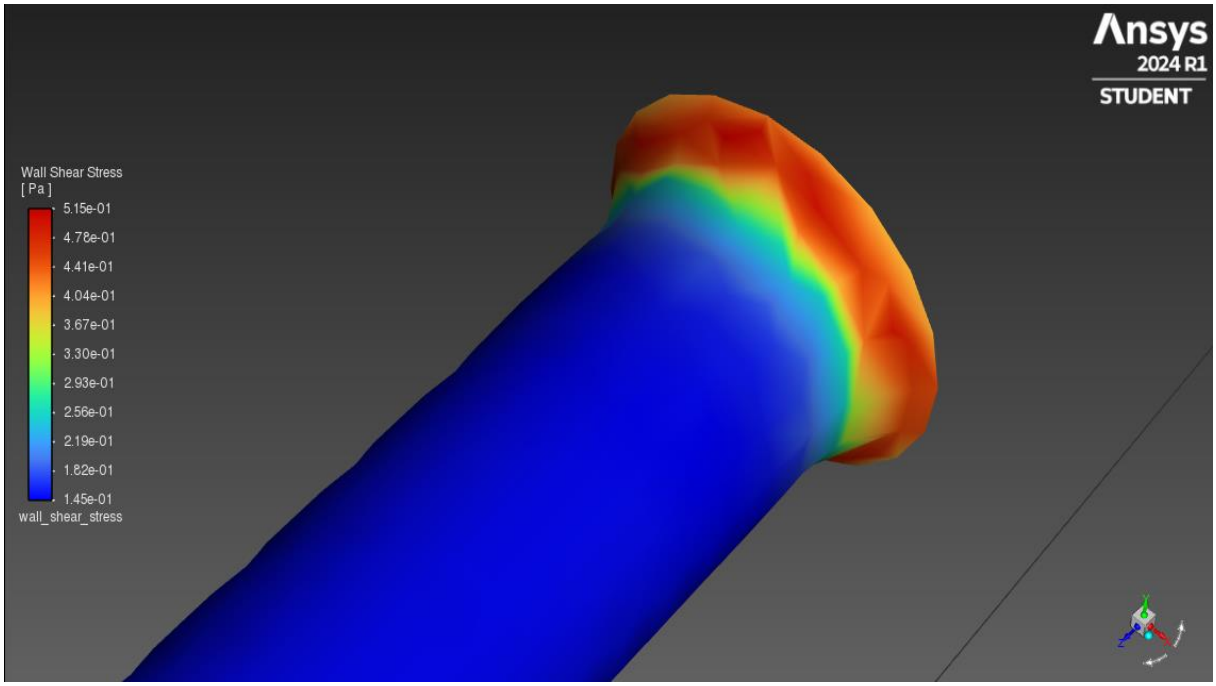

Figure 6.25: Paul Rounded Inlet Tube 2.5µL/min Wall Shear Stress at Inlet

6.4 Analysis Summary

Sections 6.2 and 6.3 discussed the pressure drop, wall shear stress, and flow behaviour results in depth for each variation of the Baerveldt and Paul implants. This section will summarise the major findings, make further recommendations, investigate the potential for future work, and highlight some major limitations seen through the analysis process.

6.4.1 Major Findings

The analysis process revealed the significant advantage of the Paul implant compared to the Baerveldt implant in terms of pressure drop and management. At a normal physiological flow rate of 2.5µL/min, the standard Baerveldt tube saw a pressure drop of 3.84 Pa, compared to 143.5 Pa for the Paul. Converting to the standard unit for eye pressure, millimetre of mercury (mmHg), reveals a drop of 0.029mmHg for the Baerveldt, and 1.076mmHg for the Paul. These CFD results would indicate that the Paul implant is far more likely to have a positive surgical impact sooner given the considerably larger pressure drop average, which would align to the rising popularity of the Paul implant in Australia. It is worth noting that successful GDD surgery is a gradual process as these implants have considerable time to lower eye pressure gradually, with a study showing follow up appointments occur at a mean value of 78.3 ± 44.0 months (Bhattacharya, S.K. et al. 2010).

The success of the theoretical finned geometries displayed varied results across the two types of implants. Section 6.2 and 6.3 revealed that due to an exposure to more surface area at the centre of the

tube, the double fin geometry had an elevated shear stress concentration on the outer walls. This stress concentration, along with the significant reduction in area caused by the crossed fins, has resulted in the double fin being classed as a problematic solution. On the other hand, the single fin appears to be more viable as the flow is only slightly disturbed, while remaining consistent in other aspects like pressure drop, velocity, and wall shear stress concentration. The aim of the finned variants was to investigate how the flow could be disturbed to effectively combat the effects of biofouling, without considerably altering the current flow patterns. The Baerveldt single fin variation displayed considerable promise as the wall shear stress was reduced compared to other tube geometries, while the Paul single fin also performed well but had a slightly higher stress concentration due to the smaller dimensional qualities of the Paul tube. These single fin conditions are theorised to mitigate several other issues that may arise with the more extreme double finned variant.

The inlet variation study proved to be a meaningful analysis to accurately predict both surgical behaviour and a proposed theoretical solution. Comments from ophthalmic surgeons would suggest that one of the more common modes of GDD failure during surgery is the blockage of tube focused on the inlet. By citing the literature for the common GDD surgical procedures, the snipped tube model was developed and tested accordingly. The CFD results, through the wall shear and velocity streamline plots, indicated that a build-up of fluid occurs at the tip end of the snipped inlet. This directly relates to the surgical shortcomings mentioned earlier and significantly impacts the wall shear stress concentration. Although both implants are affected by this snip, the Paul tube experiences a more pronounced concentration of flow due to its smaller internal diameter. The rounded inlet, theorised to improve the flow into the drainage tube, provided promising results. The velocity streamline plots showed an organised, evenly distributed flow that followed the curved inlet face smoothly. These assumptions were verified through the wall shear stress plots, where both the Baerveldt and Paul tubes saw a reduction in maximum stress compared to the snipped inlet. While there are notable limitations and further considerations needed to accurately assess the potency of this novel solution, the rounded inlet was an interesting experimental analysis to compare to the currently used snipped inlet.

6.4.2 Expanding the Analysis

Upon completing the analysis, it is clear there is room for additional work and investigation to expand the scope and increase accuracy of the findings. These primary factors range from producing more tube variations, to revisiting existing simulations and updating them to better reflect realistic situations.

Firstly, conducting further research regarding the snipping angle would be beneficial to expand the analysis process. Only one angle of 30 degrees was investigated in this study, and thus, a wider variety of angles may provide further information on the true influence the snipped inlet has on the

pressure drop and flow patterns of the tube. Furthermore, theorising and investigating more experimental geometries may expand this analysis past the initial scope. The possibility for these variations, whether that be different fin geometries or external flow devices, is extremely broad.

Another focal point of the methodology that could be expanded is the suture investigation. Only one theorised geometry for the suture was simulated in this project. With physical inspection on how the tube behaves under the stitch, a better model may be produced to use within the study. This would not only require access to a GDD implant, but also to surgical sutures and a realistic model eye. The suture positioning in the tube model may also be changed based on the surgical techniques, as the suture was assumed to be situated in the centre for both the Baerveldt and Paul cases. These additions would not only expand the scope of the analysis, but potentially increase the accuracy of the simulations to reflect realistic surgical procedures.

While the Paul and Baerveldt implants are the most widely used in Australia, an obvious expansion avenue is to research and simulate a wider variety of GDDs. This is inclusive of the valvular alternatives, namely the AGV and Krupin. These implants, used more widely internationally, would provide the potential for additional analysis into how the valvular geometry impacts flow, and what changes may be made to optimise these devices. With a fundamental framework provided for the CFD model and its conditions throughout this study, the simulation potential is vast.

6.4.3 Limitations and Observations

As with any research project, through the methodology and results analysis stages there were certain limitations encountered that may have impacted results or affected the potential solutions. These limitations will be analysed critically, along with other noteworthy observations seen throughout the project.

Upon reviewing the results, it is observed that it would have been more accurate to simulate each tube variation with a different inlet geometry. The standard tube inlet assumes perfect, evenly distributed flow at the inlet with little to no flow deviation. While effective in theory, the snipped inlet conditions more accurately reflect actual behaviour of the aqueous humour when entering the drainage tube. The standard inlet proves to be an effective control model, but the overall simulation accuracy would have been increased with the inclusion of these alternate inlets.

Further limitations were seen throughout the theoretical calculations section regarding the finned geometries. As discussed briefly in section 5.5.2, the theory was extremely experimental due to the limited literature looking at this type of tube geometry. Subsequently, the accuracy of these results was varied and did not closely reflect the simulation results, particularly for the double fin. The limitations for the finned geometries continued after reviewing the results. In hindsight, the concept of introducing a blockage in an already severely constricted tube is problematic. The theory behind the

solution was justified, but in actual practice, these solutions may be difficult to implement. Manufacturing these precise fins at such a small scale may introduce additional errors. Furthermore, the potential for tube blockage with these fins are relatively unknown over the long term. To properly assess the validity of these designs, they would need to be rigorously tested in a physical experiment environment to investigate the resulting flow behaviour.

Further surgical and manufacturing difficulties have also been identified for the rounded inlet variation. While the results were promising and appeared to adequately propagate flow through the inlet, the difficulty of manufacturing must be considered. As previously noted for the finned geometries, the small scale at which these drainage tubes operate would make it challenging to apply a small fillet to the interior tube edge at the inlet. This must occur prior to surgery, which would eliminate the option to snip the tube. Subsequently, very careful consideration must be placed on the positioning of the GDD end plate during surgery to allow for the rounded inlet tube to fit accordingly.

The end plate of the GDDs was not considered for this analysis as much of the pressure drop occurs solely over the drainage tube. For the scope of this project, this was sufficient to investigate the tube and its variations but for an extended analysis, further insight may be gained through the inclusion of the end plates. More refined meshes may have been possible with more computational power, which would have allowed for the end plates to be included.

The remaining limitations are not crucial to the accuracy of this project, but may be incorporated in future applications to improve accuracy of the simulations. Additional simulation parameters that were excluded from this analysis that may be beneficial for future models include the temperature variation within the eye and the relevant buoyancy effects. While the influence may be small, a study on the numerical simulation of aqueous humour around the eye (Sánchez, G.M. et al. 2020) employed these conditions. This would elevate the complexity of the simulation methodology, and consequently increase the accuracy of the results. Other less critical parameters like gravity and tube orientation relative to the ground may also be employed for future studies.

6.5 Experimental Procedure Framework

The aim of this research project was to establish the initial CFD simulation model, to test both existing and novel drainage tube variations. As with any simulation project, the next logical step is to validate the simulation data through physical experimentation. This section of the dissertation will provide a brief outline of the materials required and discuss the potential methodology by citing previous research and similar studies.

One experimental method used by Panduro, R.M.R. et al. (2021) to analyse glaucoma drainage devices is the use of extirpated pig eyes. The implants can be inserted into these eyes to closely

simulate the behaviours of an actual human eye. Subsequently, this method of investigation would be beneficial for this type of experimental framework. With the pig eyes, Panduro, R.M.R. et al. devised a gravity driven flow test to test their experimental glaucoma flat drainage device. This type of experiment is used to simulate aqueous humour and the IOP by establishing a pressure gradient, reflective of actual eye conditions. The saline solution flows via gravity into the glaucoma drainage device, where outflow measurement tools assess the performance of the implant. There are several major limitations for of this type of experiment that can limit the accuracy of the results. The inability to control flow rate with a gravity driven test can cause non-physiological values. Moreover, the assumption of constant flow causes a linear pressure-flow relationship which is unrealistic in actual conditions, as a gravity driven test is unable to vary inlet flow conditions. These testing conditions also omit several biological conditions, such as the inability to mimic natural blockages, absence of eye tissue effects, and the exclusion of internal pressure variations. These conditions are difficult to simulate in a simple benchtop environment, but may be implemented in a higher-level experimental procedure.

Another flow test used by Porter, J.M. et al (1997) and Stay, M.S et al (2005) implemented a syringe-driven flow test that could more accurately control inlet flow rate. This addition required a longer experiment time, but removed some of the explicit flow rate limitations of the gravity driven test. While not perfect, the syringe allowed for a tighter control of flow which introduces a more realistic pressure-flow gradient, dynamic adjustments, and overall experimental customisation.

To devise a new methodology, the previous experimental procedures can be analysed to find their strengths, and new technology can be proposed for implementation. The use of micro-pumps and internal valves are proposed to be very beneficial in a GDD experiment application. Additionally, the use of pressure sensors at the inlet and outlet of the drainage device would allow for dynamic measurement and analysis on the drop of pressure under the specified conditions. This type of procedure would be costly, but would result in higher accuracy compared to both the gravity driven and syringe-based experiments. The combination of a micro pump and valvular system would allow for considerable customisation of inlet conditions, such as incorporating pulsating flows, imitating natural blockages, and creating a consistent flow resistance. These factors would best reflect the conditions within an actual human eye, resulting in the most accurate simulations. Furthermore, with a consistent source of power a long-term degradation simulation could be run to investigate the GDDs capability to survive over an extended period. The pressure sensor data would allow for constant observations over this period, and provide instantaneous feedback when any key variable, pipe valve, or flow condition was changed. The broad allowance for customisation with this proposed methodology would be extremely beneficial when testing existing or new GDD designs. Due to the high expected cost, it is theorised that this procedure would be most beneficial in the closing stages of the design process.

6.6 Chapter Summary

This chapter discussed and critically analysed the raw data results presented in Chapter 5. Each tube variation was compared to its the other relevant geometries using graphical figures and Ansys flow plots. The major findings surrounding the impacts of the current surgical procedure and viability of the theoretical solutions was discussed in depth for both the Paul and Baerveldt implants. The chapter concluded with a section on the major project limitations, potential for expansion, and a framework for an experimental procedure.

Chapter 7 – Conclusions

7.1 Project Summary

This project investigated the use of solid modelling and CFD for the analysis of glaucoma drainage devices. The two devices analysed, being the Baerveldt and Paul, are the most widely used implants across Australia. With a detailed literature review, these GDDs were researched to find the current surgical procedures used and the common failure modes seen throughout their implementation. Additional research was put into reviewing existing studies involving CFD in GDD and ophthalmology applications. Using this knowledge, a methodology was devised to use solid modelling software in combination with CFD to investigate both existing and devised drainage tube variations. The CFD results confirmed the suspected limitations of the surgical procedure used across the ophthalmology profession today. While the novel solutions devised to combat biofouling and tube blockage showed varied results, the process ultimately validated the potential effectiveness of using CFD in the analysis, and potential new design, of glaucoma drainage devices.

7.2 Project Objectives and Research Questions

7.2.1 Project Objectives

Upon the completion of this project, the initial project objectives and research questions can be critically reviewed to assess the successfulness of the study. The initial aims and objectives can be categorised into the following numbered sections, with a review summary below each point:

1. Familiarise with the CFD software, become more competent in its utilisation and the fundamental principles required to analyse GDD systems.

> Over the course of this project, this objective has been achieved through extensive use of the CFD software. By applying knowledge and techniques acquired through continual simulations, the fundamental principles for simulating a GDD drainage tube using Ansys were established. Further work, research, and time is required on learning how to effectively apply the share topology tool when running simulations that include both the drainage tube and end plate.

2. Conduct background research via the literature review to investigate GDD technology, including common surgical techniques and known methods of failure. Research the most common GDDs used in Australia, employ these implants for the remainder of the study.

As evident in Chapter 2, the extensive literature review covered all the above. Through the research, the Paul and Baerveldt implants were identified as the most widely used GDD in Australia, and the relevant surgical techniques were discussed.

3. Research and analyse previous CFD studies in the field of glaucoma and glaucoma drainage devices. Review this research to find the appropriate theoretical calculations, along with exploring other similar methodologies to guide the project.

Section 2.4.2 of this dissertation discussed the most relevant CFD studies in the field of glaucoma and glaucoma drainage devices, highlighting the key variables and unique methods used within the studies. A few of these studies were later referred to when formulating the methodology for this research project. Additional parameters, such as the governing theoretical calculations, were also discovered throughout the literature review.

4. Utilise Creo Parametric to model several variations of the drainage tubes for the most common GDDs, citing the literature review for the models representing the realistic surgical procedures. Theorise and model novel solutions to the most common failure modes for GDDs.

As outlined in Chapter 4, this objective was achieved through the modelling of the six tube variations. Backed by research and the literature review, the surgical techniques were accurately represented through the solid models. The theoretical solutions were also produced, with varying levels of success as discussed in the limitations section 6.4.3.

5. Run simulations for the developed models within ANSYS Fluent over a variety of flow rate conditions.

This objective was also achieved as the simulations employed six different flow rates, which is reflected in similar studies outlined in the literature review.

6. Analyse the CFD results, and produce tabular and graphical representations of the data. Make critical observations on the influence the different tube variations have on the fluid flow profile, along with investigating the key variables of pressure drop and wall shear stress. This comparative analysis will provide insight into the effects of the current surgical procedures and the novel solutions proposed via the research gathered within the literature review.

Chapters 5 and 6 cover this objective, as critical analysis was provided for the simulation data by comparing through graphical, tabular, and plot representations. The key variables were discussed, along with key findings regarding the models that reflect the surgical procedures and novel solutions.

7. Draw final conclusions, recommend future work, outline the success and parameters of the CFD model, and reflect on the overall process of the research project.

Chapter 6 and the remainder of this Chapter 7 has achieved this objective by concluding the project through the final recommendations.

7.2.2 Research Questions

Along with discussing the initial objectives, a reflection on the research questions outlined at the end of the literature review is required to assess how the project has progressed:

How do different GDD tube geometries affect the fluid dynamics within the eye, as analysed through CFD simulations?

As outlined in Chapter 6, the different GDD tube geometries have a noticeable impact on the dynamics of fluid in the eye of a glaucoma patient. The Paul and Baerveldt implants returned significant differences in pressure drop, due to the smaller internal diameter of the drainage tubes. These value discrepancies continued through the simulation process, with each tube variation producing varying results to its counterpart. CFD has confirmed throughout this study that tube diameter is one of the most influential factors on the effectiveness of the GDD implants through the controllable pressure drop.

How effective is CFD at investigating the impact the current surgical procedure has on the Baerveldt and Paul implant tubes?

The current surgical procedure used when implanting a GDD has been studied via the use of CFD simulations. The suspected limitations of this procedure have also been confirmed by the results, primarily through the flow plots. The concentration of fluid at the snipped end of the tube during surgery is problematic, causing blockages and flow restriction directly at the inlet. Cross referencing to the pressure drop and wall shear stress data confirms these suspicions. It may have been difficult to diagnose these issues without the use of CFD software, confirming the research question regarding the overall effectiveness of CFD in this application.

What alternative methods may be possible within the tubes and at the inlet to combat the common failure modes of GDDs, and how do these results compare through CFD analysis?

The theorised solutions to biofouling and tube blockage varied in effectiveness, as documented in Chapter 6. The finned geometries were devised and simulated with CFD to investigate the potential of positive flow disruption. The simulation results were promising, but it was concluded that in built obstruction mechanisms may be problematic long-term. The rounded inlet variation, imposed to combat tube blockage during surgery, appears to be quite a viable

solution. However, there are some additional limitations surrounding this solution that has been discussed further in section 6.4.3. Both the CFD simulation and solid modelling processes used during the brainstorming of potential solutions appeared to be extremely effective. The option for rapid change using the modelling software allowed for these solutions to be tweaked where required. This project has found that the combination of solid modelling and CFD in these applications is extremely useful, and a viable tool to use in future studies.

7.3 Final Statements

In amongst the difficulties and alterations across the course of the year, this project successfully completed the initial objectives and answered the specified research questions. Some general statements can be delivered to summarise and reflect on the key results found throughout the dissertation:

- GDD pressure drop performance is highly influenced by the internal diameter of the drainage tube, as reflected by the much larger drop in pressure over the Paul implant comparatively to the Baerveldt.
- The current GDD surgical procedure, particularly through the snip on the end of the drainage tube, is insufficient for the efficiency of the implant. The snip causes a fluid concentration and partial blockage at the inlet, reducing the implants effectiveness over time.
- The suture used by surgeons to limit initial flow rate is effective at reducing pressure drop as confirmed via the CFD simulation data.
- The proposed finned geometries have theoretical upside but may be problematic in practice, due to the minute scale of these additions, and the potential for long term tube blockage.
- The rounded inlet variation appears to be a more viable than the snipped inlet, but also brings potential complications and limitations regarding manufacturing and surgical implementation.
- The combination of solid modelling and CFD allows for a structured simulation process to quickly test solutions without having to employ an entire experimental set up for each design iteration. In the long term, this type of analysis would save time and money allowing for investigation into a wider variety of theoretical tube variations.

7.4 Project Limitations and Further Work

As discussed more deeply in Chapter 6 (section 6.4.3), this project has had its various limitations. These can be categorised into the following major points:

- Incorporating the surgically snipped inlet geometry for all simulations would have improved accuracy by reflecting real flow behaviour.
- The theoretical calculations for the finned geometries were highly experimental due to limited literature, resulting in varied and less accurate results.
- The fins may introduce practical challenges, such as manufacturing precision at small scales and the potential for tube blockage.
- The rounded inlet was promising but faces manufacturing and surgical difficulties, particularly due to the small scale of the drainage tubes.
- End plates of the GDDs were not considered in this project, though including them and refining the mesh could enhance future analyses.
- Additional parameters like temperature variation, buoyancy, gravity, and tube orientation were not included but may improve future simulations.

The future work has also been covered in section 6.5, where an outline of an experiment has been discussed to validate the simulation data. This can be summarised into the following major steps:

- Proposed use of micro-pumps and internal valves in GDD experiments could significantly improve accuracy and control.
- Pressure sensors at the inlet and outlet would enable precise, dynamic measurement of pressure drop.
- A micro-pump and valve system would allow customized inlet conditions, such as pulsating flows and consistent flow resistance, closely mimicking actual eye conditions.
- This setup could support long-term degradation simulations, providing data for extended GDD performance analysis.

This dissertation serves as a valuable proof of concept for a wide variety of future work in this field. Building on this report, fellow students or outside researchers can look to continuing the CFD simulations combined with the formulation of physical experiments to test existing GDDs and new tube variations. Furthermore, there is significant potential to use the CFD model presented within this study as a foundational building block in the initial stages of the design for a brand new GDD. CFD is a highly powerful engineering tool that has been underutilized in medical device development. This project has attempted to address that gap, guiding improvements for this already established problem.

References

Agrawal, P. and Bhardwaj, P, 2020. Glaucoma drainage implants. *International Journal of Ophthalmology*, 13(8), pp.1318–1328.

Agujetas, R., Kudiesh, B., Fernández-Vigo, J., García-Feijóo, J., and Montanero, J. 2021, 'Analytical model for managing hypotony after implantation surgery of a glaucoma drainage device', *Biomechanics and modeling in mechanobiology (Internet)*, vol. 20, Springer Science+Business Media, no. 6, pp. 2061–2070.

Aref, A. 2023, *Paul Glaucoma Implant - EyeWiki*, eyewiki.aao.org, viewed 2 April 2024, <https://eyewiki.aao.org/Paul_Glaucoma_Implant>.

Bhattacharya, S.K, Goel, M., Lee, R. and Picciani, R. 2010, 'Aqueous Humor Dynamics: A Review', *The Open Ophthalmology Journal*, vol. 4, no. 1, pp. 52–59

Conlon, R., Saheb, H., and Ahmed, I.I., 2017. Glaucoma treatment trends: A Review. *Canadian Journal of Ophthalmology*, 52(1), pp.114–124.

Coote, M.A. 2017, *Glaucoma Drainage Devices | Glaucoma Australia*, Glaucoma.org.au, viewed 13 March 2024, <https://glaucoma.org.au/news-details/research/glaucoma-drainage-devices>.

Dassault Systèmes, 2022, *How to Optimize the Meshing Process for CFD and FEA*, blog.spatial.com, Dassault Systèmes, viewed 23 May 2024, <https://blog.spatial.com/what-is-meshing-optimization>.

Fitt, A.D and Gonzalez, G. 2006, 'Fluid Mechanics of the Human Eye: Aqueous Humour Flow in The Anterior Chamber', *Bulletin of Mathematical Biology*, vol. 68, no. 1, pp. 53–71

Gardiner, B.S., Smith, D.W., Coote, M. and Crowston, J.G. 2010, 'Computational Modelling of Fluid Flow and Intra-Ocular Pressure following Glaucoma Surgery', in TW Secomb (ed.), *PLoS ONE*, vol. 5, no. 10, p. e13178.

Go, M., Niklas Ulrich, J., and Fleischman, D. 2017, 'Intraocular and extraocular hemorrhage associated with ligature release of non-valved glaucoma drainage implant', *American Journal of Ophthalmology Case Reports*, vol. 5, Elsevier BV, pp. 114–116.

Gupta, S., and Jeria, S., 2022. A review on glaucoma drainage devices and its complications. Cureus.

Huffman, J. 2023, *What Is Hyphema?*, American Academy of Ophthalmology, American Academy of Ophthalmology, viewed 19 March 2024, <https://www.aao.org/eye-health/diseases/what-is-hyphema>.

Jena, S. and Tripathy, K. 2022, *Vitreous Hemorrhage*, PubMed, StatPearls Publishing, Treasure Island (FL), viewed 19 March 2024, <https://www.ncbi.nlm.nih.gov/books/NBK559131/#:~:text=Any%20blood%20in%20the%20vitreous>.

Johnson & Johnson Vision, 2019, *BAERVELDT® Glaucoma Implants*, Johnson & Johnson Vision, viewed 2 April 2024, <https://www.jnjvisionpro.com/products/baerveldt-glaucoma-implants>.

Kang, Y.K.,, Shin, J.P., and Kim, D.W., 2022. Long-term surgical outcomes of Ahmed valve implantation in refractory glaucoma according to the type of glaucoma. BMC Ophthalmology, 22(1).

Kara, E. and Kutlar, A. 2010, 'CFD analysis of the Ahmed Glaucoma Valve and design of an alternative device', *Computer Methods in Biomechanics & Biomedical Engineering*, vol. 13, Taylor & Francis, no. 6, pp. 655–662.

Karaçali, O. 2019, 'Computational Fluid Dynamics Analysis of Titanium Outflow Pipe Implant for Glaucoma Treatment in Biomechanical Engineering', *Acta Physica Polonica A*, vol. 135, Polish Academy of Sciences, no. 4, pp. 561–563.

Koh, V. Triolo, G. Lim, KS. Barton, K. Chew, P. Aquino, C. Sng, C. Ho, H. Rojanapongpun, P. Tantisevi, V. Kheong, FS. Tham, C. and Chan, P. 2020, 'Treatment Outcomes Using the PAUL Glaucoma Implant to Control Intraocular Pressure in Eyes with Refractory Glaucoma', *Ophthalmology Glaucoma*, vol. 3, no. 5, pp. 350–359.

Mastropasqua, L., Carpineto, P., Ciancaglini, M. and Zuppardi, E. 1996, 'Long-Term Results of Krupin-Denver Valve Implants in Filtering Surgery for Neovascular Glaucoma', *Ophthalmologica*, vol. 210, Karger Publishers, no. 4, pp. 203–206.

Mivision, 2021, *Streamlined: Baerveldt Implants*, mivision.com.au, Mivision, viewed 20 May 2024, <https://mivision.com.au/2021/03/streamlined-baerveldt-implants/>.

Moodley, A. and Williams, S.E.I. 2021, 'PAUL Glaucoma Implant: a novel experience at a tertiary institution in Johannesburg, South Africa.', *South African Ophthalmology Journal*, vol. 16, Sabinet Online, no. 3, pp. 14–19, viewed 7 October 2024, <https://go.gale.com/ps/i.do?id=GALE%7CA688765078&sid=googleScholar&v=2.1&it=r&linkaccess=abs&issn=22188304&p=AONE&sw=w&userGroupName=anon%7Ed007e51e&aty=open-web-entry>.

NASA, 2015. *Navier-Stokes Equations*, NASA.gov, NASA, viewed 4 April 2024, <https://www.grc.nasa.gov/www/k-12/airplane/nseqs.html>.

Nguyen, Q.H., Budenz, D.L. and Parrish, R.K. 1998, 'Complications of Baerveldt Glaucoma Drainage Implants', *Archives of Ophthalmology*, vol. 116, no. 5, pp. 571–575, viewed 19 March 2024, <https://jamanetwork.com/journals/jamaophthalmology/fullarticle/262358>.

Optometry Australia, 2019, *Pharma Open Access: IOP medications available in Australia - Optometry Australia*, Optometry Australia, viewed 6 March 2024, <https://www.optometry.org.au/ scope_of_practice/pharma-open-access-iop-medications-available-in-australia/>.

Panduro, R.M.R., Monterrey, C., Mantari, J.L., Canahuire, R., Alvarez, H., Miranda, M. and Elsheikh, A., 2021. Computational and experimental analysis of a Glaucoma flat drainage device. Journal of Biomechanics, 118, p.110234.

Park, H., Raffiee, A.H., John, S.W.M., Ardekani, A.M. & Lee, H. 2018, 'Towards smart self-clearing glaucoma drainage device', *Microsystems & Nanoengineering*, vol. 4, no. 1.

Porter, J.M., Krawczyk, C.H. and Carey, R.F. 1997, 'In Vitro Flow Testing of Glaucoma Drainage Devices', *Ophthalmology*, vol. 104, no. 10, pp. 1701–1707.

Qin, Q., Zhang, C., Yu, N., Jia, F., Liu, X., Zhang, Q., Chen, M. & Wang, K. 2023, 'Development and material characteristics of glaucoma surgical implants', *Advances in ophthalmology practice and research*, vol. 3, Elsevier BV, no. 4, pp. 171–179.

Raja, A, Bhimani, S, Alim, H, Salman, M, Shaikh, A.S, Raja, S, Sayeed, B.Z, Feroze, A & Ahmed, M 2023, 'Meta-analysis of Molteno glaucoma implants and Ahmed glaucoma valves: insights into efficacy and safety for complex glaucoma', *Frontiers in ophthalmology*, vol. 3, Frontiers Media.

Ramdas, W. D., Pals, J., Rothova, A. & Wolfs, R.C.W. 2018, 'Efficacy of glaucoma drainage devices in uveitic glaucoma and a meta-analysis of the literature', *Graefe's Archive for Clinical and Experimental Ophthalmology*, vol. 257, no. 1, pp. 143–151.

Reddy, A. and Salim, S. 2012, *Choroidal Effusions*, American Academy of Ophthalmology, viewed 19 March 2024, <https://www.aao.org/eyenet/article/choroidal-effusions#:~:text=Choroidal%20effusion%E2%80%94an%20abnormal%20accumulation>.

Sánchez, G.M., Del Pozo, C.E., Medina, J.R., Naude, J. and Solorzano, A.B., 2020. Numerical simulation of the aqueous humor flow in the eye drainage system; a healthy and pathological condition comparison. Medical engineering & physics, 83, pp.82-92.

Sheybani, A. 2023, *Uveitic Glaucoma - EyeWiki*, Eyewiki.org, viewed 19 August 2024, <https://eyewiki.org/Uveitic_Glaucoma>.

SimScale, 2018, *What is CFD | Computational Fluid Dynamics?*, SimScale, viewed 2 April 2024, <https://www.simscale.com/docs/simwiki/cfd-computational-fluid-dynamics/what-is-cfd-computational-fluid-dynamics/>.

Skalicky, S 2024, *Glaucoma Treatment | Glaucoma SLT Therapy | Dr Simon Skalicky*, www.drsimonskalicky.com.au, Dr. Simon Skalicky, viewed 6 March 2024, <https://www.drsimonskalicky.com.au/glaucoma-specialist/slt-the-gentle-glaucoma-therapy/>.

Sng, C. 2022, *Dr. Chelvin Sng: Why Paul Glaucoma Implant is changing the future of Glaucoma*, Chelvin Sng Eye Center | Glaucoma | Cataract | Retina Specialist Singapore, Chelvin Sng Eye Center, viewed 2 April 2024, <https://www.drchelvinsng.com/dr-chelvin-sng-why-the-paul-glaucoma-implant-is-changing-the-future-of-glaucoma/#:~:text=In%202012%2C%20my%20colleague%20Professor>.

Soebijantoro, I. and Noor, N.A. 2020, 'Tube Length Adjustment and Tube Trimming Technique in Refractory Glaucoma', *Case Reports in Ophthalmological Medicine*, 2020, pp. 1–6.

Stay, M.S., Pan, T, J., Brown, D., Ziaie, B. and Barocas, V.H. 2005, 'Thin-Film Coupled Fluid-Solid Analysis of Flow Through the Ahmed™ Glaucoma Drainage Device', *Journal of Biomechanical Engineering*, vol. 127, ASM International, no. 5, pp. 776–781.

Tencom Ltd., 2023, *Computational Fluid Dynamics (CFD) in Product Design: Incorporating FRP*, Tencom.com, Tencom Ltd., viewed 1 June 2024, <https://www.tencom.com/blog/computational-fluid-dynamics-cfd-in-product-design-incorporating-frp>.

Villamarin, A., Roy, S., Hasballa, R., Vardoulis, O., Reymond, P., and Stergiopulos, N. 2012, '3D simulation of the aqueous flow in the human eye', *Medical Engineering & Physics*, vol. 34, Elsevier BV, no. 10, pp. 1462–1470.

Wang, Q., Thau, A., Levin, A.V. and Lee, D.J. 2019, 'Ocular hypotony: A Comprehensive Review', *Survey of Ophthalmology*, vol. 64, Elsevier BV, no. 5, pp. 619–638.

Wittenberg, M. and Gilbert-Kawai, E. 2014, *Hagen–Poiseuille equation (and laminar flow)*, Cambridge University Press, Cambridge University Press, Cambridge, pp. 19–20, viewed 2 April 2024, <https://www.cambridge.org/core/books/abs/essential-equations-for-anaesthesia/hagenpoiseuille-equation-and-laminar-flow/002FAC2F4EB3F9C1592A3FE5782C2A20>

Appendix A – Project Specification

Date: 12/02/2024

Title: Optimisation of Glaucoma Drainage Devices through Solid Modelling and CFD Flow Behaviour

Name: James O'Neill

Student ID: [redacted]

Supervisors: Steven Goh, Zahra Faraji Rad

Introduction and Background:

Glaucoma is a slowly developing eye disease that causes sudden vision loss for people of all ages. This disease, which is one of the world's leading causes of blindness (Gupta, S. and Jeria, S. 2022), causes a rise in intra-ocular pressure (IOP) due to a build-up of aqueous humour fluid within the eye. This causes irreversible damage to the optic nerve, resulting in anything from minor damage to complete vision loss, depending on the severity of the case (Cleveland Clinic, 2022).

Glaucoma has been studied extensively throughout the years to develop treatment methods to reduce the effects of this disease. Subsequently, there has been very promising innovation into minimally invasive glaucoma surgeries (MIGS). These surgeries, targeted exclusively at patients with low to mild glaucoma, primarily consist of stent implants that gradually decrease and regulate eye pressure. These implants have several benefits, including reduced recovery time, minimal alteration to natural anatomy, and higher overall safety due to a reduced risk for post operative complications (Gurnani, B. Tripathy, K. 2023).

While there have been constant innovations into MIGS and mild glaucoma treatment options, advancements in technology for more aggressive and developed cases of glaucoma have stalled in the last few decades. The primary existing technology for these cases is the implementation of a glaucoma drainage device (GDD). These devices are reserved for patients who experience optic nerve damage through uncontrolled IOP, despite using maximal glaucoma medication (Kang, Y. Shin, J. Kim, D. 2022). The various types of GDDs currently available all share similarities with the initial Molteno implant, first tested in 1969 (Gupta, S. and Jeria, S. 2022). Subsequent designs, such as the Baerveldt implant, Krupin implant, and the Ahmed glaucoma valve, have not been significantly improved on since the early 1990s (Netland, P.A, and Ashburn, F.S, 2018). While GDDs are a great achievement in the world of medical science, there are many complications that come with their implementation, such as the potential for hypotony, endophthalmitis, extrusion, migration of the plate, and erosion of the mucous membrane, to name a few (Gupta, S. and Jeria, S. 2022).

This serves as the basis to the importance of this research project, as by using modern computational fluid dynamics software to analyse and optimise current GDD designs, there is the possibility of finding improvements in GDD technology.

Objectives and Aims:

The primary objective of this research project is to use Computational Fluid Dynamics (CFD) software to both understand, and potentially improve on, how glaucoma drainage devices effect aqueous humour fluid flow within the human eye.

Specific Objectives:

- 3D model an optimised glaucoma drainage device in accordance with research from the literature review.
- Perform CFD analysis on this device and analyse the results.
- Draw conclusions by comparing the findings to current glaucoma drainage devices.

Expected Outcomes:

- Assess the validity of using CFD software in GDD applications.
- Increased understanding into what factors influence GDD effectiveness.
- Provide research on an optimised GDD design through the CFD results.

Work Plan:

Initial Gantt Chart Plan (from ENG4110 – Engineering Research Methodology):

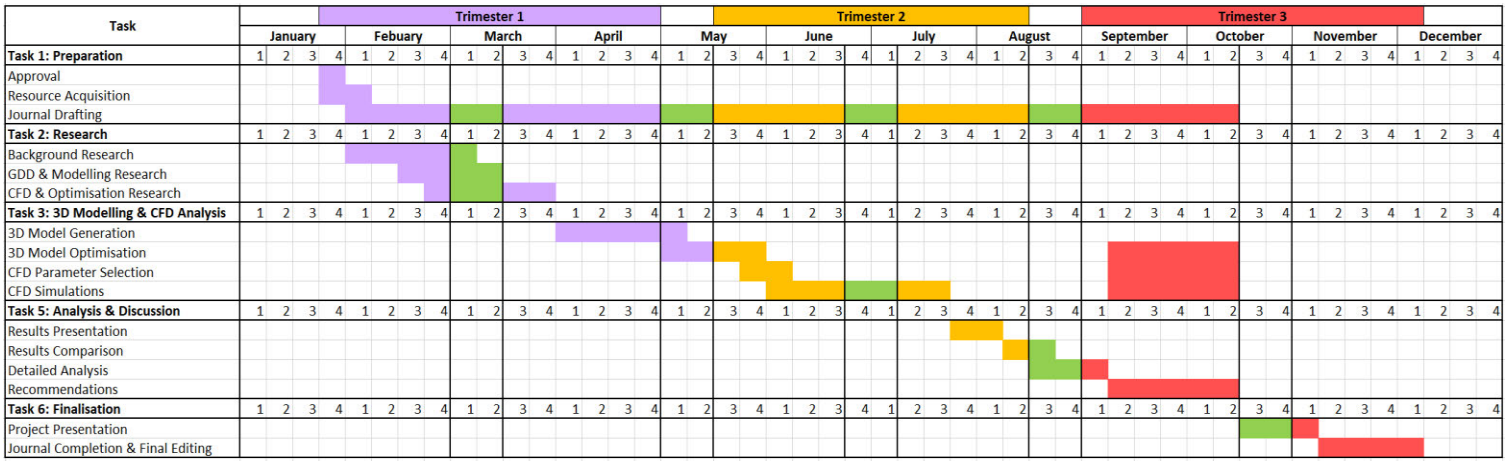

Timeline:

- **Month 1: Project Proposal and Initiation**
  - Develop the work plan, initiate background research, and clarify research project objectives.
- **Months 2-3: Literature Review, Initiate Solid Modelling and CFD Analysis**
  - Conduct an in-depth literature review on current glaucoma drainage devices, possible improvements, previous studies and applicable CFD techniques and parameters to be used in the analysis.
  - Initiate the modelling and optimisation stage.
- **Months 4-6: CFD Simulations and Optimisation**
  - Fully develop the models, run CFD simulations, and attempt to optimise the design through the findings.
- **Months 7-8: Results Analysis**
  - Finalise CFD simulations.
  - Report, analyse, and compare the results of the optimised design.
  - Draw conclusions about the effectiveness of the design and the use of CFD in this application.

- **Months 9: Report Writing**
    - Compile findings into a final report. Discern the key features that had the most impact on the GDD design, with reference to the CFD results.
- **Month 10: Finalization and Presentation**
    - Review and finalize the report.
    - Prepare the presentation, summarizing all key findings, CFD results and further recommendations.

Resources:

- **Equipment:**
    - Computer laboratories available at the university
- **Software:**
    - Microsoft Office for journal drafting, calculations, etc.
    - Ansys Student for CFD analysis, available both for download and on the university campus computers
    - Creo for modelling, available through UniSQ Turbo and on the university campus computers
- **Access:**
    - Access the university library resources and online databases for literature review.

References:

Cleveland Clinic, 2022. Glaucoma: Symptoms, causes, types & treatment. [online] Cleveland Clinic. Available at: <https://my.clevelandclinic.org/health/diseases/4212-glaucoma> [Accessed 8 Feb. 2024].

Gupta, S., and Jeria, S., 2022. A review on glaucoma drainage devices and its complications. Cureus.

Gurnani, B., and Tripathy, K., 2023. Minimally invasive glaucoma surgery. [online] National Library of Medicine. Available at: <https://www.ncbi.nlm.nih.gov/books/NBK582156/> [Accessed 8 Feb. 2024].

Kang, Y.K.,, Shin, J.P., and Kim, D.W., 2022. Long-term surgical outcomes of Ahmed valve implantation in refractory glaucoma according to the type of glaucoma. BMC Ophthalmology, 22(1).

Netland, P.A., and Ashburn, F.S., 2018. The evolution of glaucoma drainage implants. Journal of Ophthalmic and Vision Research, 13(4), p.498.

Appendix B – Risk Assessment

6038	RISK DESCRIPTION	STATUS	TREND	CURRENT	RESIDUAL
	Final Year Research Project	Live		High	Medium

RISK OWNER	RISK IDENTIFIED ON	LAST REVIEWED ON	NEXT SCHEDULED REVIEW
James O'Neill	22/10/2024	22/10/2024	22/01/2025

THIS IS A RESTRICTED RISK ASSESSMENT
My thesis has not been finalised yet, and while there is no confidential information, I am unsure of the proper practice in this regard.

RISK FACTOR(S)	EXISTING CONTROL(S)	CURRENT	PROPOSED CONTROL(S)	TREATMENT OWNER	DUE DATE	RESIDUAL
Car accident travelling to the University	Control: Inbuilt car safety features, engineering controls (road rules etc.), law enforcement controls	High	Ensuring I am driving while fully concentrated and fully rested, ensuring vehicle is regularly serviced and up to safety standards (brake checks, etc.)		22/10/2024	Medium
Bad posture causing back pain and other health complications leading to long term health effects	Control: Regular breaks, Ergonomic chair	High	Massage equipment to reduce any prevent pain		22/10/2024	Medium
Tiredness, frustration, reduced efficiency, reduced mental health	Control: Regular breaks, outlet activities	High	Scheduled activities to force break		22/10/2024	Medium
Dehydration - Headaches, delirium leading to serious personal injury/death	Control: Water bottles, regular breaks	Medium	Electrolyte tablets to ensure hydration		22/10/2024	Low
Eye strain - from blue light/monitors leading permanent eye damage	Control: Night mode to reduce blue light, regular breaks, correct monitor positioning	Medium	Ergonomics research to determine optimal placement of monitor screens		22/10/2024	Low
Modelling/CFD Software Failure - potential complete loss of work, reduced efficiency	Control: Software backups, file backup Control: Additional hard drive backups to have an external copy of all simulations and models	Low				Very Low
Power Outage - Reduced efficiency due to WiFi outage, potential loss of work	Control: Existing electrical protection	Low	Additional surge protectors			Very Low

Computer Failure - Potential complete loss of work, reduced efficiency	Control: OneDrive/Cloud backups	Low	Additional hard drive backups to have an external copy of all work completed			Very Low

ATTACHMENTS
RMP_Offline Version.docx

Appendix C – Additional CFD Simulation Plots

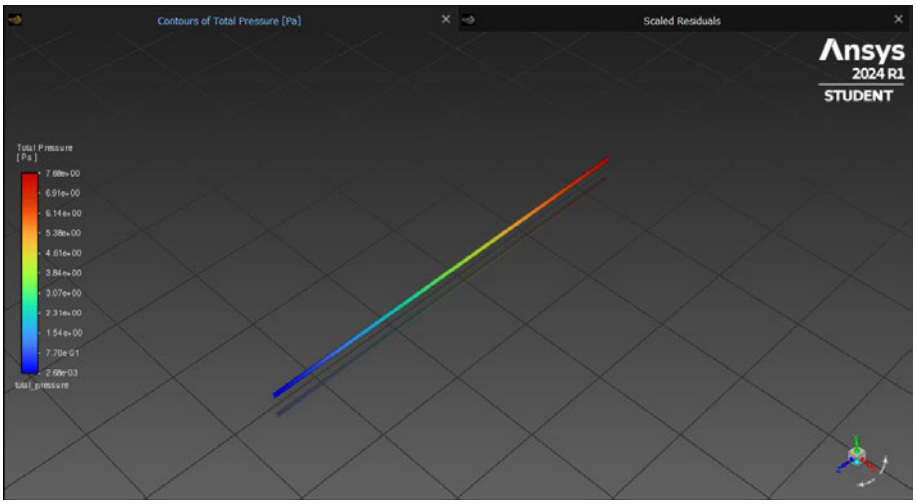

Figure C.1: Baerveldt Standard Tube 5µL/min Pressure Contour Plot

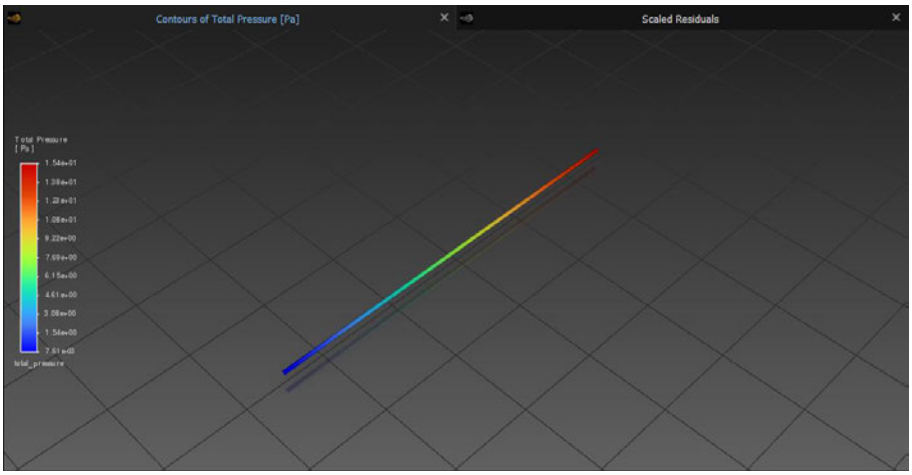

Figure C.2: Baerveldt Standard Tube 10µL/min Pressure Contour Plot

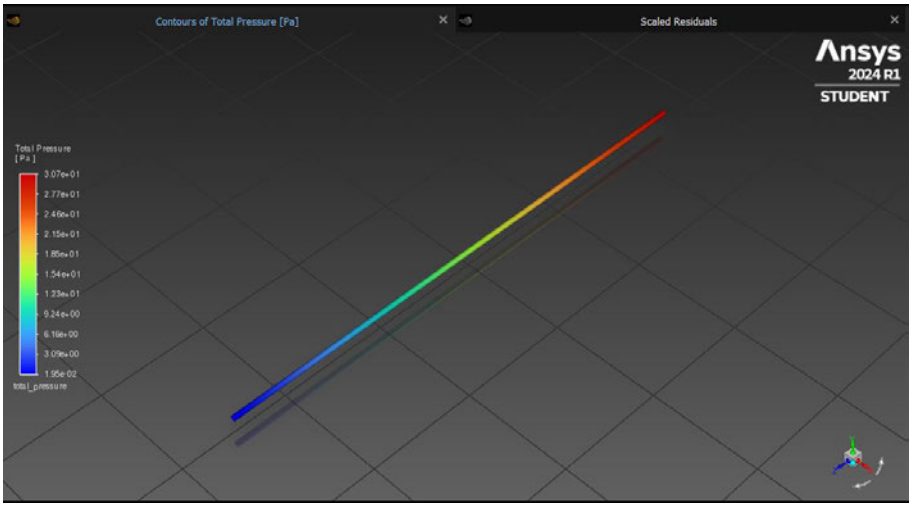

Figure C.3: Baerveldt Standard Tube 20µL/min Pressure Contour Plot

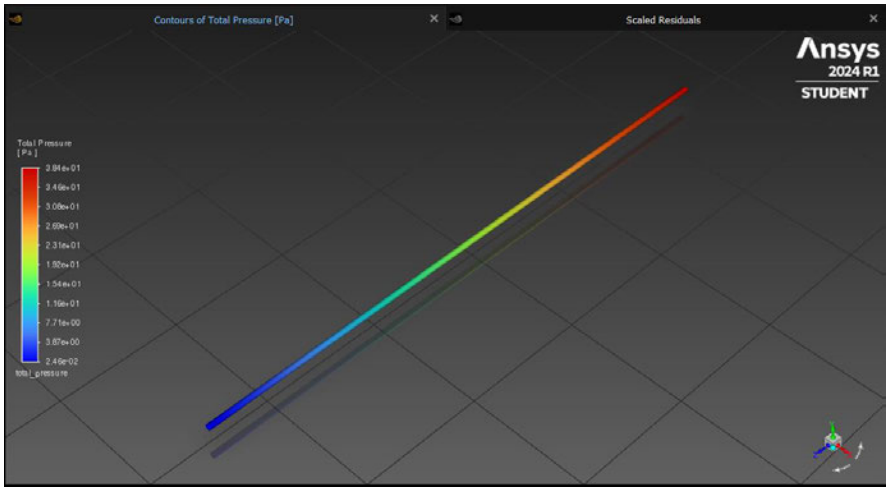

Figure C.4: Baerveldt Standard Tube 25µL/min Pressure Contour Plot

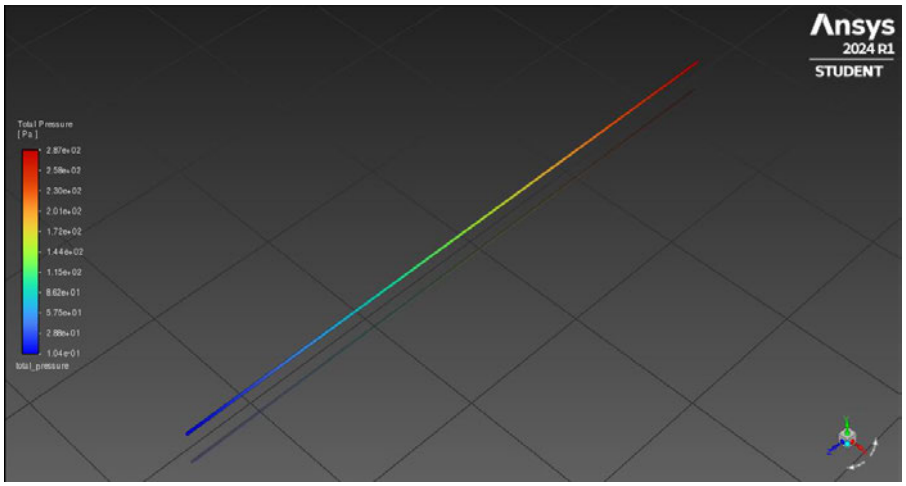

Figure C.5: Paul Standard Tube 5µL/min Pressure Contour Plot

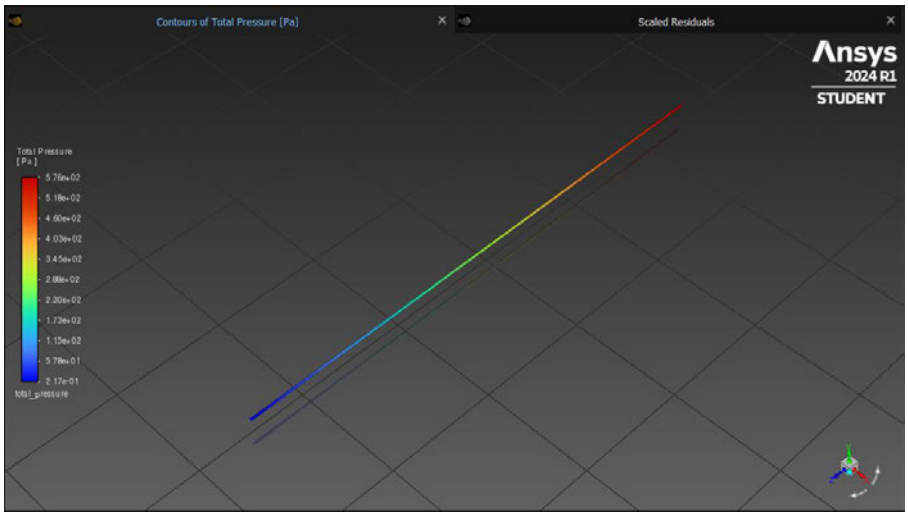

Figure C.6: Paul Standard Tube 10µL/min Pressure Contour Plot

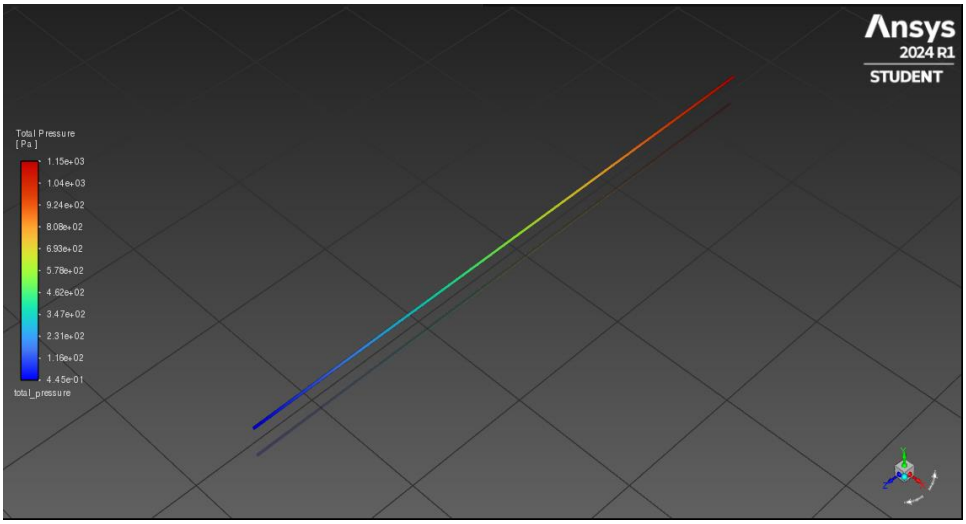

Figure C.7: Paul Standard Tube 20µL/min Pressure Contour Plot

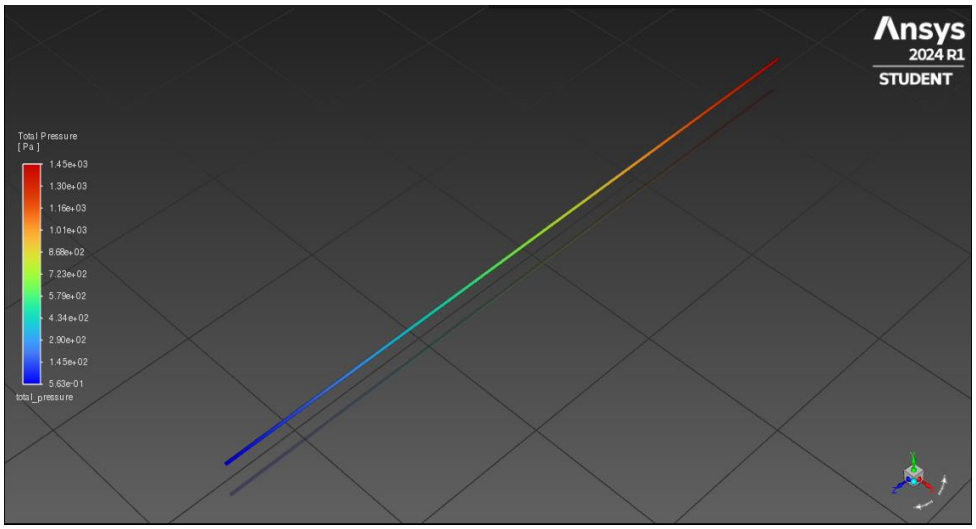

Figure C.8: Paul Standard Tube 25µL/min Pressure Contour Plot

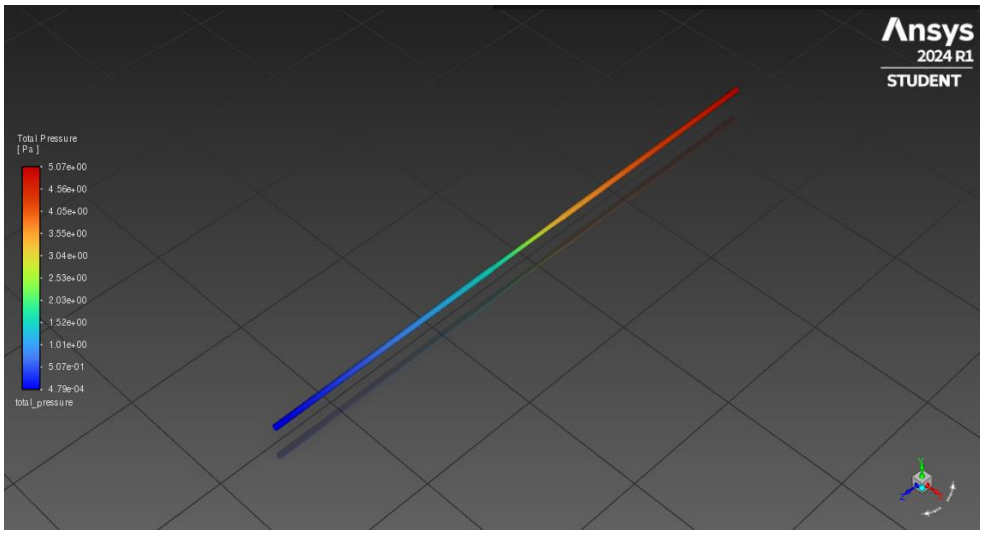

Figure C.9: Baerveldt Sutured Tube 5µL/min Pressure Contour Plot

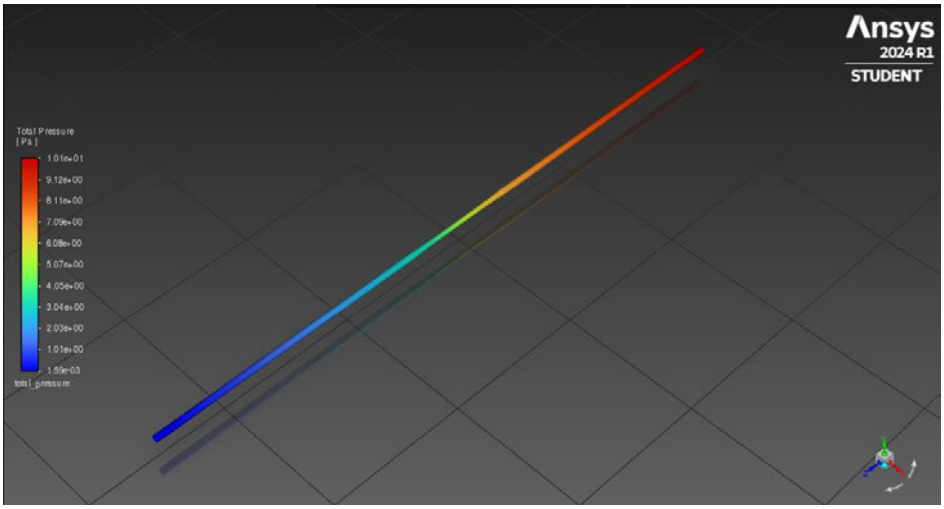

Figure C.10: Baerveldt Sutured Tube 10µL/min Pressure Contour Plot

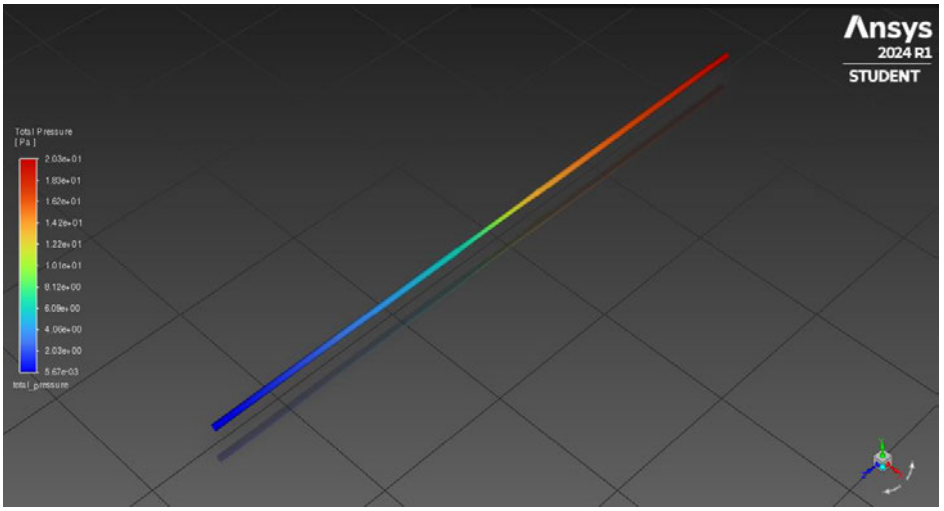

Figure C.11: Baerveldt Sutured Tube 20µL/min Pressure Contour Plot

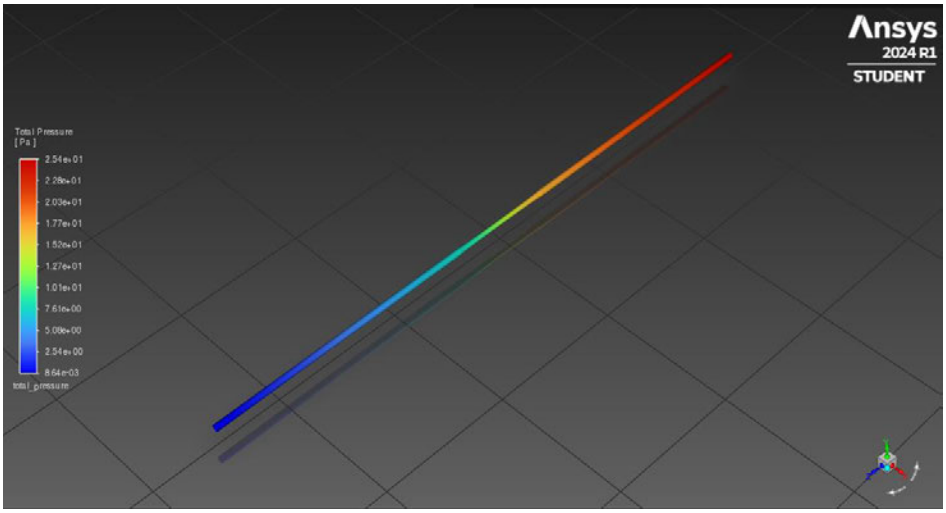

Figure C.12: Baerveldt Sutured Tube 25µL/min Pressure Contour Plot

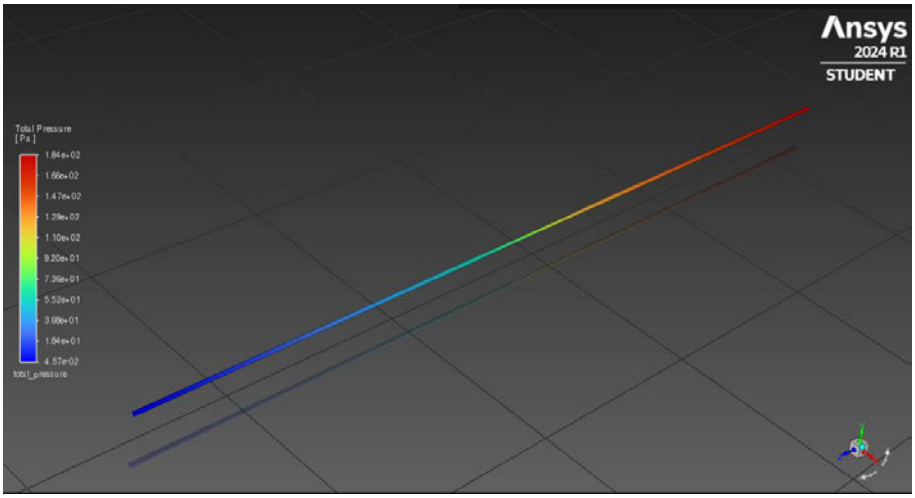

Figure C.13: Paul Sutured Tube 5µL/min Pressure Contour Plot

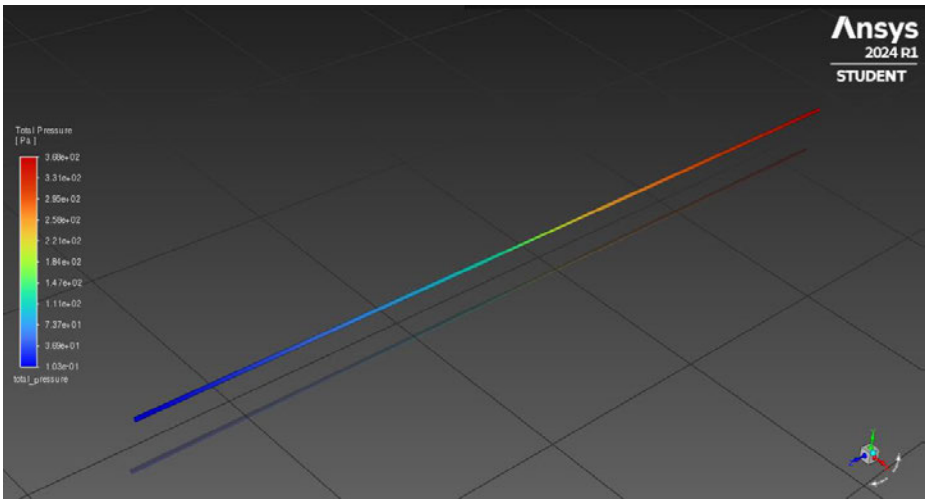

Figure C.14: Paul Sutured Tube 10µL/min Pressure Contour Plot

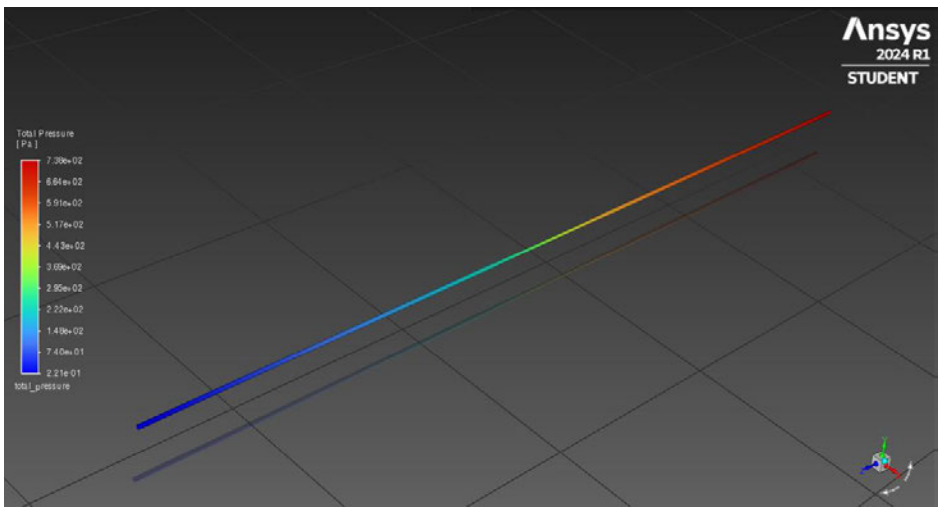

Figure C.15: Paul Sutured Tube 20µL/min Pressure Contour Plot

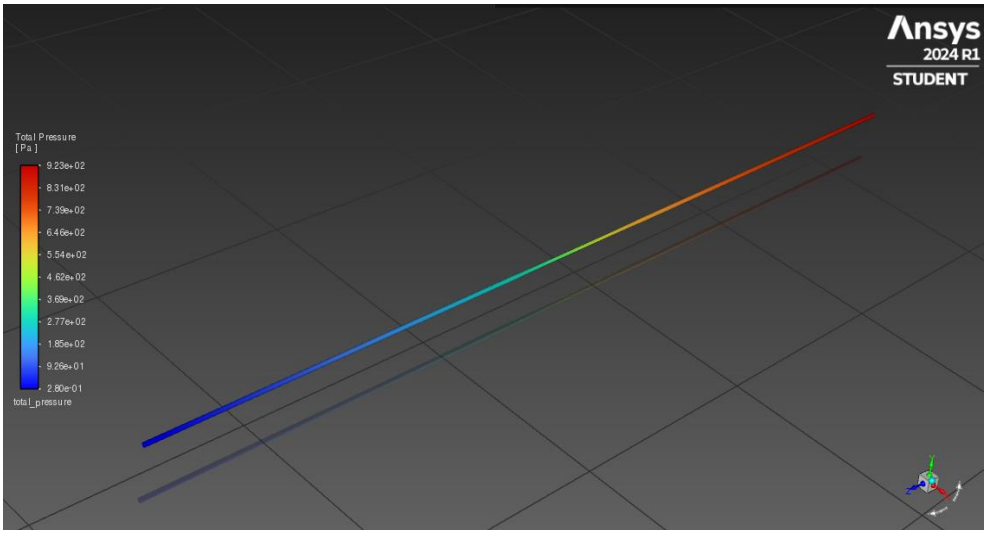

Figure C.16: Paul Sutured Tube 25µL/min Pressure Contour Plot

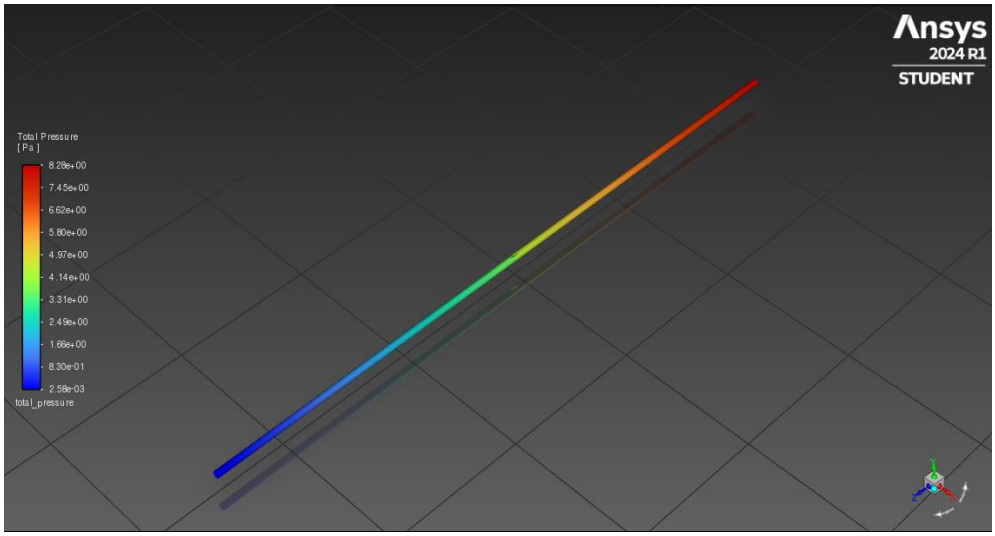

Figure C.17: Baerveldt Single Fin Tube 5µL/min Pressure Contour Plot

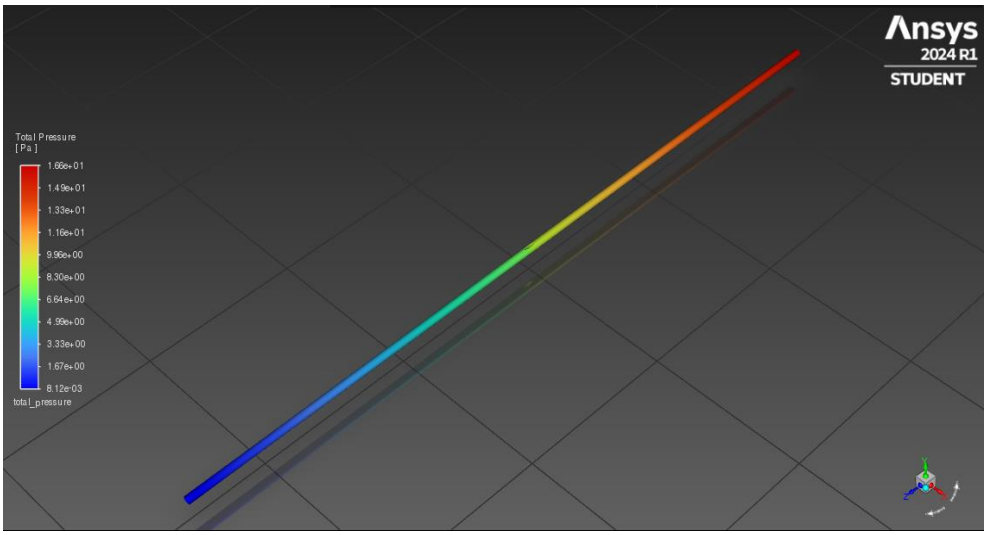

Figure C.18: Baerveldt Single Fin Tube 10µL/min Pressure Contour Plot

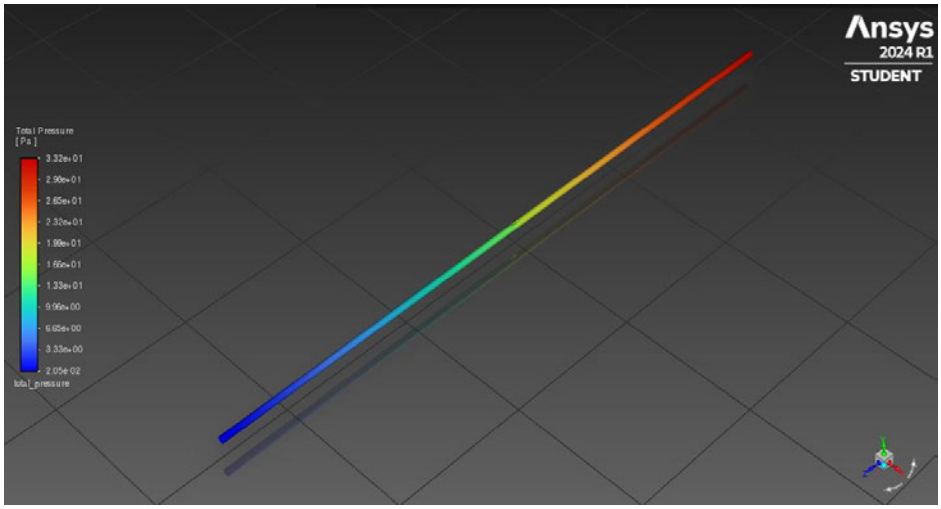

Figure C.19: Baerveldt Single Fin Tube 20µL/min Pressure Contour Plot

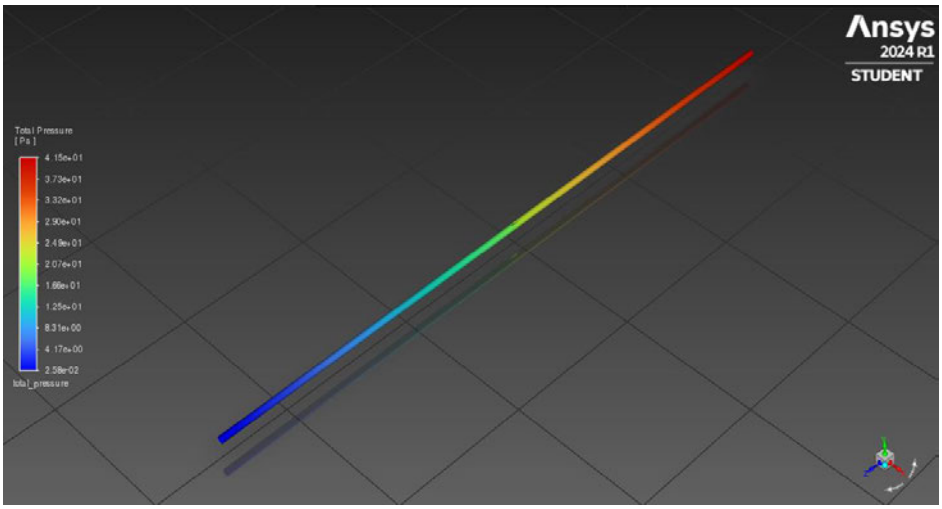

Figure C.20: Baerveldt Single Fin Tube 25µL/min Pressure Contour Plot

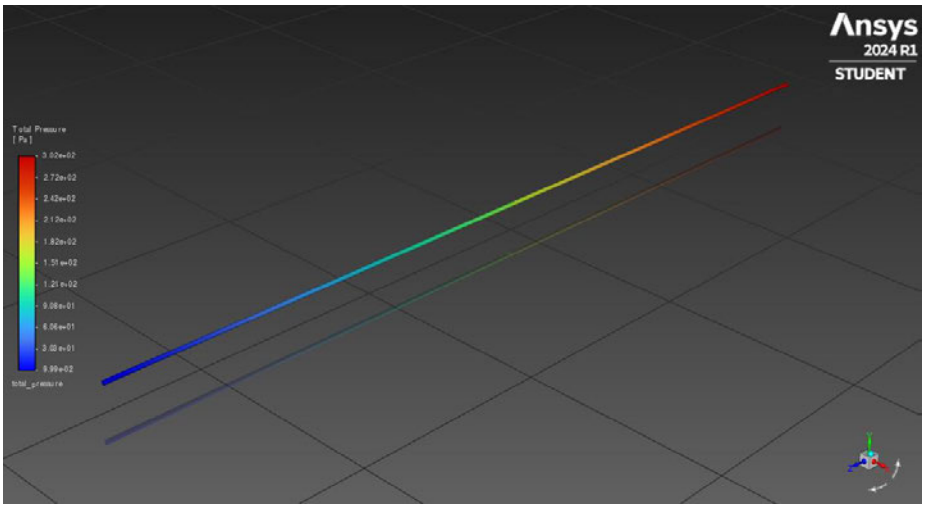

Figure C.21: Paul Single Fin Tube 5µL/min Pressure Contour Plot

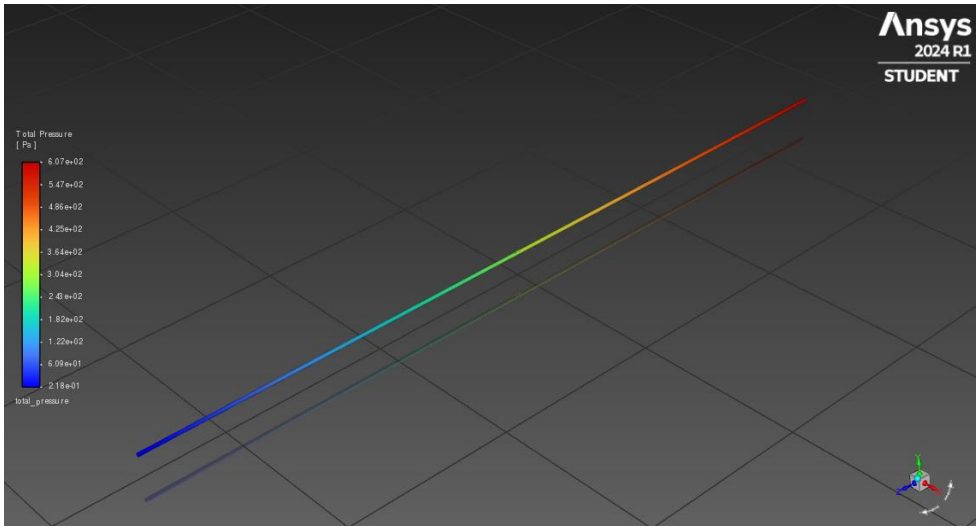

Figure C.22: Paul Single Fin Tube 10µL/min Pressure Contour Plot

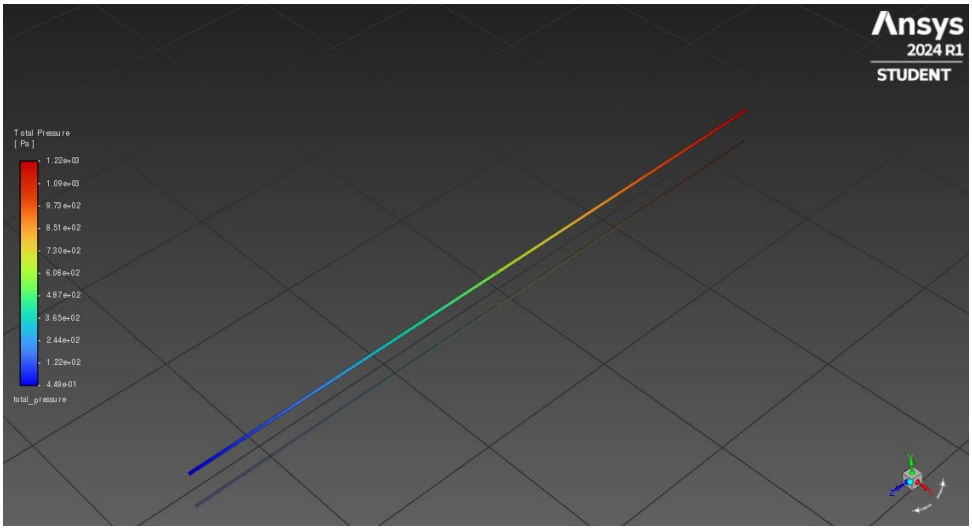

Figure C.23: Paul Single Fin Tube 20µL/min Pressure Contour Plot

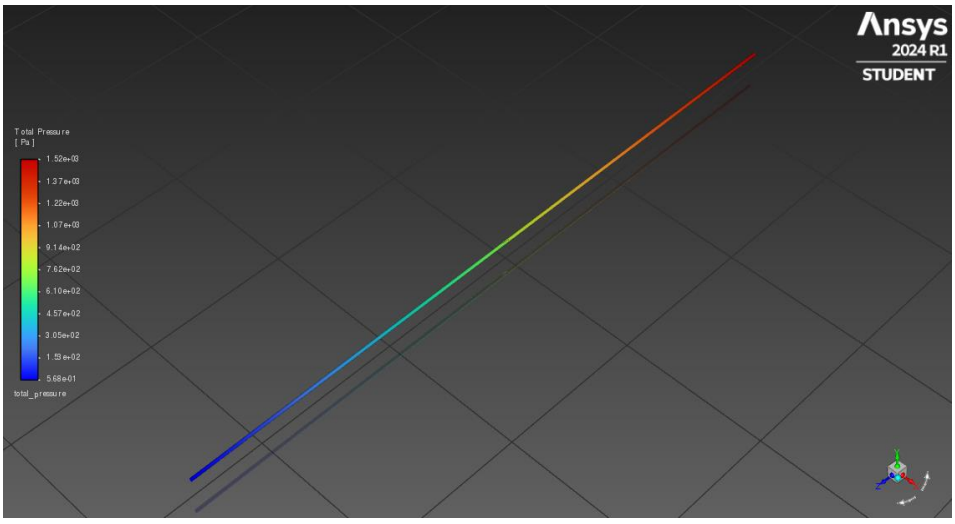

Figure C.24: Paul Single Fin Tube 25µL/min Pressure Contour Plot

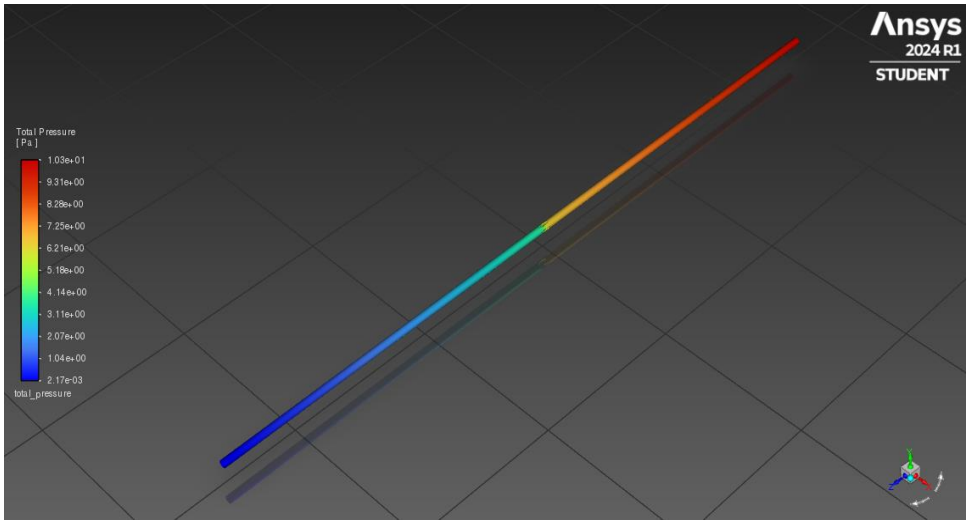

Figure C.25: Baerveldt Double Fin Tube 5µL/min Pressure Contour Plot

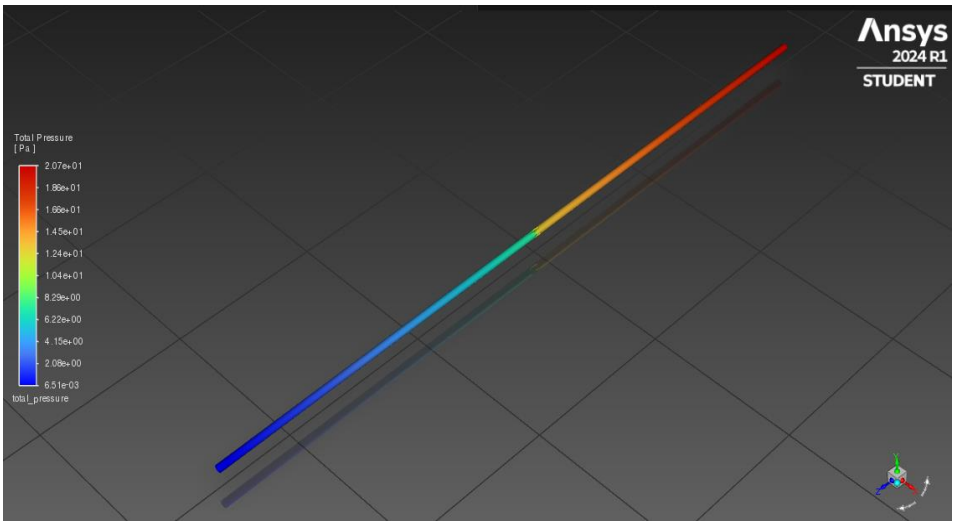

Figure C.26: Baerveldt Double Fin Tube 10µL/min Pressure Contour Plot

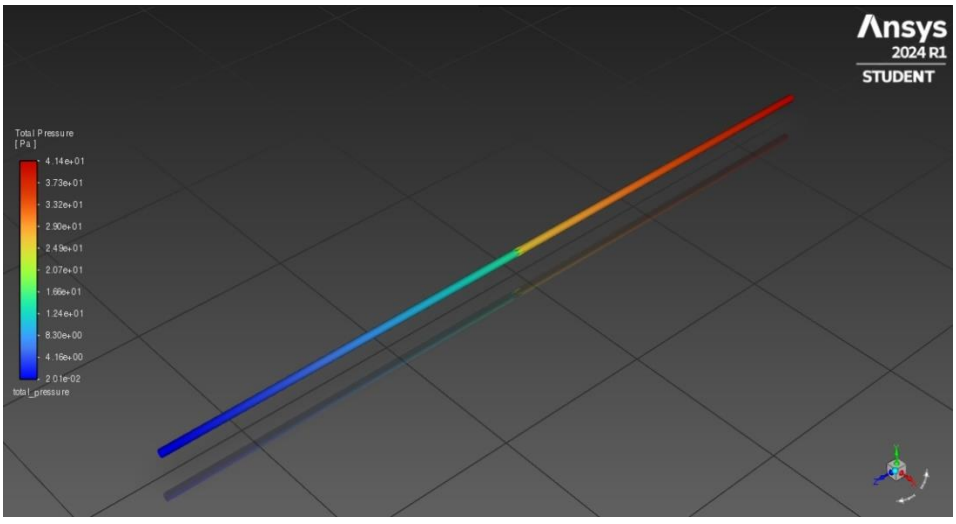

Figure C.27: Baerveldt Double Fin Tube 20µL/min Pressure Contour Plot

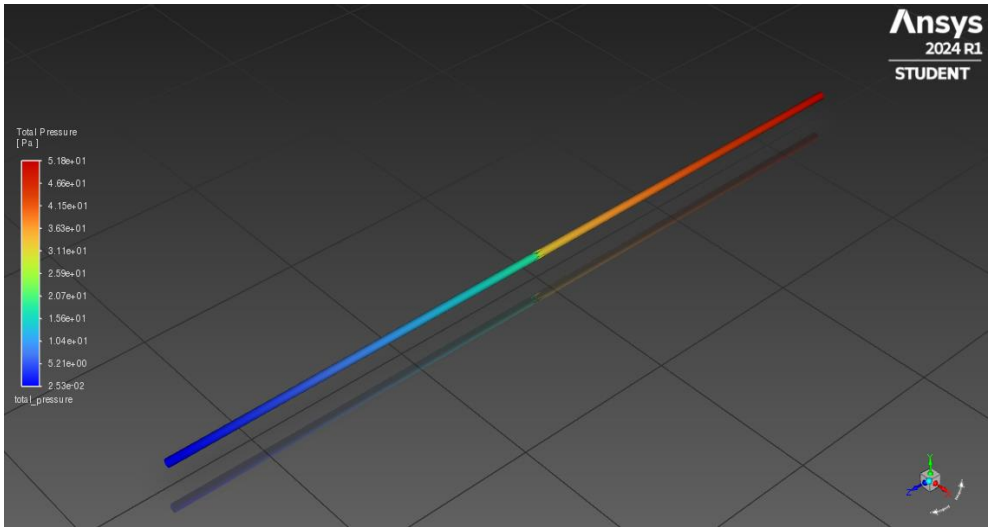

Figure C.28: Baerveldt Double Fin Tube 25µL/min Pressure Contour Plot

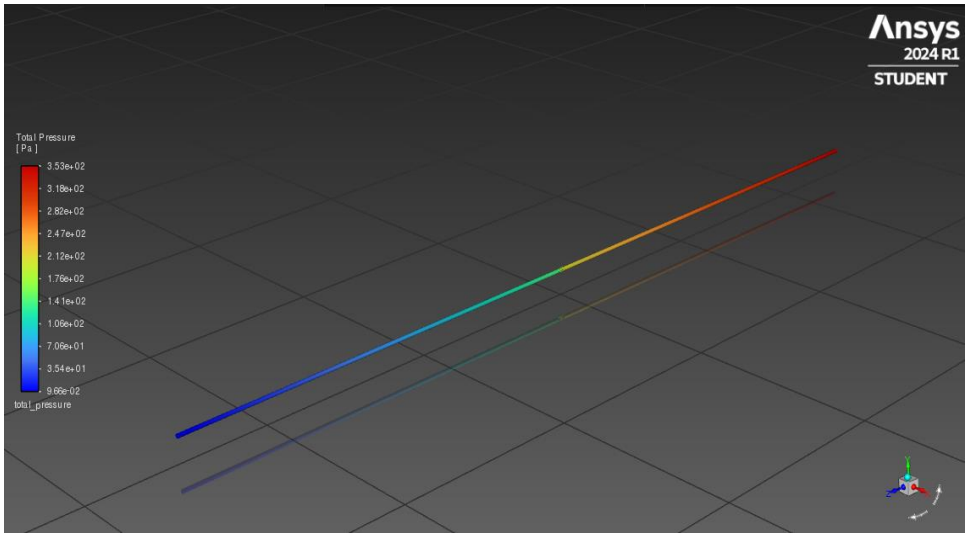

Figure C.29: Paul Double Fin Tube 5µL/min Pressure Contour Plot

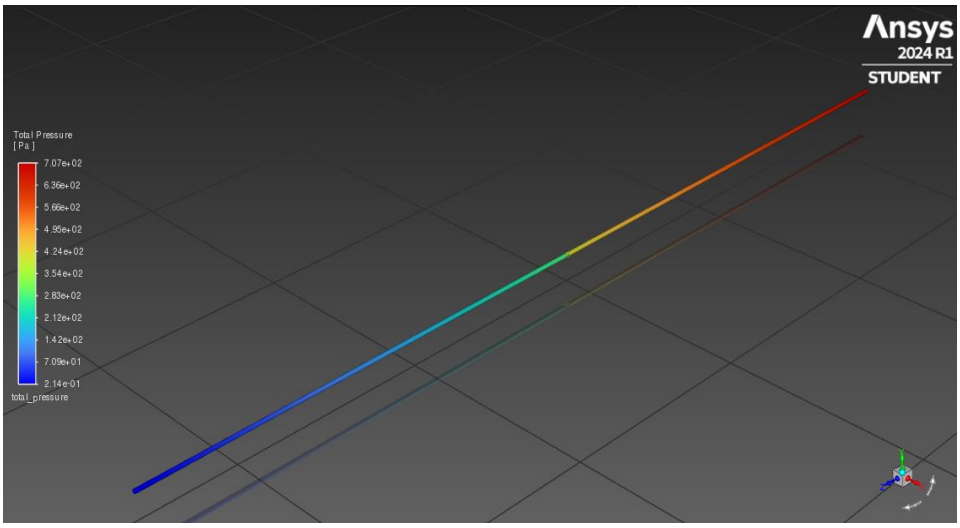

Figure C.30: Paul Double Fin Tube 10µL/min Pressure Contour Plot

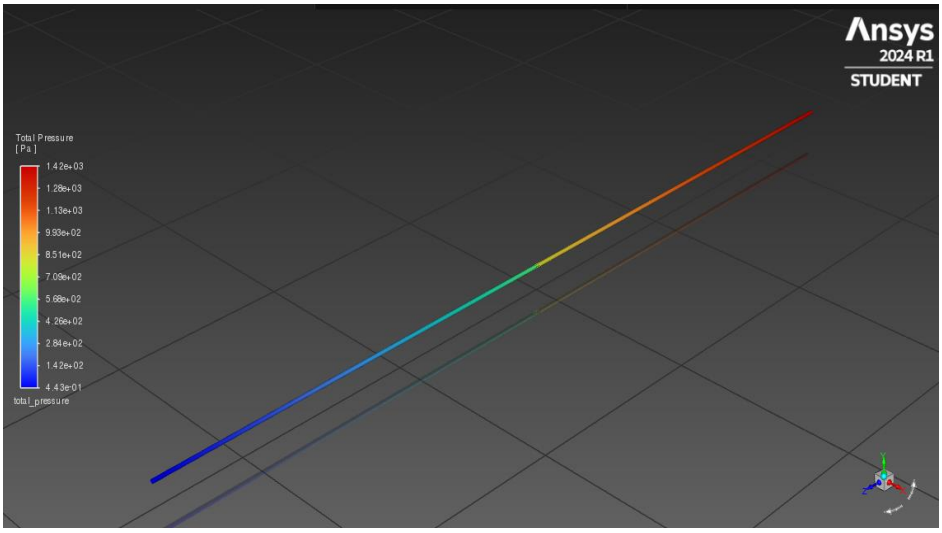

Figure C.31: Paul Double Fin Tube 20µL/min Pressure Contour Plot

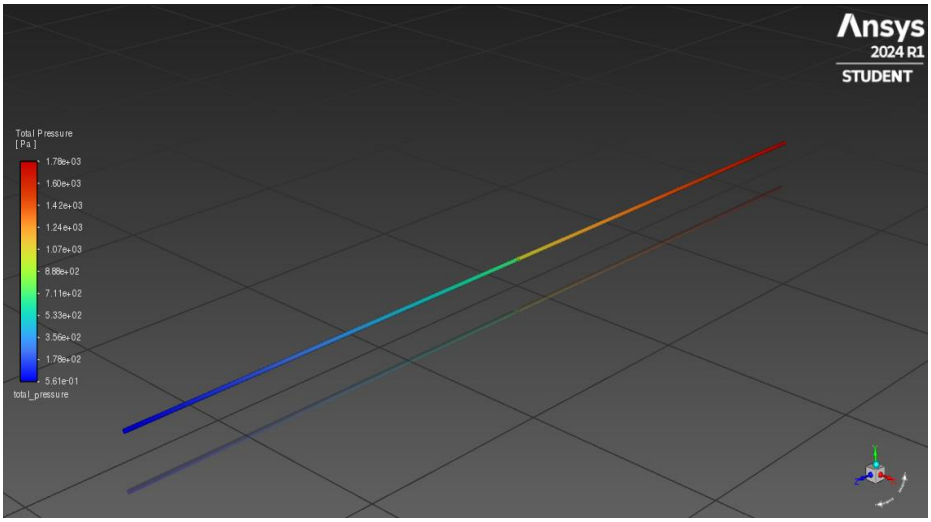

Figure C.32: Paul Double Fin Tube 25µL/min Pressure Contour Plot

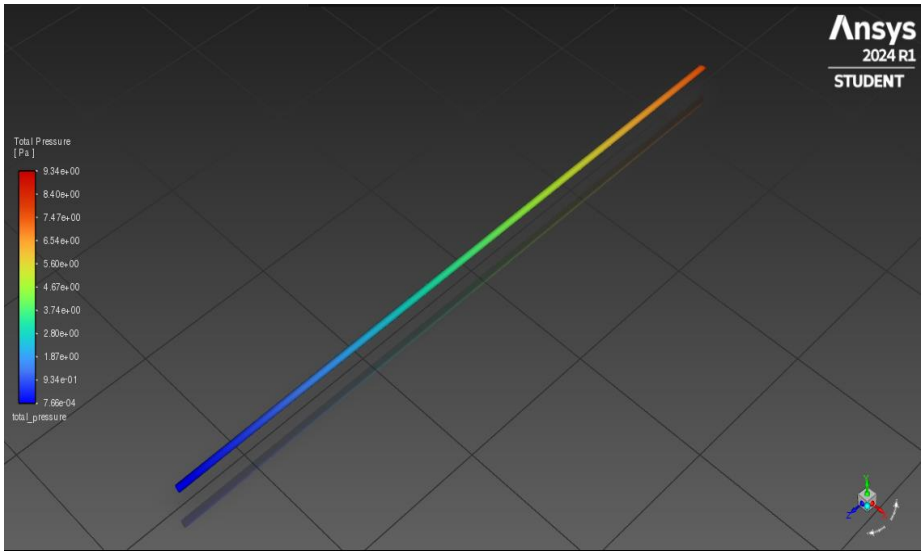

Figure C.33: Baerveldt Snipped Tube 5µL/min Pressure Contour Plot

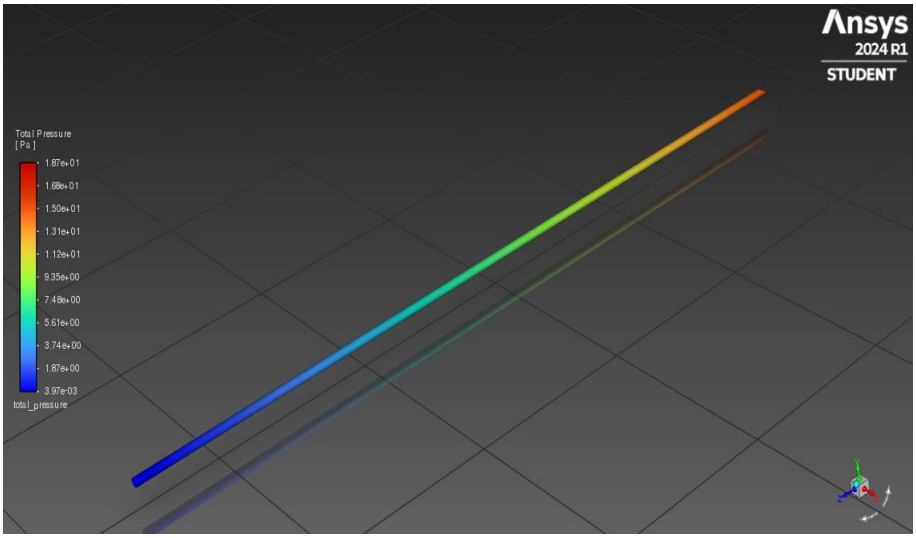

Figure C.34: Baerveldt Snipped Tube 10µL/min Pressure Contour Plot

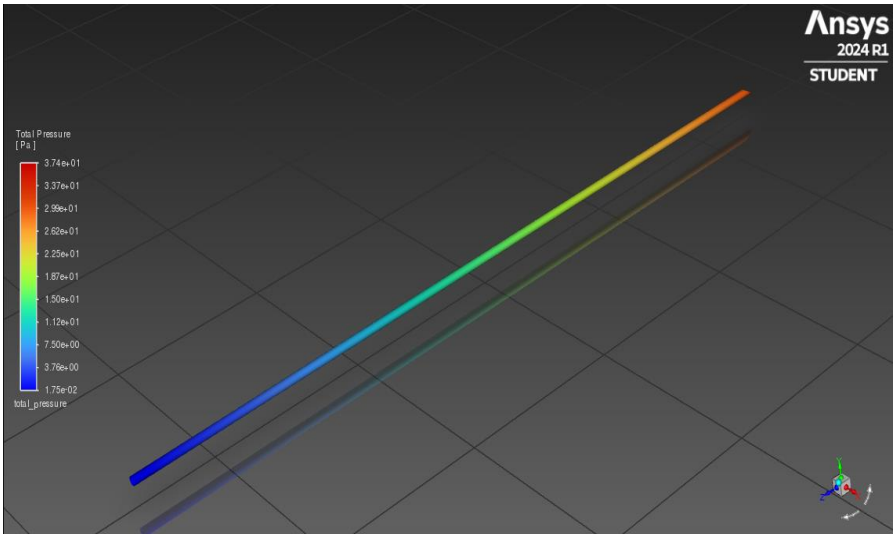

Figure C.35: Baerveldt Snipped Tube 20µL/min Pressure Contour Plot

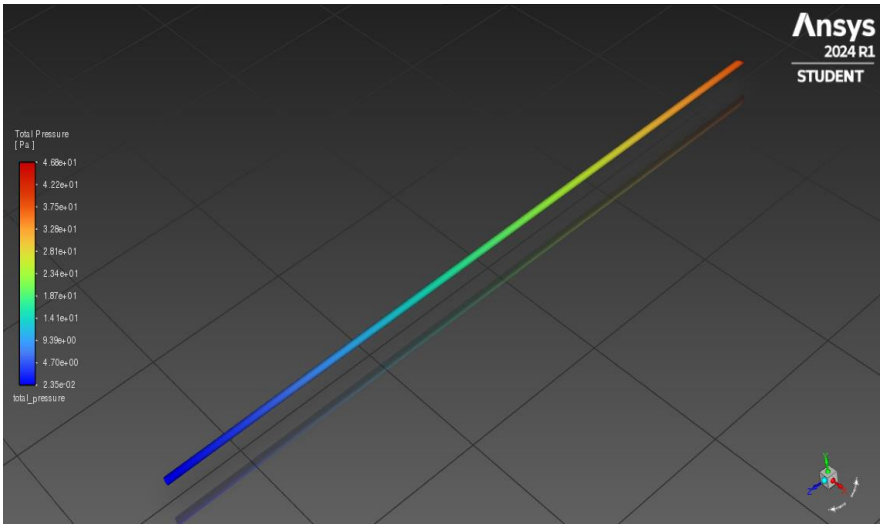

Figure C.36: Baerveldt Snipped Tube 25µL/min Pressure Contour Plot

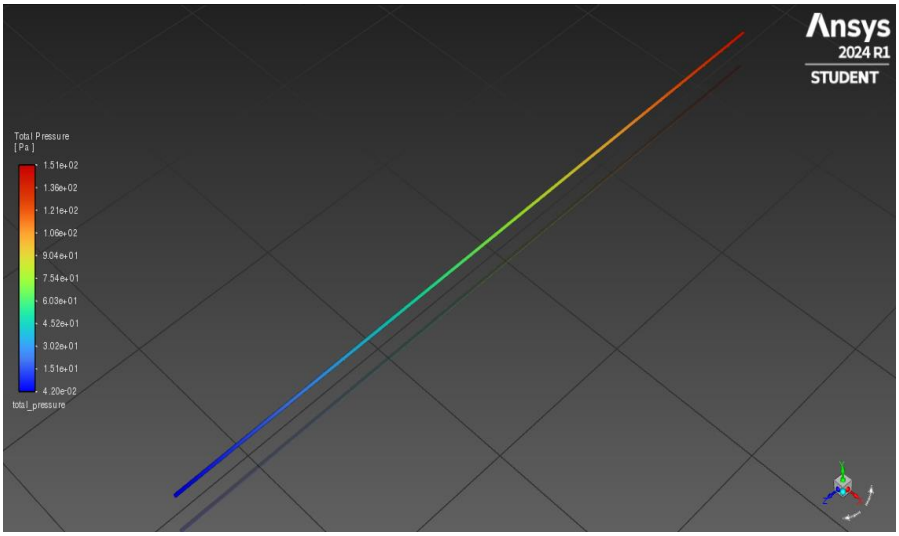

Figure C.37: Paul Snipped Tube 5µL/min Pressure Contour Plot

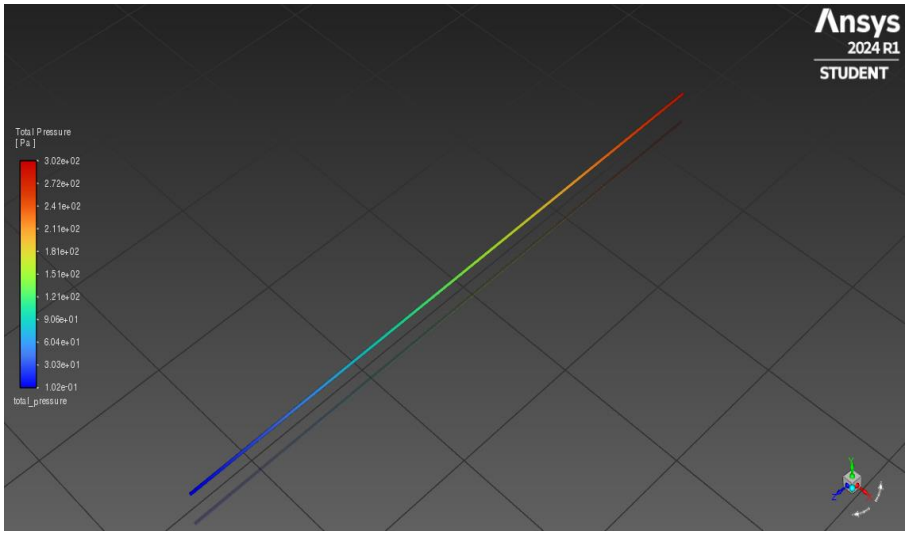

Figure C.38: Paul Snipped Tube 10µL/min Pressure Contour Plot

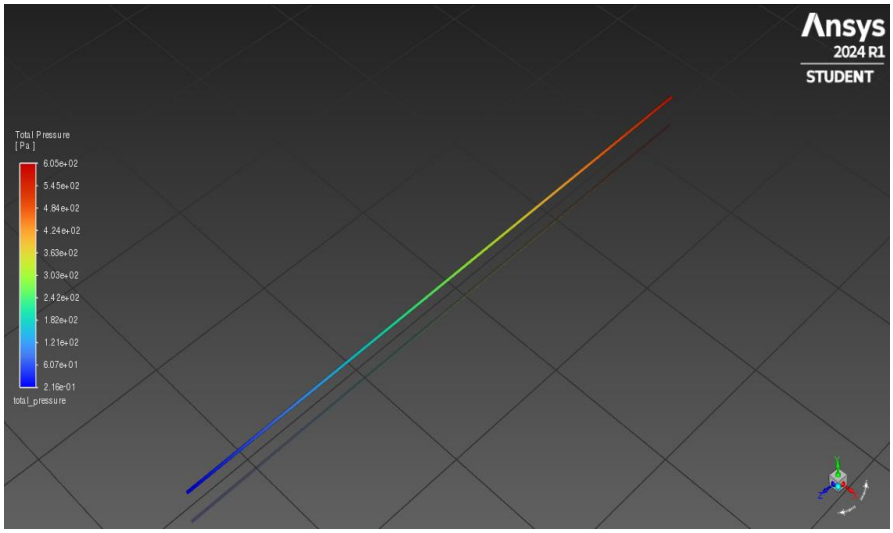

Figure C.39: Paul Snipped Tube 20µL/min Pressure Contour Plot

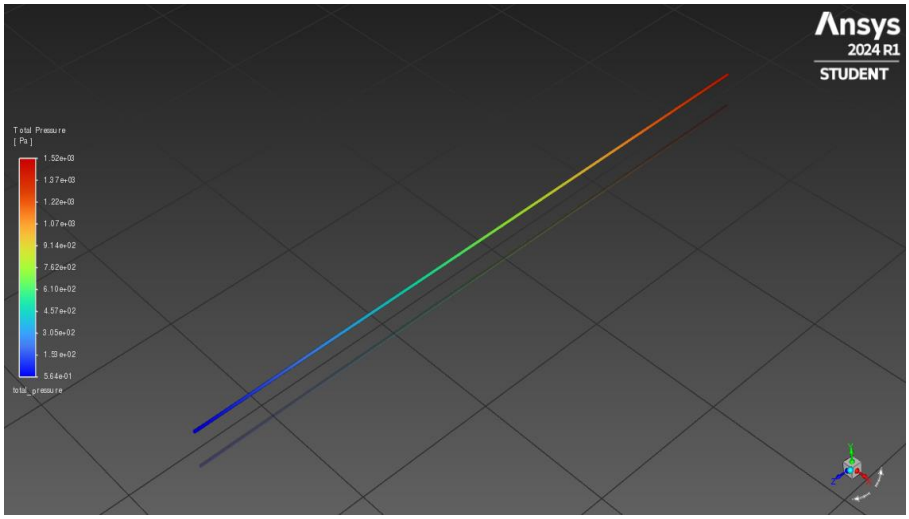

Figure C.40: Paul Snipped Tube 25µL/min Pressure Contour Plot

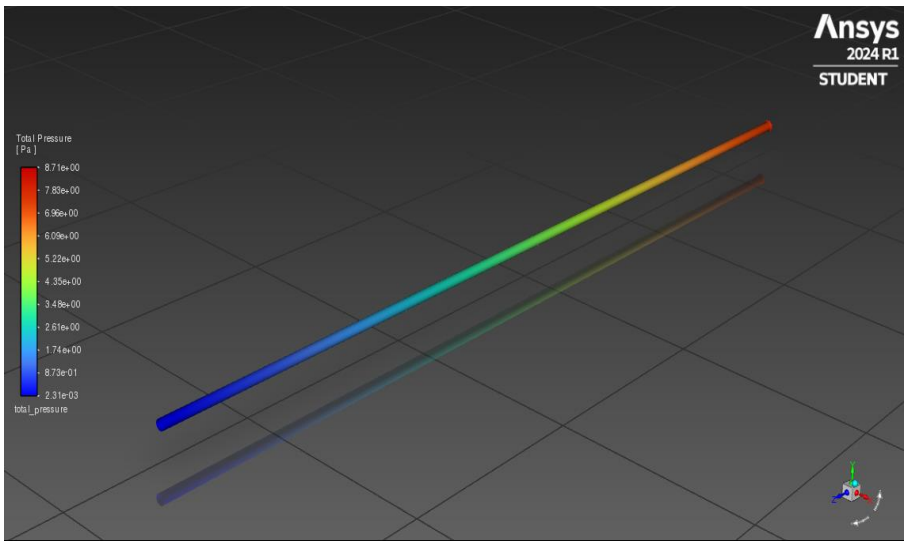

Figure C.41: Baerveldt Rounded Inlet Tube 5µL/min Pressure Contour Plot

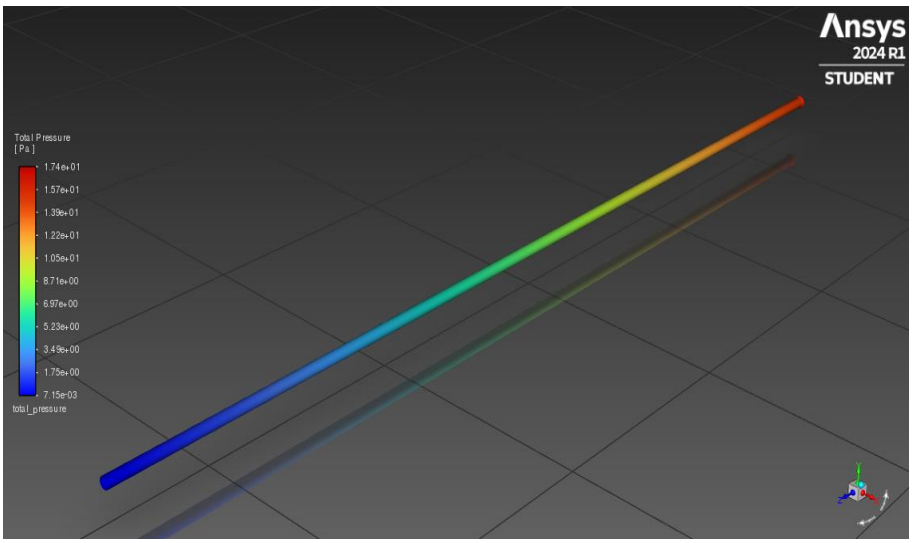

Figure C.42: Baerveldt Rounded Inlet Tube 10µL/min Pressure Contour Plot

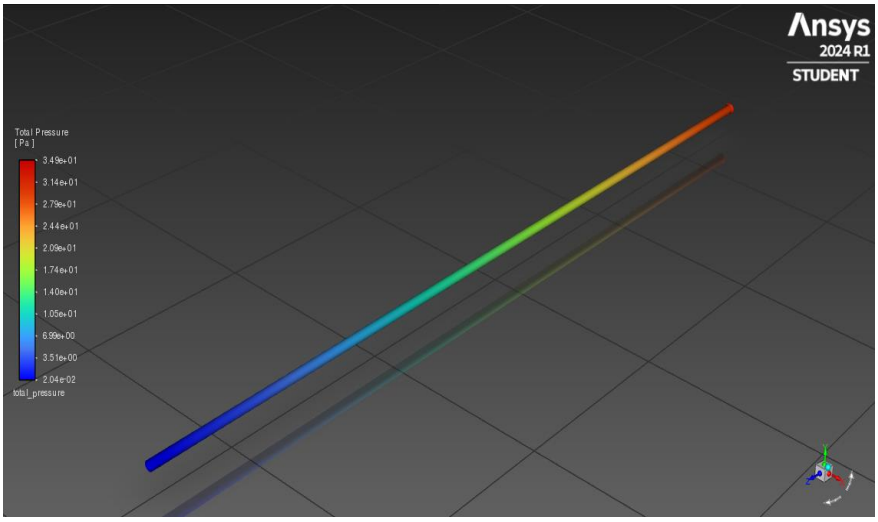

Figure C.43: Baerveldt Rounded Inlet Tube 20µL/min Pressure Contour Plot

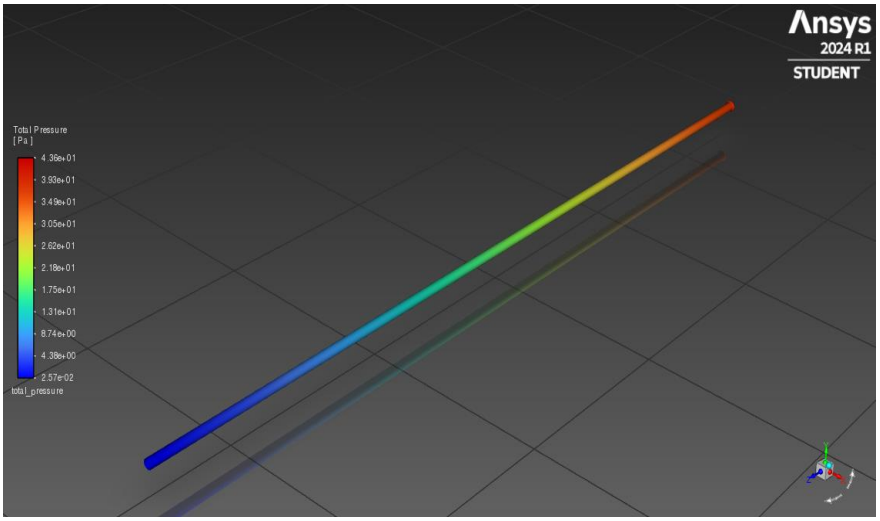

Figure C.44: Baerveldt Rounded Inlet Tube 25µL/min Pressure Contour Plot

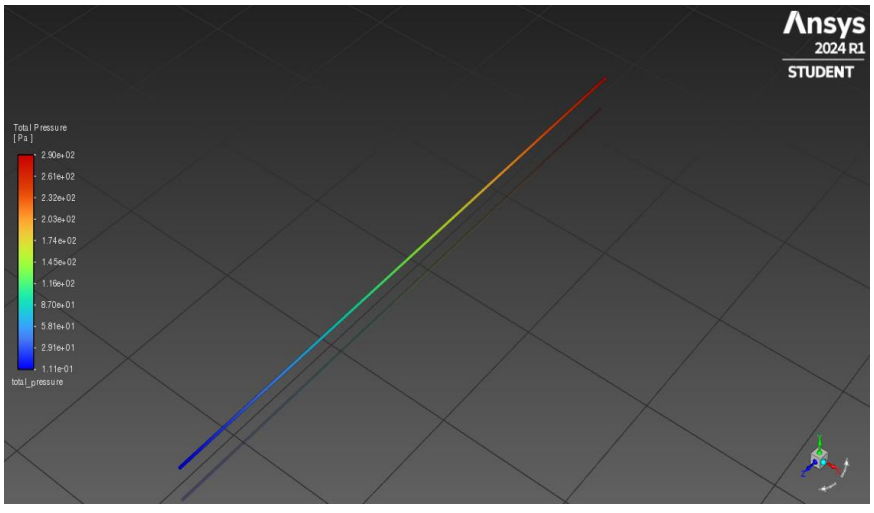

Figure C.45: Paul Rounded Inlet Tube 5µL/min Pressure Contour Plot

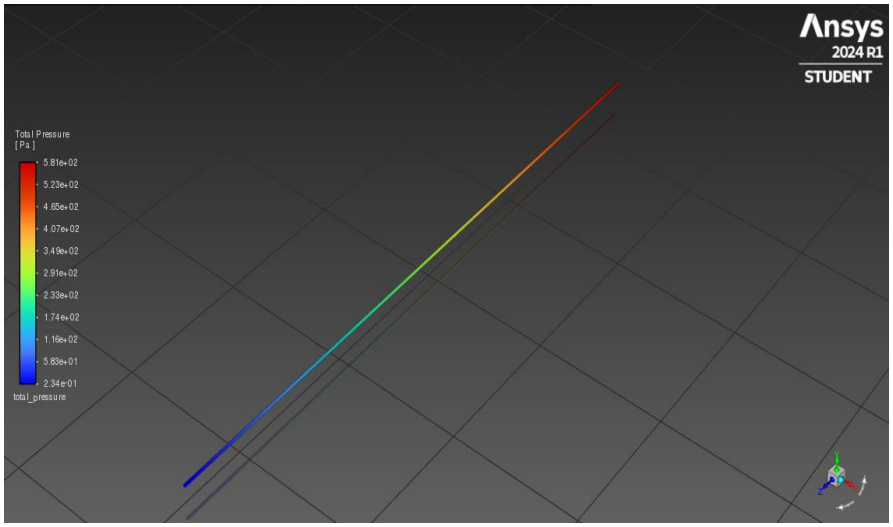

Figure C.46: Paul Rounded Inlet Tube 10µL/min Pressure Contour Plot

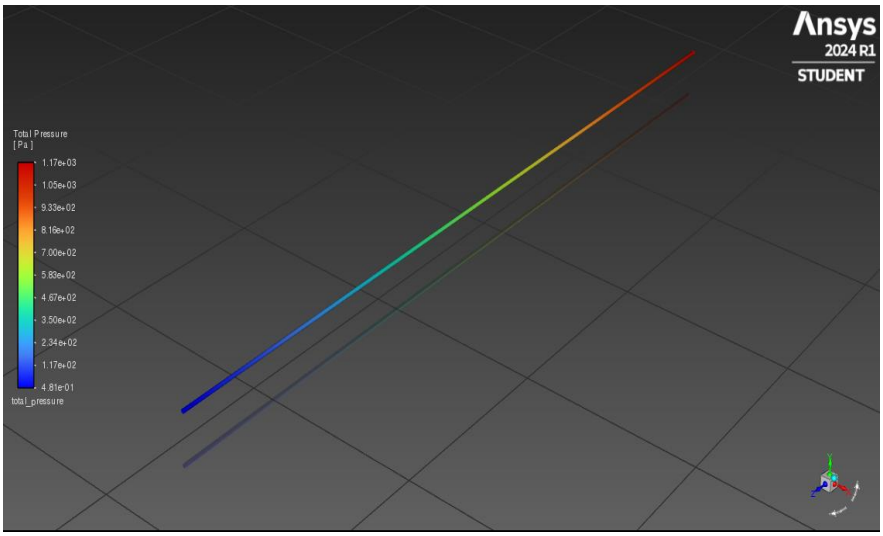

Figure C.47: Paul Rounded Inlet Tube 20µL/min Pressure Contour Plot

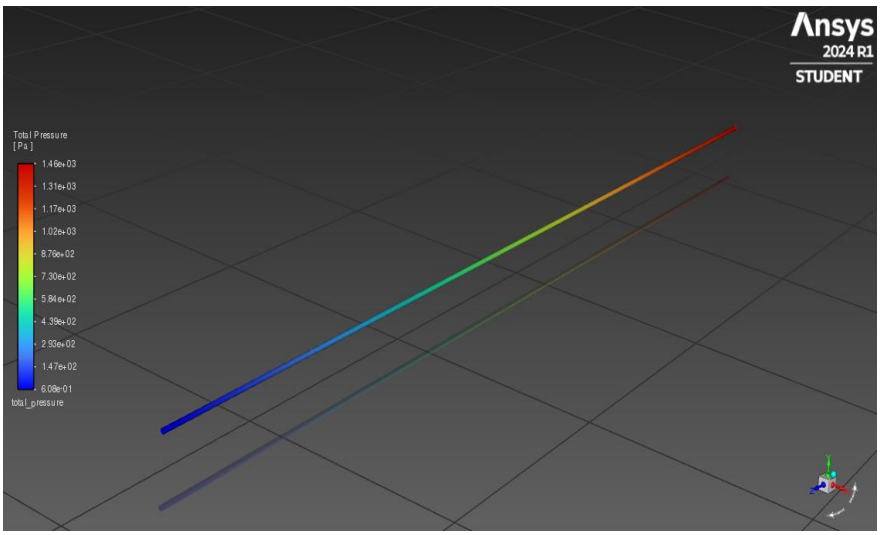

Figure C.48: Paul Rounded Inlet Tube 25µL/min Pressure Contour Plot

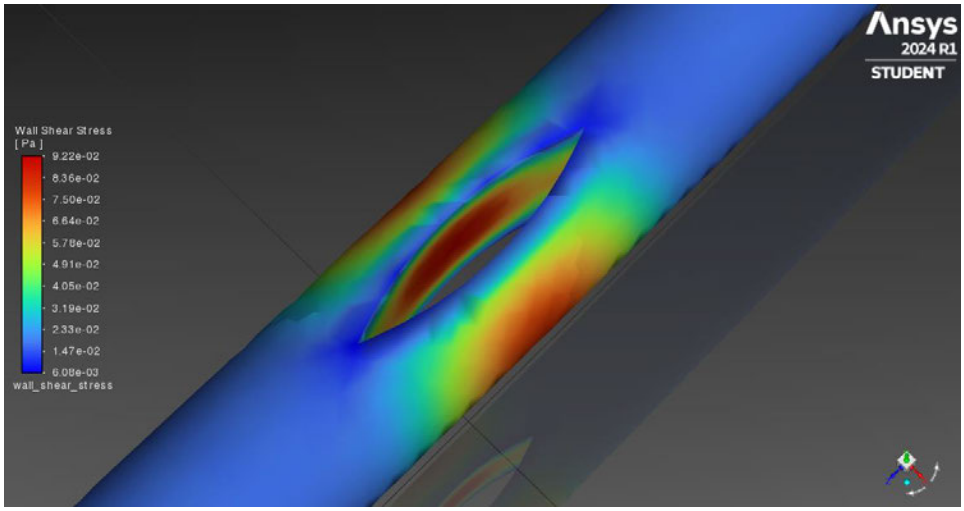

Figure C.49: Baerveldt Single Fin Tube 5µL/min Wall Shear Stress Distribution

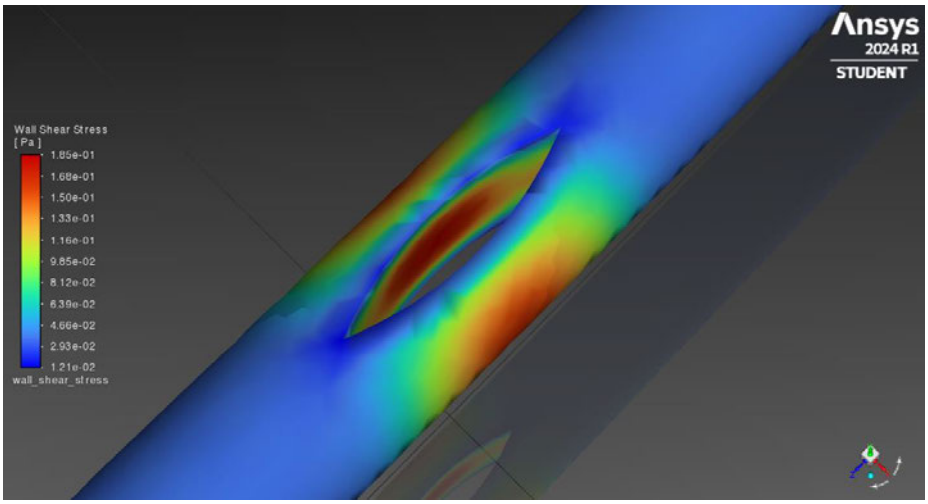

Figure C.50: Baerveldt Single Fin Tube 10µL/min Wall Shear Stress Distribution

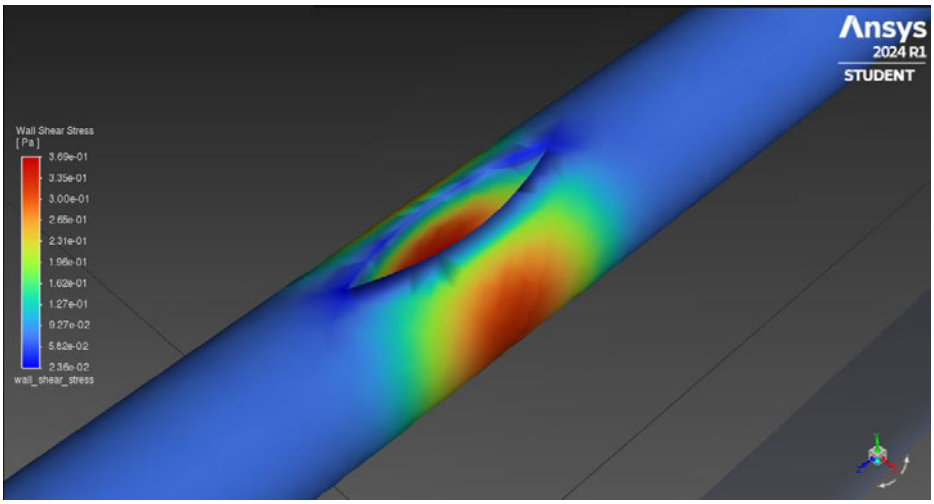

Figure C.51: Baerveldt Single Fin Tube 20µL/min Wall Shear Stress Distribution

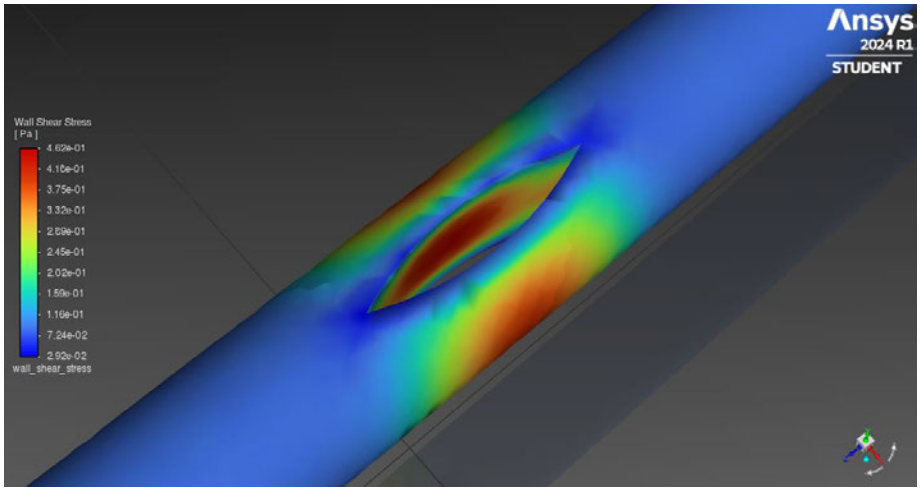

Figure C.52: Baerveldt Single Fin Tube 25µL/min Wall Shear Stress Distribution

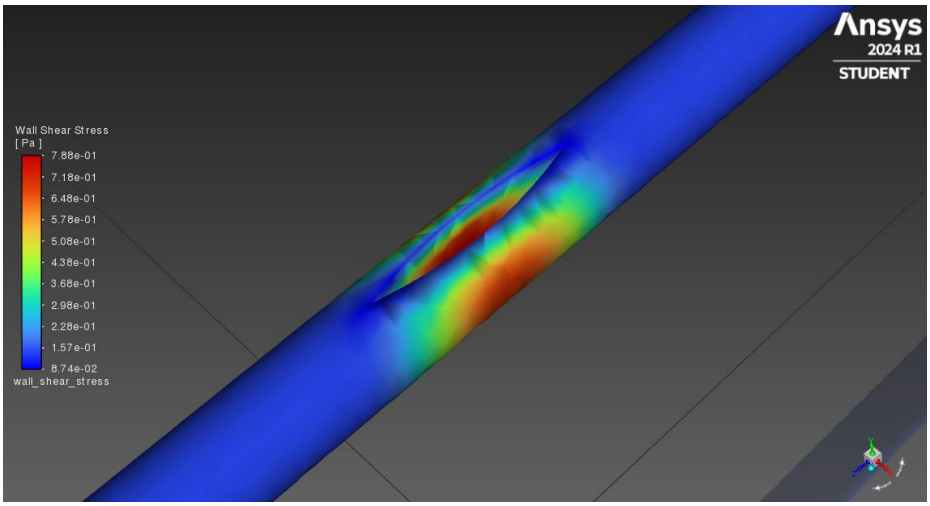

Figure C.53: Paul Single Fin Tube 5µL/min Wall Shear Stress Distribution

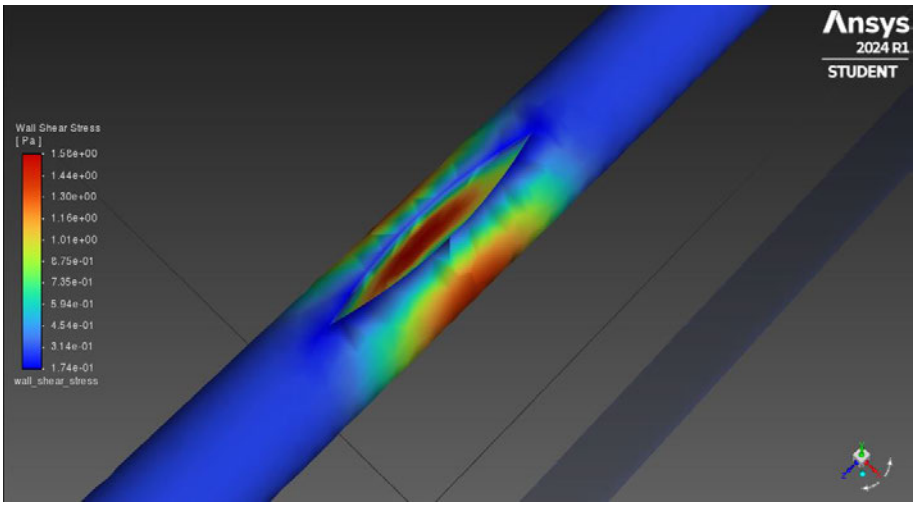

Figure C.54: Paul Single Fin Tube 10µL/min Wall Shear Stress Distribution

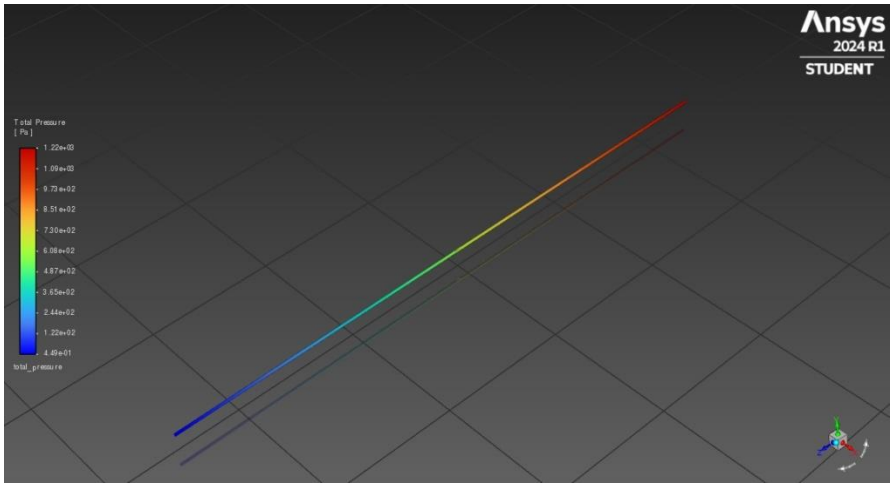

Figure C.55: Paul Single Fin Tube 20µL/min Wall Shear Stress Distribution

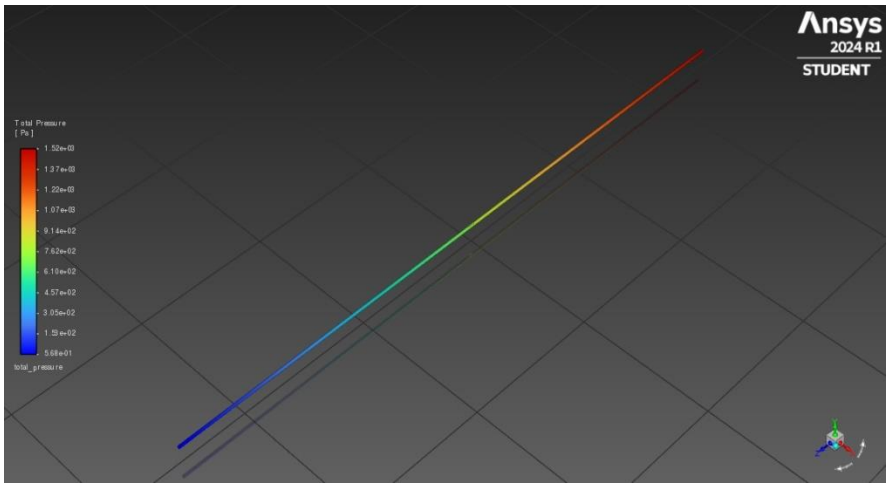

Figure C.56: Paul Single Fin Tube 25µL/min Wall Shear Stress Distribution

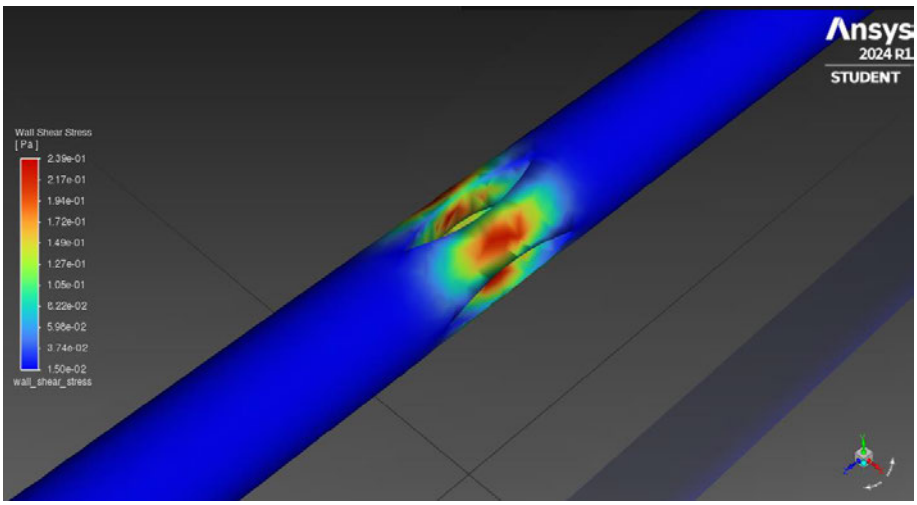

Figure C.57: Baerveldt Double Fin Tube 5µL/min Wall Shear Stress Distribution

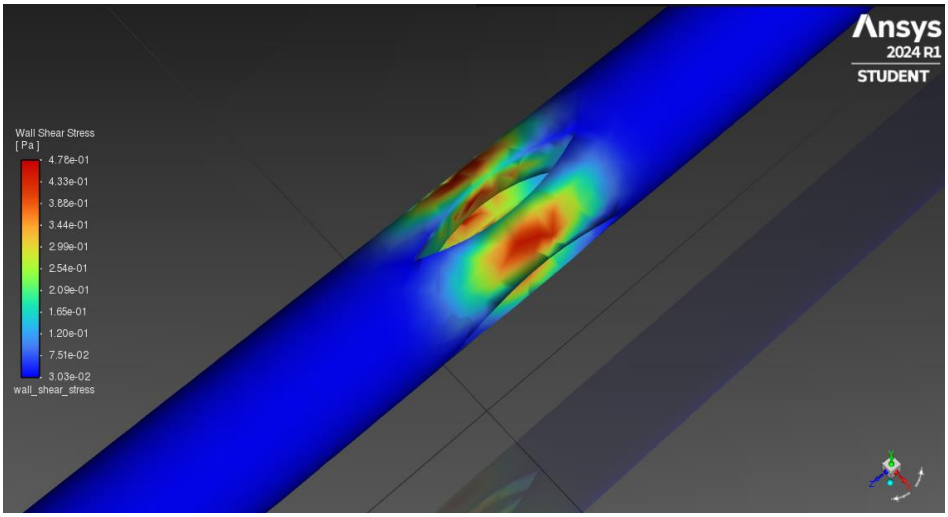

Figure C.58: Baerveldt Double Fin Tube 10µL/min Wall Shear Stress Distribution

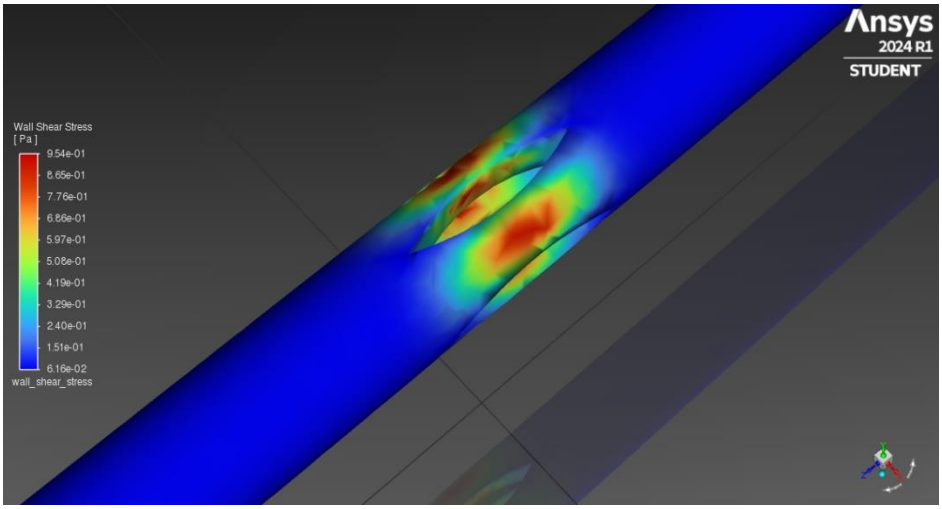

Figure C.59: Baerveldt Double Fin Tube 20µL/min Wall Shear Stress Distribution

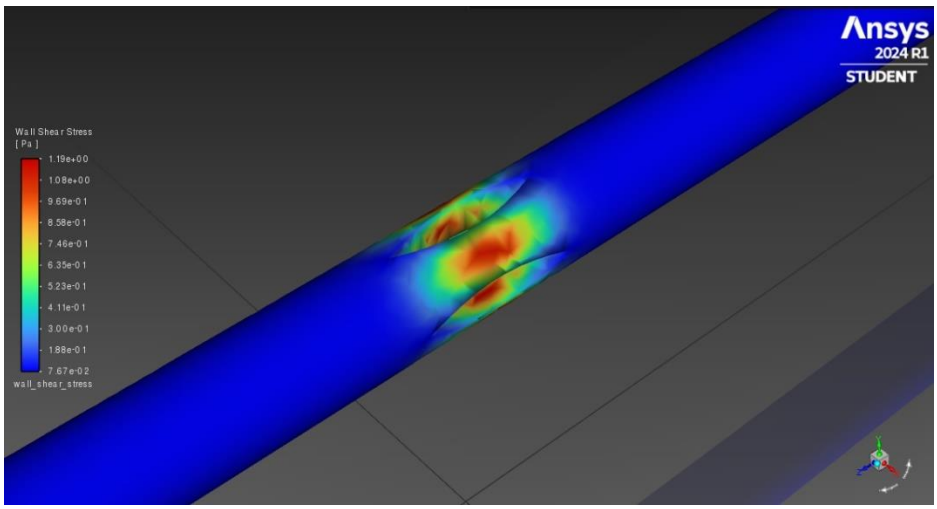

Figure C.60: Baerveldt Double Fin Tube 25µL/min Wall Shear Stress Distribution

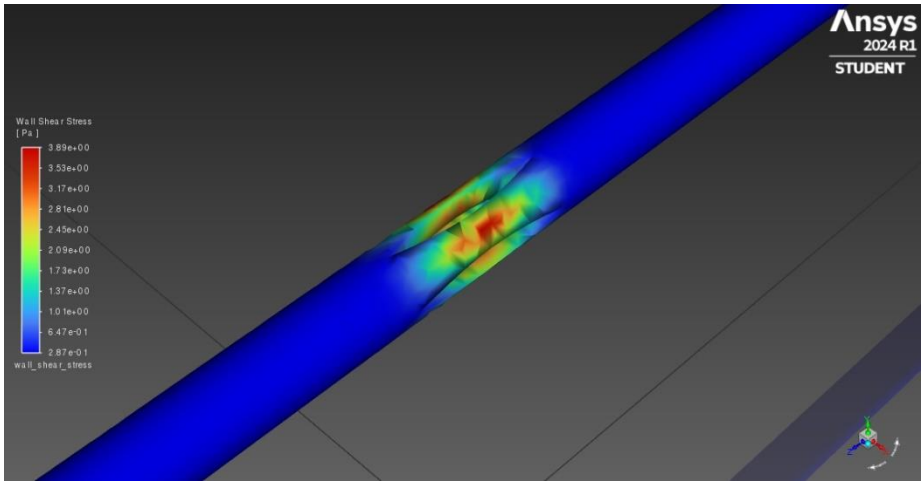

Figure C.61: Paul Double Fin Tube 5µL/min Wall Shear Stress Distribution

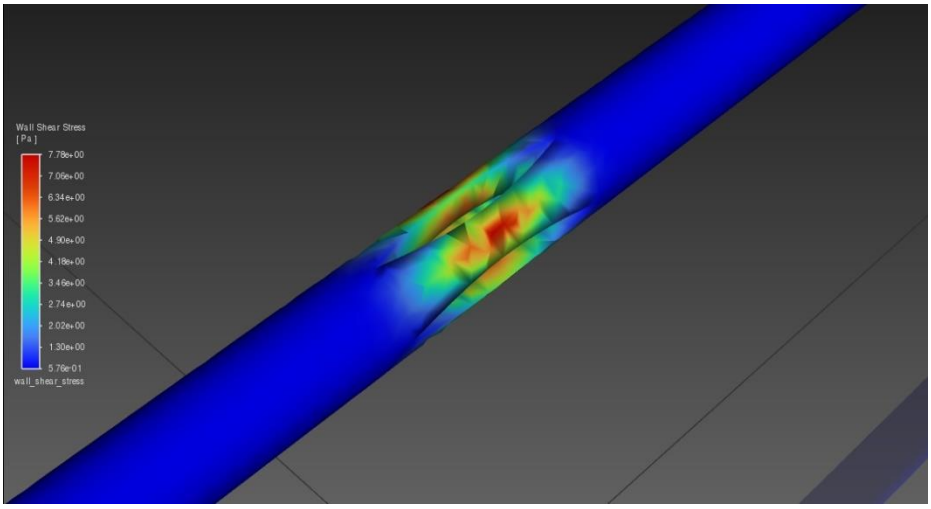

Figure C.62: Paul Double Fin Tube 10µL/min Wall Shear Stress Distribution

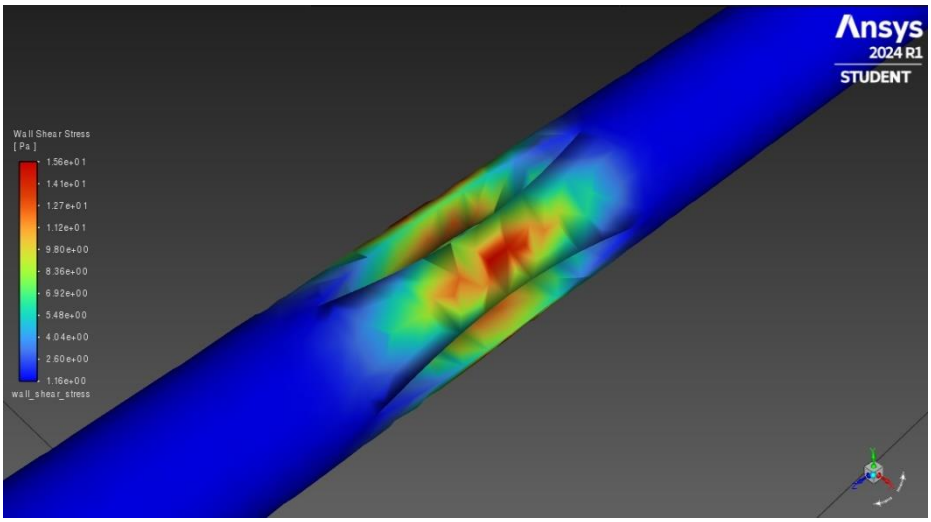

Figure C.63: Paul Double Fin Tube 20µL/min Wall Shear Stress Distribution

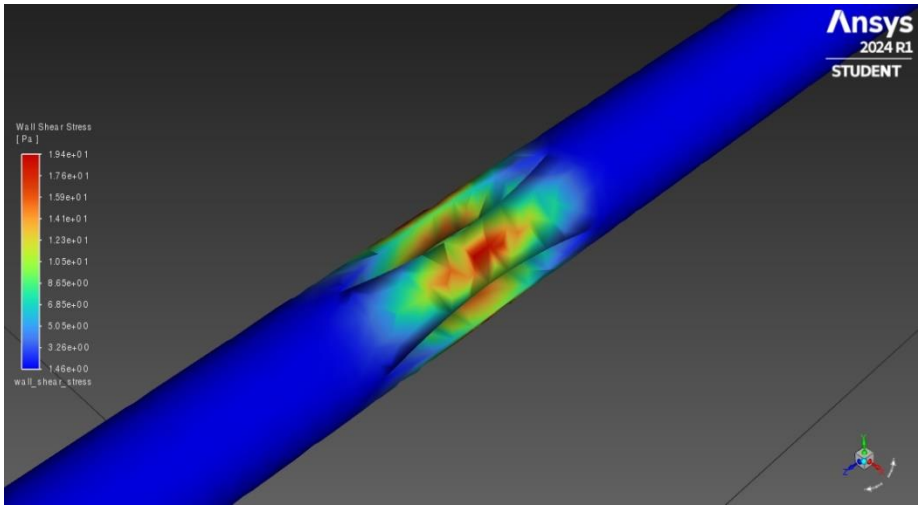

Figure C.64: Paul Double Fin Tube 25µL/min Wall Shear Stress Distribution

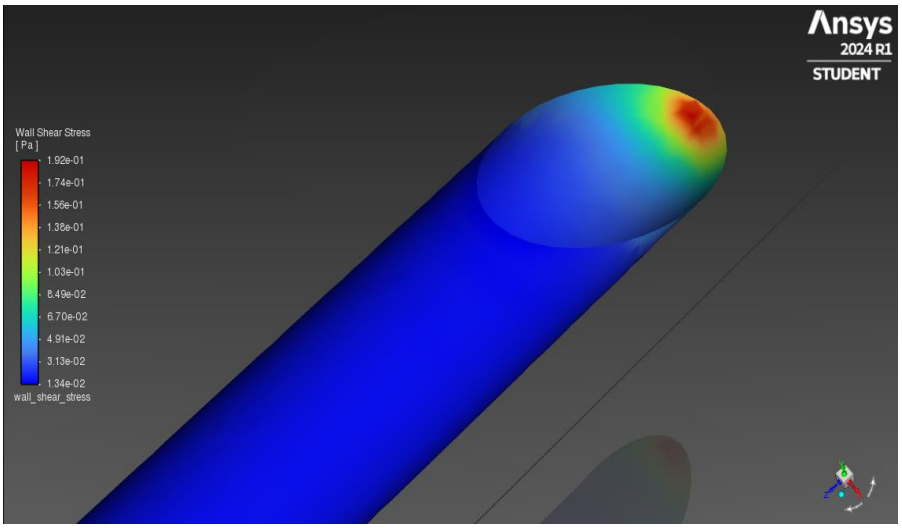

Figure C.65: Baerveldt Snipped Tube 5µL/min Wall Shear Stress Distribution

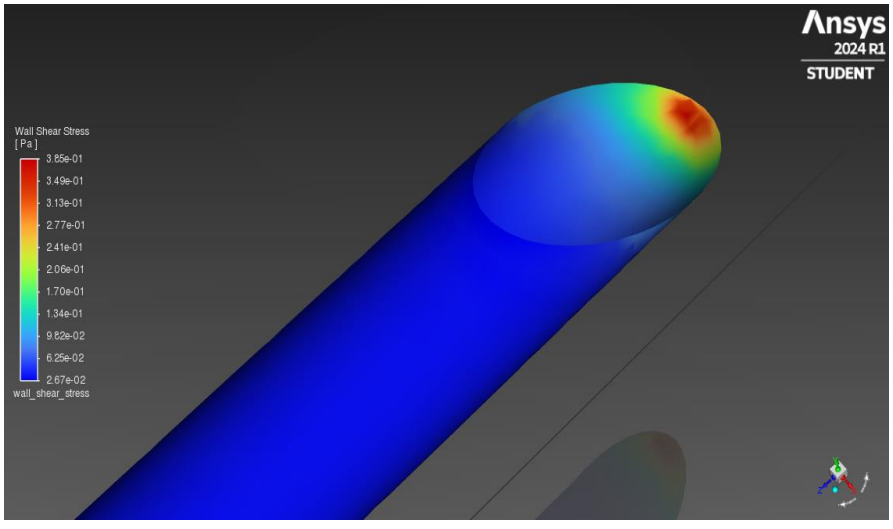

Figure C.66: Baerveldt Snipped Tube 10µL/min Wall Shear Stress Distribution

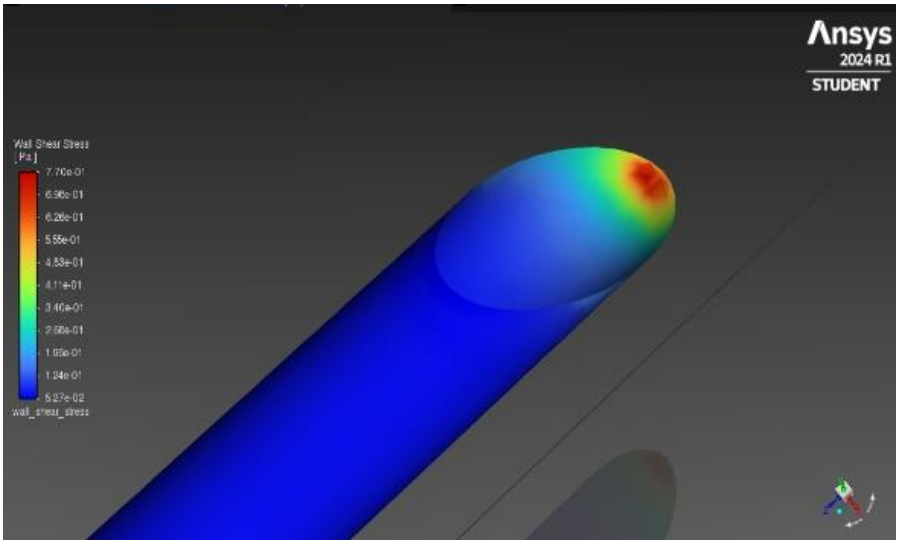

Figure C.67: Baerveldt Snipped Tube 20µL/min Wall Shear Stress Distribution

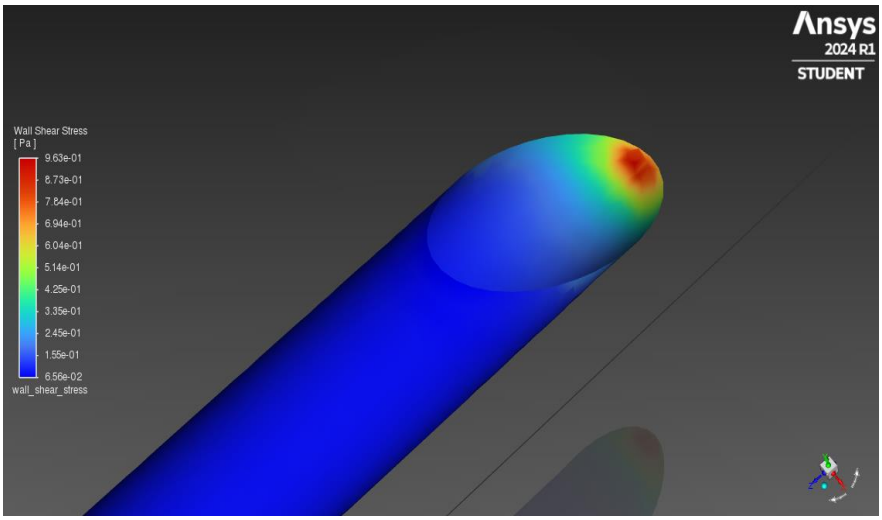

Figure C.68: Baerveldt Snipped Tube 25µL/min Wall Shear Stress Distribution

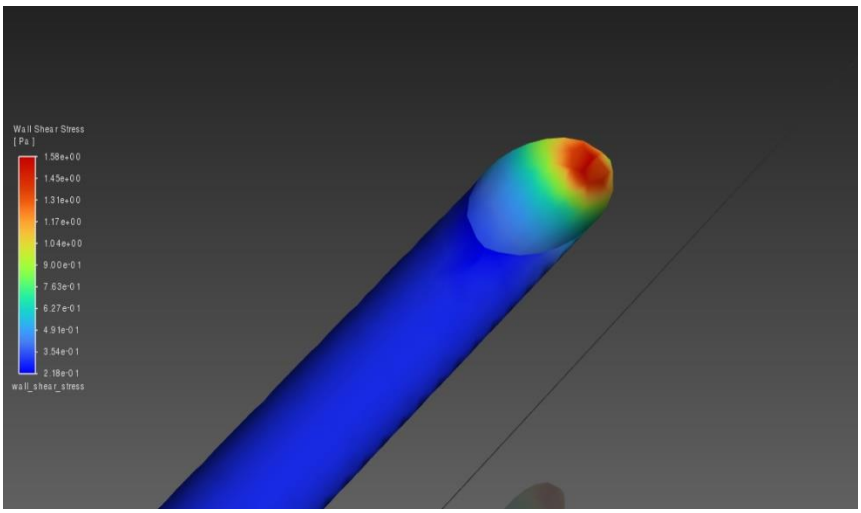

Figure C.69: Paul Snipped Tube 5µL/min Wall Shear Stress Distribution

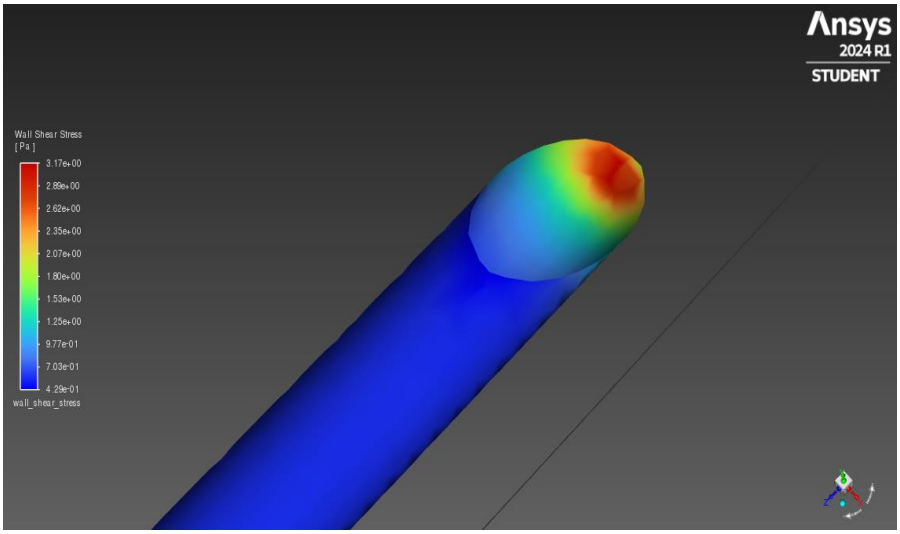

Figure C.70: Paul Snipped Tube 10µL/min Wall Shear Stress Distribution

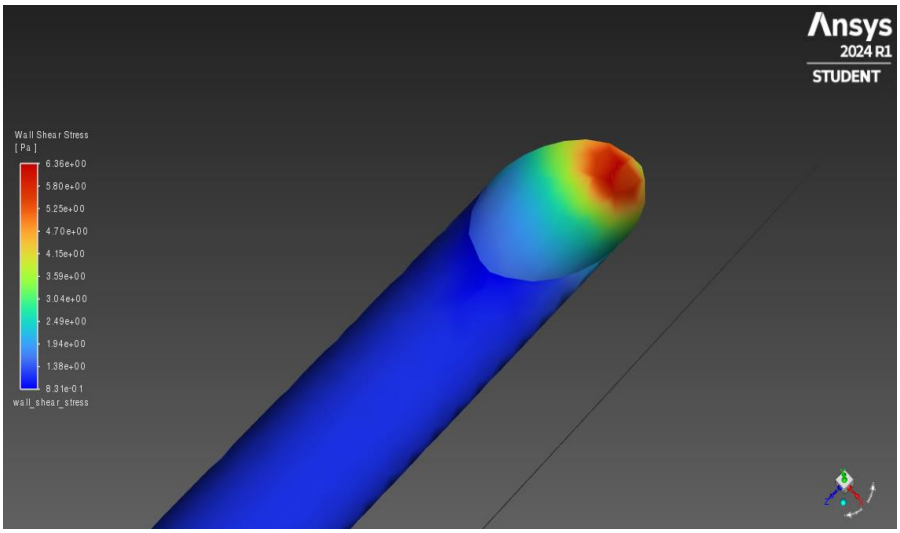

Figure C.71: Paul Snipped Tube 20µL/min Wall Shear Stress Distribution

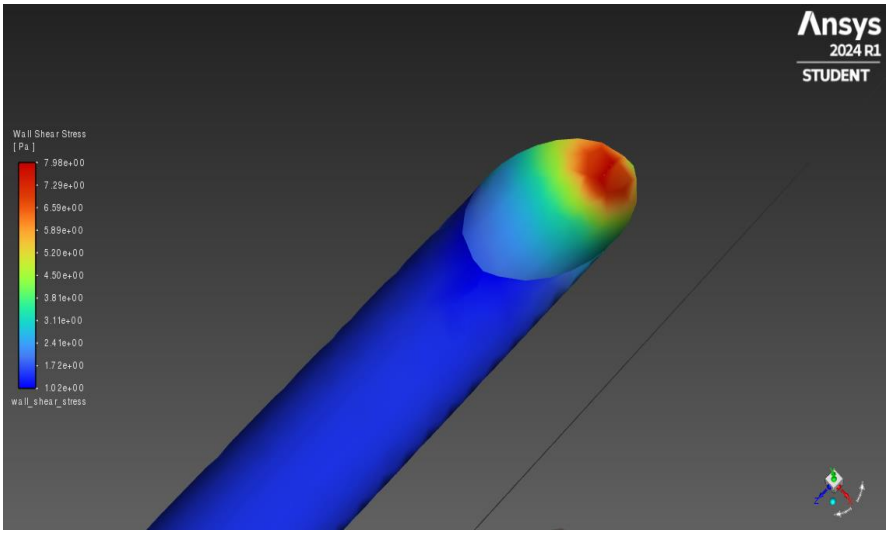

Figure C.72: Paul Snipped Tube 25µL/min Wall Shear Stress Distribution

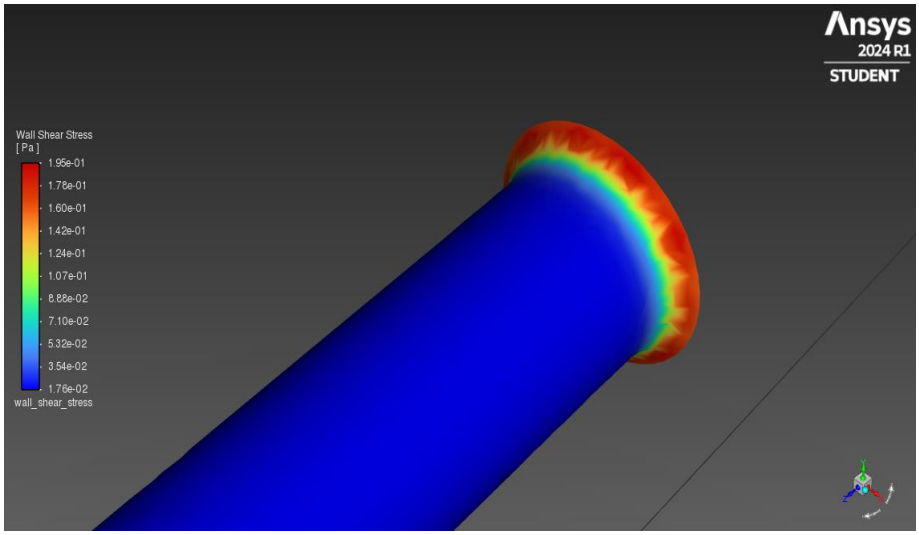

Figure C.73: Baerveldt Rounded Inlet Tube 5µL/min Wall Shear Stress Distribution

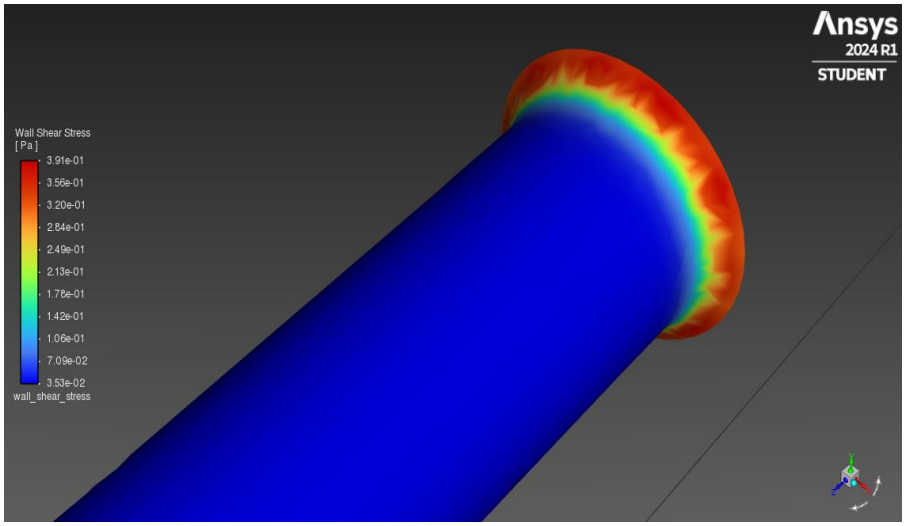

Figure C.74: Baerveldt Rounded Inlet Tube 10µL/min Wall Shear Stress Distribution

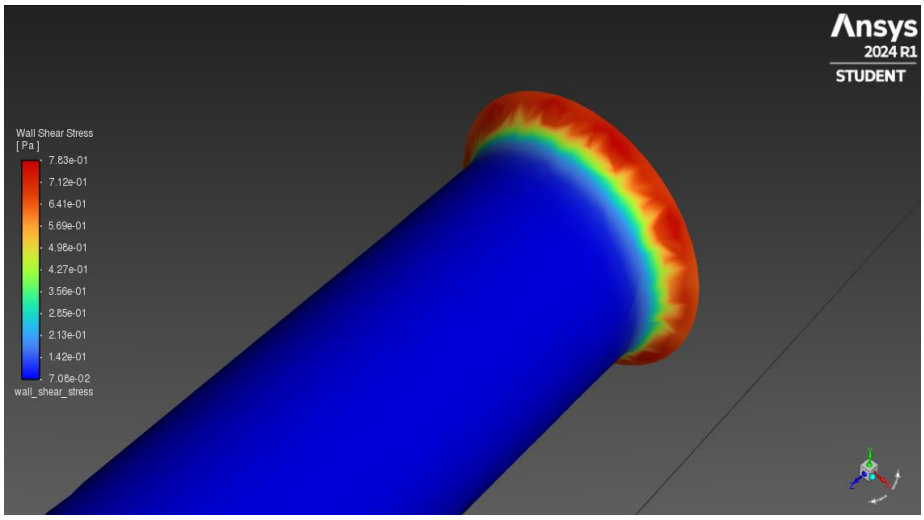

Figure C.75: Baerveldt Rounded Inlet Tube 20µL/min Wall Shear Stress Distribution

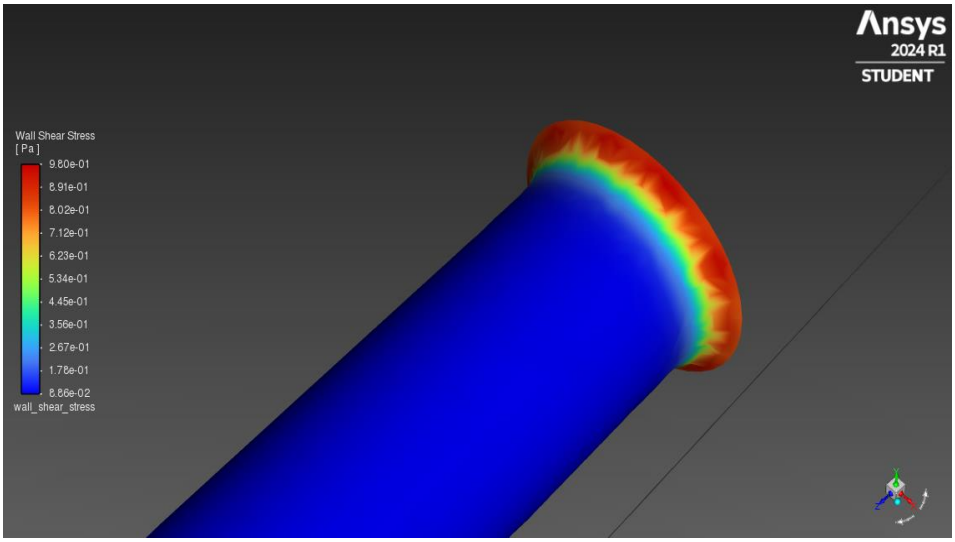

Figure C.76: Baerveldt Rounded Inlet Tube 25µL/min Wall Shear Stress Distribution

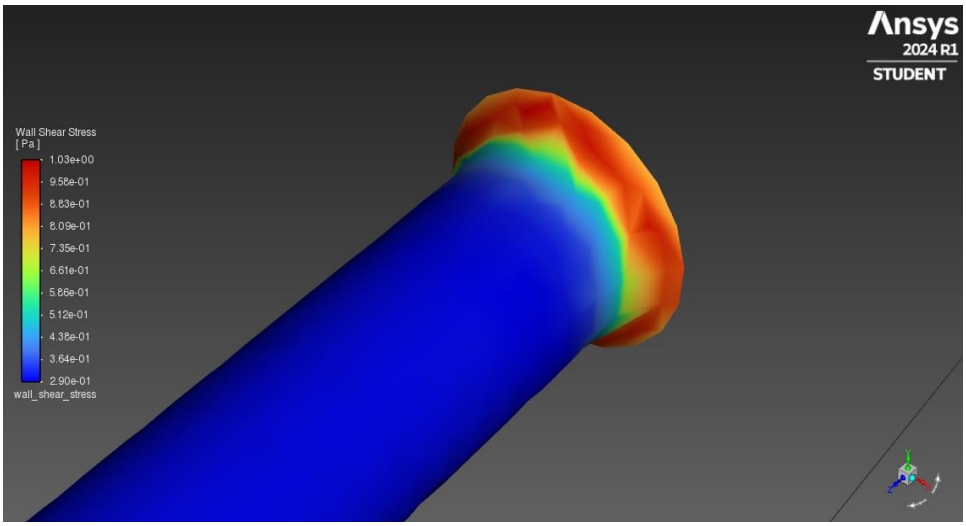

Figure C.77: Paul Rounded Inlet Tube 5µL/min Wall Shear Stress Distribution

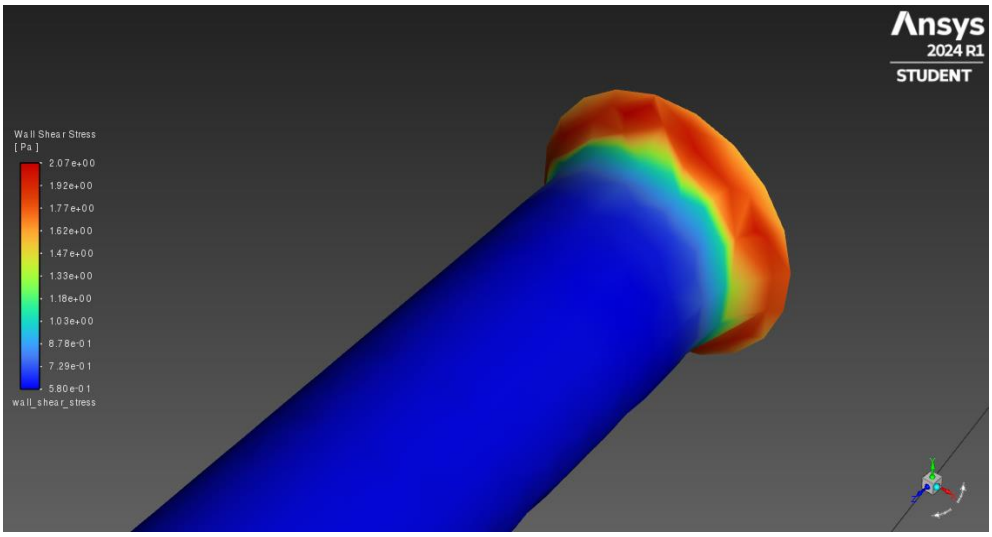

Figure C.78: Paul Rounded Inlet Tube 10µL/min Wall Shear Stress Distribution

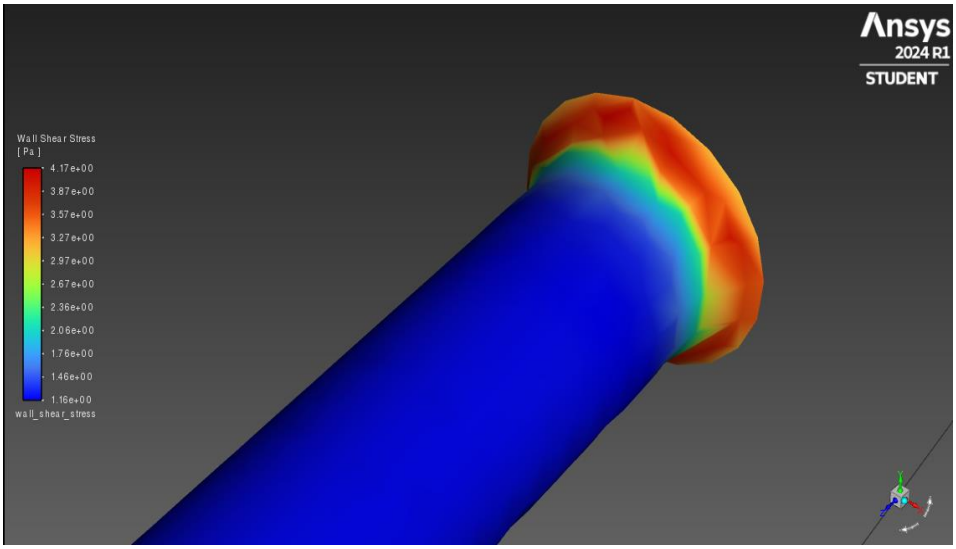

Figure C.79: Paul Rounded Inlet Tube 20µL/min Wall Shear Stress Distribution

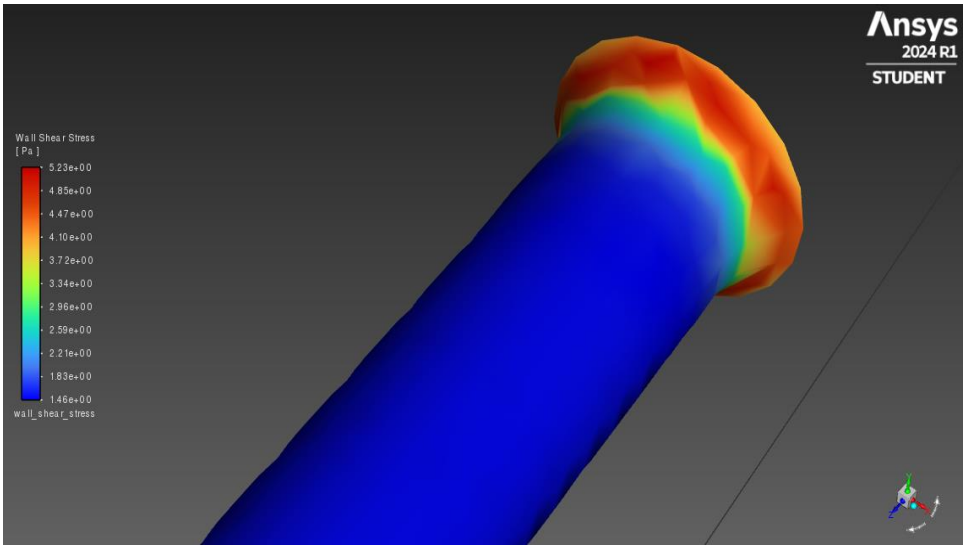

Figure C.80: Paul Rounded Inlet Tube 25µL/min Wall Shear Stress Distribution